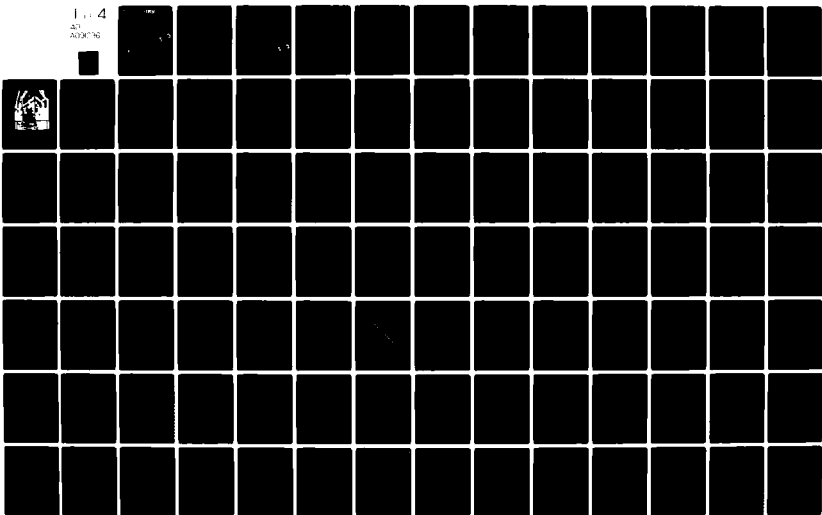AD-A091 296   ALABAMA UNIV IN HUNTSVILLE SCHOOL OF SCIENCE AND ENG--ETC F/G 20/5
              DEVELOPMENT AND ANALYSIS OF CLOSED CYCLE CIRCULATOR ELEMENTS.(U)
              MAY 80 C C SHIH, G R KARR, J F PERKINS   DAAK40-78-C-0219
UNCLASSIFIED UAH-RR-244   DRSMI/RH-80-9-TR   NL

1 OF 4
AD
A091296

LEVEL

UAH Research Report No. 244

Technical Report TR-RH-80-9

DEVELOPMENT AND ANALYSIS OF CLOSED CYCLE CIRCULATOR ELEMENTS

Cornelius C. Shih
Principal Investigator

The University of Alabama in Huntsville
School of Science and Engineering
Huntsville, AL 35899

DTIC
SELECTED
NOV 7 1980

B

May 1980

Final Technical Report: Contract DAAK40-78-C-0219

APPROVED FOR PUBLIC RELEASE: DISTRIBUTION UNLIMITED

Period Covered: July 31, 1978 - May 31, 1980

Prepared for

Directed Energy Directorate
U. S. Army Missile Laboratory
U. S. Army Missile Command
Redstone Arsenal, AL 35809

80 10 7 032

REPORT DOCUMENTATION PAGE		READ INSTRUCTIONS BEFORE COMPLETING FORM
1. REPORT NUMBER Technical Report TR-RH-80-9 ✓	2. GOVT ACCESSION NO. AD A091296	3. RECIPIENT'S CATALOG NUMBER
4. TITLE (and Subtitle) Development and Analysis of Closed Cycle Circulator Elements		5. TYPE OF REPORT & PERIOD COVERED Final Technical Report July 31, 1978 – May 31, 1980
		6. PERFORMING ORG. REPORT NUMBER ✓ UAH Research Report No. 244
7. AUTHOR(s) Cornelius C. Shih Gerald R. Karr James F. Perkins		8. CONTRACT OR GRANT NUMBER(s) DAAK40-78-C-0219
9. PERFORMING ORGANIZATION NAME AND ADDRESS University of Alabama in Huntsville School of Science and Engineering Huntsville, AL 35899		10. PROGRAM ELEMENT, PROJECT, TASK AREA & WORK UNIT NUMBERS
11. CONTROLLING OFFICE NAME AND ADDRESS Headquarters U. S. Army Missile Command ATTN: DRSMI-IYD/Florence, Redstone Arsenal, AL		12. REPORT DATE May 1980
		13. NUMBER OF PAGES 321
14. MONITORING AGENCY NAME & ADDRESS(if different from Controlling Office)		15. SECURITY CLASS. (of this report) Unclassified
		15a. DECLASSIFICATION/DOWNGRADING SCHEDULE

16. DISTRIBUTION STATEMENT (of this Report)

APPROVED FOR PUBLIC RELEASE: DISTRIBUTION UNLIMITED

17. DISTRIBUTION STATEMENT (of the abstract entered in Block 20, if different from Report)

18. SUPPLEMENTARY NOTES

19. KEY WORDS (Continue on reverse side if necessary and identify by block number)

laser circulator, fluid and thermal characteristics of recirculating flows, acoustic attenuators, numerical analysis of the recirculating flow

20. ABSTRACT (Continue on reverse side if necessary and identify by block number)

A series of experiments with various flow rates of laser gas and coolants under several levels of energy inputs has been conducted on the Army Closed Cycle Circulator for pulsed EDL to collect sufficient data for flow calibration and coefficient determination. Verification of the theoretical models depicting the functions of the heat exchangers in maintaining the thermal balance in the flow through the steady and transient states are made through comparison with results of the experimental analysis.

DD FORM 1473 EDITION OF 1 NOV 65 IS OBSOLETE
1 JAN 73
S/N 0102-014-6601

Unclassified

TABLE OF CONTENTS

PREFACE

This research project entitled "Development and Analysis of Closed Cycle Circulator Elements" under the Army Contract (DAAK40-78-C-0219) for the period from July 31, 1978 to May 31, 1980 has been completed and reported in two sections.

The first section presents our efforts expended on the development and analysis of closed cycle circulator elements from the standpoint of fluid and thermal engineering. Results of these efforts are reported by Cornelius C. Shih, Gerald R. Karr, David Walker, Bill Jones, Kate McMyler, Martin Dahm, Tom Turner, and David Herda.

The second section presents our efforts expended on the development of computer codes for optical analysis pertinent to the unstable resonators as they apply to excimer lasers. Results on these efforts are reported by James F. Perkins.

Our supporting staff including Kathy Wagner, Nick Crowe and Louise Fogle have effectively assisted our effort in writing this report.

<div align="right">

Cornelius C. Shih
Principal Investigator

</div>

SECTION 1

DEVELOPMENT AND ANALYSIS OF CLOSED CYCLE CIRCULATOR ELEMENTS

I.   Introduction

In the development of the pulsed Electric Discharge Laser (EDL), the use of Closed Cycle Circulator for removing the heated laser gas from the cavity section has been determined to be advantageous over open cycle systems from the standpoints of run time and gas economy. However, the lack of technical data on: the characteristics and stability of fluid and thermal properties of the recirculating laser gas flow under the pulsed energy input; plasma formation; level pumping ability; shock wave attenuation capability; heat exchanger capability; gas contamination rates; and the gas reactor capability, has strongly justified the need of developing a laboratory-scale Closed Cycle Circulator at a relatively low cost to investigate the above mentioned problem areas and obtain experimental data of the circulator performance under simulated pulsed laser operations.

The program undertaken presently by Army Missile Laboratory [1] has as its objectives to develop the Closed Cycle Circulator, to experimentally analyze the circulator performance under various pulsed energy input conditions, and to compare with theoretical analysis of the circulator performance. At the conclusion of the program, the data obtained and analyzed as well as the knowledge and experience gained will result in the establishment of design criteria and detailed component performance specifications for a low risk circulator system of future generation, minimizing overall weight and volume.

In the design of the circulator system, a size of the circulator was so chosen to yield scaling laws for satisfying possible system design requirements, and a hot cathode electron beam gun and drive were selected to provide high current density. A pulsed power supply having a 50 KV peak voltage and 1000 ampere peak current will be gated on and off synchronically with the E-beam gun allowing appropriate delay time for plasma formation of 5x5x25 cm. The laser cavity size was selected on the basis of the available discharge power capability and a possible magnitude and frequencies of acoustic waves generated in the cavity. The circulator size in length was designed to accommodate a pulse repetition rate up to 125 pps without wave interferences within the flow loop. In the final, a significant cost saving has resulted from this particular design of the circulator system due to the selections of size, configuration, bearing seal, and control system.

Through this program, the circulator system will be developed for the purpose of studying the component's requirements and technical methods of solution to the following areas of problems pertinent to the pulsed electric discharge laser technology:

1) Acoustic attenuators to improve homogeneity to a designed level of density fractional gradient with a minimum flush factor.

2) Circulator system performance in response to start-up, pre-lasing, heat input lasing, heat removal at various flow conditions.

3) Laser gas stability, composition, and contamination during the circulator operation and the verification of Closed Cycle pulse laser gas stability and plasma chemistry models.

2

4) Heat exchanger requirements with respect to the medium homogeneity and pressure loss in the flow loop.

5) Validation of the analytical models through computer programs for steady state and unsteady cases under pulsed energy input at various levels and repetition rates.

6) Suitability of a high speed radial flow compressor for pulsed energy input operations.

7) Materials evaluation and selection for components compatible with the Closed Cycle laser operation in the E-beam environment and their effects.

8) Compressor bearing and seal design evaluation and their improvements.

9) Experiments on power gain at the laser cavity.

II. General Description and Specifications

The Army Closed Cycle Circulator System consists of the following components [2]:

1) A motor driven compressor to circulate gas in a closed duct system for electrical discharge laser experiments.

2) A diverter valve and bypass to permit varying the gas flow in the main part of the duct system. The diverter valve consists of linked flapper valves in the main part of the duct system and in the bypass. These are arranged to operate in opposite ways so that as the flapper in the main duct closes the flapper in the bypass opens and less of the gas flows in the main duct and more in the bypass.

3) A compressor exit heat exchanger to remove the heat of compression. This is a shell and tube type with gas flow through the tubes.

4) A cavity inlet heat exchanger to condition the gas to the desired cavity temperature. This is also shell and tube with gas flow through the tubes.

5) A compressor inlet heat exchanger to remove the heat of lasing or in the case of bypass operation, the heat of compression from the gas before the latter enters the compressor. This is also shell and tube with gas flow through the tubes.

6) Ducting to connect the various units. Heating tapes are provided for the ducts.

7) Bellows at the compressor inlet and exit to isolate the compressor from the thermal expansion and contraction of the ducts.

8) A flowmeter to measure the gas flow.

9) Honeycomb and screen to remove turbulence from the gas flow prior to entering the laser cavity.

10) A laser cavity designed by GE&M Directorate, Army Missile Laboratory

11) A water coolant supply including tank, centrifugal pump, relief and throttling valves for the compressor exit and inlet heat exchangers. The tank is fitted with a provision for liquid nitrogen cooling of the water.

12) A freon TA coolant supply including supply tank, catch tank, gear pump, relief and throttling valves for the cavity inlet heat exchanger. The supply tank is fitted with a provision for liquid

4

nitrogen cooling of the freon TA. The supply tank, pump, cavity inlet heat exchanger and lines are insulated with 2-inch polyurethane foam. During the chilling operation freon TA is pumped continuously through the complete loop (run tank, heat exchanger, catch tank, and returning again to the run tank). This same operating mode may be used during a lasing test, or optionally, the catch tank can be isolated from the run tank by means of the manual valve provided.

13) A gas system is for purging the outside face of the compressor seal during evacuation of the duct, for adding makeup gas to the system, and for applying gas pressure to the inside face of the compressor seal at start up to lift off the seal.

14) A control system for starting and stopping the compressor, water pump, and freon TA pump; and for controlling the positions of the diverter valve and the three heat exchanger throttling valves. An independent servo control is provided to maintain cavity pressure constant by controlling a vent valve on the duct.

15) An instrumentation sub-system to measure pressures and temperatures at various locations around the duct for the purpose of operating the system to obtain cavity inlet temperatures from 200°K to 300°K.

16) In addition to the basic instrumentation system of 15 there are provisions for installing 6 Kistler pressure transducers at various locations around the duct, for installing 6 hot wire anemometers of which 3 are upstream and 3 downstream of the

5

cavity, and for installing gas sampling probes before the
cavity and after the reactor.

17) An e-beam gun and power modulator for generating energy
pulse input at various pulse rates and magnitudes.

18) An interferometer subsystem to measure optically the
medium homogeneity on an integrated base at the cavity section.

19) A mass spectrometer subsystem to measure chemical compositions
of the laser gas at various locations in the circulator.

20) Safety provisons during the circulator operation are made by
installing two gas monitors for freon TA and one monitor for
oxygen to detect the danger levels of respective gases for human
safety and fire and explosion hazards of the building.

21) Two acoustic attenuators are designed and fabricated to be in-
stalled upstream and downstream of the cavity for the purpose of
attenuating acoustic waves generated by the pulsed energy input
operation.

22) A gas reactor or so-called catalytic converter is designed and
fabricated to be installed downstream from the cavity so as to re-
move foreign elements from the laser gas with a designed composition.

Figures II-1 and II-2 present general views of the Closed Cycle
Circulator system (C^3 system).

The circulator system characteristics and weight breakdown of the
system components are listed in Tables 1 and 2 respectively.

Specifications of the components are delineated below:

(A) Circulator System

6

TEMPERATURE PROBE
PRESSURE PROBE
GAS SAMPLE PROBE
HOT WIRE ANEMOMETER
KISTLER PORT
MASS SPECTROMETER PORT

HEAT EXCHANGER TWO

HEAT EXCHANGER THREE

HEAT EXCHANGER ONE

CERAMIC HONEYCOMB

ACOUSTIC SCREEN PACK ASSEMBLY

REACTOR
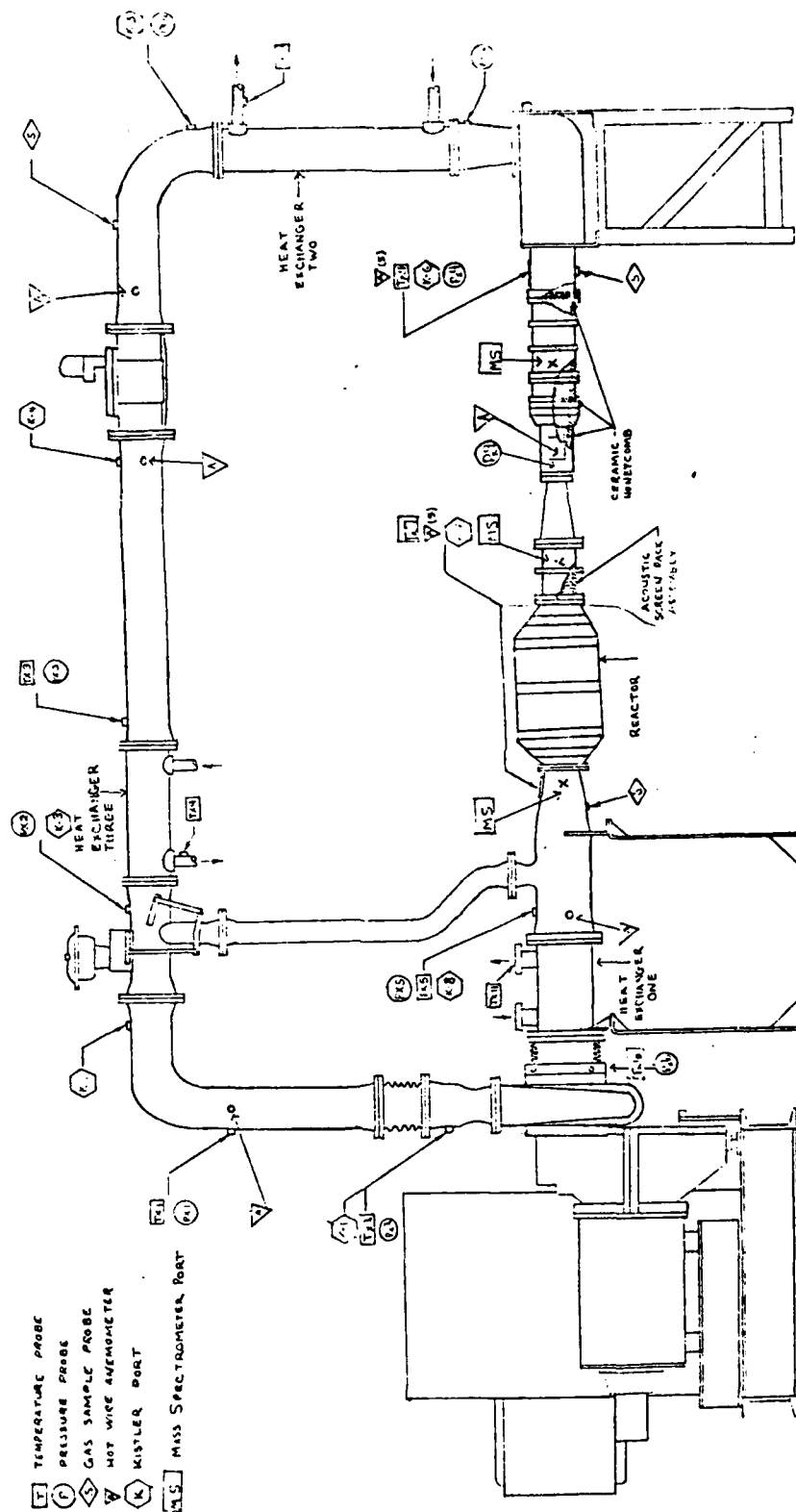
Figure II-1.
Schematic of CCC System

ARMY CLOSED CYCLE CIRCULATOR
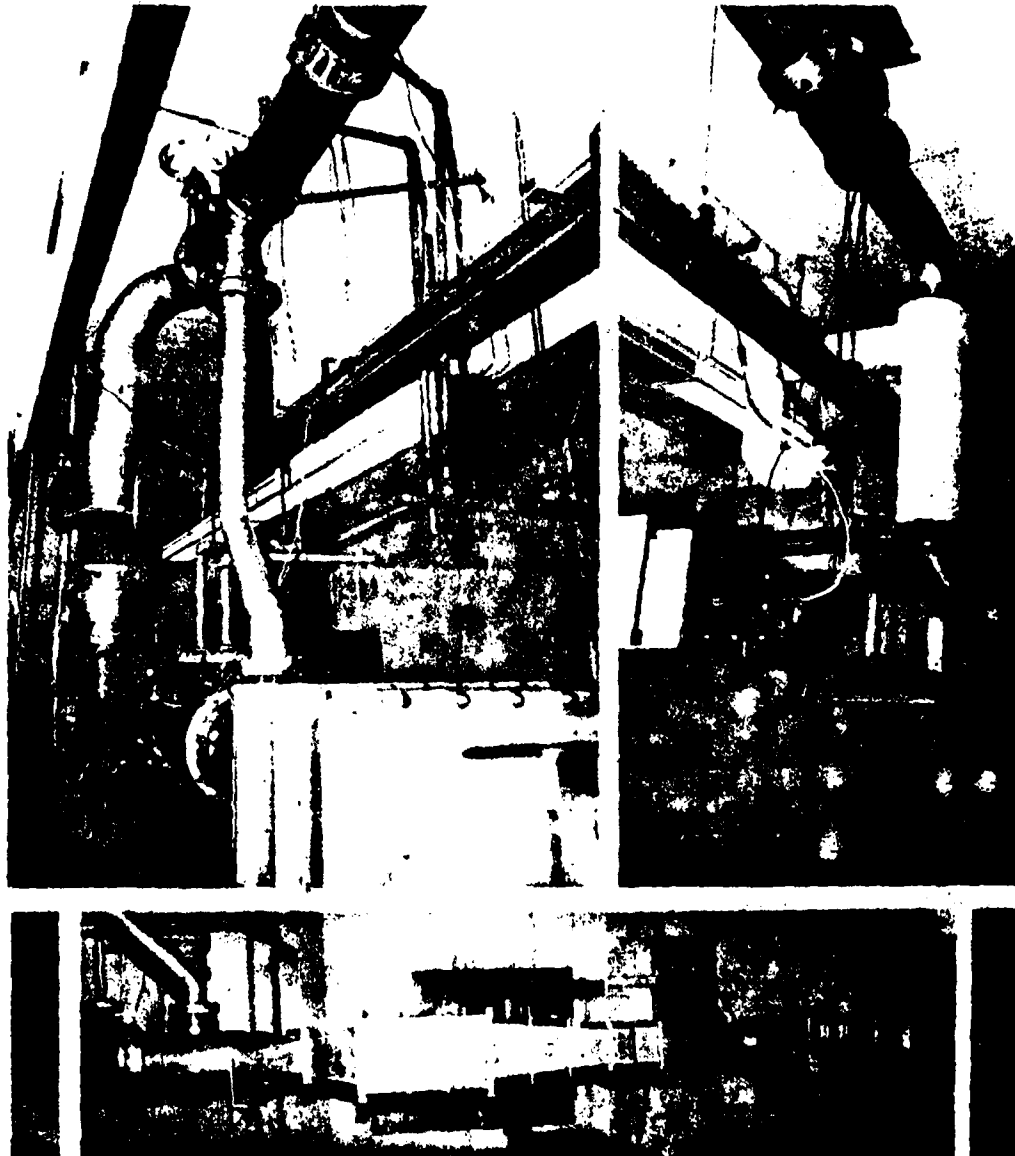
Figure II-2. General View

1. Compressor

The single stage compressor consists of an overhung open type 19 vane impeller, inlet shroud, and 11 vane diffuser installed in a cast steel housing. The impeller is mounted directly on the high speed pinion shaft which is supported in two tilting pad bearings. The main motor drives the pinion through a gear type coupling and single step speed increaser gear supported in two sleeve bearings. The gears are of hardened steel and ground to AGMA standards. The gearbox is horizontally split in the pinion plane permitting easy inspection of the high speed bearings and removal and installation of the rotor assembly. The compressor shaft is sealed with a Crane Type 28 Kinetic Wedge gas seal for positive static sealing. A unitized fabricated steel base supports the drive motor, gear casing and compressor housing. It also forms the oil pump and contains the lubrication system for the unit. The lubrication system for the drive motor is self-contained and the gearbox lubrication is supplied by the unit system. Lube oil cooling is accomplished by a separate shell and tube oil to water heat exchanger. The unit is supplied with an electric/pneumatic control system which monitors all critical parameters and provides permissive circuits along with alarm and shutdown circuitry for safe operation of the equipment.

The specifications for the unit are as follows:

Inlet	10-inch ANSI 125 lb. flange
Outlet	6-inch ANSI 125 lb. flange

Gas 3:2:1 molar mix of $He:N_2: CO_2$

Molecular weight	18.8
Cp/Cv	1.48
Inlet pressure	11.4 psia
Inlet temperature	$116°F$
Inlet volume	2425 cfm

TABLE 1. CLOSED-CYCLE CIRCULATOR SYSTEM CHARACTERISTICS

Operating conditions

Gas composition (nominal 3:2:1 mix)

Helium, mole percent	50.0
Nitrogen, mole percent	33.3
Carbon dioxide, mole percent	16.7
Mass flowrate, lb/sec	0.3 to 1.4

Pressure drop (maximum at 1.4 lb/sec) (psid)

Total loop	(8.4)
Compressor exit heat exchanger	0.6
Flowmeter	0.5
Cavity inlet heat exchanger	0.43
Cavity plus acoustic attenuators	6.0
Cavity exit heat exchanger	0.36
Compressor pressure ratio (maximum)	1.8

10

Compressor speed (rpm)	33,000
Laser cavity inlet temperature (^{o}K)	200 to 300
Laser Cavity pressure (psia)	15
Static conditions	
Pressure	
Maximum (psia)	30
Minimum (microns)	500
Coolant storage conditions	
Water	
Capacity (gallons)	110
Pump outlet pressure (psia)	35.1
Freon TA	
Capacity (lb)	110
Pressure at 180° (psia)	100 (Approx.)

TABLE 2. CCC SYSTEM WEIGHT BREAKDOWN

	Pounds
Compressor and drive	6760
Interconnect ducting (including flanges)	320
Compressor exit heat exchanger	84
Flowmeter	80
Cavity inlet heat exchanger	103
Cavity simulator	108
Cavity exit heat exchanger	92
Water supply system	105
Freon TA supply system	168
Controls	200

		Pounds
Motor-driven water pump		100
	Dry weight	8120
Water		889
Freon TA		142 (Approx.)
	Wet weight	9151

Outlet pressure	20.52 psia
Outlet temperature	271°F
Pressure ratio	1.8
Brake horsepower	136
Power	460V, 3 phase, 60 cycle
Driver speed	1780
Compressor speed	26,000

The compressor manufacturer, Turbonetics, Inc., tested the unit and reported the actual performance to be as follows:

Inlet pressure	11.4 psia
Inlet temperature	116°F
Inlet volume	2485 cfm
Pressure ratio	1.91
Horsepower	134
R (Molecular weight 18.67)	82.76

The compressor is fitted with a Crane Packing Company Type 28 gas seal. This seal consists of a stationery carbon ring and a rotating chromed stainless seal mating ring. The parts are in contact when

12

stationary and the leakage will be less than 6 scfm at a pressure differential of 15 psid with the duct and compressor evacuated.

The specified 5.6 torr cu. ft. per minute corresponds to 12.79 scim. When the mating ring rotates the station carbon ring lifts off slightly to eliminate rubbing contact which would cause overheating and destruction at a pressure differential of 5 psid, with the compressor discharge at 20 psia. Provisions are required for introducing a pressure differential of 5 psid (9.3 scfm) at start to lift off the seal and for replacing this with discharge pressure once the compressor is operating.

An Allen Bradley Combination Starter 712-FAB282 is provided for starting the compressor motor.

2. Compressor Exit Heat Exchanger

This assembly is a young Radiator Company shell and tube heat exchanger Model HF803-DR-1P less the end bonnets. The tubes are 3/8 inch, baffle spacing is 2-1/4 inch, and the coolant makes 1 pass. The specifications for the unit are as follows:

Inlet and Outlet

Flange OD	11 inch
Flange ID	8 inch
Bolt Circle	16-1/2 inch bolts on a 9-3/4 inch bolt circle

Length	28-1/8 inch

Gas   3:2:1 molar mix of $He:N_2:CO_2$

Molecular weight	18.7
Gas Flow	1.4 lbs/sec
Inlet pressure	20.1 psia
Inlet temperature	$741^{\circ}R$
Pressure drop	.6 psid
Outlet temperature	$576^{\circ}R$

Coolant

Water flowing at 4.0 lbs/sec and inlet conditions of 19.7 psia and $540^{\circ}R$. Pressure drop 5 psid and outlet temperature $560^{\circ}R$

Heat removal	79.2 BTU/sec

3. Cavity Inlet Heat Exchanger

This assembly is a Young Radiator Company shell tube heat exchanger Model HF804-DR-1P less the end bonnets. The tubes are 3/8 inch, baffle spacing is 2-1/4 inch, and the coolant makes 1 pass. The specifications for the unit are as follows:

Inlet and Outlet

Flange OD	11 inch
Flange ID	8 inch
Bolt Circle 16-1/2 inch bolts on a 9-3/4 inch bolt circle	

Length	37-1/8 inch

Gas 3:2:1 molar mix of He:N_2:CO_2

Molecular Weight	18.7
Gas Flow	1.4 lbs/sec
Inlet Pressure	19.2 psia
Inlet Temperature	576°R
Pressure Drop	.6 psid
Outlet Temperature	350°R

Coolant

Normal freon TA flowing at 3.1 lbs/sec and inlet
conditions of 35 psia and 296°R. Pressure drop 14
psid and outlet temperature 355°R

Heat Removal	105.2 BTU/sec

4. Compressor Inlet Heat Exchanger

This assembly is a Young Radiator Company shell and
tube heat exchanger Model F-1002-DR-1P less the end
bonnets and mounting feet. The tubes are 3/8 inch,
baffle spacing is 2-1/4 inch, and the coolant makes
1 pass. The specifications for the unit are as follows:

Inlet and Outlet

Flange OD	14-7/8 inch
Flange ID	10-3/8 inch
Bolt circle	16-1/2 inch bolts on a 13-3/8 bolt circle

15

Length	23.63 inch

Gas 3:2:1 molar mix of $He:N_2:CO_2$

Molecular Weight	18.7
Gas Flow	1.4 lbs/sec
Inlet Pressure	11.9 psia
Inlet Temperature	$660^{o}R$
Pressure Drop	.6 psid
Outlet Temperature	$576^{o}R$

Coolant

Water flowing at 2.0 lbs/sec and inlet conditions of 19.7 psia and $540^{o}R$. Pressure drop of 5 psid and outlet temperature $560^{9}R$

Heat Removal	40.4 BTU/sec

5. Ducting

The ducting connects the compressor, heat exchangers, flowmeter and lasing cavity together and provides structure to support the elements. The main portion of the duct consists of 8-inch diameter aluminum pipe and standard Flowline Corp. flanges with transitions at the compressor outlet to 6-inch diameter and at the compressor inlet to 10-inch diameter. A 4-inch bypass connects the compressor outlet to the inlet. Bellows are provided at outlet and inlet to isolate the compressor from thermal expansion and contraction of the ducts. At the cavity

inlet and outlet the cross section of the duct changes to
a rectangle 15 cm by 40 cm (5.91 inches by 15.75 in).
The cavity inlet elbow is provided with vanes, honeycomb and
a screen to reduce velocity variations in the gas to a min-
imum at entrance to the cavity. The cavity inlet elbow
is also fitted with a manifold for the introduction of
liquid nitrogen to prechill the elbow to the desired cav-
ity inlet gas temperature. The manifold surrounds the
elbow except for the section immediately preceding the
cavity inlet where a removable shroud continues the
manifold in order to allow access to the instrumentation
in this area. The liquid nitrogen is introduced before
the elbow turn and just after the cavity inlet heat ex-
changer and after gasifying flows around and along the
elbow to exit at the end of the elbow through the shroud
just before the inlet to the cavity. The ducting is
designed for a flow of 1.3 lbs/sec. of a 3:2:1 molar
mixture of $He:N_2:CO_2$ with a pressure drop of less than
2.5 psid.

The ducting also includes a provision for extend-
ing the cavity from 60 inches to 120 inches by removing a
spool piece and replacing it with another.

6. Diverter Valve

The diverter valve was designed to provide the

17

following angles and flows based on the analog model:

TEMP. IN CAVITY $^{\circ}$R	MAIN DUCT GAS FLOW LBS/SEC	VALVE FLAPPER ANGLE FROM CLOSED POSITION	
		MAIN DUCT	BYPASS DUCT
360	1.3	35.0°	20.3°
360	.13	8.6°	40.6°
540	1.3	60.0°	1.1°
540	.13	8.7°	40.5°

The actuator mount has been designed to mount the actuator in two positions, such that the operating angle of the flappers may be approximately halved and the sensitivity doubled when operating at the cold condition. In addition, extra length has been provided on the actuator links between the two flappers so that new holes may be drilled to provide a different relationship between the flappers.

7. Water System

The water system consists of a galvanized steel tank with a lid. The tank holds 110 gallons of water and is fitted with a dished bottom having a 1-1/2 inch female NPT. The tank outlet is connected to the 1-1/2 pump inlet. The Pacific Pumping Company Model 1250-5 centrifugal pump specifications are as follows:

18

Flow	50 gpm
Head	81 ft.
Pressure	35.1 psi
Driver speed	3450 rpm
Driver horsepower	2
Electrical Power	460V, 3 phase, 60 cycle

The outlet pump discharge is fitted with a 1-inch Lukenheimer Fig S 658 relief valve set for 50 psi with a return to the tank. The discharge is also connected to the compressor exit and inlet heat exchangers through throttling shutoff valves.

The specifications for these valves are as follows:
Compressor exit heat exchanger valve

Masoneilan 1-inch Camflex Valve, Model 35-35200, Full Trim, C_v 14, Carbon Steel Body

Compressor Inlet Heat Exchanger Valve

Masoneilan 1-inch Camflex Valve, Model 35-35200, Reduced Trim, C_v 5.6, Carbon Steel Body

The discharge from the heat exchangers is piped to drain or can be recirculated to the water tank.

An Allen Bradley Combination Starter, 712-AAB 242 is provided for starting the water pump motor.

8. Freon TA System

The Freon TA System consists of two 55 gallon

gallon stainless steel tanks, one for supply and one for catching the discharge from the heat exchanger. Each tank has a 2-inch NPT female outlet fitted with a 2-inch Goddard Valve Corporation gate valve. The tank outlets are connected to the 1-1/2 inch pump inlet. The Lobee Pump and Machinery Company Model 12 LOL gear pump specifications are as follows:

Flow (water)	22 gpm
Pressure	100 psi
Driver Speed	1745 rpm
Pump speed	900
Driver horsepower	5
Electric power	460V, 3-phase, 60 cycle

The pump discharge is fitted with a 1-1/2 inch Teledyne Farris Engineering Type 1876-M relief valve set for 100 psi with a return to the supply tank. The pump discharge is connected to the cavity inlet heat exchanger through a throttling shutoff valve.

The specification for this valve is as follows:
Cavity inlet heat exchanger valve

Masoneilan 1-inch Camflex Valve, Model 35-35200,

Full Trim, $C_v 14$, Stainless Steel Body

The discharge from the heat exchanger is piped to the catch tank. An Allen Bradley Combination Starter

20

712-BAB 242 is provided for starting the Freon TA pump
motor.

9. Liquid Nitrogen System

The liquid nitrogen system requires a supply of
liquid nitrogen at low pressure to the three ASCO 8222D2LT
cryogenic solenoid valves.

The valves on the water tank and the freon TA tank
feed liquid nitrogen to immersed coils of copper tubing,
vented to the atmosphere. The valve on the cavity inlet
elbow discharges directly into a jacket surrounding the
elbow and the gasified nitrogen flows around the elbow
and exits to the atmosphere at the cavity inlet.

10. Gas System

The gas system requires a supply of makeup gas
at no more than 250 psi. This gas is passed through a
Monnier 201-5200-6 filter and 107-5002-6 regulator which
reduces the pressure to 50 psi. The gas then flows to
the three branches for makeup gas, purge gas and seal
gas. The specifications for these systems are as follows:

Makeup Gas System

Control Solenoid ASCO 8210-C94

Orifices LADISH 72111 1-inch orifice unions drilled
as follows:

FLOW PERCENT OF MAIN DUCT FLOW	LBS/SEC	ORIFICE DIAMETER INCHES
.5	.0065	.104
1.0	.013	.147
2.0	.026	.209
3.5	.0455	.277
5.0	.065	.339

Purge Gas System

Control Solenoid ASCO 8223-A21

Orifice LADISH 72111 1/2-inch orifice union drilled
as follows:

FLOW LBS/SEC.	ORIFICE DIAMETER INCHES
.000146	1/64

(5.3 SCI/sec)

Seal Gas System

Control Solenoid ASCO 8223-A21

Orifice LADISH 72111 1/2-inch orifice union drilled
as follows:

FLOW LBS/SEC	ORIFICE DIAMETER INCHES
.030	.209

(0.62 SCF/sec)

Check Valve Hoke 6211 F4B

11. Control System

The control system for the CCC consists of electrical and pneumatic controls assembled in a control console. An Allen Bradley H31C lock switch is provided to control the electrical power to the console. The compressor, however, can be operated with controls at the compressor if the switch on the compressor is turned to local instead of remote. The water and freon TA pumps are only controlled from the console.

The compressor was procured with failsafe circuitry and instrumentation to ensure a safe automatic shutdown in the event of any of the following:

High oil temperature

Low oil pressure

Low oil level

High discharge temperature

Low seal gas differential pressure

In addition, the compressor cannot be started if any of the following conditions exist:

Low oil temperature

Low oil level

Low seal gas differential pressure

The compressor is also provided with a surge sensor which lights the remote alarm light if surge occurs.

23

The existence of any of the above conditions lights an identifying light at the compressor.

The CCC control console accordingly has a minimum of controls for the compressor. These are as follows:

Compressor ready light

Allen Bradley Pilot Light 800T-P16G

Compressor alarm light

Allen Bradley Pilot Light 800T-P16R

Compressor start switch

Allen Bradley Switch 800T-A1A

Compressor operating light

Allen Bradley Pilot Light 800T-P16G

Compressor stop switch

Allen Bradley Switch 800T-B6A

The ready light signifies that the above noted conditions for starting have been met. The alarm light provides an initial warning of high oil temperature, low oil pressure, low oil level or high discharge temperature. If the condition becomes worse, automatic shutdown occurs. In the case of low seal gas differential pressure no warning occurs before automatic shutdown. In the case of surge automatic shutdown does not occur. The alarm light on the control console lights and the light identifying the condition is lighted at the compressor control panel and remains on until the reset is pushed. In the case of

low oil temperature at start the ready light on the console
does not light and the identifying light on the compressor
does.

The water and Freon TA pumps are each provided with a
similar start switch, operating light, and stop switch.

The control console also incorporates Allen Bradley
H17B on/off switches for the following:

(1)   Seal gas solenoid with a 10-second timer for
      automatic shutoff

(2)   Makeup gas solenoid

(3)   Liquid nitrogen solenoids for the water and
      freon TA tanks and the cavity inlet elbow.

The purge gas solenoid is controlled by an Allen Bradley
H31B Lock Switch mounted on the compressor.

The pneumatic portion of the control system requires
an inlet gas supply at a pressure of no more than 150 psi.
This gas supply is introduced into a Monnier 202-2100-2
filter mounted in the console and the pressure is then
reduced to 20 psi by a Monnier 101-1004-2 regulator also
mounted in the console. The output pressure from the
regulator is then distributed to four Monnier 101-3004-2
regulators mounted in the control panel. Operation
of these regulators will apply 0 to 20 psi to the control
valve actuator to which the regulator output is connected.

The actuators are of the spring return type, hence the
actuator motion is proportional to the pressure applied.
The pressures of the four regulators are read on Haskel
F60P4-2 pressure gauges. The gauges are also mounted in
the panel each one above the regulator being measured.
The four valves so controlled are the diverter valve of
section 2.5 and the three throttling shutoff valves in the
heat exchanger coolant systems of sections 2.6 and 2.7.

The 20 psi pressure is also distributed to a
pneumatic servo control system for controlling cavity
pressure. This consists of a Foxboro 43AP-FA4 Pneumatic
Indicating Controller, which senses cavity pressure and
controls a vent valve with positioner.

The specification for this valve is as follows:

Vent Valve

Masoneilan 1-inch Camflex Valve, Model
35-35200, Full Trim, C_v 14, Carbon Steel
Body with 7600 Positioner (Linear)

(B) Instrumentation System

1) Instrumentation Subsystem for the Circulator operation

The instrumentation system is a Hy-Cal Engineering
Model CSD-948-A. The Model CSD-948-A is a self-contained,
21 channel signal conditioning system. Eleven channels

26

are temperature, 9 channels are pressure and one channel is flow. The temperature inputs are from platinum resistance sensors, the pressure inputs are semi-conductor strain gauge transducers, and the flow input is a 4 to 20 mA signal. The system consists of analog signal conditioning modules housed in a steel box. Analog outputs are carried by a 30 ft. shielded cable to a console and connected to digital panel meters that indicate pressure, temperature and flow. These are mounted in the control console. All analog outputs are available from a separate connector for analog recording. Screw terminals on the front panel are provided for connecting the input sensors. The sensors are equipped with 35 ft. leads individually shielded. Input power for the CSD-948-A is 117 VAC via a grounded "U" line cord. The power is routed through an RFI filter and isolation transformer within the signal conditioning housing.

Common mode and normal mode R. F. noise appearing on the power line are rejected by the use of an RFI filter and an isolation transformer. The isolation transformer contains a faraday shield between primary and secondary which is grounded and features low capacitive coupling between windings. The RFI filter in series with the power line attenuates the normal mode interference before

27

it can disturb the signal conditioner power supplies.

Signal conditioner circuits are mounted on cards accessible through a hinged rear panel for service or adjustments. Cards may be removed in groups of 3 for servicing without disturbing the rest of the system.

The specification for the system is as follows:

Signal condition channels	21
Temperature signal conditioners (TX1 through TX11)	11
Range of temperature inputs	$-115^{\circ}C$ to $+199.9^{\circ}C$
Accuracy of temperature (Including sensor and digital indicator)	$\pm 4^{\circ}C$
Analog recorder output (temperature)	1 mV/$^{\circ}C$
Pressure signal conditioners (PX1 through PX9)	9
Range of pressure inputs (PX2, PX7 and PX8)	0 to 3877 TORR
Accuracy of pressure (Including sensor and digital indicator)	± 26.7 TORR
Range of pressure inputs (PX1, PX3, PX4, PX5, PX6 and PX9)	0 to 1520 TORR

Accuracy of Pressure (Including sensor and digital indicator)	$\pm$ 6.2 TORR
Analog recorder output (pressure)	1mV/TORR
Flow signal conditioner (FX1)	0 to 25.0 meters/sec
Accuracy of flow input (4 to 20 mA input)	$\pm$ .1% of SPAN
Analog recorder output (flow)	100 mV/meter/sec
Input power	117 VAC 50/60 Hz

Although the readout portion of the flowmeter system is included in the above instrumentation system, the turbine meter itself and its direct reading totalizer with flow rate option were procured separately. The turbine meter is a Daniel Industries, Inc., 8-inch, 125 lb. CWP Electro Magnetic Gas Turbine Meter having the following specifications:

Operating pressure max 125 psi

Flanges	DRILLED TO MATCH 150 psi ANSI
Maximum flow SCFH* at 25 psi	161800
Minimum flow SCFH* at 25 psi	4927

---

*14.73 psia, 60°F, .6 SP.GR.

Pulses/actual cubic foot	24
Pulses/actual cubic meter	847
Frequency at max flow Hz	400

The direct reading totalizer with flow rate option is a Daniel Industries, Inc., 2239-1112 Direct Reading Totalizer, having the following specifications:

Turbine Meter Inputs

A. Type

DC coupled for nominal 14 V square wave or pulse

B. Input threshold

1. Positive going waveform: +7 V

2. Negative going waveform: +5 V

C. Open circuit input terminal voltage +6 V

D. Input resistance

20 KΩ, dc to 400 Hz; decreasing to 9 KΩ at 3 kHz and above

E. Frequency range

1. Totalizer:

0 to 4 kHz

2. Rate:

10 Hz to 4 kHz

Outputs

A. Flowrate

1. Type

a. Voltage

   0 to 10 V, 5 mA maximum load

b. Current

   4 to 20 mA, 950 Ω maximum load.

   Zero and span of current output internally

   adjustable ±25% of full scale with respect to

   the rate meter and the 0 to 10 V output.

2. Electrical

   a. Ripple

      < 2 mV rms at 32 Hz

   b. Response time

      0 to 90%, 1 sec., maximum

   c. Linearity

      0.1% of full scale (32 Hz to 1 kHz range)

      0.25% of full scale (1 kHz to 4kHz range)

   d. Average temperature coefficient

      < 0.015%/$^\circ$F over operating range when

      calibrated at 1 kHz as full scale

   As noted in the discussion of the Hy-Cal Engineer-

ing system, the 4 to 20 mA signal from the direct

reading totalizer is connected to the input of the

system. This is scaled so that 20 mA is equivalent to

102556 actual cubic feet per hour or 25 meters per

second flowing in a duct having a 7.98 inch inner

diameter.

31

2) Instrumentation Subsystem for Time-dependent Measurements

of Velocity, Pressure and Temperature in the Circulator.

a) Pressure Measurement

The instrument used for pressure measurements is a
battery of four Piezotron pressure sensing units each of
which consists of a piezoelectric pressure transducer
(Type 201B5) and a coupler (549B) connected with a
128M cable. The unit is then connected to an oscillo-
scope for the readout of voltage signals. Specifications
of the Piezotron miniature pressure sensor or transducer,
and the Piezotron coupler are presented in
Appendix B.

The pressure of up to 100 psi was sensed by the
mini-gage which gives a direct, high level, voltage
signal with less than 100 ohms output impedance and
high frequency response of 50 kHz and low frequency
response of 0.005 HZ. The sensor then converts the
pressure into electrical voltage with bias of up to
11 ± 2 volts. The power required by the transducer to
operate is supplied by the coupler, and the signal from
the transducer to the readout equipment is transmitted
through the coupler over a single inexpensive cable.
This eliminated all of the inherent piezoelectric high
impedance problems of electrical leakage, cable noise

and signal attenuation and allows the transducers to be used in contaminated environments and with long and moving cables at low noise and without use of charge amplifiers.

The calibration of the transducers was performed at the factory, and the values of the calibration were noted to be, on the average for all probes, 50 mv per psi for the pressure measurement up to 100 psi. The calibration curve relating the voltage output and the pressure is noted to be quite lenient.

b) Temperature Measurement

Due to the extremely transient nature of temperature variation in the recirculating flow as a result of the pulsed laser operation, a sensor of high frequency response in excess of 1 KHz is considered necessary for the temperature measurement. Search of an adequate sensor resulted in the selection of a hot-wire sensor made of 0.00015 in. diameter tungsten wire coated with platinum powdery film. The hot-wire sensor is connected to the Temperature and Switching Module (Thermo-Systems Model 1040) which in turn connected to the power supply (Model 1031-10A).

The Module consists of a bridge circuit and amplifier in an open loop configuration so the hot-wire sensor

which is ordinarily used as an anemometer probe can be switched to function as a resistance thermometer. Since there is a linear proportionality between the voltage output and the temperature, the calibration can be simply performed by adjusting the zero gain set potentiometers to a desired temperature range using the calibrate pots of two temperatures.

c) Velocity Measurement

For the measurement of velocities, hot-wire probes the same as those used for the temperature measurement are applied. The probe is connected to the constant temperature anemometer module (Model 1010A). The amplified output signal from the anemometer is sent to the Linearizer (Model 1005B) so that the voltage signal is processed in such a way that it became linearly related to velocity of the gas flow.

The use of these modules ensures the frequency response above 500 KHz with power output as high as 1.5 amps. The noise associated with the anemometer is noted to be less than 0.007% equivalent turbulent intensity. Frequency response to the Linearizer is found to be up to 400 KHz and the accuracy of linearization can reach ± 0.2%. With these special features of the instrument, it is able to measure both average

34

velocity and turbulence in one-dimension.

Calibration of the probe is performed by using a
Thero-Systems Calibrator (Model 1125) in accordance
with the furnished instructions. The readout system
for both temperature and velocity is the Tektronix
type oscilloscope (Type 564-3A74-3B3).

3) Interferometer Subsystem for Optical Measurements

Introduction

The optical cavity is an area of primary con-
cern in any laser system. In this section we propose to
determine laser cavity characteristics under potential
lasing conditions with optical diagnostics.

The laser cavity of the Closed Cycle Circulator
is currently being considered as a amplifier, i.e., no
mirrors will be used for outcoupling of power (Figure II-3).
The diagnostic test in this mode of operation is medium
quality.

Medium quality measurement is the most important
diagnostic to be measured optically. This test is broken
down into two categories: a medium homogeneity category
in which quantitative results will be obtained from steady
state flow in the laser cavity; and a clearing time cate-
gory, a qualitative visualization of shock structure
created by E-Beam injection in the cavity with the impact
of multiple geometry. The latter category will be measured
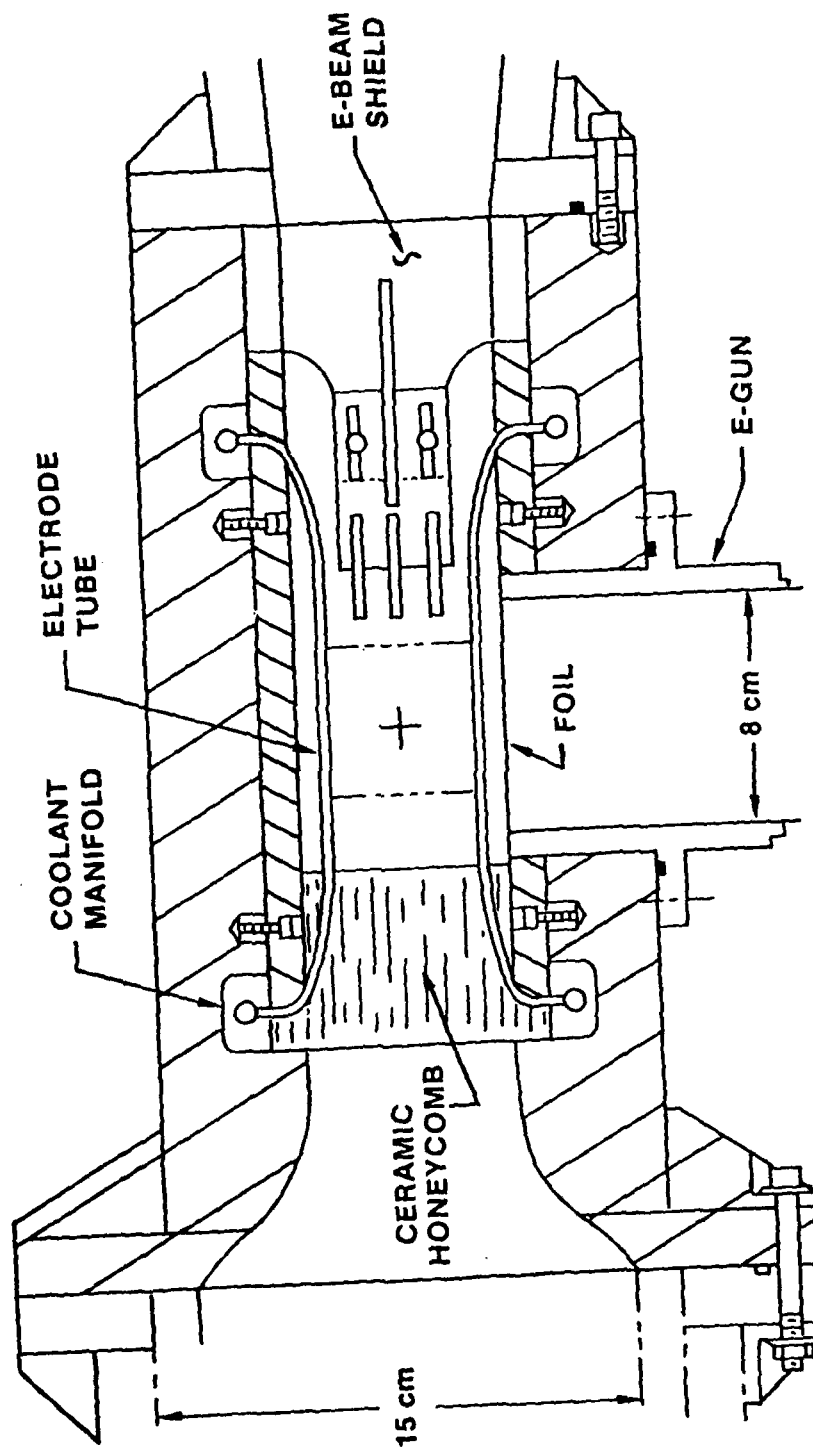as a function of time.

35

Figure II-3 Closed cycle circulator cavity.

(1) Medium Homogeneity

(a) Basic Concepts: Interferometry is the basic inves-
tigative tool for medium homogeneity measurements. Its prin-
ciple of operation is based upon detection of optical path
differences (Phase differences) along a line of sight.
Figure II-4 shows a planar wavefront in the x, y plane
incident from the left. The laser gas medium is shown flow-
ing in the region from z_0 to z_1, z being along the optical
axis. The phase, ϕ, at any point in the x, y plane (assuming
small deviations of the light rays along the z axis) is given
by

$$\dot{\phi}\ (x,\ y,\ z)\ =\ 2\pi\ \lambda \int_0^{z'} n\ (x,\ y,\ z)\ dz \qquad (II-1)$$

where n is the local index of refraction of the media and
the wavelength of the illuminating beam. The index of re-
fraction if related to the density, ρ, of the gas mixture by

$$n(x,\ y,\ z)\ =\ 1\ -\ \beta\rho\ (x,\ y,\ z) \qquad (II-2)$$

where β is the Gladstone-Dale constant of the gas mixture.
The phase is then related to gas density by

$$\phi\ (x,\ y,\ z)\ =\ 2\pi/\lambda \int_0^{z'} \{1\ -\ \ (x,\ y,\ z)\}\ dz. \qquad (II-3)$$

However, only the phase distortions caused by the gas in the
region from z_0 to z_1 are of interest. These would be given by

37

$$\Delta\phi(x,y) = \int_{z_0}^{z_1} \{1 + \beta\rho(x, y, z) - n_0\} \, dz \quad \text{(II-4)}$$

The classical interferometers, e.g., Mach-Zender and Michelson interferometers, obtain $\Delta\phi$ by superimposing a planar wavefront reference beam with the perturbed test beam. The resulting interference pattern is recorded photographically. Figure II-5 shows the Mach-Zehnder configuration. Coherent light from a collimated source is shown incident upon the apparatus from the left. The coherence length of the source must be greater than the path length difference in reference and test beam. The light passes through beamsplitter A which divides the beam into a test beam and a reference beam. The reference beam passes to a folding mirror and onto beamsplitter B where it is recombined with the test beam to produce interference fringes. The test beam passes through the perturbing media in the laser reference in the laser cavity and is folded into the reference beam. The intereference pattern is then focused into a camera for recording on photographic film. In this apparatus the test beam passes once through the cavity.

The Michelson interferometer is shown in Figure II-6. In this case the reference beam is split at the beamsplitter and is returned upon itself by mirror A. The test beam is likewise returned upon itself by mirror B making a double pass through the
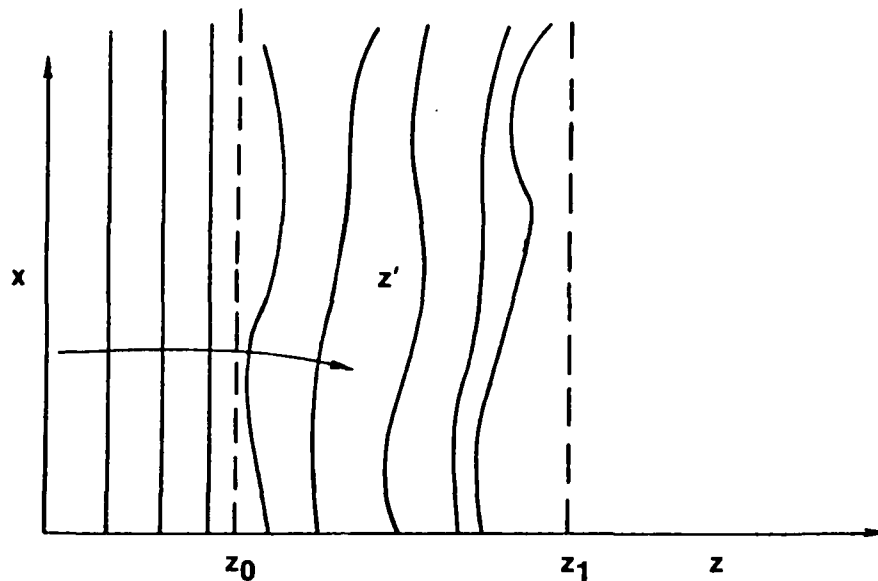
38

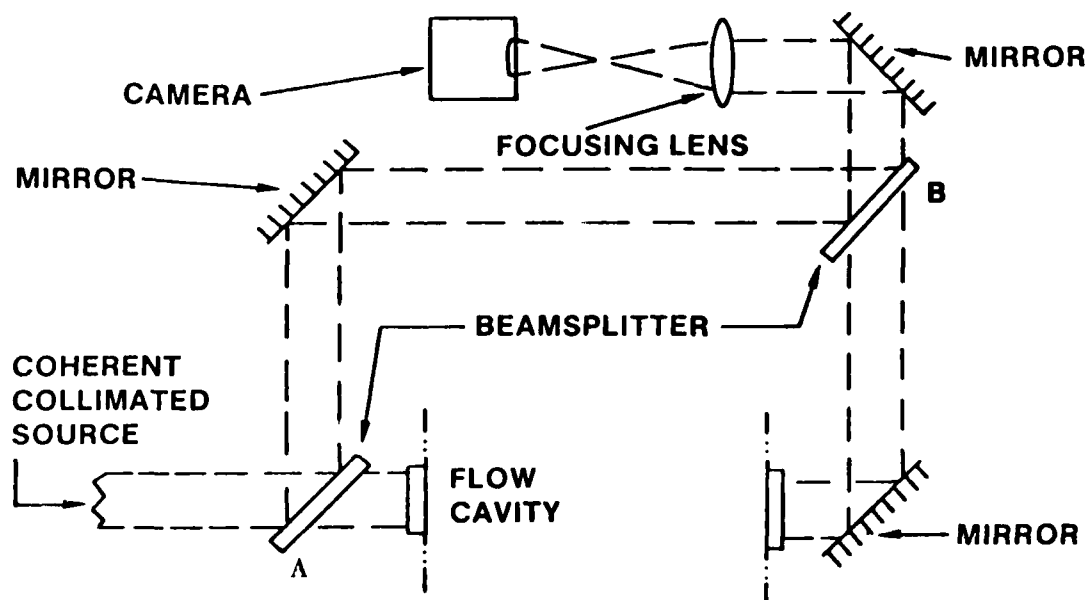Figure II-4 Transmission of light through an inhomogeneous media.
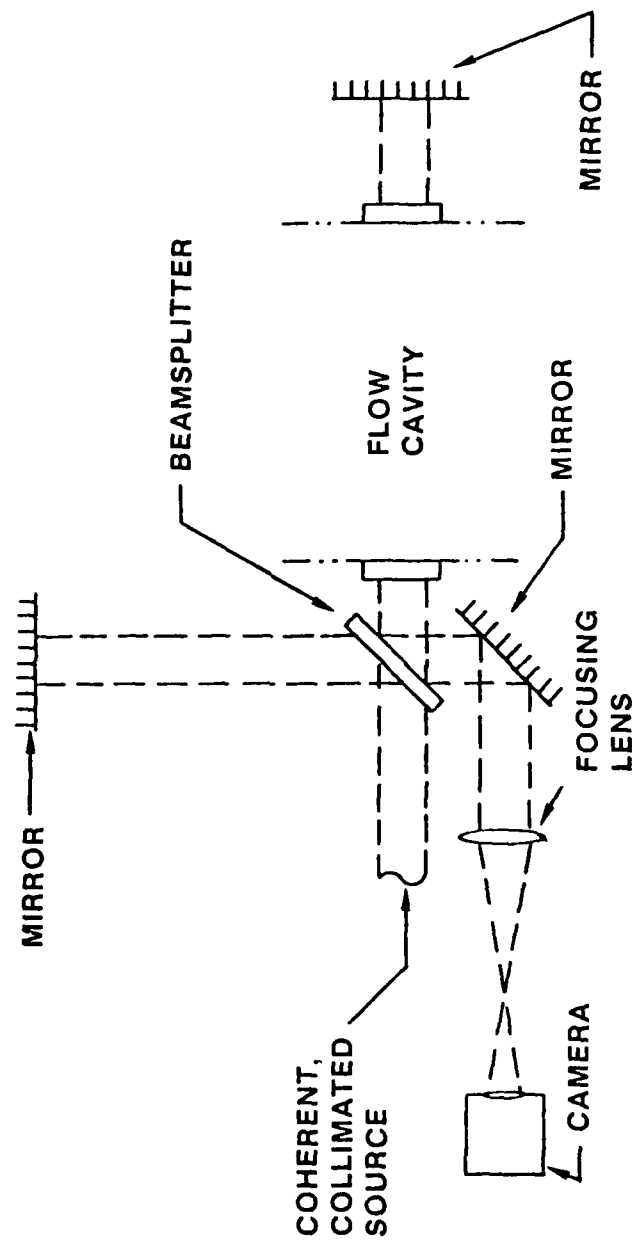

Figure II-5   Mach-Zender interferometer.

39

Figure II-6   Michelson interferometer.

40

laser cavity. The fringe pattern formed with the recombination of the beams is recorded in a similar manner to the Mach-Zehnder interferometer. The Michelson interferometer is more sensitive because of the double pass of the test beam through the laser cavity. However, for extremely strong flow disturbances, this apparatus can produce ambiguous results, the rays of the test beam not returning through the media along the same path.

(b) Experimental Configuration. The experimental set-up (Michelson) for taking a single interferogram during steady state flow conditions is shown in Figure II-7. A Q-switched pulsed ruby laser (20 nsec pulse width) serves as a source. A coaxially aligned helium neon laser is used to align the entire optical train. A beam expander enlarges the laser beam into a large (8 inch) collimated beam incident on the interferometer. The interference fringes formed on the image of the flow cavity are focused on a camera.

The repetition rate of the pulsed ruby laser is limited to 1 pulse per 20 seconds. For real time interferometric analysis, the ruby laser will be replaced with a argon-ion laser of 4 w cw power. A Fastex motion picture camera having a frame rate of 10,000 frames per second would be used to record the interferograms.

(c) Reduction of Interferograms. An interferogram taken by the Mach-Zehnder or Michelson interferometer is a contour plot of phase across the aperture of the laser

cavity. The aberrations resulting from the passage of the
planar wave test beam through the laser cavity derived from
subtraction of a reference interferogram (taken prior to
the test) from a test interferogram. We wish to determine
the degradation such aberrations produce in the Fraunhofer
pattern (far field pattern) of the laser cavity aperture.
From the Huygens-Fresnel principle {4,5} the amplitude of
a wave near the focus of an optical system is given by

$$U(P) = -i/\lambda \ \frac{Ae^{-ik'r}}{R} \iint\limits_{S} \frac{e^{ik'(\phi + s)}}{s} \ ds \qquad (II-5)$$

where

R = radius of curvature of the reference wave (large).

k' = propagation factor $(2\pi/\lambda)$.

λ = wavelength of incident light.

A/R = amplitude of the wave in the exit pupil.

s = distance from a point on the reference wave to
    the observation point.

ϕ = aberration function.

S = exit pupil area.

If the point of observation P is at the focus of
the reference wave, equation (II-5) becomes:

$$U(P) = -i/\lambda \frac{A}{R^2} \iint\limits_{S} e^{ik'\phi} \ ds.$$

42

The intensity at P is given by

$$I = I(P) = |U(P)|^2 = \frac{A^2}{\lambda_2 R_4} \left| \iint_s e^{ik'\phi} ds \right|^2. \quad (II-6)$$

In the absence of aberrations, $\phi = 0$, and Equation (II-6) becomes

$$I_0 = \frac{A^2 \, S^2}{\lambda^2 \, R^4} \quad (II-7)$$

The normal intensity at the center of focal pattern (far field pattern)

$$I/I_0 = \frac{1}{S^2} \left| \iint_s e^{ik'\phi} ds \right|^2 \quad (II-8)$$

Expanding $e^{ik'\phi}$ and integrating termwise, the normalized intensity is

$$I/I_0 = \left| 1 + ik\overline{\phi} - \underline{\quad} \overline{\phi}^2 - \underline{ik^3} {}_\phi{}^3 + \ldots \right|^2 \quad (II-9)$$

For small aberrations (small ϕ) we make the approximation

$$I/I_0 \simeq |1 + ik'\phi|^2 = 1 - k^2(\overline{\phi}^2 - \overline{\phi}_0^2) = \quad (II-10)$$

$$1 - 4\pi^2/\lambda^2 \ (\overline{\phi}^2 - \overline{\phi}_0^2).$$

Equation (II-10) is the standard RMS wavefront deformation equation. A simpler, rough approach is to obtain a normalized density change, $\Delta\rho \quad \frac{\Delta S\lambda}{BL} \quad (II-11)$

43
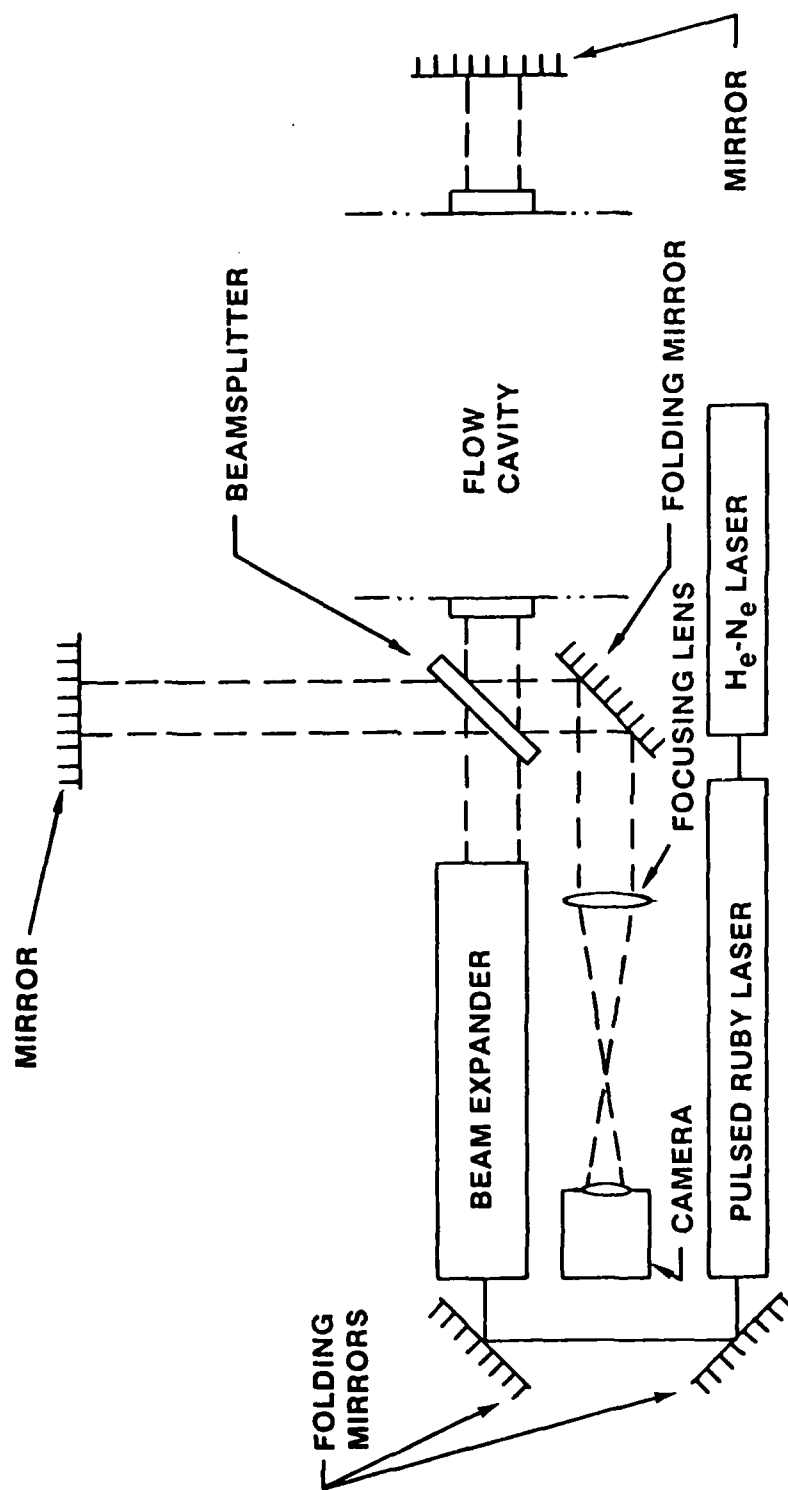
Figure II-7   Typical experimental configuration.

44

where

ΔS = maximum fringe shift across the cavity.

λ = wavelength of the probe laser.

β = *Gladstone-Dale constant for the laser gas mixture* at the laser wavelength.

L = length of traversed gas media.

Obtaining ρ, the average density of the media we have

$$\frac{\Delta\rho}{\rho} = \frac{\Delta S\lambda}{\beta L\rho} \qquad\qquad (II-12)$$

The classical Mach=Zehnder and Michelson interferometers give interferograms which are phase contour plots. Interferograms obtained from a shearing interferometer require additional processing before phase information is derived.

Reduction of a shearing interferogram is shown by Figure II-7. First the fringes are arbitrarily numbered in consecutive order. Then reference points equal to the shear and parallel to the shear direction are placed on the test interferogram and on a reference interferogram. Interpolated fringe orders are obtained at each reference point on both interferograms. Proceeding from one edge of the interferograms to the other, the difference in orders at each point are taken and summed to those taken at previous points. This represents the phase at each reference point.

45

To obtain a complete phase contour map of the aperture, the reference point set may be arbitrarily translated. Figure IV-6 represents shear in one direction (the y-direction). Complete phase information required shear in the orthogonal direction (in this case the x-direction).

After phase is calculated, data reduction follows the course described previously.

4) Mass Spectrometer Subsystem for Time Dependent Measurements of Gas Composition

The output of any laser instrument using chemical molecular species as the lasing medium, is dependent upon the population inversion of these species. The input electric discharge power can be reduced by small concentrations of species which attack free electrons. Thus, any change in the concentration of the lasing molecules or the formation of deactivating species will directly affect the total output power of the laser. This is true whether lasing is made to occur by a direct chemical reaction or by external stimulation such as an electrical discharge. Thus, the knowledge of the concentration of the lasing and certain other molecules is of great importance not only in the understanding of the chemical processes occurring in the laser, but can also serve as a monitor to correlate any changes in the laser output with changes in the gaseous concentrations.

46

Various analytical instruments are currently used as diagnostic tools in laser investigations. Each instrument is capable of yielding only a specific type of scientific information. Thus, a variety of instruments is needed to investigate the laser processed and operation of any potential laser application.

The mass spectrometer is one of those essential analytical instruments which is used to analyze and monitor atomic and molecular concentrations of any species present in a gaseous environment.

Among the various commercially available types of mass spectrometer such as the quadrapole, magnetic, and time of flight, the latter has the broadest capabilities and maximum speed. It is also one of the least complex. It uses straight-line trajectory paths for all the ions formed in the source, employs a planar grid source, and collects all the ion masses on each cycle of the instrument with a magnetic multiplier ion detector. One may monitor every mass peak by an oscilloscope at intervals ranging from 1- to 50-μsec depending upon the pulsing frequency of the particular instrument.

The mass spectrometer chosen to be used to detect and monitor various chemical species during operation of the small scale closed cycle circulator is a Bendix Model

MA-3A instrument. It has a spectral frequency of 30 kHz and a mass range of 0 to 500 atomic mass units. It is capable of detecting and monitoring most gaseous molecules in the parts per million range.

A total of five different molecular species will be monitored by means of an analog scanner and a four-channel monitor which are accessories to the Bendix Mass Spectrometer. Both of these accessories are essential in order to use the instrument in a quantitative mode of operation. Both integrate the current output of each mass peak over a relatively large number of mass spectrum and present the integrated signal in an analog form for recording. The four-channel monitor operates in a multiplex mode, sampling each chosen mass for 128 cycles of the pulsing rate (3 to 5 milliseconds) and then shifting to the next mass peak. In this way, each of the four peaks is sampled every 15 to 20 milliseconds. Thus a considerable number of quantitative readings can be obtained during a 60 second run time specified in the closed cycle circulator laser description. In this manner, it may then become possible to correlate certain events in the laser cavity with variations in the molecular concentration of specific species. The laser gas will be sampled at two locations as shown in Figure II-8.

The gases in the laser cavity exhibit viscous flow whereas those in the mass spectrometer exhibit molecular flow. The change from the viscous to the molecular nature of flow may be

48
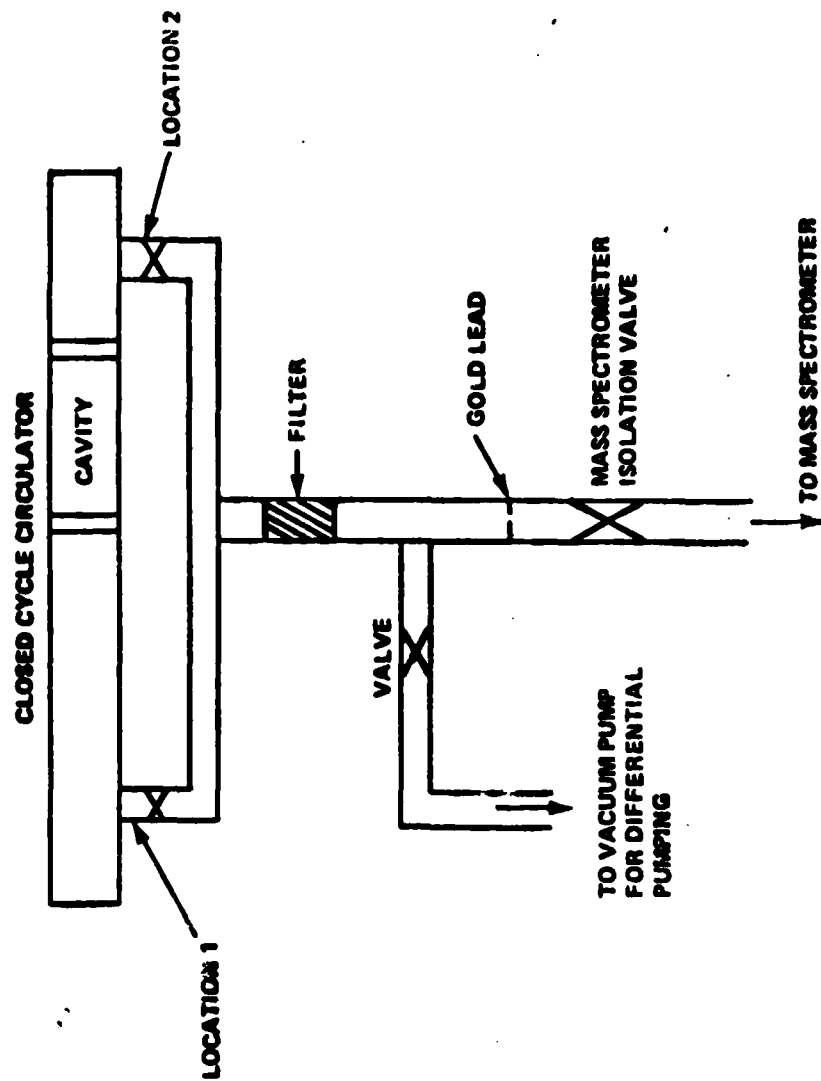
Figure II-8   Sampling of laser gas at two locations.

49

accomplished in different ways. One technique is to probe
with various leaks. Another method is the use of leak valves
such as the Veeco PV-IQ valve. Such a valve is capable of
going from fully closed to fully open in 2 milliseconds. A
preselected flow to the mass spectrometer will be achieved by
a very fast precision leak valve.

Differential pumping is necessary to prevent an ex-
cessive amount of gases from entering the mass spectrometer
and causing it to flood.

The mass spectrometer is an extremely sensitive in-
strument and is easily affected by external forces such as
electric and magnetic fields (EMI). The presence of high
electric fields, as may exist in the proposed closed cycle
circulator electric discharge laser, necessitated the location
of the mass spectrometer to an area where such forces are
minimized. Complete EM-I shielding of the equipment is re-
quired to obtain accurate and reliable scientific information
free from the EMI.

The planned recording and data acquisition of the data
obtained from the mass spectrometer are shown in Figure II-9.

The five monitored gases as shown in Figure II-9 are H_2
(hydrogen), N_2 (nitrogen), and CO_2 (carbon dioxide), and O_2
(oxygen), and NO (nitric oxide). The time listing of any five
desired gases may be monitored by adjustment of the proper
controls of the mass spectrometer. Hydrogen must be monitored

50
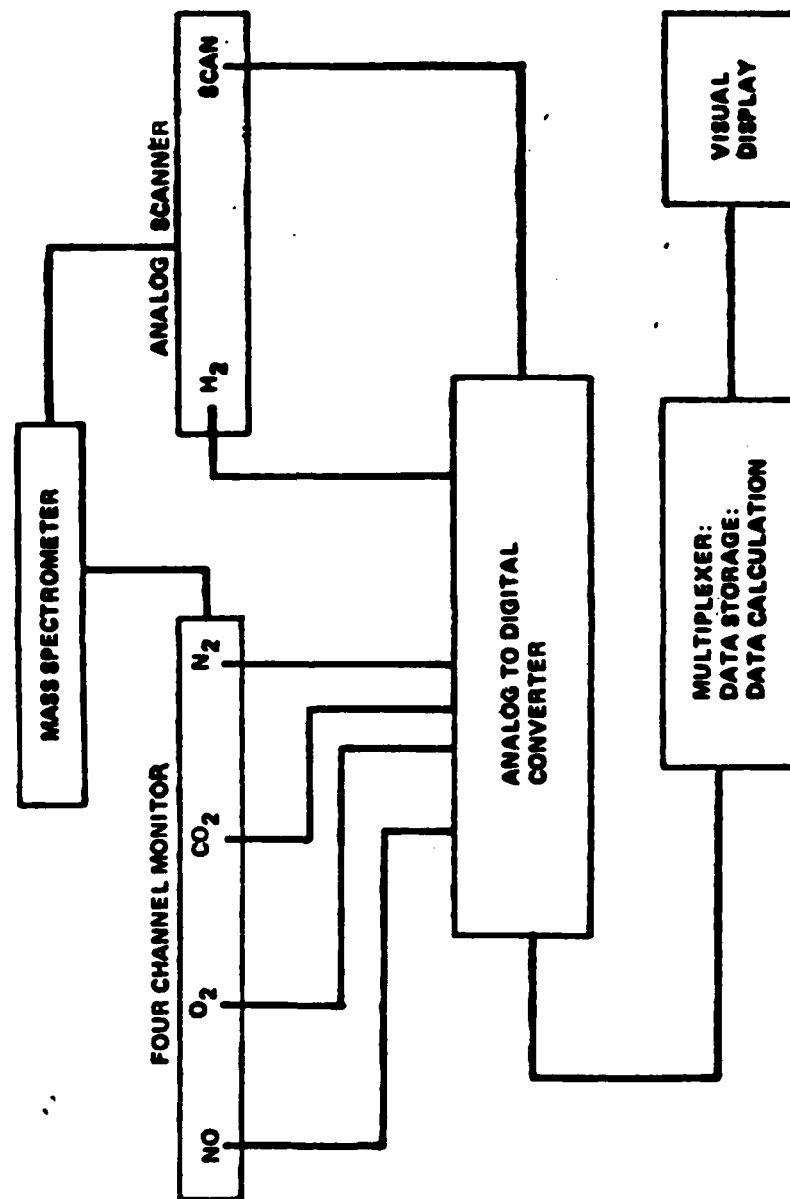
Figure II- 9   Block diagram of the data.

51

with the analog scanner because of its relative mass spectrometer sensitivity. The analog scanner is considerably more sensitive than the four-channel monitor. N_2 and CO will be detected as one peak by the MA-3 because they have the same mass, 28. However, techniques and computer programs are currently available that allow one to also determine the time history of CO in the system. The scan control of the analog scanner allows one to qualitatively detect the presence of other gases which are not being monitored in any one experiment. The scanner may be triggered so that it will scan from mass 2 to mass 100 in less than 1 second.

In conclusion, the MA-3 time of flight mass spectrometer is an extremely valuable instrument, having many applications for chemical and electric discharge laser investigations. It allows one not only to monitor time changes in concentration of the prevalent gases but also to obtain a complete profile of other species. Its use in the closed cycle circulator project will provide a data base for meaningful plasma-chemistry analysis and laser gas stability determination.

c) E-Beam Gun and Power Modulator

The hot cathode E-beam triode gun with its driver and a vaccuum subsystem, and a power modulator is used for applying energy inputs to the Circulator.

Technical specifications are given below:

52

(1) E-Beam Triode Gun

(a) Beam voltage - 125 to 200 kV.

(b) Foil area - 8 X 28 cm.

(c) Discharge area - 5 X 25 cm.

(d) Post foil pulse current density for beam voltage of 200 kV - 1 to 100 mA/cm^2.

(e) Pulse width - 1.5 to 31 μsec.

(f) Current rise time - 0.5 μsec.

(g) Current fall time - 1.5 μsec.

(h) Pulse repetition rate - 1 to 125 pps.

(i) Maximum on time per burst - 60 sec.

(j) Special feature - RF grid drive capable of 1% to 10% amplitude modulation of the gun current and frequency variable from 0.1 to 5 MHz.

(k) Controls - Separate controls are provided for repetition rate, pulse width and burst duration. Controls are available to operate with either single pulse or pulse burst mode. Following the last pulse of burst, the system will transmit an "off" signal to the power modulator and the circulator.

(2) Power Modulator

(a) Pulse voltage to load - 10 to 50 kV.

(b) Pulse length - 0.5 to 30 μsec.

(c) Rise time - 0.5 μsec.

(d) Fall time - 1.0 μsec.

53

(e) Pulse repetition rate - 1 to 125 pps.

(f) Maximum energy per pulse - 650 joules.

(g) Maximum on time - 60 sec.

(h) Average output power capability - 100 kW.

(3) Acceptance Test for Discharge Modulator

(a) Modulator shall be operated into a 50 ohm resist-
ive load with 1000 A load with 1000 A load current. The
pulse width shall be 13 μsec with 125 pulses per second.
Operating time shall be 60 seconds.

(b) Ability to limit current and voltage to preset
values shall be demonstrated.

(4) Acceptance Test for E-Beam Gun Assembly

(a) Post foil current density. Using a scanning collect-
or having an aperture of 0.5 x 2 cm, a uniformity of $\pm 10\%$ must
be demonstrated over the 5 x 25 cm discharge foil area.
Measurements will be made at $1 mA/cm^2$ for 30 μpsec pulses and
100 $mA/cm2$ for 5 μsec pulses. The gun voltage will be 175 kV.

(b) Pulse width variability shall be demonstrated at 10
mA/cm^2 at 50, 100, and 125 pulses per second. The gun voltage
shall be 200 kV.

(c) Pulse repetition shall be demonstrated at 10 mA/cm^2,
10 μsec pulse width. The gun voltage shall be 200 kV.

(d) Sixty second burst operation shall be conducted at
10 mA/cm^2, 10 μsec, 125 pulses per second.

(e) RF modulation 0.1 to 5 MHz at 175 kV and 30 mA/cm^2
for 30 μsec pulses 10% modulation shall be demonstrated.

54

(C) Discussion of Capability

Figure II-10 is a block diagram of the E-beam gun, power modulator, and the closed cycle gas circulator. The current in the E-beam gun is grid controlled and will be able to deliver 125 to 200 kV electrons to a foil window in the wall of the closed cycle gas circulator system. The current density after passing through the foil can be varied from 1 to 100 mA/cm^2. A special feature will be the ability to RF modulate the current in the frequency range of 0.1 to 5MHz. The current modulation level can be varied from 1 to 10%. Figure II-11 shows the allowed and nonallowed operating margin. The E-beam gun power supply will be able to deliver up to 5kW average power.

The master control will be used to actuate the pulse width, pulse repetition rate for burst mode or a single pulse. It will also turn on the E-beam current 0.5 µsec before it turns on the power modulator and turns it off 0.5 µsec after the power goes off.

The power modulator will be able to deliver pulse currents in the range of 100 to 1000 amps to the gas load. The gas load voltage can be varied from 10 to 50 kV. The modulator will have protective circuitry which will prevent damage to the modulator in the event of a load arc. In addition, the output pulse will be limited to a preset value in the event no load current develops or is less than the set value.

55
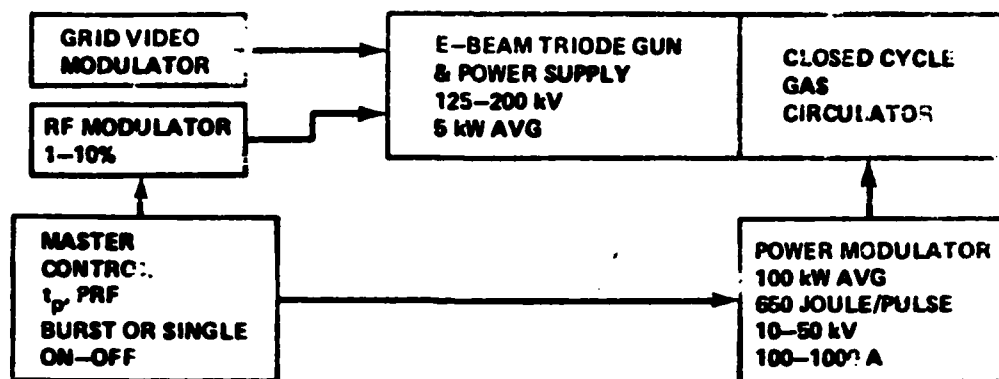
Figure II-10   Block diagram of E-beam gun,
power modulator, and closed cycle gas circulator.
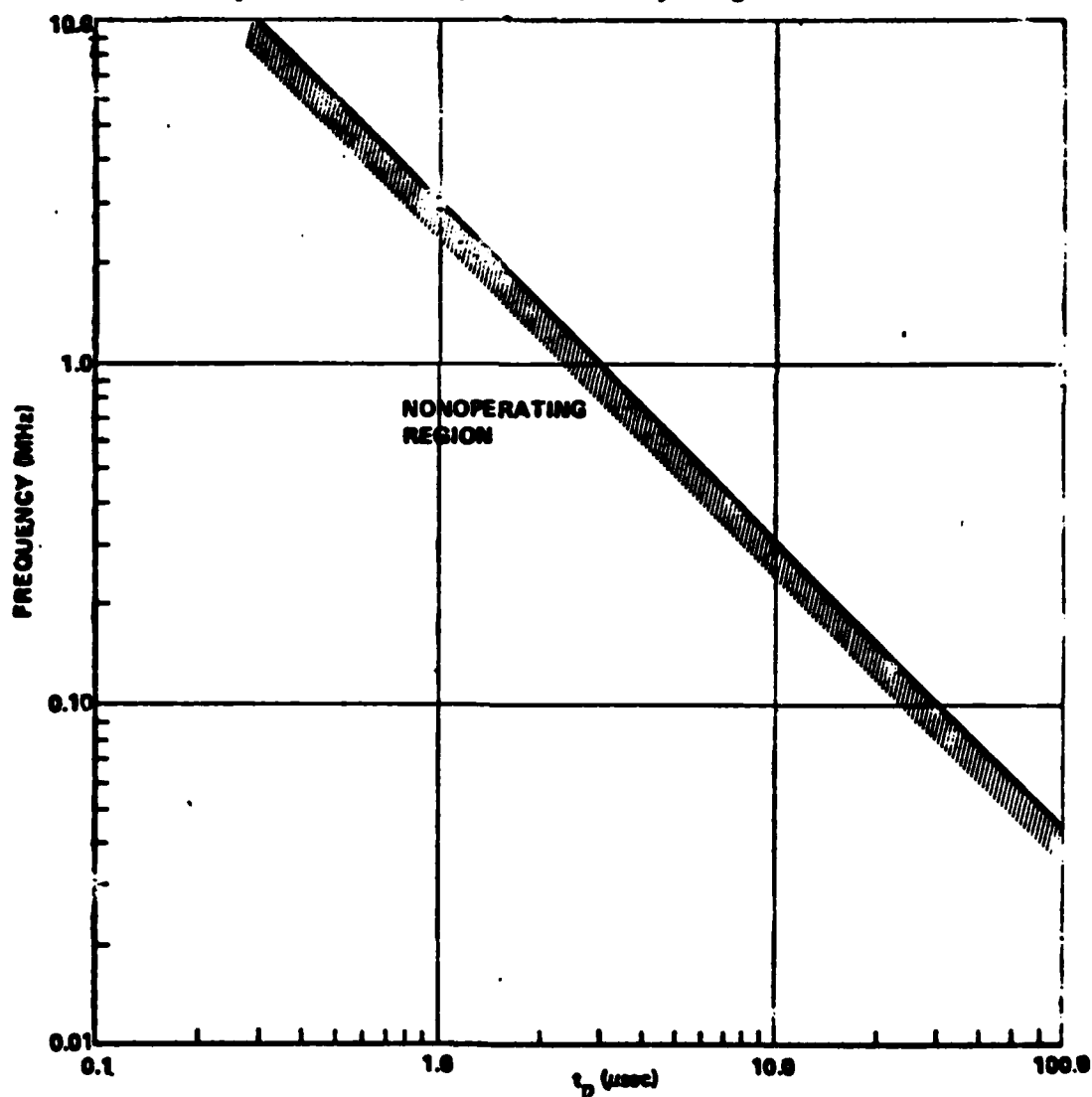
Figure II-11   Modulating frequency versus pulse width
showing the nonoperational space allowed.

(D) Data Acquisition and Recording

The long acquisition and recording system includes a
64-channel (single-ended) analog-to-digital converter (ADC)
for the interface to the test instrumentation. There is
considerable flexibility available in the configuration of
the ADC input voltage range (see the specifications below).
The ADC includes a software programmable variable gain amp-
lifier. Maximum specified data rate is 100,000 samples per
second, but with the overhead burden of programs operating
under the executive monitor, 10,000 to 20,000 samples per
second may be a more reasonable figure. The ADC has inter-
rupt capability so that much more efficient programming is
possible given the availability of programmer manpower.

There presently is no clock in the system. Clock
boards are available, however, and can be added at any time.
The executive monitor will support both line and programmable
clocks.

Depending on test requirements, data will be recorded
on floppy disc or transmitted to a remote computer for record-
ing on hard disk or magnetic tape, or both simultaneously.
The diskette has limited space (256 Kbytes), while the communi-
cations line has limited bandwidth; therefore, an appropriate
compromise will be necessary as to amount and frequency of
data supplies.

At the completion of any given test run, there will be
several options available to experimenters for obtaining

their data. Limited amounts of numerical data may be out-
putted on the 30-character-per-second console device.
Copies of data may be obtained from the floppy diskette
source. Data may be transmitted to a computer via modem
and telephone. Because of the planned link to the graphics
computer in Building 8972, hard copy plots from the CRT
terminal, 7-track magnetic tapes, and 23KJ Disk-Pack capa-
bilities may also be available. There is at present no
line printer capability available. Hard copies of scaled,
reduced numerical data would be available from the graphic
terminal hard copy device.

Specifications of the system components are presented
as follows:

1. Processor/Controller:

    a. PDP-11/04 with M9301 bootstrap

    b. 8K memory

    c. Console keyboard with 30 characters per
        second, 132 column printer.

    d. Floppy disk system device:
        Dual drives
        10 Kbytes/sec maximum transfer rate
        128 Kbytes of storage per diskette

    e. Four levels of hardware prioritized interrupt
        plus NPR

    f. I/O:
            Console Keyboard/printer
            Floppy diskette
            Analog-to-digital converter
            Serial asynchronous interface, 75 to 9600
            baud, full duplex

2. Analog-to-Digital Converter:

   a. ADAC Model 600-11

   b. 12-Bit Digitizing

   c. Number of inputs (randomly selectable):

64 single-ended, or   (all inputs must be
32 true differential, or   of one type only)
64 pseudo-differential

   d. Input voltage range:

Basic Range (Hardware) Selected (Volts)	Range Modification Using Programmable Gain Amplifier (under software control) (volts)			
	x1	x2	x5	x10
±10	±10	±5	±2	±1
±5	±5	±2.5	±1	±0.5
0-10	0-10	0-5	0-2	0-1
0-5	0-5	0-2	0-1	0-0.5

   e. Conversion time: Maximum of 100,000 samples per second.

   f. Aperture time: 20 μsec

   g. Interrupt capability for maximum response time

3. Software:

   a. RT-11 executive monitor system

   b. Assembler (Macro-11)

   c. Editor

   d. Linker, Librarian, files handler, etc. (Some of the capabilities of the software system and utilities will be restricted because of the small amount of memory.)

4. Data I/O:

Analog: (a) 64 channels of analog-to-digital converter input

(b) No analog outputs (ADC has an unim-
                         plemented capability to provide two
                         channels of analog output)

        Digital: (a) No parallel digital inputs

                 (b) No parallel digital outputs

                 (c) One serial asynchronous I/O channel,
                      full duplex 75-9600 band, full modem
                      control, but no modem available

    Test data results: (a) Console printer hard copy

                        (b) Diskette (standard density, IBM
                             soft-sectored)

                        (c) Transmission via serial interface
                             to IGDS in Building 8972:
                               Data plots on graphic display
                               terminal w/hardcopy
                               Recording on 2315 disk cartridge
                               Recording on 7-channel magnetic
                               tape (nonstandard format)

The following figure II-12 illustrates flow diagram of

data acquisition and recording system.

(E) Safety Provisions

Since there are possibilities of oxygen deficiency in the

room where the circulator is installed due to the discharge of

liquid nitrogen from the cooling elbow into the room, an

oxygen detector with hazard alarm set at 20% volume or less

(Model ISA-30, Enmet Corp.) was installed on the room wall.

For safeguarding from possible freon TA leaks from the

heat exchanger loop, two freon TA detectors with hazard alarm

set at 10,000 PPM or more (Model ISA-3, Enmet Corp.) were

installed: one at the freon TA pump: and one on the room wall

over the heat exchanger. The detection level may be lowered

                              60
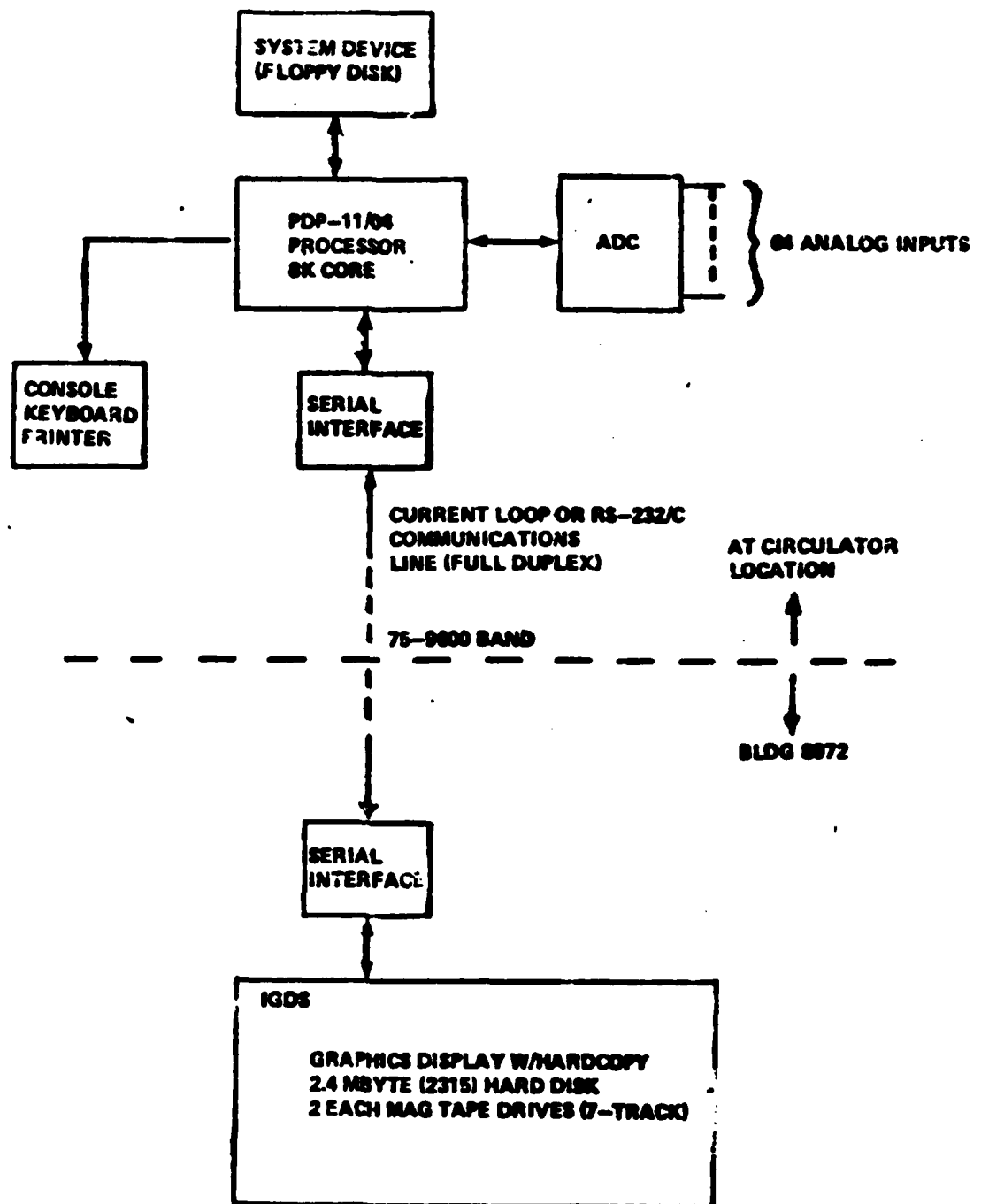
Figure II-12   Flow Diagram of Data Acquisition and Recording System.

61

to 300 PPM with another detector for human health hazard in the near future according to the safety office requirements.

In addition, a double door is requested to be installed in the room for the purpose of venting the hazardous gases outside with a large fan. This task is assigned to the Post Facility Engineers.

(F) Acoustic Attenuators

Two acoustic attenuators, one for upstream and one for downstream of the cavity, were designed and fabricated by Industrial Acoustics Company of New York under technical direction of Prof. Ingard of MIT. The details dimensions are shown in Figure II-13 and II-14.

Technical basis of the attenuator design is explained in Dr. Ingard's report to the Army dated August 1978.

(G) Gas Reactor

In view of the possibility that laser gas may be contaminated or decomposed due to the pulsed energy input at the cavity which in turn causes material degassing or chemical reaction, the need of developing a catalytic converter capable of handling the laser gas at the specified temperature, pressure and flow rates. Materials required to construct such a reactor have been acquired, but the necessary engineering design has not been completed due to the lack of pertinent data of the cavity flow.

1½" Flange

4"
Attenuator

Foam Rubber
Acoustical Fill

Section A-A

26"

2"

13"
Perf. Straight

10"
Perf. Tapered

$5 \, ^{7}/_{8}"\, ^{+\,0}_{-\,^{1}/_{16}}$

A

A

Upstream Attenuator
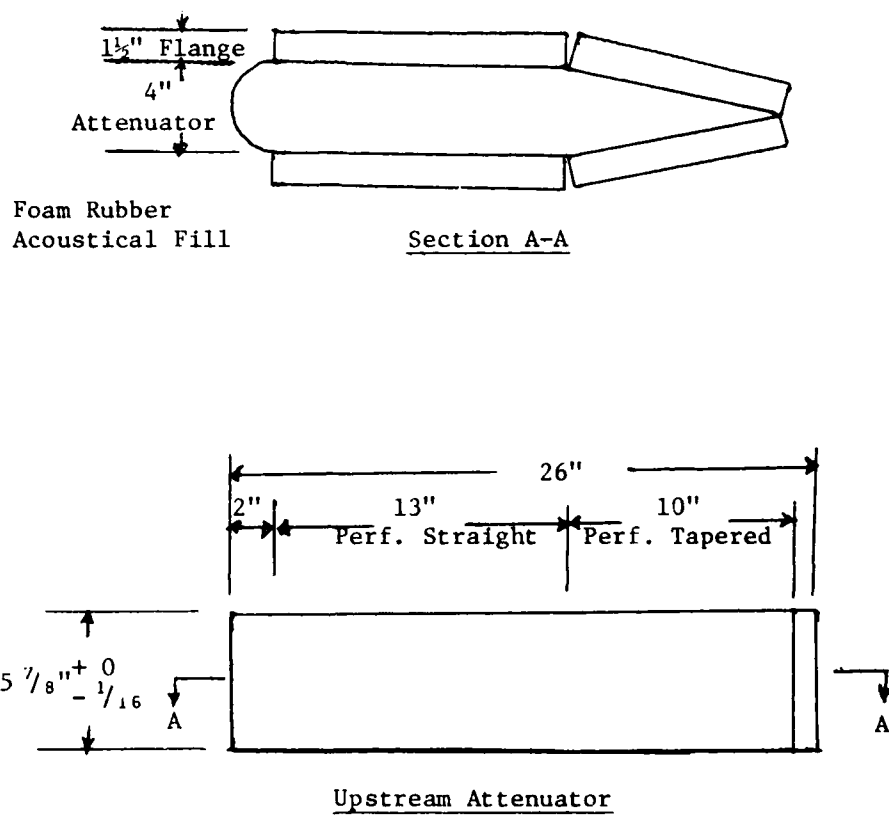
Figure II-13 Schematic of Upstream Acoustic Attenuator

63

2" Gas Passage

4"
Attenuator

2" Gas Passage

4"
Attenuator

2" Gas Passage

29" Casing
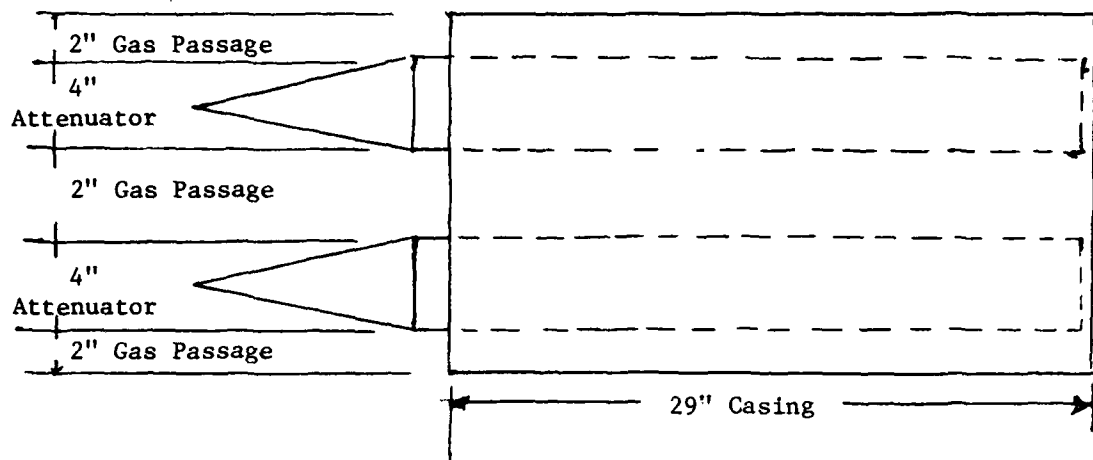
Down Stream Attenuator Assembly

10"
Non-Metallic
Perforated
Min. 22% O.A.

30"
Perforated Steel Face Sheets
Minimum 22% Open Face Area

$5^7/_8$" $3^1/_4$"

Attenuator Elevation

Out-to-Out
16" ± $^1/_{32}$"

$6^1/_4$" ± $^1/_{32}$

Out
to
Out

Section A-A
¼ Scale

Owens-Corning 704 or EQ.

Casing (INCL TOP) 16 GA. Galv. Steel
All Other Sheet Metal 22 GA. of Heavier Galv. Steel
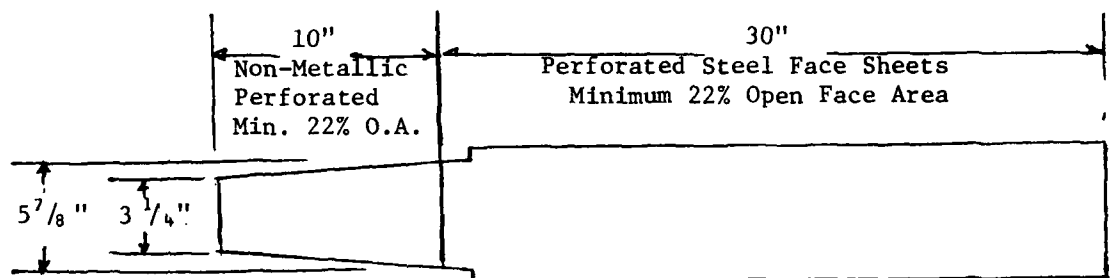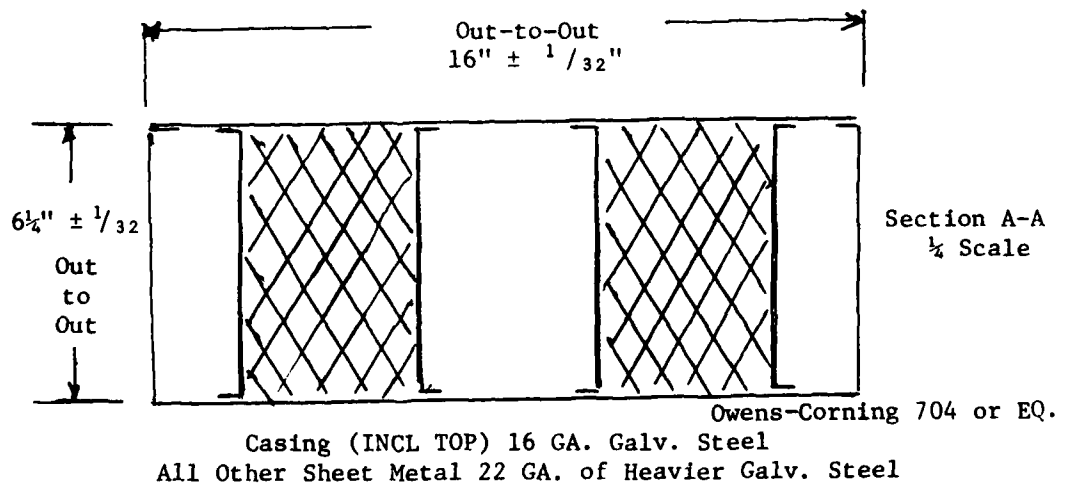
Figure II-14   Schematic of Downstream Acoustic Attenuator

64

III. System Operation and Control

The control system may be categorized as follows: (1) gas circulator control elements, i.e., valve and sensors; (2) the electronic-control assembly; (3) the remote control operational panel. The gas circulator control elements are shown in Figure III-1. They provide all the functions necessary for preparation and operation of the gas circulator.

The control valve signals are received by an electronic control assembly as shown in Figure III-2. This assembly conditions all valve and sensor signals that interface with the gas circulator control elements; provides controller network and reference signals for the closed loop turbo-compressor speed control; provides all sequential logic for system preparation and operation; and provides emergency control logic for safe shutdown and self-protection to the gas circulator. The electronic control assembly (located near the gas circulator) has two interface panels: the closed-cycle gas circulator control harness and the remote control operational panel. The remote control operational panel is the control system link for the operator. It provides the operator with all information necessary for safe, efficient operation; displays critical system parameters; provides the switches and dials necessary for preparation and operational functions; warns the operator of out-of-spec parameters that may be an indication of an impending failure; informs the operator of the status of the system operation and status of propellant supply; provides an emergency of stop, safety interlocks; and controls external duct heaters.
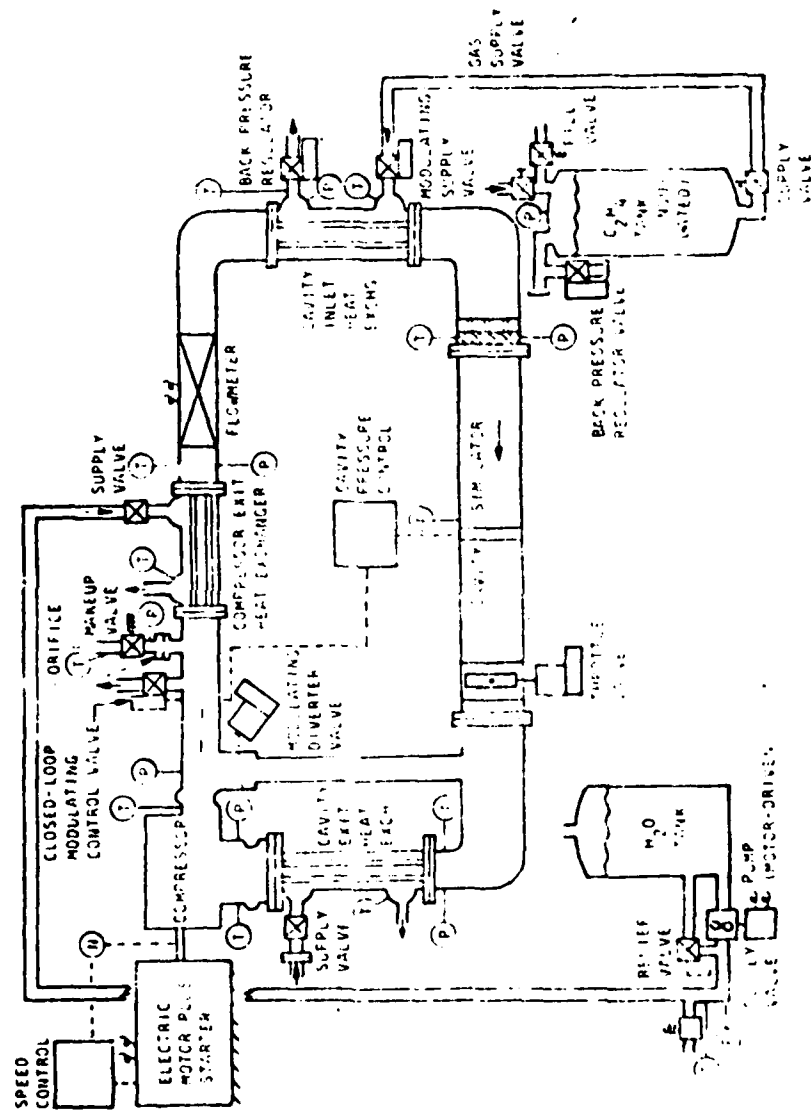
Figure III-1 CCC control elements.

SUBSCALE GAS CIRCULATOR SYSTEM

ELECTRONIC CONTROL ASSEMBLY
- CLOSED-LOOP CONTROL
- SIGNAL CONDITIONING (VALVE AND SENSOR)
- SEQUENTIAL LOGIC
- EMERGENCY CONTROL LOGIC

POWER SUPPLY

VALVE SIGNALS

SENSOR SIGNALS

REMOTE CONTROL OPERATIONAL PANEL
- CRITICAL PARAMETERS DISPLAYED
- OPERATIONAL SWITCHES AND CONTROL SETTINGS
- EMERGENCY STOP
- OUT-OF-SPEC. WARNING SIGNALS
- SAFETY INTERLOCK
- OPERATIONAL STATUS LIGHTS
- FLARE IGNITER CONTROL
- PROPELLANT SUPPLY INFORMATION
- EXTERNAL DUCT HEATERS

Figure III-2   CCC Control System

(1) <u>Preoperative CCC Functions</u>. The system is first evaluated
by attaching a facility vacuum line to the gas vent valve Figure III-1. The
turbocompressor oil system is decoupled to prevent oil leakage past the
seals into the compressor. A hard vacuum is drawn (operational panel)
vacuum pressure indication), and external duct heaters are activated to
vaporize any trapped moisture in the system.

A leakage test is then performed on the system. A clean gas mix is
next introduced through the fill valve until the proper mass content is
achieved. The mass of gas required to achieve a 15-psia cavity inlet
pressure under lasing conditions is predetermined in the form of an average
gas density throughout the loop. This is established by pressure and tem-
perature transducers. Before coupling the turbocompressor oil system,
compressor seal buffer gas is introduced by opening the solenoid valve.
In many cases, the precharging of the system with mixed gas will result in
subatmospheric pressure throughout the loop and, hence, compressor seal
buffer gas is required to prevent oil or oil vapor from entering the
system.

The premixed gas supply tank is precharged with high-pressure
gas. A pressure regulator at the discharge of this tank is set at approxi-
mately 100 psia. (The tank and regulator are not shown in Figure III-1, and
are not considered part of the closed-cycle gas circulator
system.) A fill valve orifice is selected to deliver from 0.5 to 5.0
percent of total system flowrate, depending on the rate of depoisoning
desired during lasing operation.

The water and freon TA coolant tanks are filled with their isolation valves closed. The freon TA coolant tank is filled at ambient pressure (at a corresponding saturated liquid temperature of $170^{O}K$). The GN_2 supply valve is closed and the cap is removed from the tank vent valve. As heat from the environment enters the tank during a prestart waiting period, vapor pressure in the tank will rise to a maximum of 23 psia, at which point the tank vent valve opens holding that pressure and a corresponding saturated liquid temperature of $320^{O}R$.

(2) <u>Closed Cycle Gas Circulator Startup</u>. Preliminary to starting up of the compressor, the water tank pump is started up, and the Freon TA pump also started up. The gas diverter is set to a full bypass position. The gas throttle valve is set to a wide-open position. The compressor, oil pressure, and scavenge pumps are energized. A start signal by the operator at the control panel initiates acceleration of the compressor. Due to the reduced impedance of the bypass line, the acceleration power requirements are minimized. The cavity exit heat exchanger wave flow valve will remain closed during the acceleration until such time as the gas temperature at the heat exchanger exit exceeds $315^{O}K$. At this point, a thermal switch will open the solenoid valve allowing water to flow through the heat exchanger and thereby holding the exit gas temperature at the desired $320^{O}K$ temperature. When the compressor reaches maximum speed, the motor frequency control will electrically modulate motor current, thereby holding the desired speed. If lasing is to be accomplished at a $200^{O}K$ cavity inlet temperature, then the walls of the freon TA heat exchanger must be prechilled to approximately 185° to permit nucleate boiling heat transfer on the coolant side of the heat exchanger. This

69

prechilling operation is accomplished by opening the Freon TA throttle

valve wide open, which is remotely controlled from the operators panel.

The heat exchanger back-pressure regulator maintains 23-psia coolant

vapor pressure. The gas diverter valve, controlled at the operator

control panel, is set to a zero bypass condition, allowing full gas

flow to the freon TA heat exchanger. When the gas exit temperature

reaches $320^{\circ}R$, the prechilling operation is completed and the system is

in readiness for lasing.

(3) <u>System Operation</u>. The gas diverter valve is modulated at the

control panel until the desired cavity flowrate is indicated by the

flowmeter. Cavity inlet pressure is noted, and the gas vent and/or fill

valve is actuated as required to vary the system gas inventory. It is

important to note, however, that the nonlasing cavity inlet pressure

will in general be lower than the pressure under lasing conditions. To

prevent a substantial pressure transient immediately following lasing, it

is desirable to establish the proper gas weight in the system in the "ready"

condition.

Cavity inlet temperature is noted. If lasing is to take place at

$200^{\circ}K$ the coolant throttle valve is opened wide and the adjustable back-

pressure regulator is varied until desired exit gas temperature is

achieved. The throttle valve is sized to provide a coolant flowrate

such that approximately an 80 percent exit quality will exist at the

coolant exit line under maximum power operation of the system. At

reduced power operation (reduced gas flowrate), the use of freon TA

coolant can be conserved by closing the coolant throttle valve and thereby reducing coolant flowrate. This valve should be adjusted closed until a rise in coolant exit temperature is noted indicating that some super heating is taking place in the exit line. An exit gas quality of less than 100 percent could then be re-established by a readjustment of the throttle valve to a more open position, until the exit gas stabilizes.

If lasing operation is to take place at a cavity inlet temperature substantially higher than 200°K, then the freon TA heat exchanger operates in a superheating mode. The adjustable back-pressure regulator is set for 23 psia. The coolant throttle valve is adjusted until the desired exit gas temperature is achieved.

Upon activating the lasing switch on the operators panel, the solenoid fill valve is opened, introducing clean gas mix at a rate established by the orifice size. Lasing operating with 0.5- to 5-percent depoisoning is established by selection of the proper orifice. At the same time that lasing is initiated, the cavity pressure control is activated. This represents the only closed-loop control in the closed-cycle gas circulator system aside from the frequency speed control of the compressor motor drive. The cavity pressure control is shown in Figure III-3. A pressure signal at the cavity inlet is compared with a reference value of 15.0 psia. If an error exists between these two values, a proportional signal passes through a compensation network to establish a vent valve position reference which, in turn, is compared to a feedback position signal from the valve. A position error signal

71

then actuates the servovalve to hold the desired position, and thereby

maintain cavity inlet pressure at the selected value. Since the gas vent

valve is sized to handle up to 5 percent of maximum gas circulator flow,

there is no change necessary to the control should a different gas fill

orifice be selected to change the depoison rate. During lasing operation,

if it is desirable to vary cavity inlet pressure, this can be accomplished

by simply selecting the new desired pressure reference at the control

panel. The gas vent servovalve will automatically modulate to hold the

selected cavity inlet pressure at the same depoison rate.

As shown on the control schematic Figure III-3, the system provides

for either automatic or manual control of cavity inlet pressure depending

on the switch setting. With contact B closed, the cavity inlet pressure

is controlled manually by setting a gas vent valve position reference at

the control panel. With contact A closed, a pressure reference is set

up at the control panel and closed-loop control of cavity inlet pressure

is established. The control system is so designed as to provide "bumpless

transfer" between manual and closed-loop control. This means that a

smooth transition will take place when switching between the two controls.

Variations in cavity inlet temperature can be achieved by remote position-

ing of the coolant throttle valve at the control panel. This will vary

the coolant flow rate and hence the superheat temperature at the coolant

exit.

Figure III-3   Cavity Pressure Control Schematic.

The diagram contains the following labels:

CCC SYSTEM

GAS VENT VALVE

POSITION SIGNAL CONDITIONER

PRESSURE SIGNAL CONDITIONER

X_T

X_{REF}

CONTROLLER NETWORK

X_{REF}

LASING SIGNAL

B   A

SWITCH

X_{REF}

P_{REF}
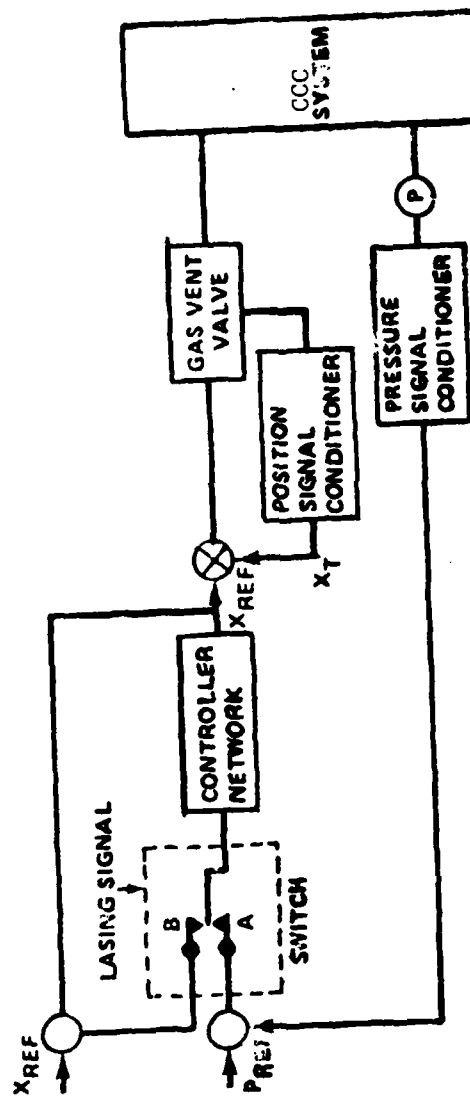
(1)   THE LASING SIGNAL ACTUATES SWITCH WHICH CLOSES
        CONTACT A, ACTIVATING CLOSED LOOP PRESSURE CONTROL

(2)   THE NON-LASING SETTING OF SWITCH (CONTACT B) PERMITS
        REMOTE MANUAL POSITIONING OF GAS VENT VALVE

73

IV. Calibrations and Preparation of the Instrumentation System

A. Hot-Wire Anemometer Calibration for Velocity Measurement

1. Theory: When the hot-wire anemometer is calibrated for velocity measurement, the basic function of the anemometer is to keep the hot-wire at a specific temperature (known as the operating temperature). As flow passes over the hot-wire, the temperature of the wire drops. The anemometer must therefore step up the voltage across the hot wire to keep the wire at its operating temperature. Given several known velocities and their corresponding voltages, a plot of velocity vs. voltage can be constructed. This will yield an approximately 1/4 power curve. By applying curve fitting techniques, a relationship for velocity in terms of voltage can be derived. Henceforth, whenever the hot wire is exposed to a flow and a certain voltage is read, that voltage is merely read into the equation and the velocity of the flow can be found.

2. Procedure: The hot wire (and probe support) is positioned in front of a hole in a pressure chamber. The flow of gas into this chamber is controlled through means of a pressure regulator, and the pressure inside the chamber is read from a manometer. A thermometer is also mounted in the chamber so that the fluid temperature in the chamber can be found.

74
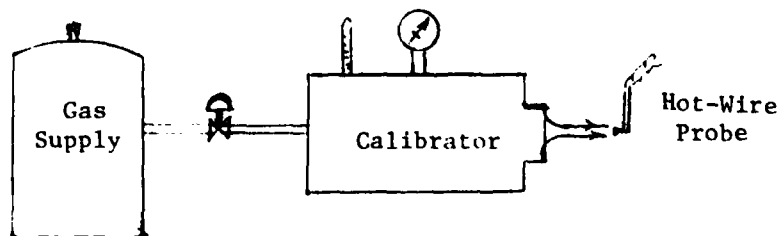
Using this apparatus, the pressure and temperature of the gas inside the
chamber (which is causing a specific flow across the hot wire outside the
chamber) can be found. Then, using the relation:

$$V = \sqrt{2 \times k \times R \times 32.2 \times (459.6 + Temp) \times \frac{1 - \dfrac{\text{Baro Press }(14.7)/760 + \text{Baro Press } 14.7}{\text{Press}} \cdot \frac{1}{760}}{k-1}}$$

Where: R denotes the gas constant
         k denotes the specific heat ratio

the velocity of the flow across the probe can be found. By adjusting the
regulator to several settings, the several known velocities needed for the
calibration can be found.

The necessary voltages corresponding to these velocities are
found at the same time as the velocities by simply reading a digital
voltmeter which is hooked up to the anemometer. The only preparation that
the anemometer requires is that the operating temperature be set. This is
done as follows:

1. Attach the Hot Wire and Probe Support to the PROBE jack on the
anemometer with axial cable.

2. Set the resistance dials to zero.

3. Turn anemometer to STAND BY and switch power on.

4. Using the 0-3 volt scale, adjust the REF SET knob so that the anemometer
reads 2 volts.

5. Depress the RES MEAS toggle and note anemometer voltage. If it decreases,
the resistance setting on the resistance dial is too low. If it increases, the
setting is too high. By interacting between adjusting the resistance setting

75

and depressing the toggle, the cold resistance can be found (cold resistance will be at point where the voltage does not change when the toggle is depressed).

6. The cold resistance is then multiplied by a given overheat ratio (a constant which depends on the type of fluid which the wire is exposed to) to get the operating resistance. This number is set into the resistance decks and specifies to the anemometer the operating temperature.

Once the operating temperature is set, the REF SET knob is adjusted so that the anemometer reads 15 volts. The anemometer is then switched to RUN, and the previously described procedure is used to calibrate the Hot Wire.

B. Hot-Wire Anemometer Calibration for Temperature Measurement With a High Dynamic Response

1. Theory: When using Hot Wires to measure temperature fluctuations, the anemometer serves to measure the change in voltage across the Hot Wire which is caused by a change in the Wire's temperature. Since the resistance of, and therefore the voltage across, a conductor changes with temperature, we can derive an equation relating the change in voltage to the change in temperature:

$\Delta V = K \Delta T$ where K = constant

If only one of the variables (preferably T_{final}) is not known, we can solve the equation for this variable.

2. Procedure: The equation used is as follows:

$V - V_o = R_o J_o \, OI \, (T - T.)$

where:

V_o = initial voltage

V = final voltage

76

R_o = cold resistance of wire at initial temperature

J_o = temperature co-efficient of resistance for sensor being used

T = final temperature

T = initial temperature

0 - amplifies gain   (1000 standard)

I = current through sensor (1.5 ma standard)

Solving for T:

$$T = \frac{V-V_o}{R_o J_o} GI + T_o$$

T_o can be measured at the experiments start, as can V_o R_o, J_o, G and I
are known constants. V is measured with an oscilloscope.

Typical Data

Δv= 2.T divisions . 1.5 volts/div=1.05 volts

T_o = 38°C

R_o = 6.59r

J_o = 3.5x10^{-5}

G = 1000

i = 1.5

$$T = \frac{1.05}{6.59(3.5 \times 10^{-2})\ (1000)\ (115)} + 39$$

T = 69.3°C

Measured Temperature = 72°C

% error: $\frac{169.3-721}{69.3}$ x100 = 3.9%

C. Determination of Hot-Wire Anemometer Linearization Coefficients.

When calibrating probes according to the method discussed, 4 separate

pieces of data are collected and inputed to a computer. The 4 pieces of

data follow:

1. The barometric pressure
2. The pressure read off the manometer
3. The temperature in degrees Fahrenheit
4. The voltage across the probe, or the bridge voltage

The output is the original voltage with a corresponding velocity. A func-

tion can then be found to relate the velocity in terms of voltage from a

curve fit program. When the probe is in use then, the velocity of the flow

across the probe can be determined by plugging that voltage into the func-

tion found from the curve fit program.

Data for Calibration of Probe 10
Barometric Pressure = 747.74

Pressure	Temperature	Volts
0	74.5	2.03
.02	74.5	2.59
.04	74.5	2.68
.06	74.5	2.75
.08	74.5	2.80
.10	74.5	2.83
.12	74.5	2.86
.14	74.5	2.89
.16	74.5	2.92
.18	74.5	2.94
.20	74.5	2.96
.30	74.5	3.05
.40	74.5	3.09
.50	74.5	3.14
.60	74.5	3.18
.70	74.5	3.21
.80	74.5	3.24
.90	74.5	3.27
1.00	74.5	3.30
1.30	74.5	3.36
1.60	74.5	3.41
1.90	74.5	3.45

2.20	74.5	3.49
2.50	74.5	3.51
2.70	74.5	3.54
3.00	74.5	3.56

With the Temperature, Barometric Pressure, and Pressure from the Manometer, a velocity is calculated which corresponds to a voltage but is not dependent on it. So, at another time, a different velocity may be calculated for the same manometer pressure due to changes in barometric pressure and temperature, but the voltage would change also because of the different velocity. For these particular conditions, the velocity that was calculated is shown below.

Volts	Velocity
2.03	0
2.59	11.923
2.68	16.862
2.75	20.652
2.80	23.844
2.83	26.659
2.86	29.202
2.89	31.542
2.92	33.719
2.94	35.763
2.96	37.696
3.05	46.166
3.09	53.303
3.14	59.589
3.18	65.272
3.21	70.495
3.24	75.357
3.27	79.922
3.30	84.237
3.36	96.022
3.41	106.500
3.45	116.027
3.49	124.821
3.51	133.027
3.54	138.222
3.56	145.663

Linearizer: Setup and Procedure

The 1052 Signal Linearizer is a device which uses 4 coefficients to straighten out a voltage-velocity graph. The calibration procedure usually ends with the bridge voltage ranging from around 2 volts for zero flow to about 3.5 volts for 150 ft/sec velocity. Normally, this range results in a 4th power function relating the voltage and velocity. The linearizer takes the inputed voltage, (in our case anywhere from 2v to about 3.5v) and stretches it out over a range of 0 to 10v.

The main purpose of the linearizer is to give a graph which is easier to read off velocities corresponding to voltages and to make it easier to read electronic devices which would be monitoring the output signal, whether linearized or not.

Procedure for Setting up the Linearizer

The coefficients that are used depend on the characteristics of each probe and therefore are calculated from a probe's voltage-velocity relationship. The coefficients used here were calculated on a computer at the lab, utilizing aspects of the TSI program given in the handbook on the 1052 Linearizer.

To begin, attach a digital voltmeter to the output jack on the linearizer. Turn the knob to OUTPUT. Under INPUT, turn the knob to COEF. SET and then place all the toggles under POLYNOMIAL COEFFICIENTS in the neutral position. Of the four coefficients calculated, check to see if all the coefficients are less than 10. If they are all less then 10, then put the toggle under OUTPUT in the X1 position. If a coefficient is greater then 10 but less than or equal to 20 put that toggle in X.1 position. Take the

80

first coefficient, A, and place the A toggle in either the positive or negative position determined by the polarity of A. Then adjust the potentiameter corresponding to A until the number displayed on the digital voltmeter is the same as the coefficient. When this is completed, return the toggle to the neutral position and go to the next coefficient. Repeat all steps until all coefficients are set. Then place all toggles into the correct position whether positive or negative. A check at this point is to see if the voltmeter is reading 10v. (Note: If toggle is in X.1 position then the voltmeter would read 1 v.) The coefficients are now set. To set the span, turn the knob under INPUT to either REAR or EXTERNAL. REAR is used if taking voltages directly from a probe while EXTERNAL is used when supplying a voltage through a source. To check to see if the linearizer coefficients are correct, supplying a voltage is the most efficient course. Put in the base voltage of the probe. This value should correspond to zero after linearization. Adjust the output at the digital voltmeter until it reads zero by adjusting the ZERO SUPPRESS. When zero is reached, then input full scale voltage. A linearized signal of 10v should result. Adjust the SPAN (FINE) until 10v is reached. For these purposes, SPAN (COURSE) is set at 3. Return to base voltage to see if the linearizer is still producing 0v. If not, once again adjust ZERO SUPPRESS. Return to full scale voltage to see if the linearizer is still producing 10v. If not, adjust SPAN (FINE). The linearizer is now ready for different input voltages. A graph of the linearized output of a probe's voltage follows as compared to the raw input data. The calculated coefficients are also shown. This graph and the calculations are for Probe 10. The program used to Calibrate first the velocity and finally the linearizer coefficients is also shown.

81
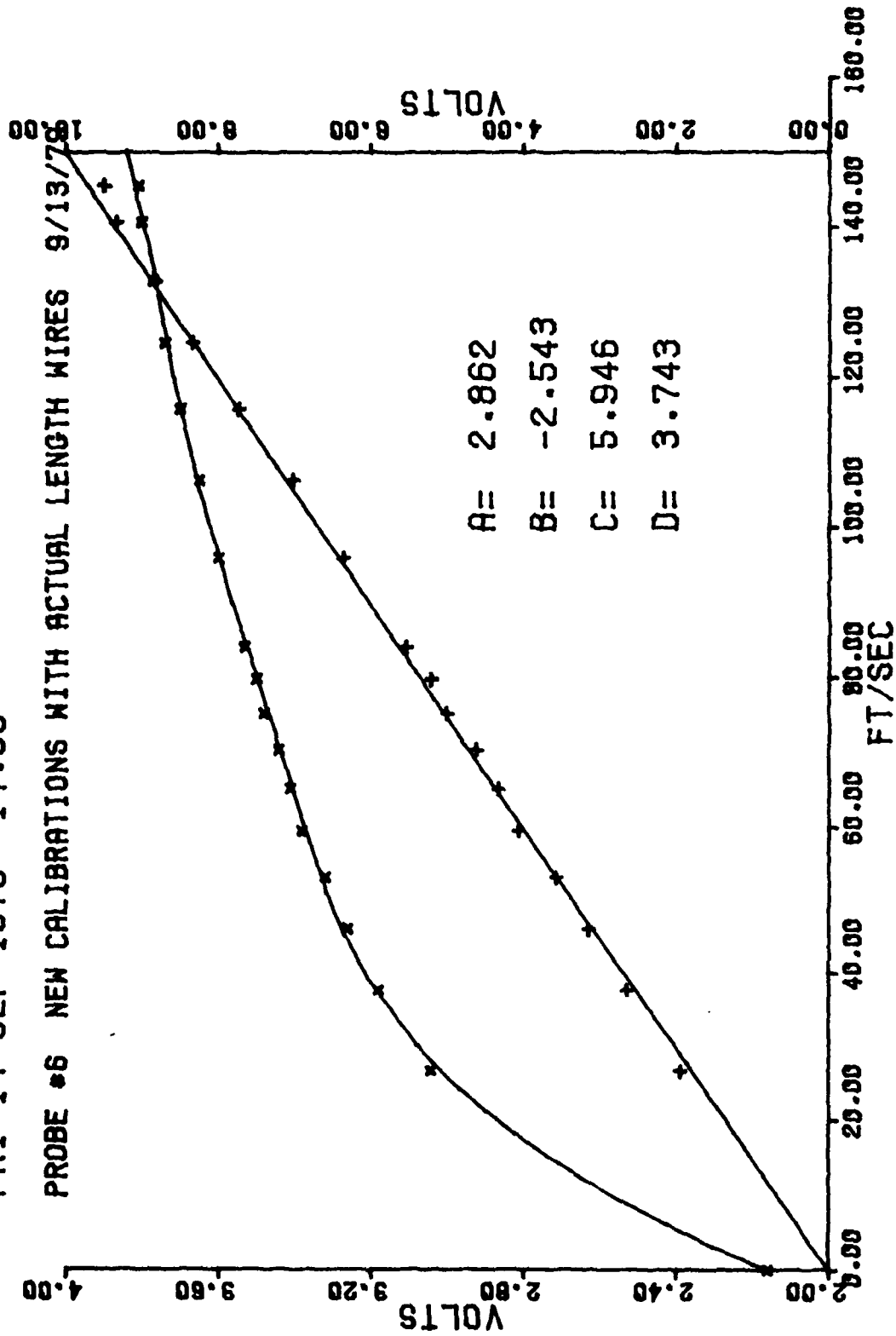
Figure IV-1 Typical Calibration Curves of a Hot-Wire Probe with Computed-Aided Plotting

82

Computer Program

for

Hot-Wire Probe Calibration and Linearization

83

```
0001        FTN,L
0002            PROGRAM PLOT7(), 1 AUG 79
0003            DIMENSION POWER (50), FLOW (50), CALFL(50),
                R(13), A(8.8), S(7).
0004        &WEIGHT (50)
0005            DIMENSION COEFF(5), ERROR(21), X52(8,8)
0006            DIMENSION IPAR(5), IB(5)
0007            DIMENSION X(50), Y(50), NPK(3), MAT(18,19),
                WORK(1), IHLD(1)
0008            REAL MAT
0009            DIMENSION XCAL(23)
0010            DATA XCAL/0.,.75.3.,6.,9.,12.,15.,18.,21.,24.,27.,30.,39.,45.,
0011        &51.,60.,66.,75.,90.,105.,120.,135.,150./
0012            CALL RMPAR(IPAR)
0013            LUI=IPAR(1)
0014            IF(LUI.EQ.0)LUI=1
0015            LUO=IPAR(2)
0016            IF(LUO.EQ.0)LUO=6
0017            LUR=IPAR(3)
0018            IR(LUR.EQ.0)LUR=5
0019            IF(IPAR(5).EQ.1) CALL PLTLU(14)
0020            IF(IPAR(5).EQ.1) CALL SFACT (9.,6.5)
0021            IF(IPAR(5).EQ.1) CALL LLEFT
0022            IF(IPAR(5).EQ.1) CALL PLOT (.5,.5,-3)
0023            IP=3
0024            CALL TODAY(IB(2))
0025            IB=22
0026            PS=.03611
0027            R=82.76
0028            CK=1.48
0029            ORDER = 4
0030            WRITE(LUI, 1045)
0031    1045    FORMAT(" ENTER PROBE     ")
0032            READ(LUR,*)NP
0033            WRITE (LUO,1048)(IB(KK),KK=2, 12),NP
0034    1048    FORMAT("       SPLINE        PROGRAM",6X, 11A2.
0035        &//" PROBE         ", 12,/)
0036            WRITE(LUI,1055)
```

84

```
0037      1055    FORMAT(" ENTER P(TORR)")
0038              READ(LUR,*)P
0039              WRITE(LUO,1066)P
0040      1066    FORMAT(" P(TORR)=    ",F7.3,/)
0041      010     DO 1,I=1,50
0042              IF(IPAR(4).EQ.0)GOTO 1097
0043              READ(LUR.*)FLOW(I),POWER(I)
0044              IF(FLOW(I).EQ.77.)GOTO 1099
0045              GOTO 1098
0046      1097    READ(LUR,*)PRESS, TEMP, POWER(I)
0047              IF(PRESS.EQ.77.)GOTO 1099
0048              PSI=PRESS*PS
0049              IF(PRESS,EQ.0.)FLOW(I)=0.
0050              IF(PRESS.EQ.O.).)GOTO 1098

0051              FLOW(I)=SQRT((2.0*CK*R*32.2*(459.6+TEMP)/(CK-1.0))*
                  (1.0-(P*14.7
0052           &/760.0/(PSI+(P*14.7/760.0)))**(1.0-1.0/CK)))
0053      1098    CONTINUE
0054              XP=FLOW(I)*.04
0055              X(I)=FLOW(I)
0056              YP=(POWER(I)-2.0)*3.
0057              Y(I)=POWER(I)
0058              IF(IPAR(5).EQ.1) CALL PLOT(XP,YP,IP)
0059              IP=2
0060              IF(IPAR(5).EQ.1) WRITE(LUO,1010)FLOW(I), POWER (I)
0061      1010    FORMAT(2X,F12.5,F12.5)
0062      1       CONTINUE
0063      1099    CONTINUE
0064              IF(IPAR(5).EQ.1) PAUSE 0001
0065              N=I-1
0066              NPK(1)=7
0067              NPK(2)=7
0068              NPK(3)=N-13
0069              NX=3
0070              NNX=18
0071              CALL SPLIN(X,Y,NPK,NX,MAT,NNX,WORK, IHLD,E)
0072              IF(E.NE.0.)WRITE(LUO,1030)E
```

85

```
0073      1030    FORMAT(" ERROR,  E=", F6.2)
0074              DO 1011 I=1, 12
0075      1011    IF(IPAR(5).EQ.1) WRITE (LUO,1012)I, MAT(I,1)
0076      1012    FORMAT(2X,I2,E12.5)
0077              IP=3
0078              DO 1007 I=1,23
0079              XV=XCAL(I)
0080              FLOW(I)=XV
0081              CALL VALSP(XV,X,Y,MAT,NNX,YV)
0082              XP=XV*.04
0083              YP=(YV-2.)*3.
0084              POWER(I)=YV
0085              IF(IPAR(5).EQ.1) CALL PLOT (XP,YP,IP)
0086              IP=2
0087      1007    IF(IPAR(5).EQ.1) WRITE(LUO,1008)I,XV,YV
0088      1008    FORMAT(2X,I2,F12.5,F12.5)
0089              NUMBER=23
0090              ZEROE=POWER(1)
0091              ZEROF=FLOW(1)
0092              DO 142 I=1.NUMBER
0093              FLOW(I)=FLOW(I)-ZEROF
0094      142     POWER(I)=POWER(I)-ZEROE
0095              WEIGHT(1)=100.
0096              WEIGHT(2)=80.
0097              WEIGHT(3)=60.
0098              WEIGHT(4)=40.
0099              WEIGHT(5)=20.
0100              WEIGHT(6)=10.
0101              NUM1=NUMBER-1
0102              DO 2, I=7,NUM1
0103      2       WEIGHT(I)=1
0104              WEIGHT(NUMBER)=100.
0105              DO 3, I=1,3
0106      3       R(I)=0
0107              DO 4, I=1.2
0108      4       S(I)=0.
0109              Z1=0.
0110              DO 5, I=1, NUMBER
```

86

```
0111          R(1)=R(1) + WEIGHT(1)
0112          R(2)=R(2) + WEIGHT(1)*POWER(1)
0113          R(3)=R(3) + WEIGHT(1)*POWER*(1)**2
0114          S(1)=S(1) + WEIGHT(1)*FLOW(1)
0115      5   S(2)=S(2) + WEIGHT(1)*POWER(1)*FLOW(1)
0116          N1=1
0117      22  L=N1+1
0118          K1=L+1
0119          DO 7, I=1,L
0120          DO 8, J=1,L
0121          I2 = J-1+1
0122      8   A(I,J)=R(I2)
0123      7   A(I,K1) =S(I)
0124          DO 9, I=1,L
0125          A(K1,I)=-1.
0126          K2=I+1
0127          DO 10 J=K2,K1
0128      10  A(K1,J)=0.
0129      11  C=1./A(I,I)
0130          DO 13, I1=2, K1
0131          DO 14 J=K2,K1,1
0132      14  A(I1,J)=A(I1,J)-A(I1,I)*A(I,J)*C
0133      13  CONTINUE
0134          DO 30 I1 =1, L
0135          DO 31 J=K2, K1
0136      31  A(I1,J)=A(I1+1,J)
0137      30  CONTINUE
0138      9   CONTINUE
0139          DO 141, I=1,L
0140      141 X52(I,K1-2)=A(I,K1)
0141          IF(N1-ORDER)17,23,23
0142      17  N1=N1+1
0143          J=2*N1
0144          R(J) = 0.
0145          R(J+1) = 0.
0146          S(N1+1)=0.
0147          DO 21I=1.NUMBER
0148          R(J) = R(J)+(POWER)(I)**(J-1)*WEIGHT(I)
```

87

```
0149            R(J+1)=R(J+1)+(POWER(I)**J)*WEIGHT(I)
0150     21     S(N1+1)=S(N1+1)+FLOW(I)*POWER(I)**N1*WEIGHT(I)
0151            GO TO 22
0152     23     MLOOP=ORDER+1
0153            DO 32 I=1,MLOOP
0154            COEFF(I)=A(I,K1)
0155            X52(I,4)=+X52(I,4)*(POWER(NUMBER)**(I-1))
0156     32     CONTINUE
0157            IF(IPAR(5).EQ.1) PAUSE 0002
0158            IP=3
0159            DO 112 JK=2, NUMBER
0160            VP=(POWER)(IK)+ZEROE-2.0)*3.
0161            CALFLO=COEF(1)
0162            DO 113 I=2,5
0163     113    CALFLO=CALFLO+COEFF(I)*POWER(JK)**(I-1)
0164            XP=(CALFLO+ZEROE)*0.4
0165            IF(IPAR(5).EQ.1)CALL PLOT(XP,YP,IP)
0166            IP=2
0167            CALFL(JK)=CALFLO*10./FLOW(NUMBER)
0168     112    ERROR(JK)=(CALFLO-FLOW(JK))*100./FLOW(NUMBER)
0169            SPAN=10./FLOW(NUMBER)
0170            WRITE(LUO,151)
0171     151    FORMAT(/," MODEL 1052 OR 1072 LINEARIZER
                COEFFICIENTS")
0172            AA=X52(2,4)*SPAN
0173            BB=X52(3,4)*SPAN
0174            CC=X52(4,4)*SPAN
0175            DD=X52(5,4)*SPAN
0176            WRITE(LUO,1031)AA
0177            WRITE(LUO,1040)BB
0178            WRITE(LUO,1050)CC
0179            WRITE(LUO,1060)DD
0180     1031   FORMAT(" A=   ",F12.5)
0181     1040   FORMAT(" B=   ",F12.5)
0182     1050   FORMAT(" C=   ",F12.5)
0183     1060   FORMAT(" D=   ",F12.5,/)
0184            WRITE(LUO,1070)
```

```
0185    1070    FORMAT(" I FT/SEC  VOLTS  NORM V  CALC V
                ERR %  WT")
0186            DO 35, I=1, NUMBER
0187            FL=FLOW(I)*SPAN
0188            POWI=POWER(I)+ZEROE
0189            WRITE(LUO,121)I, FLOW(I),POWI, FL,CALFL(I),ERROR(I),
                WEIGHT(I)
0190    121     FORMAT(I3,F8.2,4F8.3,F6.1)
0191    C       IF(LUO.EQ.6)WRITE(LUO,1056)
0192    1056    FORMAT( "I" )
0193    C       WRITE(LUO,152)
0194    152     FORMAT(/," THESE COEFFICIENTS ARE FOR A TSI
                MODEL  ,SERIAL"/
0195            &"  CALIBRATED  OVER  THE  RANGE  OF  0
                TO  IN  AT  PSIA"/
0196            &" AND DEG . THE BRIDGE OUTPUT WAS VOLTS AT ZERO
                FLOW"/
0197            &" AND  VOLTS AT FULL SCALE. THIS DATA SHOULD BE
                USED TO SET"/
0198            &" ZERO AND SPAN.")
0199    1112    DO 1112 JK=2,N
0200            Y2=Y(JK)-Y(1)
0201            CALFLO=COEFF(1)
0202            DO 1113 I=2.5
0203    1113    CALFLO=CALFLO+COEFF(I)*Y2**(I-1)
0204            CALFL(JK)=CALFLO*10./FLOW(NUMBER)
0205            ERROR(JK)=CALFLO-X(JK))*100./FLOW(NUMBER)
0206            WRITE(LUO,1122)JK,X(JK),Y2,CALFL(JK),ERROR(JK)
0207    1122    FORMAT(I3,F8.2,3F8.3)
0208            END
0209            SUBROUTINE VALSP(XV,X,Y,MAT,NNX,YV)
0210            DIMENSION X(I),Y(I),MAT(18,19)
0211            REAL MAT
0212            I=0
0213            IF(XV.GT.X(7))I=1
0214            IF(XV.GT.X(14))I=2
0215            YV=0.
0216            DO 10 J=4.1,-1
```

```
0217      10     YV=MAT(J+4*I,1)+XV*YV
0218             RETURN
0219             END
0220             END$
```

D.   Transducer Calibration

Transducers are small sensing elements that detect pressure differ-
entiation. The end of a transducer contains a small crystal, electrically
connected, in contact with a metal diaphragm. With a change in pressure,
the diaphragm is pushed in which applies stress to the crystal. The crys-
tal deforms because of the stress and this deformation causes a voltage to
occur across the electrical connection. From the manufacturer it is known
for each transducer what the relationship of millivolts per psia is, so
the value of psia can be determined when the voltage is recorded.

The transducers for this project were calibrated in the following way.
A cylinder with openings at either end and a port in the middle was used
as the pressure chamber. The port was closed. At one end, gas was pumped
in until a certain pressure was reached. At the other end, the opening
was opened which allowed it to go to atmospheric pressure. A transducer,
connected to an oscilliscope, was placed in at the end which was at atmos-
pheric pressure. Then, with the transducer end at atmospheric and the other
end at a certain pressure, the port in the middle was opened. The change in
pressure indicated by the transducer was recorded on the oscilloscope screen.
At .02 volts per division, the voltage produced by the transducer is found
and from there, the differential pressure is found. Ideally, the pressure
calculated from the transducer should equal the pressure of the end pumped
up with gas. Realistically there are differences.

91

E. Flow Meter Calibration and Checkout

For measuring mass flow rate of the recirculating laser gas, a Daniel electro-magnetic gas turbine meter (8" size Model No. 2000-0) was mounted in the circulator. In order to ensure the accuracy of the meter, a test series was devoted to perform a calibration process. In the series, the data collected from the Daniel meter in terms of pulses per second (H2) were converted into mass rates of flow based on the conversion factor furnished by Flow Calibration Facility of Daniel Industries, Inc.

The data from the meter were compared to the data obtained from the Pitot-static tube inserted at the cavity section with reasonable accuracy. The mass flow rate measured with the Pitot-static tube at the cavity section was obtained through use of integral method for the velocity distribution curve across the cavity section.

Figures IV-2, IV-3, and IV-4 show the relationships of pulse vs. diverter valve opening, and Pitot-static pressure vs. pulse obtained experimentally from the calibration process. Three test series 13, 14 and 15 shown in figures demonstrate the repeatibility of the flow meter. Figure IV-5 presents the velocity profile measured across the cavity center plane section by the use of the Pitot-static tube. It shows some slight variation in velocity across the section, however, the average velocity obtained from the profile through the integral method, made the comparison with the flow meter data possible and verified the flow meter reliability and accuracy.

92
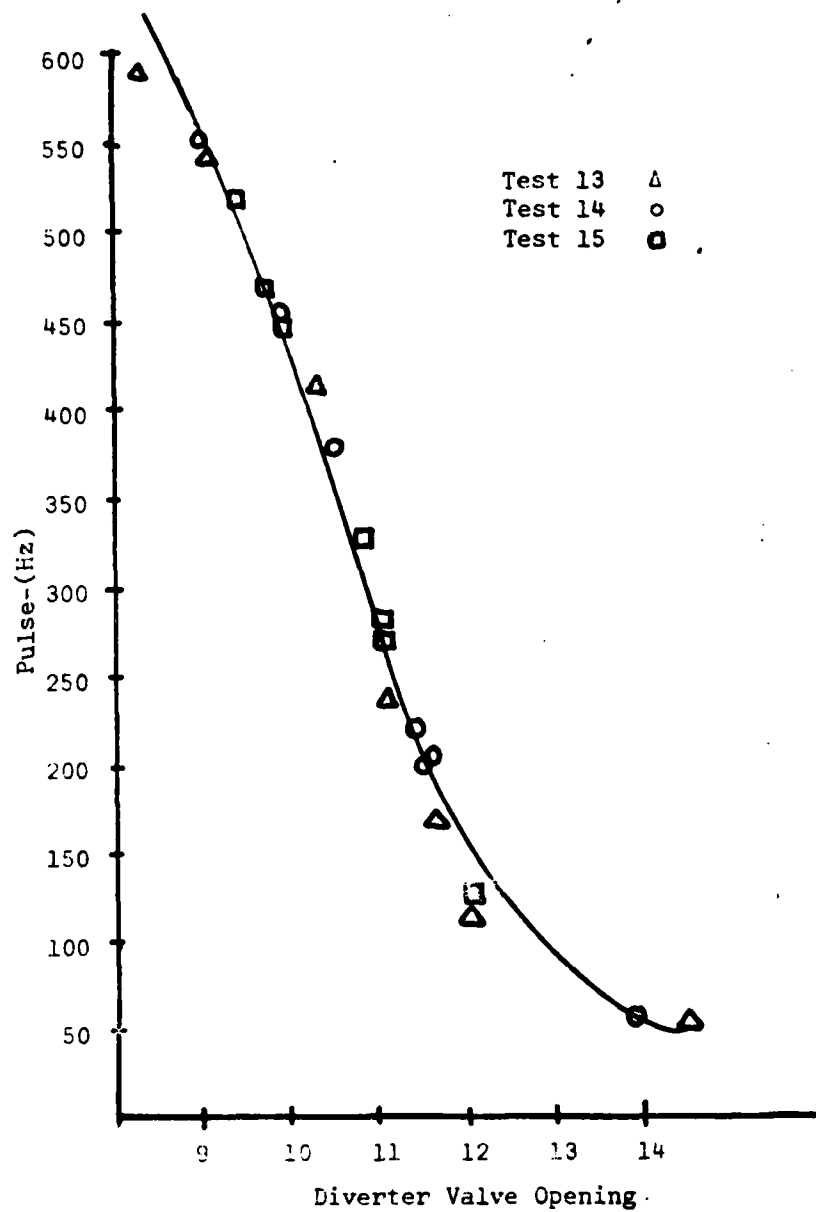
Figure IV-2
Pulse vs. Diverter Valve for Test Series 13, 14, 15.

93
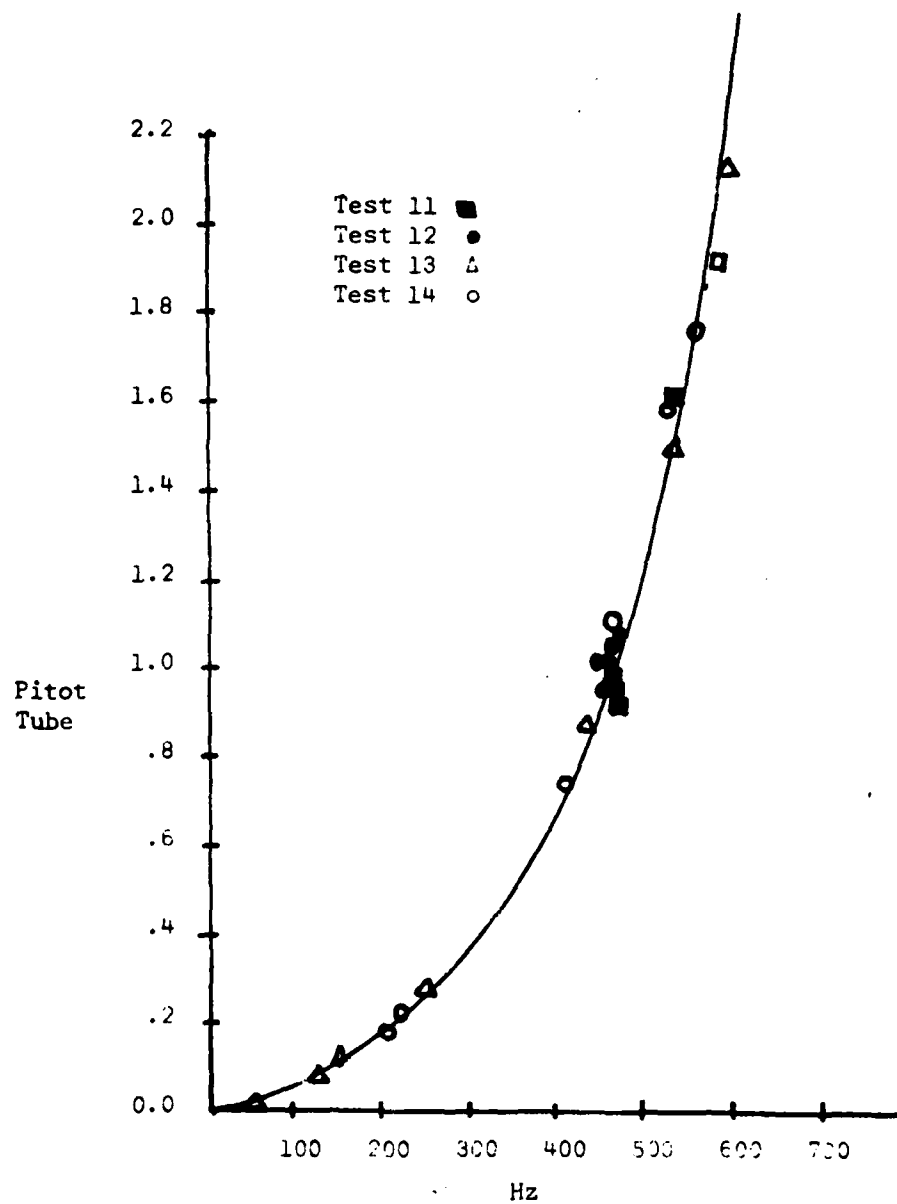
Figure IV-3   Pitot Tube Vs. Hz for Test Series 11,12,13,14

94
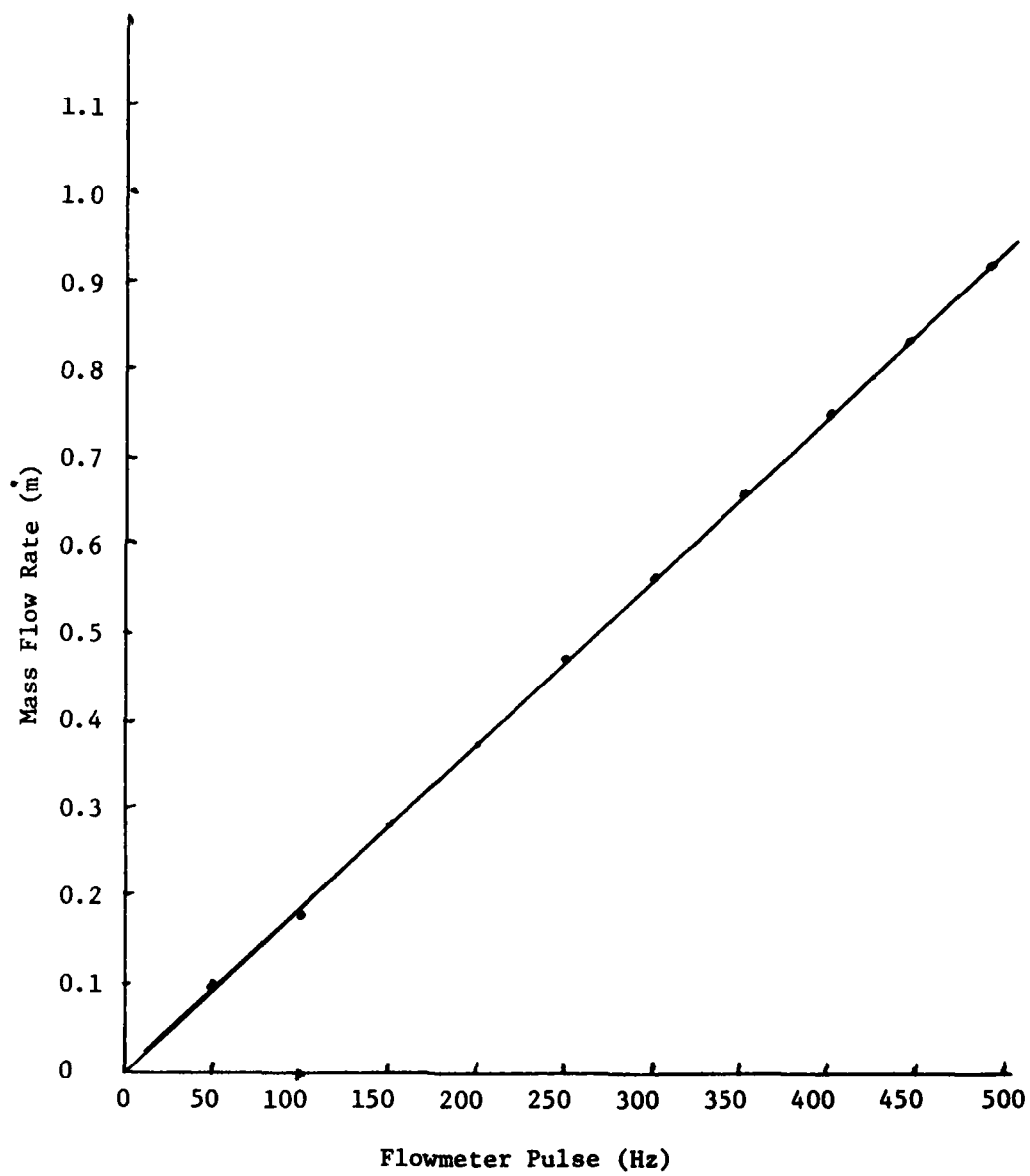
Figure IV-4   Flowmeter Pulse vs. Mass Flow Rate in the Main Loop

95
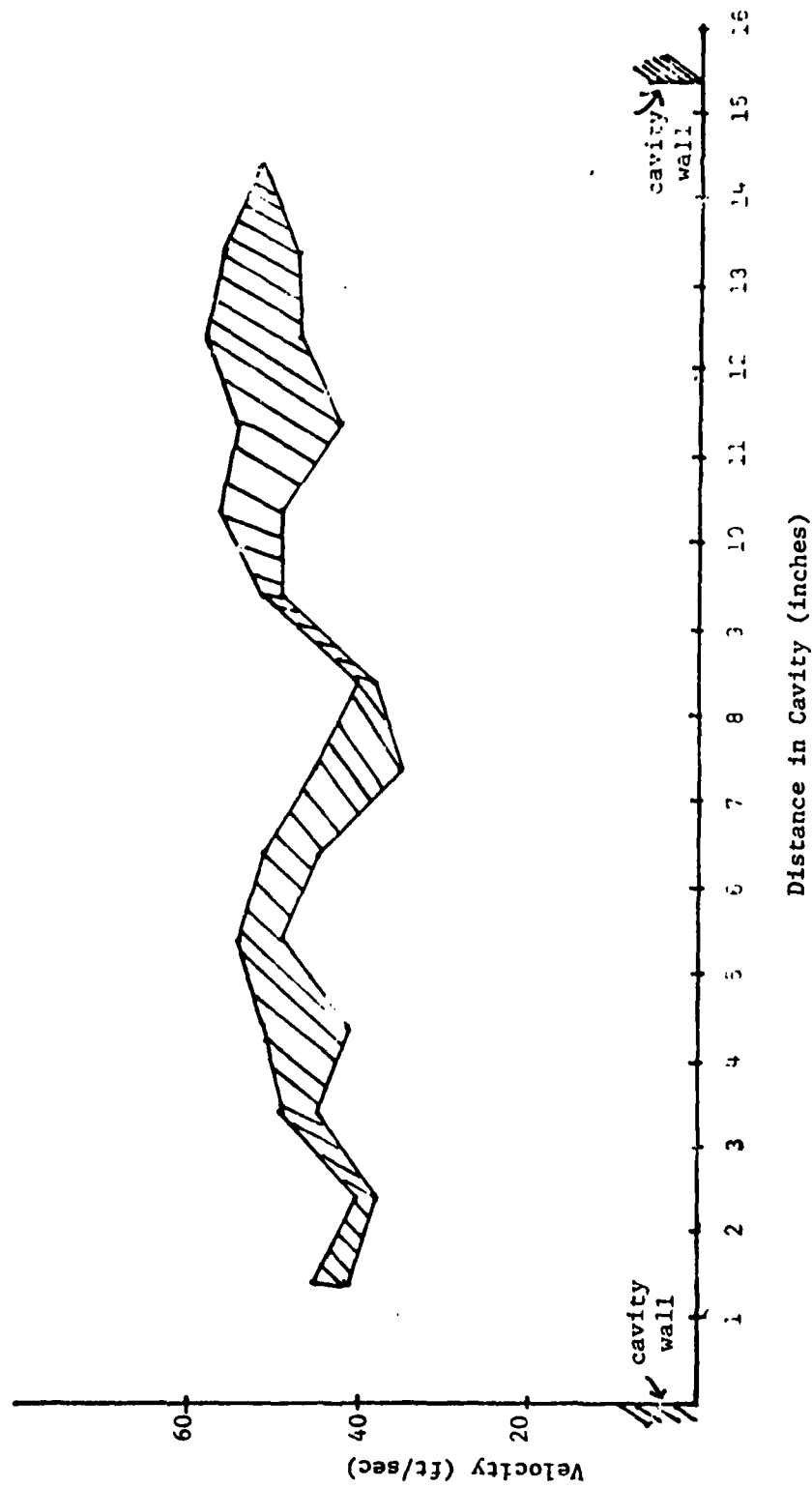
Figure IV-5. Typical Velocity Profile Across Cavity Section For Preliminary Test (Series 22)

F.   Interferogram Analysis

Laser cavities often use flowing gas systems. It is therefore import-
ant that the gas density be uniform if the laser light output is to be
uniform. Systems using large electric fields must have density uniformity
or possible arching due to sparks could result.

To experimentally determine the laser gas density, and the uniformity
in any time frame of a laser pulse, interferometry techniques are used.

In the closed cycle circulator system, light from a ruby laser is used
to analyze the gas density. The end result is a photograph of the light
that passes through the laser cavity superimposed on light which bypassed
the cavity.

Disturbances of the system must be considered. Flowing gases through
the cavity, laser pulses, or electrical sparks in the cavity are all capable
of causing disturbances. After the disturbance another interferogram is
taken.

The shift in the interferometric lenses of the two cases, before and
after the pulse, is a measure of the change in gas density. The change in
gas density is due to the sum of changes along the light path, which happens
to be the cavity length. The frequency of the interferogram light is not
always the same as the laser light in the laser cavity.

The uniformity of the laser intensity which is put out in a laser cavity
is partially dependent on the uniformity of gas density in the cavity while
the laser light is being produced. Gas uniformity within the cavity is ex-
tremely important when working with high energy lasers. It is that deviation
from uniformity which is measured.

97

Interferograms are a way of measuring the gas uniformity within the laser cavity. The photograph provides a two-dimensional map of the gas density at one point in time.

The computer programs employed can be divided into three sections: the digitizing and storing of data, the analysis of the interferometric data, which gives the gas density variations and quality factors, and further analysis of the laser system using the gas density values.

Photographs of interference lines, both a standard and an experimental, are used as the basis in determining the amount of interference that is caused by a disturbing system.

These photographs, along with other hard and software, are used to determine variables in the system. These variables can be computed by hand but because it is such a long and tedious job a computer program is employed. The program used is a combination of many programs and subroutines arranged by Dr. Arthur H. Werkheiser.

Using the Scriptographics tablet and cursor, a digitized interferogram can be acquired. This is where the computer gets the data to work with in its program.

The computer takes x-y coordinates it receives from the digitized interferogram and a two-dimensional plot of the data is generated.

Comparing the two digitized interferograms the computer can find the line shifts and from there calculate gas density changes.

The computer now takes the data it generated and applies a five-point co-location polynomial to calculate a smoothed interferograph line. It then plots into the smoothed data and determines a tilt plane to be subtracted out which will minimize the RMS sum of z values (z is the percent density change computed).

The program computes the Strehl ratio and the beam quality factor. It then prints this information on the screen along with the tilt plane parameters.

These photographs or interferograms are essential to the computer. Using the Scriptographic tablet and cursor the interferogram is digitized. Digitizing is a method of storing the x-y coordinates, which makes up the interference lines, into the computer's memory banks. Because of the way the program reads the x-y coordinates, the lines of the interferogram must be read off horizontally. Vertical interference lines must be turned around making them appear horizontal. After the interferogram has been digitized the photograph is no longer needed except for reference.

To digitize the photograph, the four corner points describing the area are given to the computer by the cursor. Now that the area is defined the interference lines can be given to the computer by way of the cursor.

After the information has been stored, the computer is ready to carry out further analysis.

The work done by the computer on these interferograms goes only as far as the digitizing step.

REFERENCE   DATA
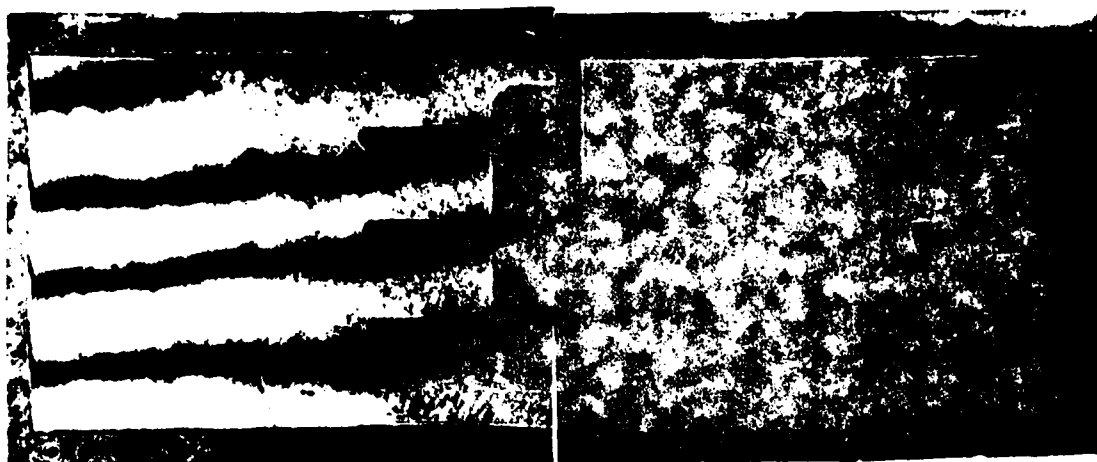
RESULTS: $(\Delta\rho/\rho$ $)$ = RMS DEVIATION
= 0.002848

REFERENCE   DATA

RESULTS: $(\Delta\rho/\rho$ $)$ = RMS DEVIATION
= 0.001079

INPUT DATA

GAS TEMPERATURE = 300°K; GAS PRESSURE = 760 BAR;
HELIUM FRACTION = 0.500: NITROGEN FRACTION = 0.333; CARBON
DIOXIDE FRACTION = 0.167; PROBE LASER WAVELENGTH = 6940
ANGSTROMS; TEST CHAMBER LENGTH = 45 cm; APPLICATION LASER
WAVELENGTH = 10600 ANGSTROMS.

Figure IV-6   Interferograms.

100

G. Operating Instructions for B&K Sound Measuring Equipment

Type 2305 B&K Recorder

Set switches to the following settings:

  Potentiometer range dB – 50

  Rectifier response – RMS

  Lower limiting frequency HZ – 50

  Writing speed – 60 mm/sec

  Power – on

  Motor – on

  Paper drive – off, forward (two switches)

  Paper speed – 3 mm/sec

  Drive shaft speed – 36 RPM

  Input attenuator – 30 dB

Type 2010 B&K Frequency Analyzer

Set switches to the following settings:

  Gain control – cal.

  Readout selector – lin. (meter), AC (recorder)

  Effective averaging time – fast

  Selectivity control – 1000 HZ

  B&T program – B var. 1

  Frequency scale – X1 log

  Frequency increment – 0

  Sweep control – manual (initially only)

Set push button switches to the following settings:

  Input – preamp

Calibration - cal. off

Frequency response - linear

Meter and recorder - analyzer

To Synchronize Recorder and Analyzer:

1. Turn paper drive switch on recorder to start until
   20 HZ line on paper lines up with pen.

2. At the instant it lines up, turn switch back to stop.
   If 20 HZ line does not stop even with the pen, repeat
   until it does.

3. On the analyzer, turn the big knob in the center until
   the display reads 0.020KHZ.

4. Turn the sweep control switch on the analyzer to Ext.
   Mech.

Microphone Calibration

1. Put male end of mike extension cable into socket marked
   Preamp Input.

2. Plug microphone with preamp into the female end of the
   mike extension cable.

3. Place the microphone into the end of the type 4220 B&K
   pistonphone.

4. On the analyzer, adjust the input section attenuator and
   output section attenuator to where the light below 120
   comes on (on the meter panel).

5. Turn the pistonphone on, meter on analyzer should read 4 dB.

6. On the recorder, adjust the input potentiometer knob until the pen is on the 24 dB line (with the analyzer 120 light on, the zero line of the recorder is 100 dB, so a reading of 24 on the recorder corresponds to the 124 dB input from the pistonphone).

7. Turn the pistonphone off, set the frequency response push button on the analyzer to selective, leave it in the selective position for all sound measurements.

8. Remove mike from piston phone.

To Make Sound Measurements

1. Install microphone in desired location.

2. Set input section attenuator and output section attenuator switches to a position where the highest sound level will be on the chart. The zero line of the chart is 20 dB below the level indicated by the lights on the meter panel of the frequency analyzer.

3. To begin sound measurements, switch the paper drive switch to start. If sound levels go off the scale of the recorder, then adjust the attenuators on the analyzer until the pen is on scale in a desired location.

4. To end sound measurements, switch the paper drive switch to stop.

V.   Trial Test Series of the Closed Cycle Circulator (CCC) Systems
        and Their Preliminary Results

Following the acceptance test run directed by Rocketdyne, Division
of Rockwell International which resulted in a month-long delay due to
major repair of the compressor, the CCC system became operational on the
first of June, 1979. The CCC system was operated for 31 trial test series
without the freon TA heat exchanger in operation because of the lack of
safety provisions approved by the Safety Office. On account of this de-
ficiency, the CCC system was not able to attain the specified temperature
level at the cavity throughout the test runs. A continued effort has been
undertaken to make the freon TA heat exchanger operational by installing
two freon TA detectors and one oxygen detector in the building area where
the CCC system is installed as well as requesting installations of a
ventilation fan and a double-door in the building outside by the Post
Facility Engineer. As soon as all of the safety provisions are completely
installed, a series of trial test runs with all components of the CCC system
operating will be conducted to evaluate the performance characteristics
of the CCC system prior to the application of pulsed energy inputs at the
cavity.

The trial test series performed to date represent an incomplete
evaluation of the CCC system performance from the viewpoint of fluid and
thermal characteristics of the recirculating flow of laser gas (N_2: CO_2:
H_e, 2:1:3:) mixture due to the absence of the LN_2 cooling and the pentane
heat exchanger in operation. Temperatures at the cavity were never
lowered below 300°K (27°C), but the pressures were attained at the level

104

of 760 $\pm$ 20 Torr during each of all test series as shown in Figures V-1, V-2, and V-3. The continuing temperature rises and pressure falls at each of all stations (4,5,6,9,11) in the circulator as shown in Figures V-1 to V-3 during the continuous run of the CCC system indicate a definite heat imbalance due to excessive heat input by the compressor and inefficient heat sink at the water heat exchangers. These phenomena can be theoretically approximated by the following differential equation:

$$\frac{dQ - dW}{C_p T} = \frac{dT}{T} - \frac{\gamma - 1}{\gamma} \frac{dP}{P} \tag{V-1}$$

where Q denotes the heat transfer into the system, W the work extracted from the system, T the static temperature, P the static pressure, and C_p the specific heat under constant pressure, and γ the specific heat ratio. When the combined effect of (dQ - dW) is positive, dT should be positive, meaning a temperature rise where dP is negative, a pressure fall.

In Figures V-4 through V-7 temperature and pressure distributions along the circulator loop for various mass flow rates in test series 12 and 13 are presented. Effects of the diverter valve are noted in Figure V-4 and V-6 at station 5 where the diverted flow at high temperature bypassing one of the heat exchangers (Hx3) is returning to the inlet of heat exchanger (Hx1). Figures V-5 and V-8 depict the pressure fall occurring for the temperature rise in accordance with theoretical relationship represented be Equation (V-1).

These figures present typical distributions of temperature and pressure throughout the circulator loop of all test series conducted to date.

The complete data of trial test series are tabulated and presented in Appendix A.

105
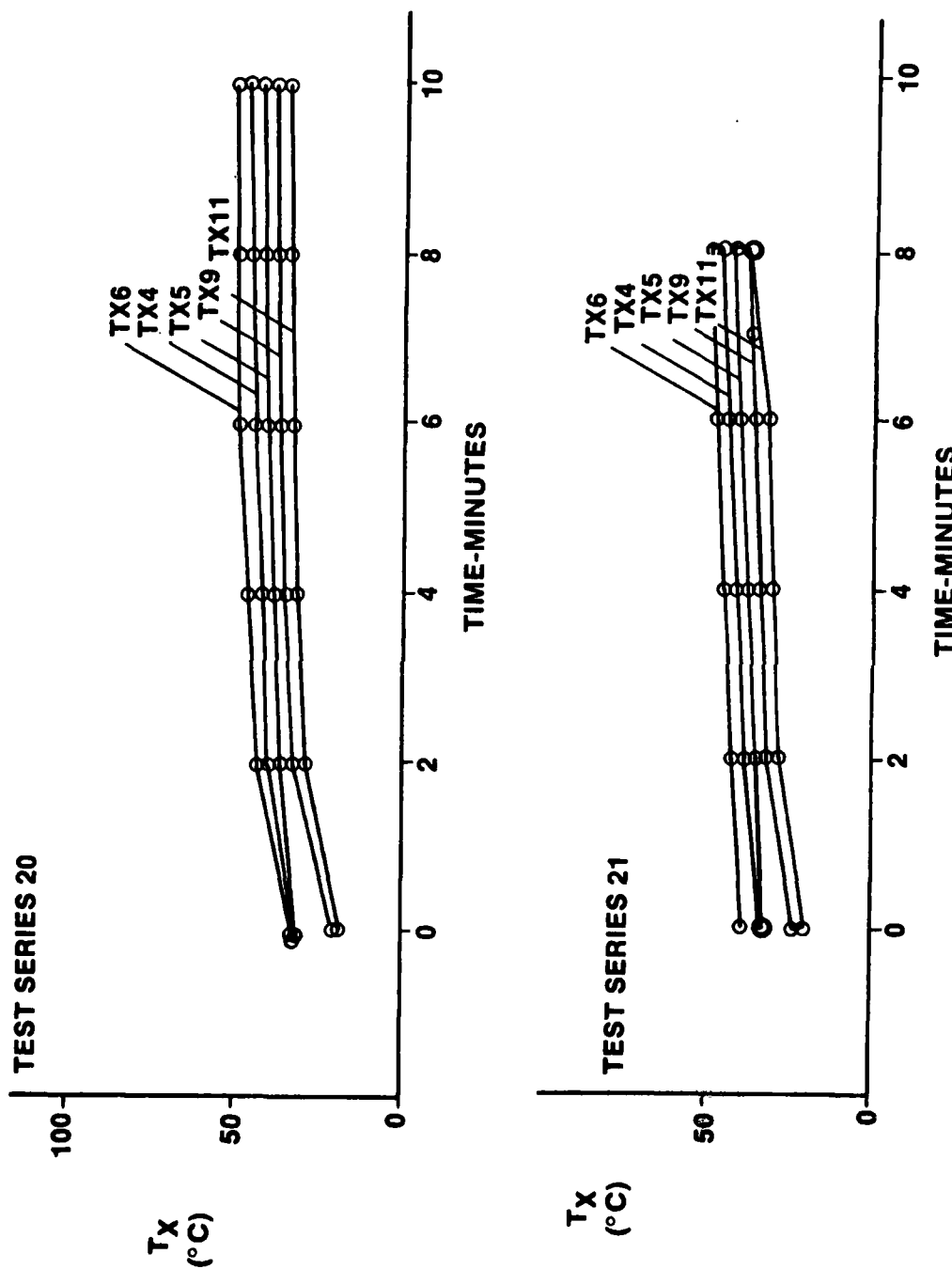
Figure V-1 Temperature versus circulator sections for test series 20 and 21.

106
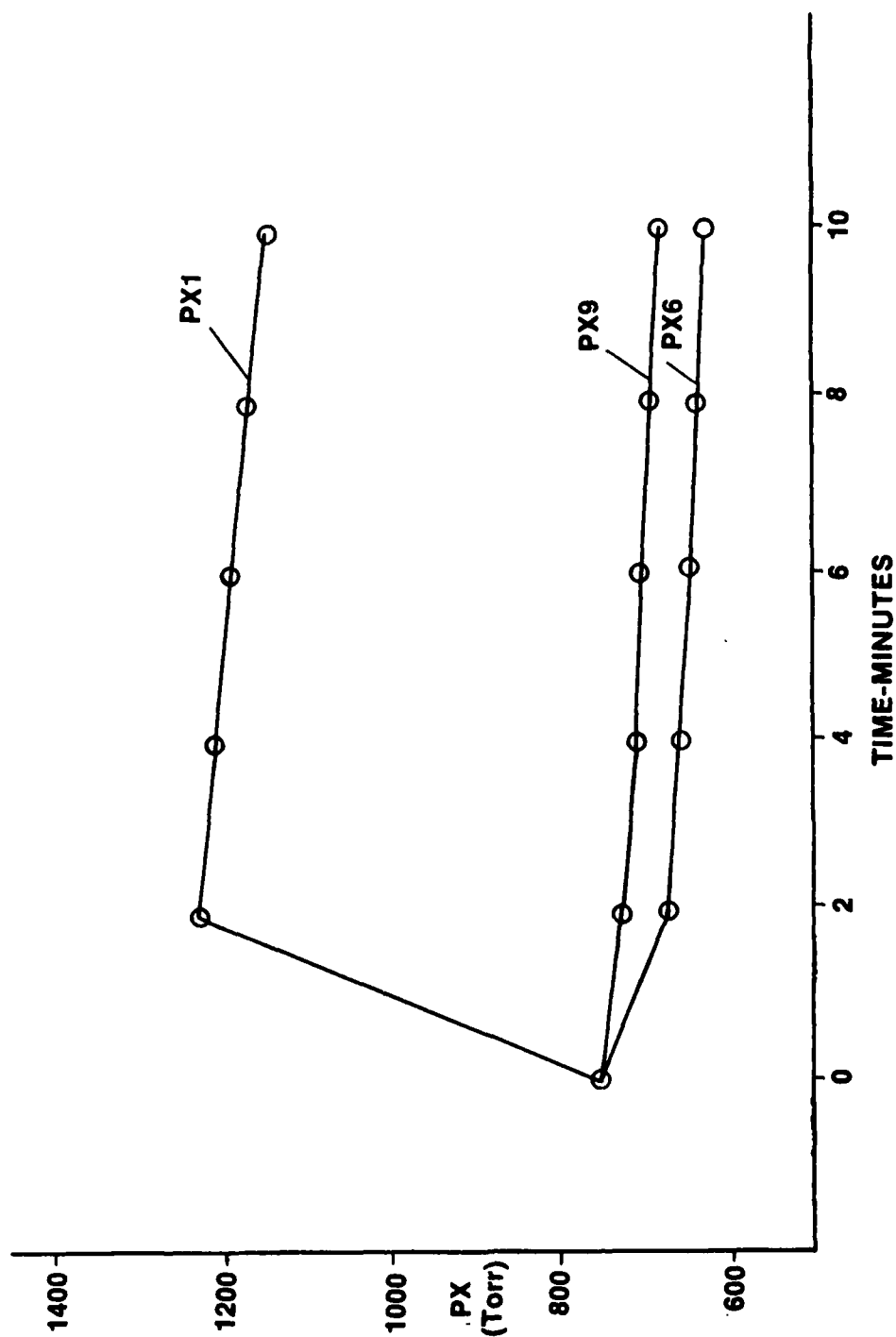
Figure V-2 Pressure versus time at circulator sections for test series 20.
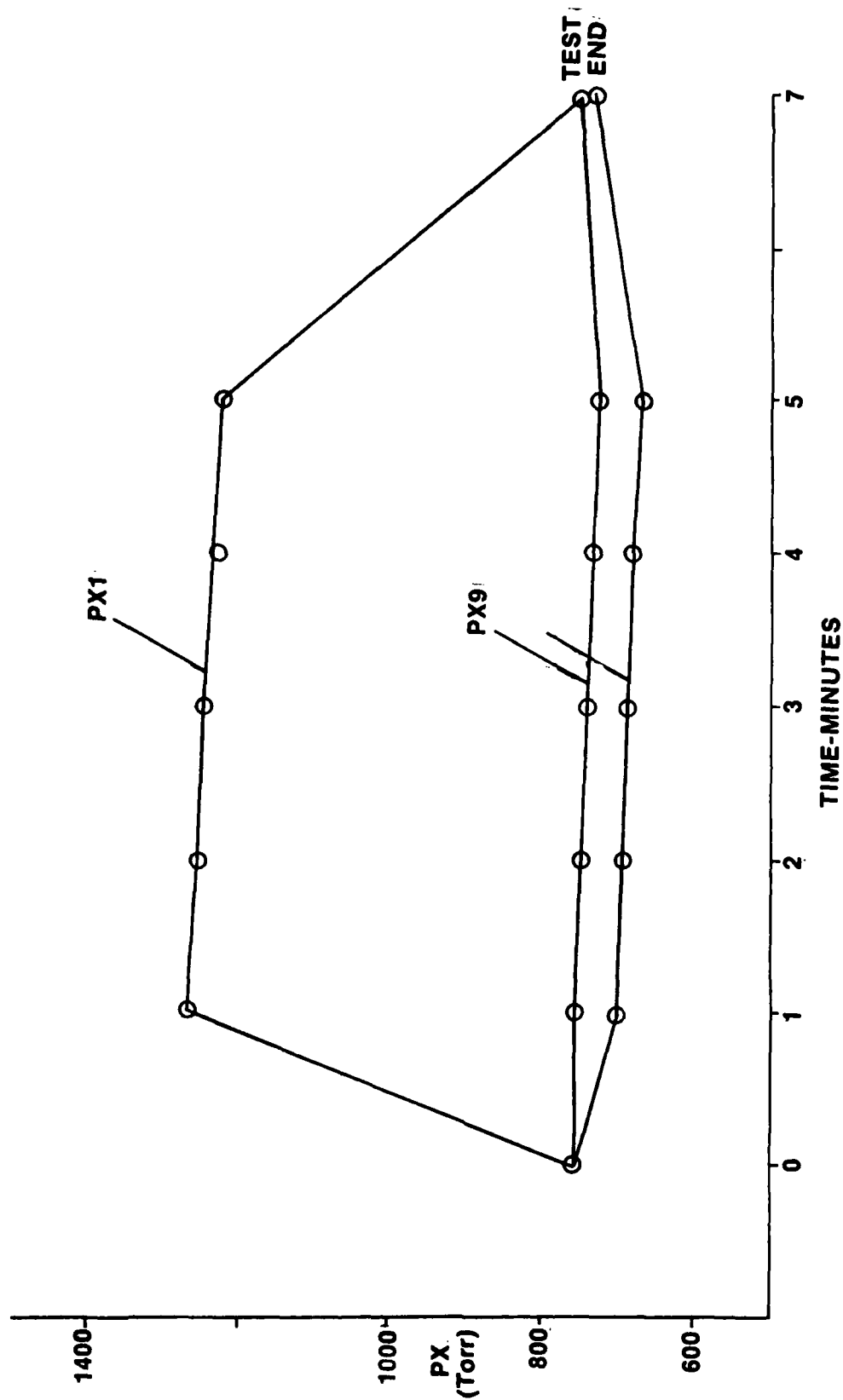
Figure V-3 Pressure versus time at circulator sections for test series 24.

MFR **VFR**

.8386 lb-m/sec 17.81 ft^3/sec

.8107 lb-m/sec 17.47 ft^3/sec

.7792 lb-m/sec 16.97 ft^3/sec

TX (TORR)

200 150 100 50 0

0 1 2 3 4 5 6 STATIONS

HX3 HX2 CAVITY HX1
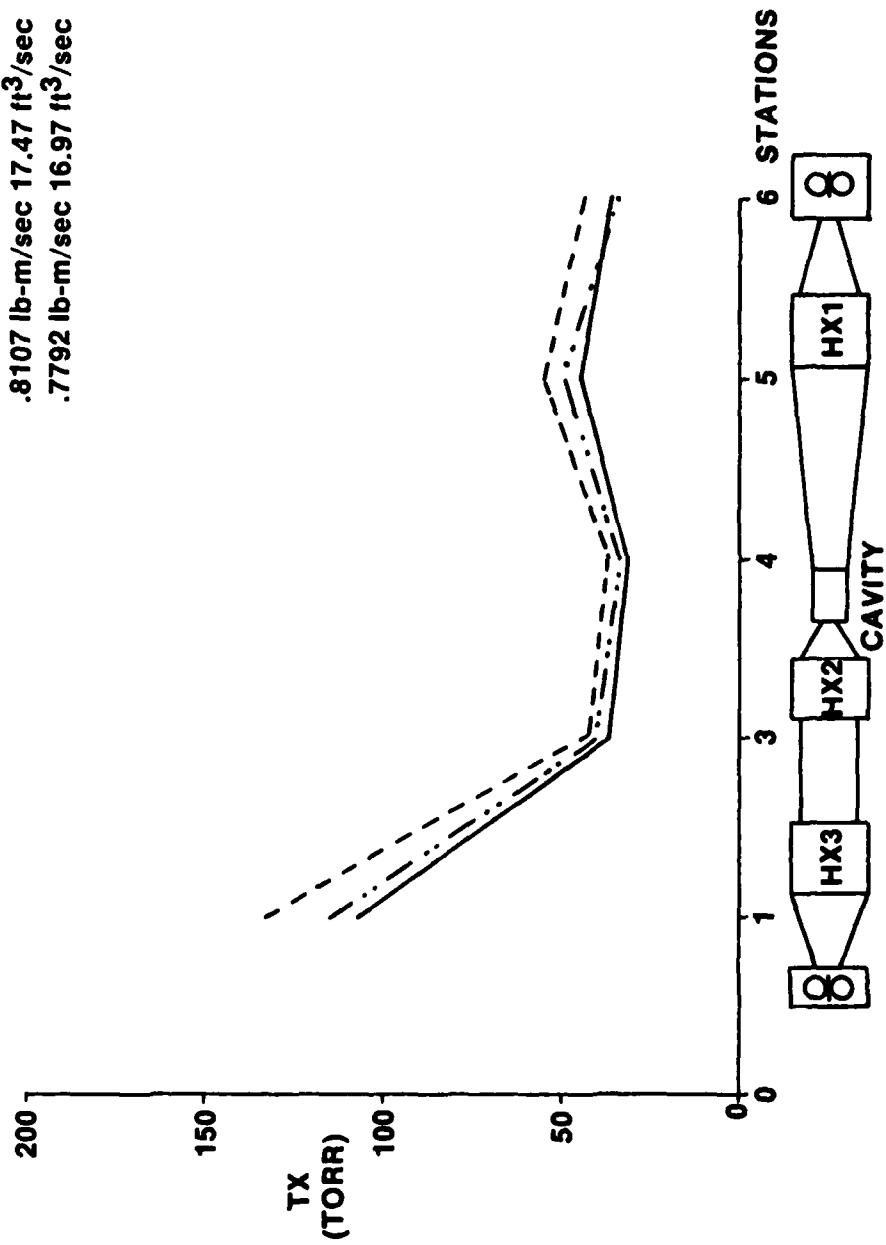
Figure V-4 Temperature distribution in circulator sections for various flow rates over a small range in test series 12.
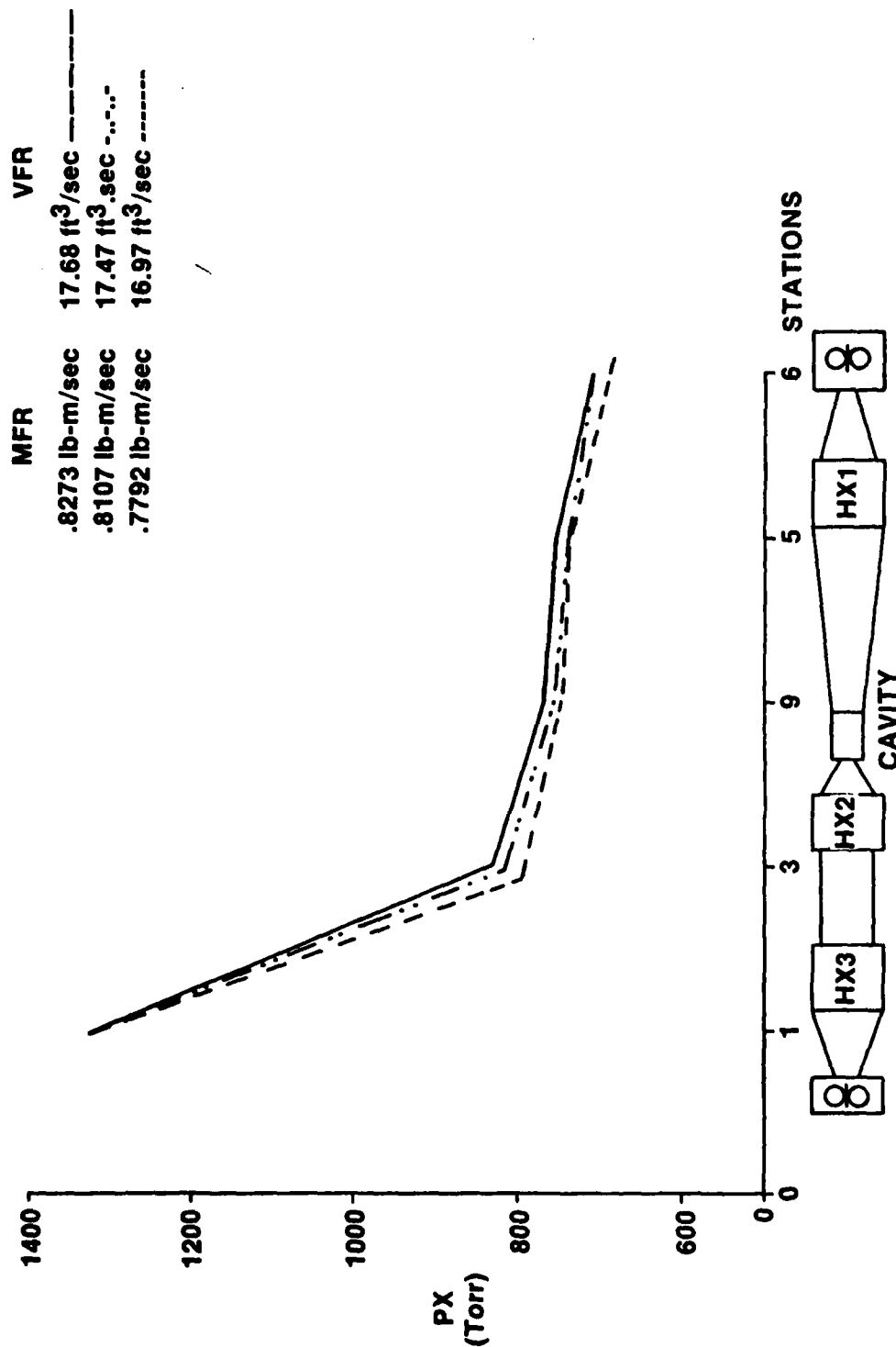
Figure V-5 Pressure distribution in circulator sections for various flow rates over a small range in test series 12.

MFR
NO FLOW
1.1328 lb-m/sec
.2148 lb-m/sec
.9477 lb-m/sec
.2827 lb-m/sec

VFR
NO FLOW
24.95 ft^3/sec
5.04 ft^3/sec
22.86 ft^3/sec
7.14 ft^3/sec

TX
(°C)

200

150

100

50

0

0   1   2   3   4   5   6   STATIONS

HX3   HX2   CAVITY   HX1
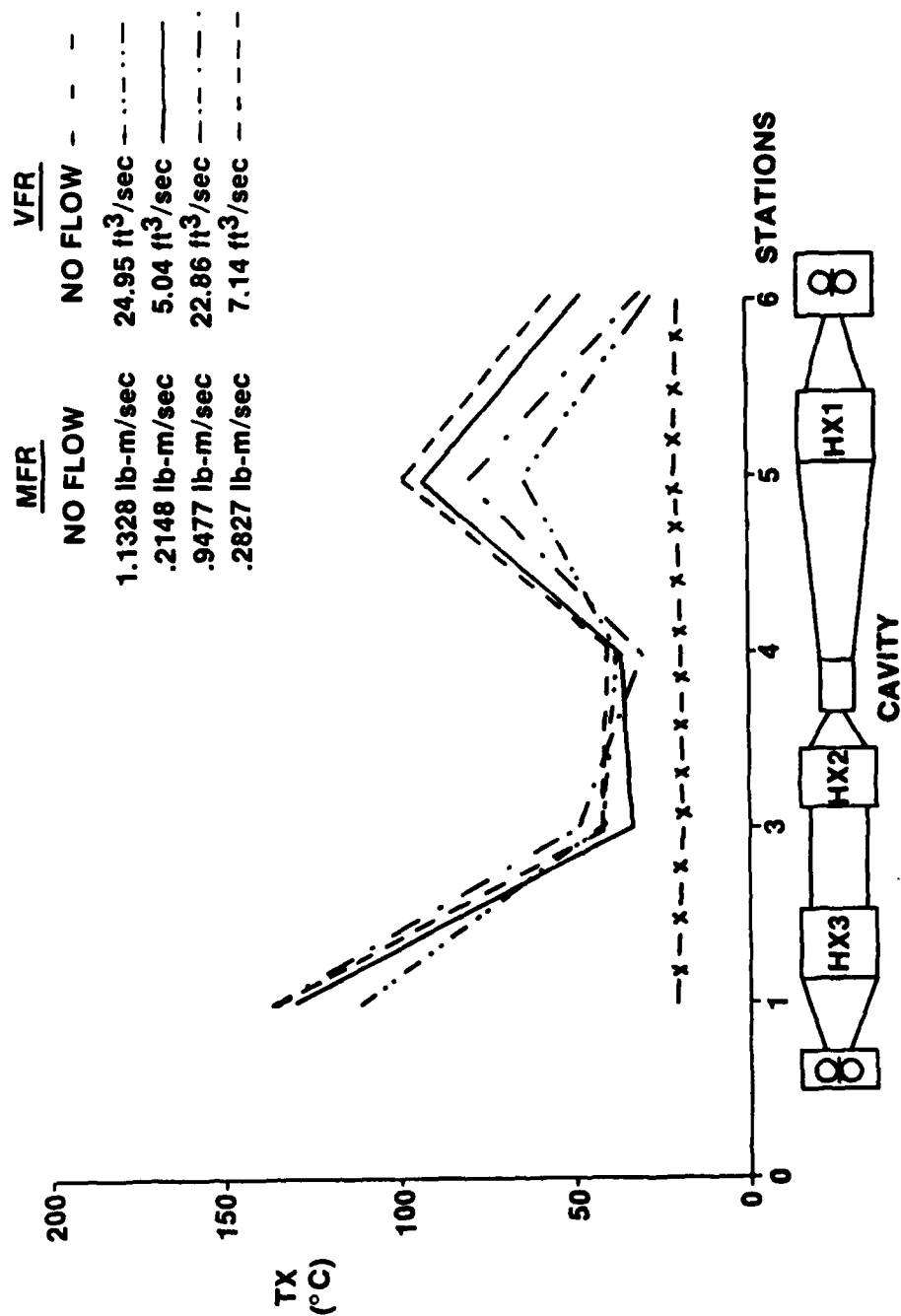
Figure V-6 Temperature distribution in circulator sections for various flow rates in test series 13.

111

Figure V-7 Pressure distribution in circulator sections for various flow rates in test series 13.

MFR

NO FLOW

1.1328 lb-m/sec
.2148 lb-m/sec
.9477 lb-m/sec
.2827 lb-m/sec

VFR

NO FLOW -x-x-x-

24.95 ft^3/sec -...·-
5.04 ft^3/sec ———
22.86 ft^3/sec -..·-
7.14 ft^3 - - - -

STATIONS

CAVITY

HX1 HX2 HX3

6 5 4 3 2 1

1400
1300
1200
1100
1000
900
800
700
600
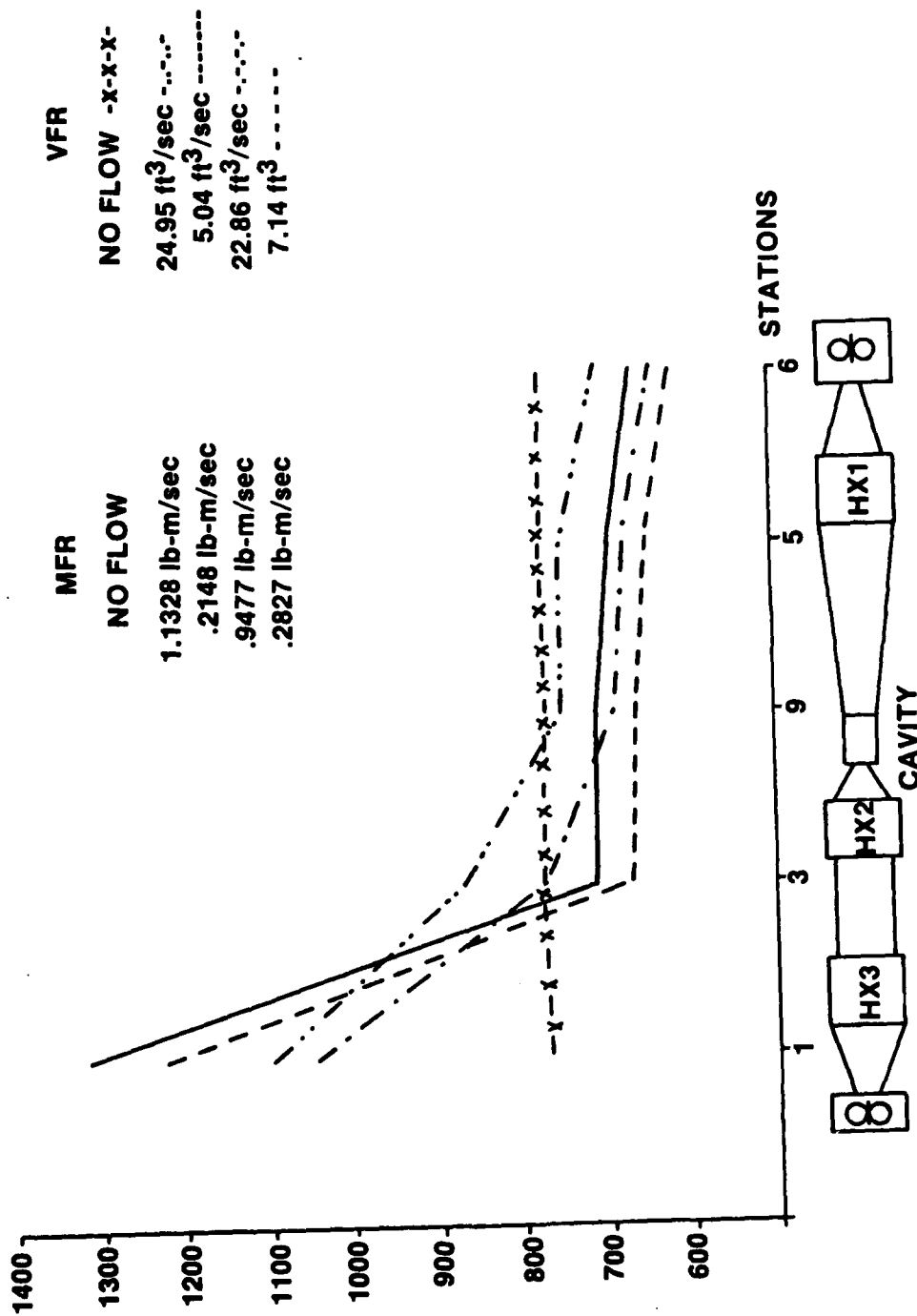
Sound Pressure Levels (SPL) in the circulator were measured with B&K instruments (Models 2035 and 2010) at pressure ports, PX9, PX7, PX6, PX1, PX3, and PX4 for four flow rates, 0.19, 0.38, 0.565, and 0.755 lbm/sec, respectively. The same sound measurements were performed for air and laser gas ($3:2:1 - H_e:N_2:CO_2$) recirculating separately in the system, and found the SPL is generally higher for the laser gas flow over the entire frequency spectrum.

Results of SPL measurements for the four flow rates of laser gas at the cavity (PX9) are presented in Figures V-8 to V-11 with both acoustic attenuators installed about the cavity, and in Figures V-12 to V-15 without the attenuators. To demonstrate the effectiveness of the attenuators, the eight curves were matched into four pairs of SPL curves, and differential SPLs with respect to the frequency spectrum were deduced for graphical presentations in Figures V-16 to V-19.   As noted in these Figures, with exceptions in low frequencies up to 200 HZ, the high effectiveness of attenuation specially in the high frequency range from 1000 to 20000 HZ was clearly demonstrated. The effect of flow rates on the attenuation appear to be minor from the limited experiments.

Cleaning and Handling Operations of the Circulator

In order to assemble and disassemble the circulator components of considerable weight in a larger vertical space, three handling devices were designed and fabricated by PDC Associates of Huntsville as shown in Figure V-20, a through f. Figures b and d depict views of the support structures for three handing cradles. Close-up details of the cradle is shown in C. A wheeled cart with elevatable top is shown in c. E and F show the fall view and vertical view of the elevatable point support.
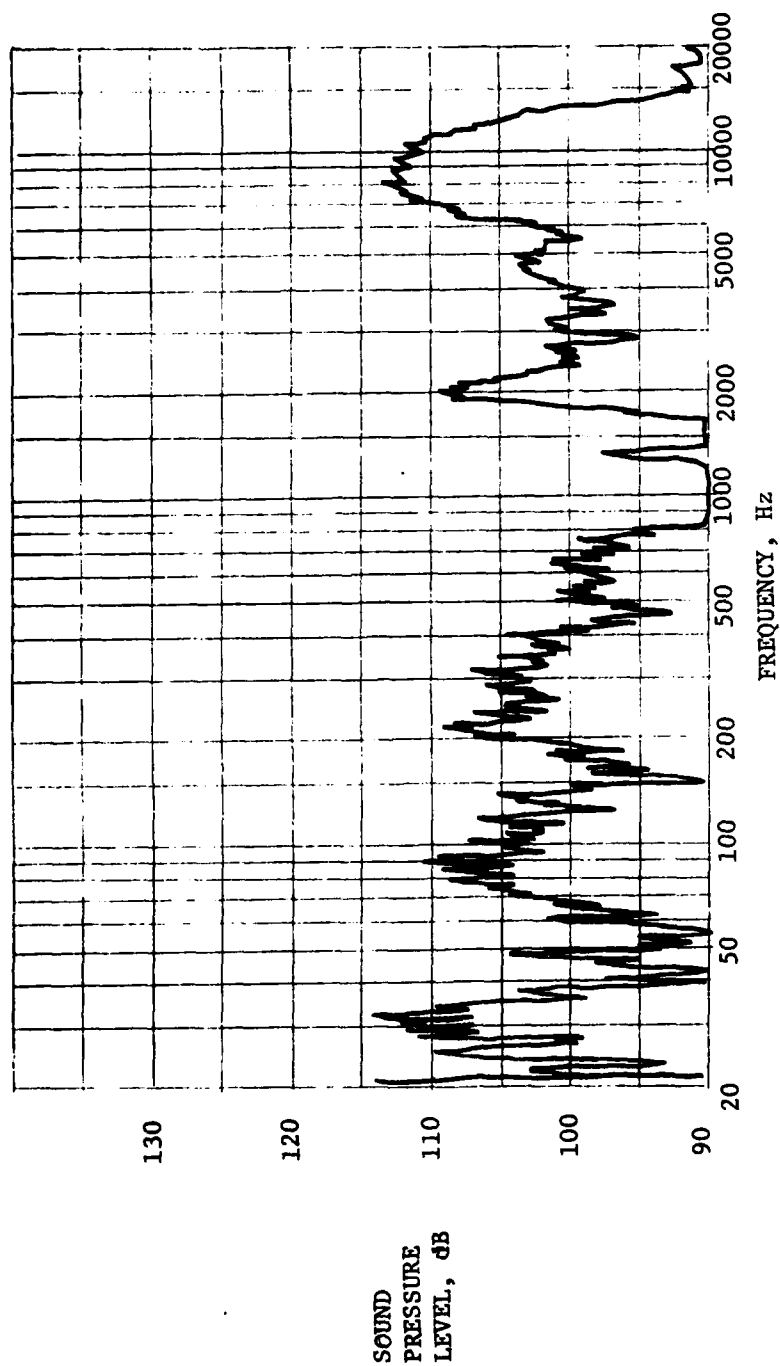
Figure V-8- SOUND PRESSURE LEVEL VS. FREQUENCY AT LASER CAVITY WITH ATTENUATORS FOR FLOW RATE OF 0.19 lbm/sec.

114
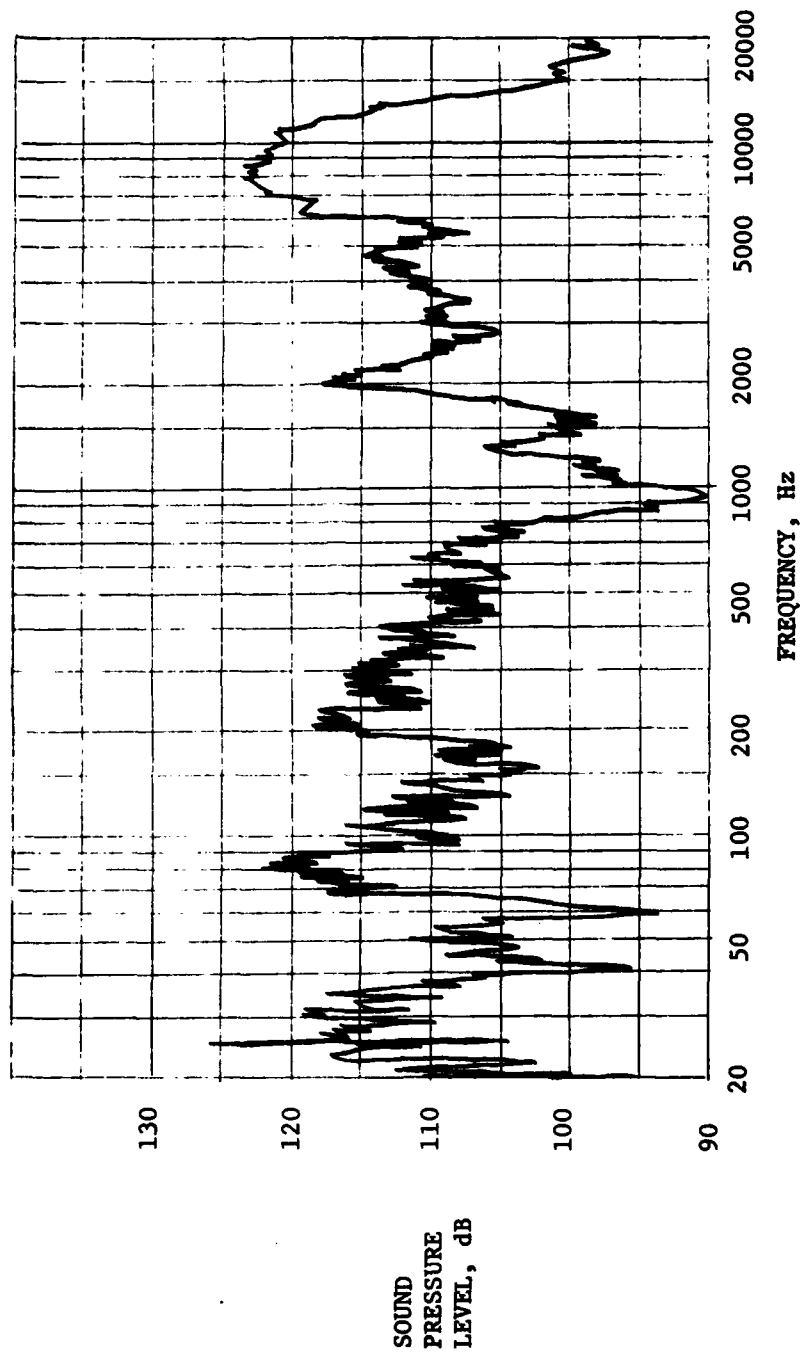
FigureV-9 SOUND PRESSURE LEVEL VS. FREQUENCY AT LASER CAVITY WITH ATTENUATORS FOR FLOW RATE OF 0.38 lbm/sec.

115
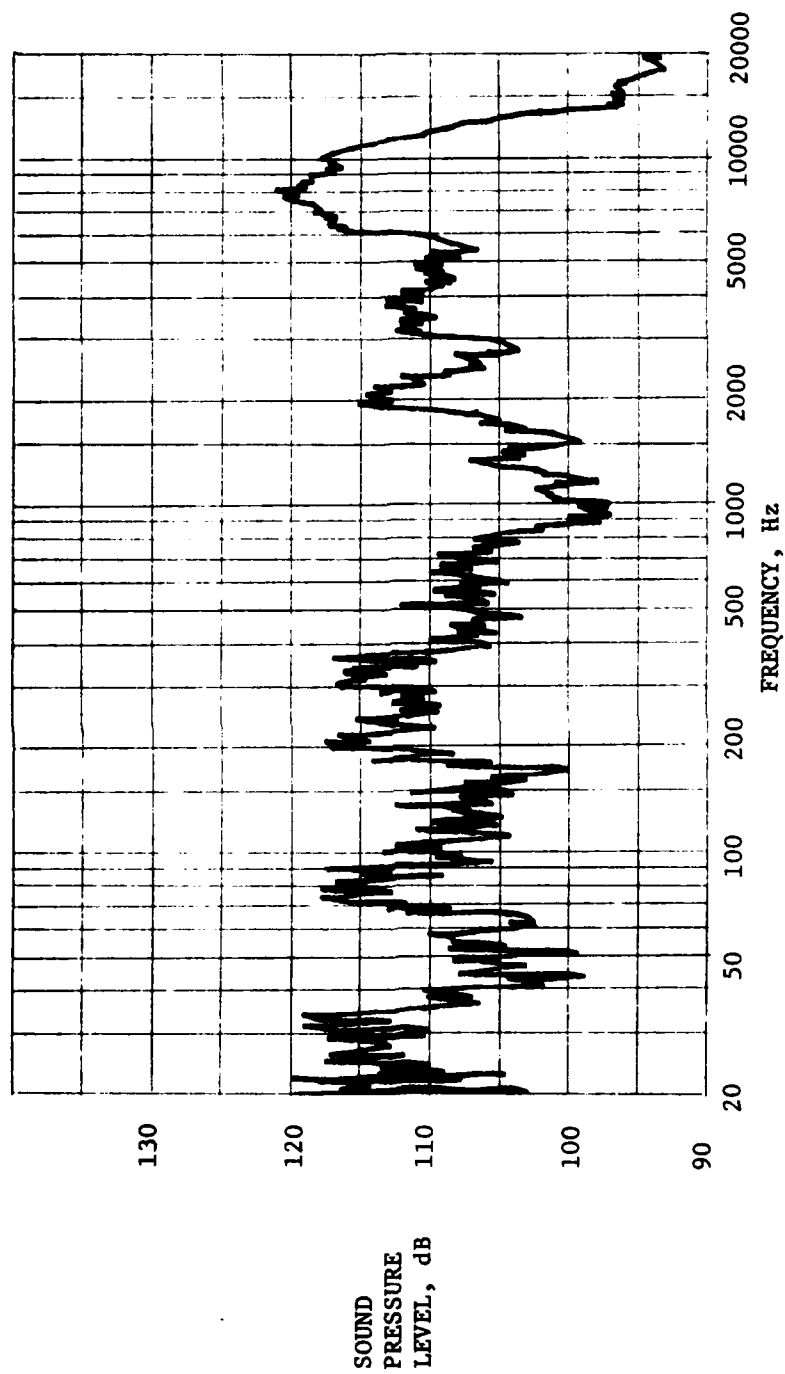
FigureV-10SOUND PRESSURE LEVEL VS. FREQUENCY AT LASER CAVITY WITH ATTENUATORS
FOR FLOW RATE OF 0.565 lbm/sec.

116
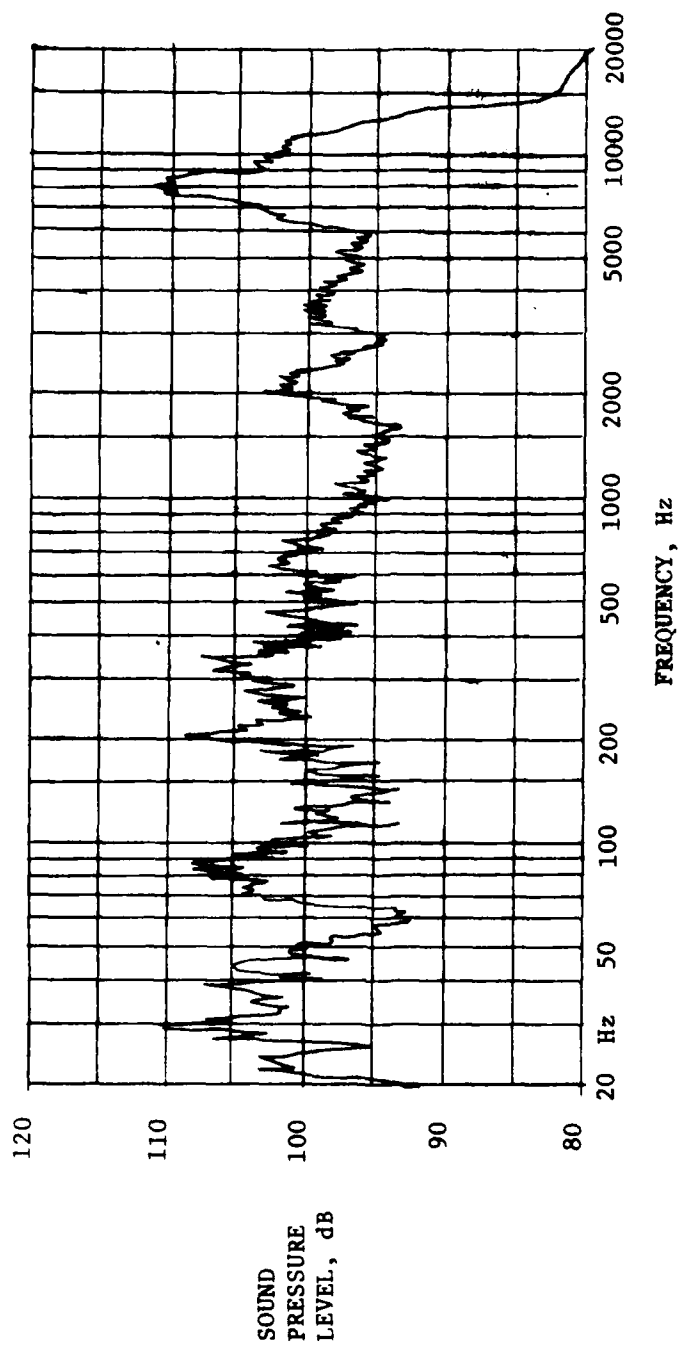
Figure V-11 SOUND PRESSURE LEVEL VS. FREQUENCY AT LASER CAVITY WITH ATTENUATORS FOR FLOW RATE OF 0.755 lbm/sec.

117
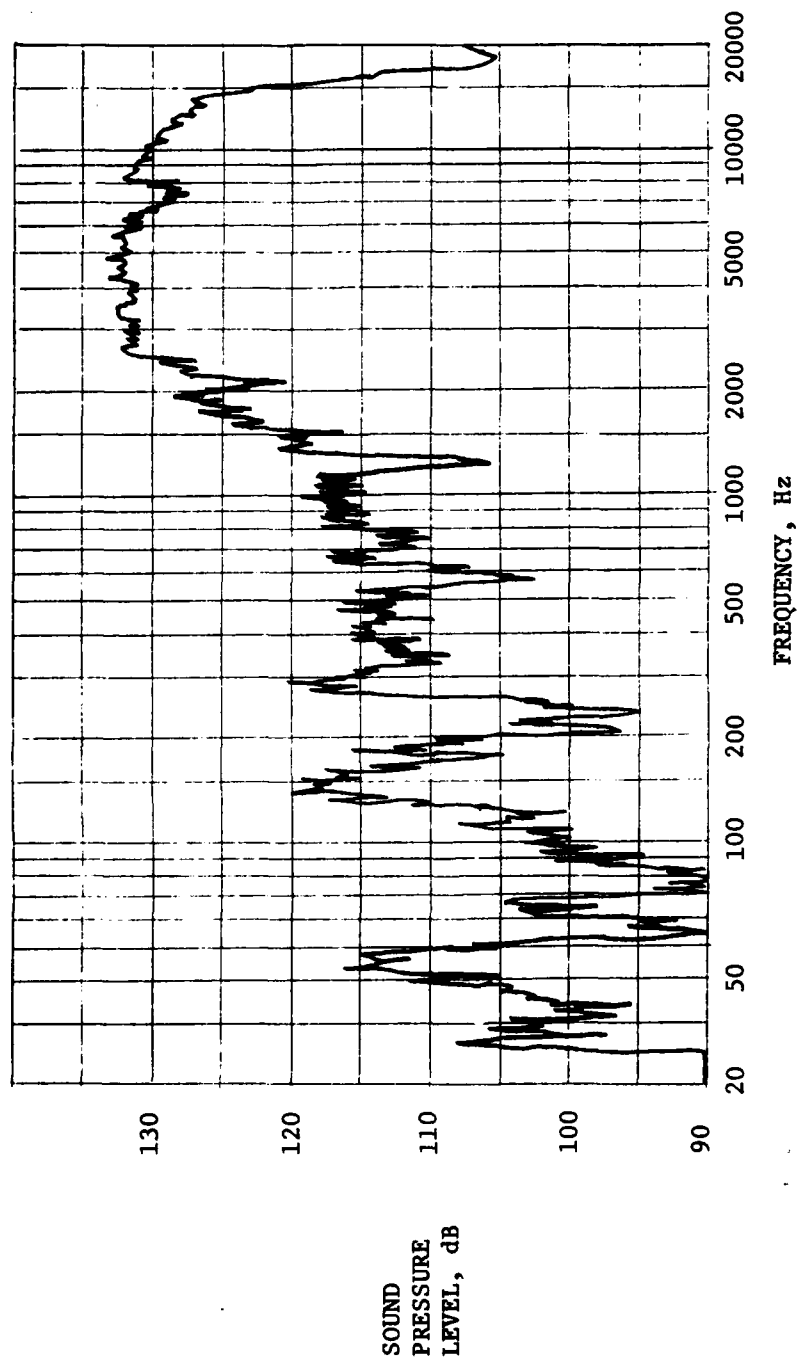
Figure V-12. SOUND PRESSURE LEVEL VS. FREQUENCY AT LASER CAVITY WITHOUT ATTENUATORS FOR FLOW RATE OF 0.19 lbm/sec.

118
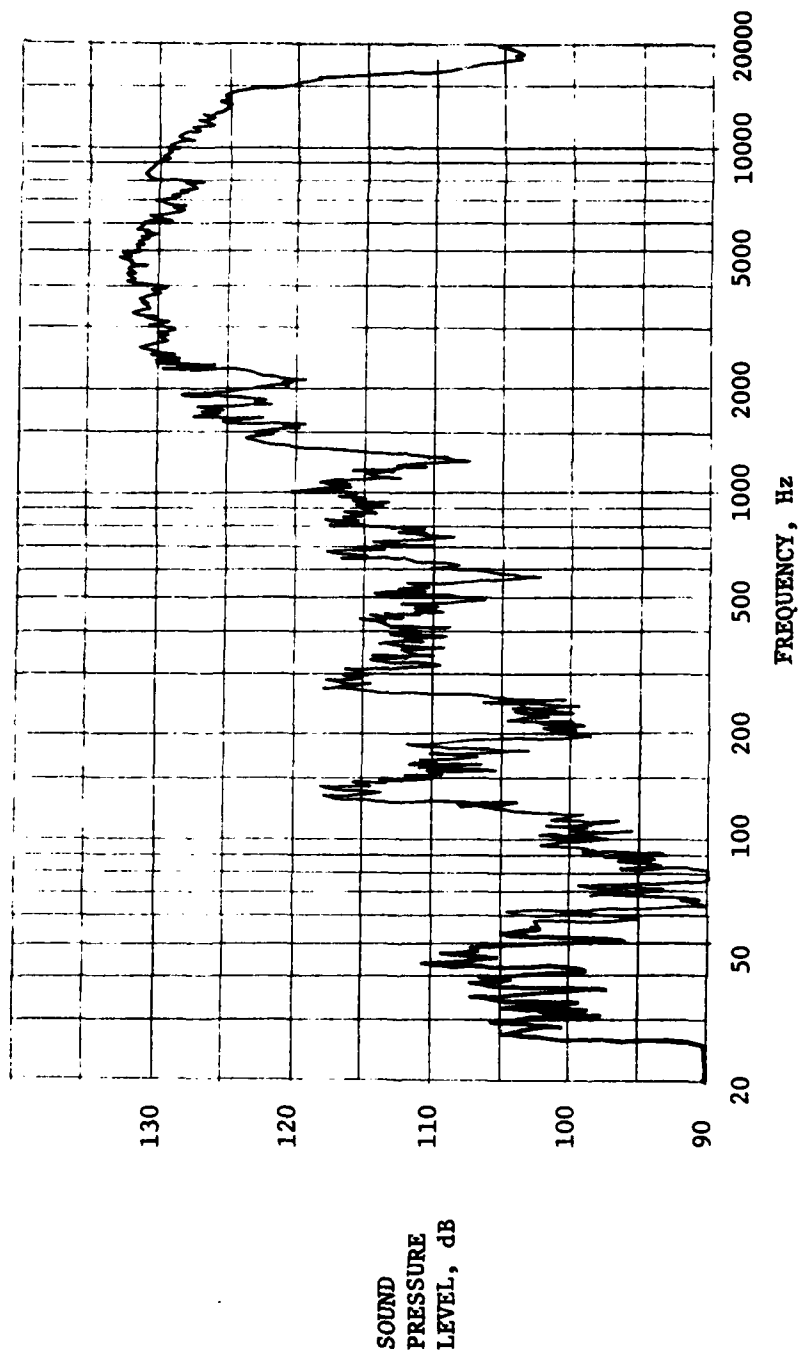
Figure V-13 SOUND PRESSURE LEVEL VS. FREQUENCY AT LASER CAVITY WITHOUT ATTENUATORS FOR FLOW RATE OF 0.38 lbm/sec.

119
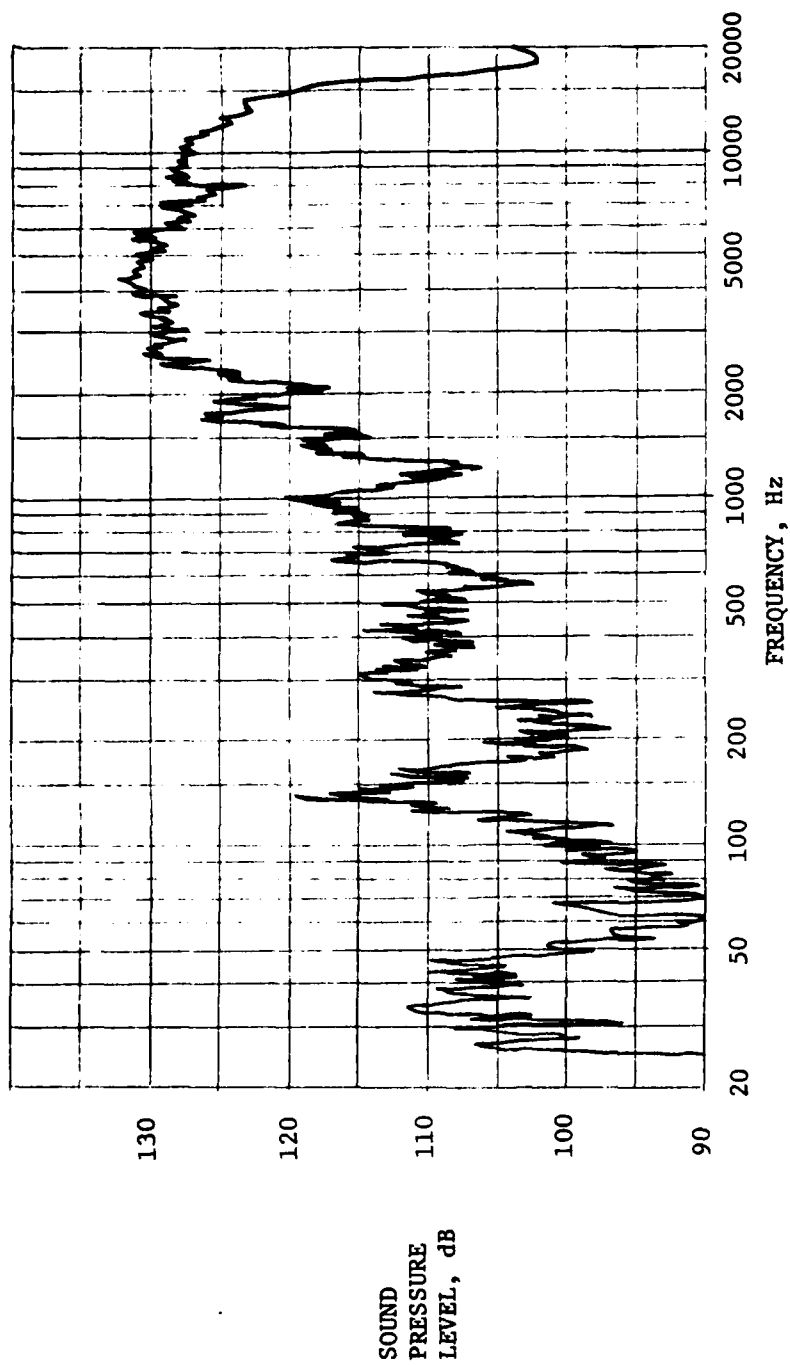
Figure V-14. SOUND PRESSURE LEVEL VS. FREQUENCY AT LASER CAVITY WITHOUT ATTENUATORS FOR FLOW RATE OF 0.565 lbm/sec.

120
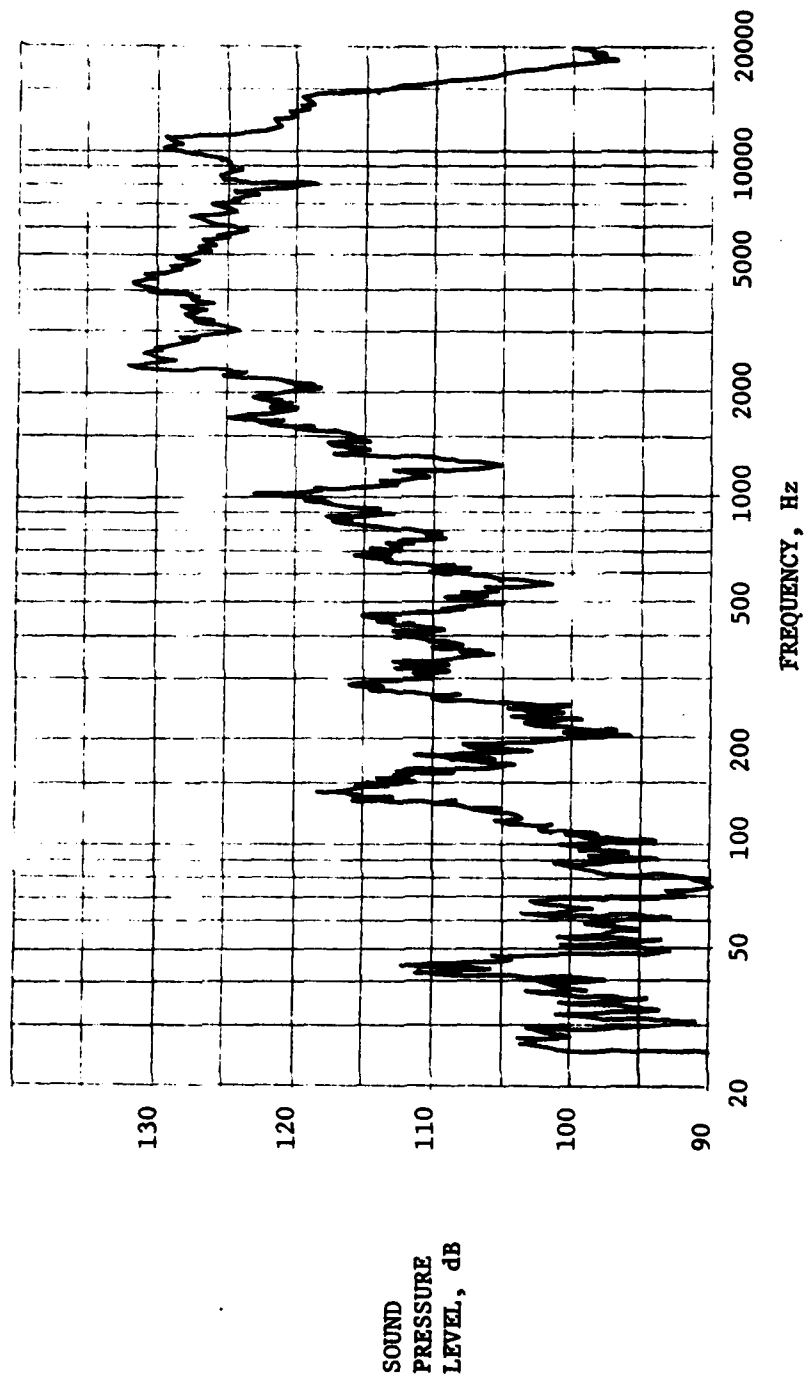
Figure V-15 SOUND PRESSURE LEVEL VS. FREQUENCY AT LASER CAVITY WITHOUT

ATTENUATORS FOR FLOW RATE OF 0.755 lbm/sec.

121
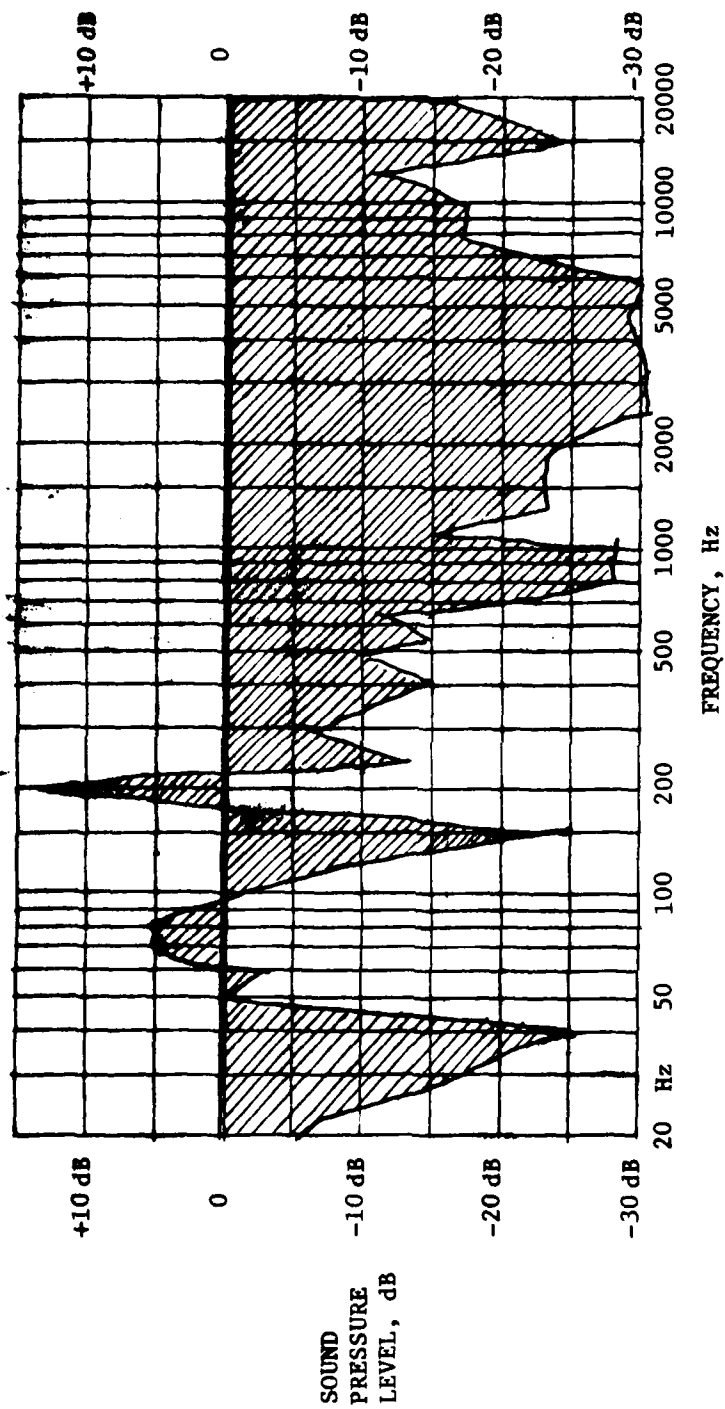
Figure V-16 SOUND PRESSURE LEVEL CHANGE VS. FREQUENCY AT LASER CAVITY WITHOUT AND WITH ATTENUATORS FOR FLOW RATE OF 0.19 lbm/sec.

122
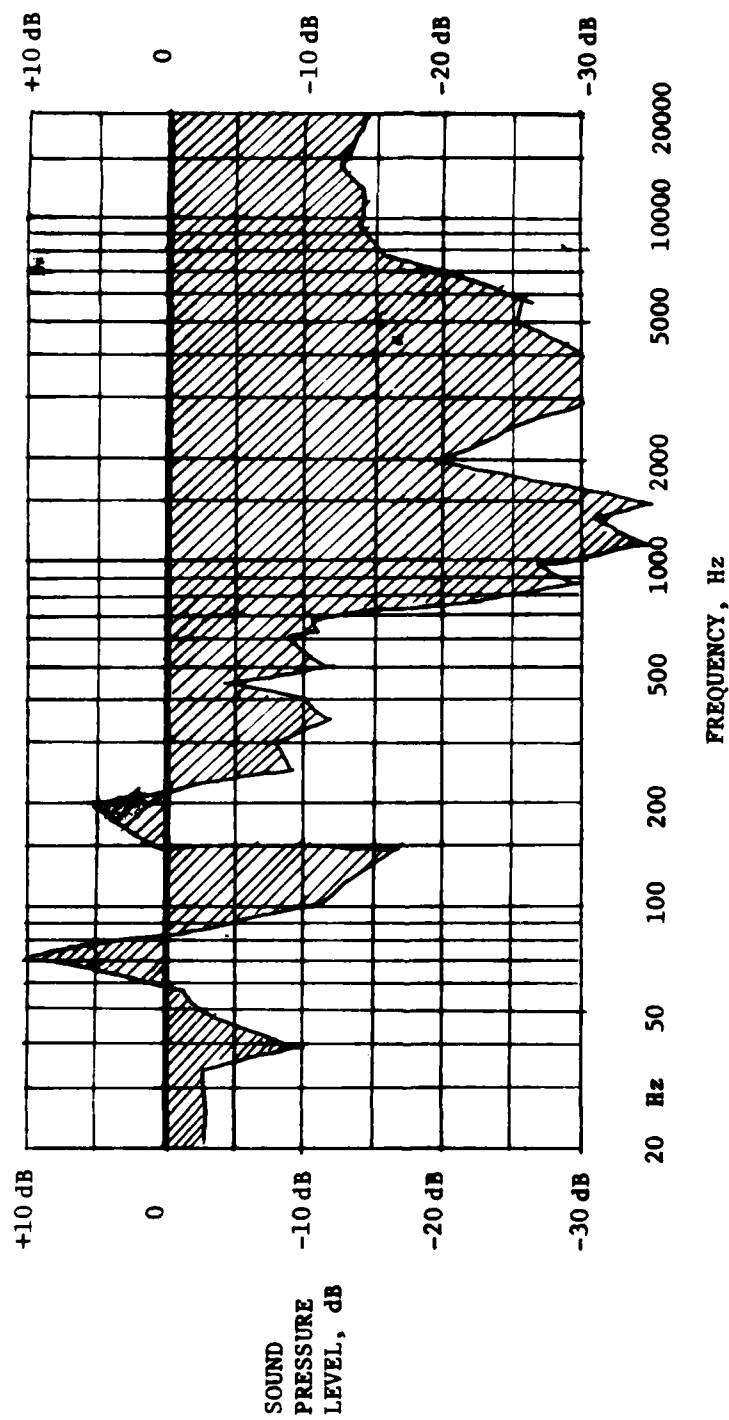
Figure V-17   SOUND PRESSURE LEVEL CHANGE VS. FREQUENCY AT LASER CAVITY WITHOUT

AND WITH ATTENUATORS FOR FLOW RATE OF 0.38 lbm/sec.

123
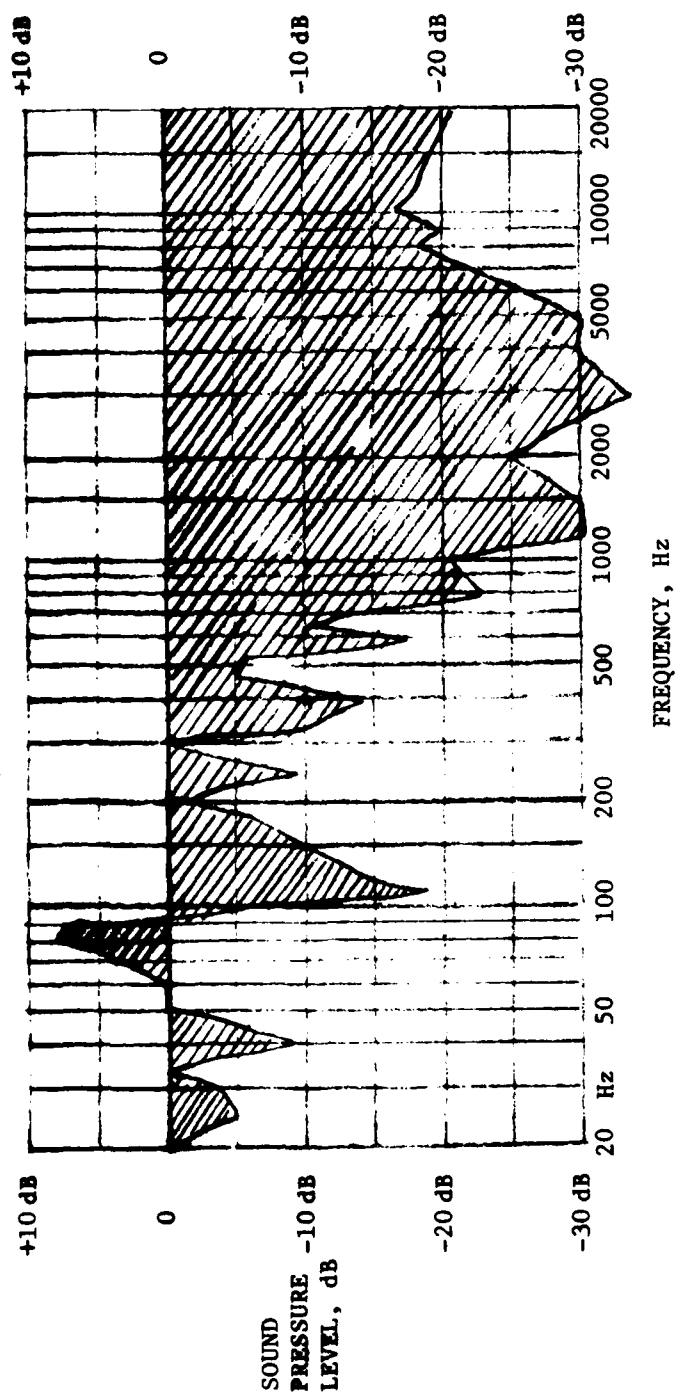
Figure V-18 SOUND PRESSURE LEVEL CHANGE VS. FREQUENCY AT LASER CAVITY WITHOUT

AND WITH ATTENUATORS FOR FLOW RATE OF 0.565 lbm/sec.

124
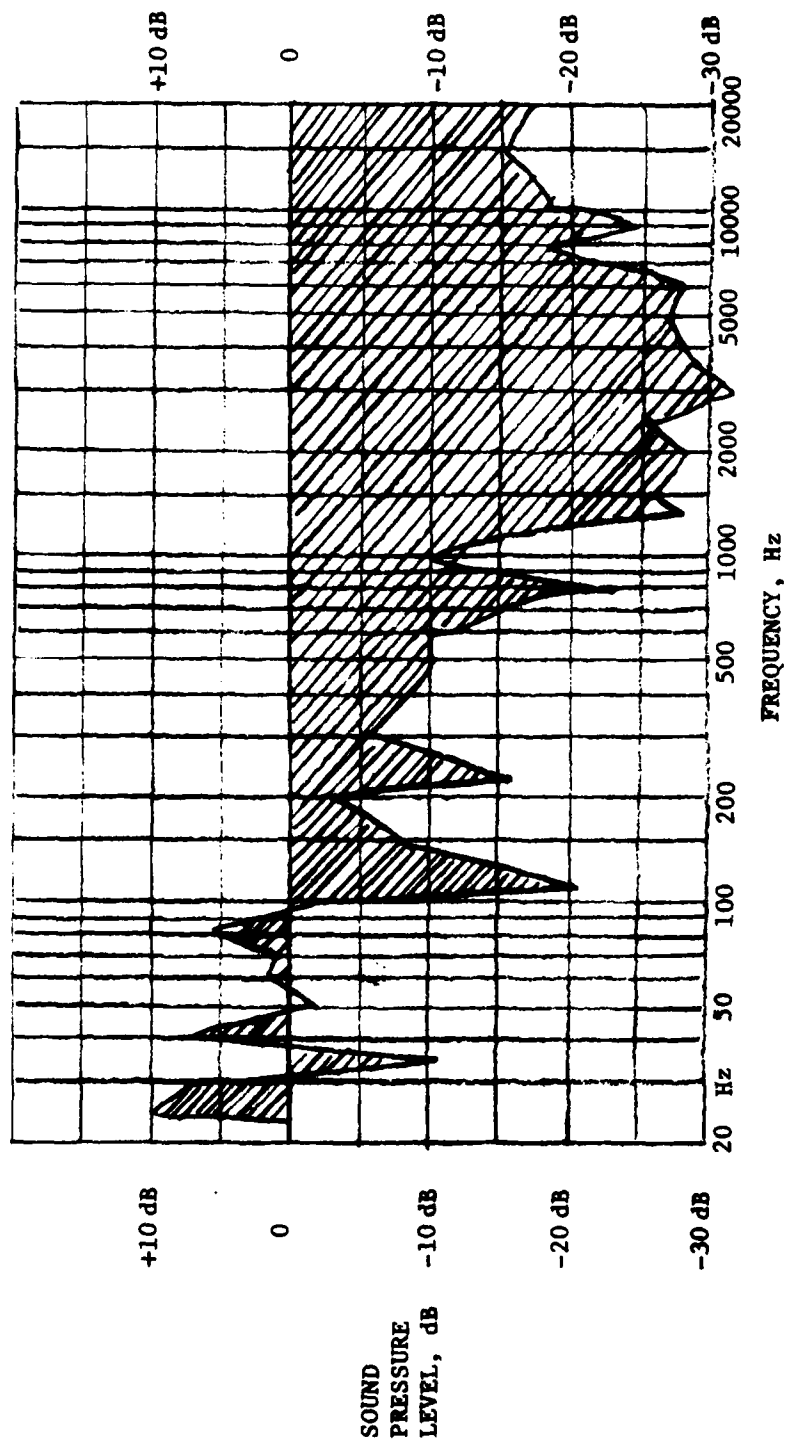
Figure V-19 SOUND PRESSURE LEVEL CHANGE VS. FREQUENCY AT LASER CAVITY WITHOUT AND WITH ATTENUATORS FOR FLOW RATE OF 0.755 lbm/sec.

Figure V-20. General views of handling devices.
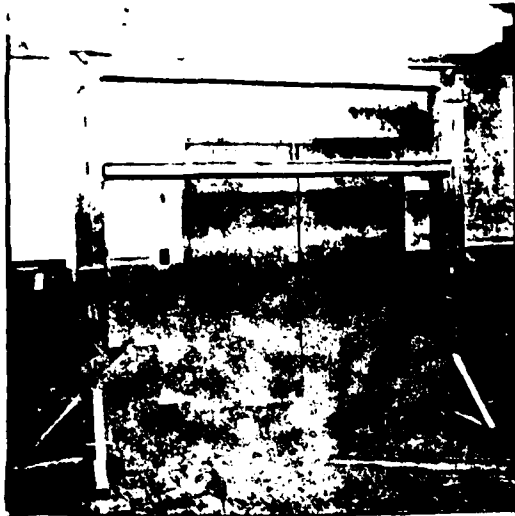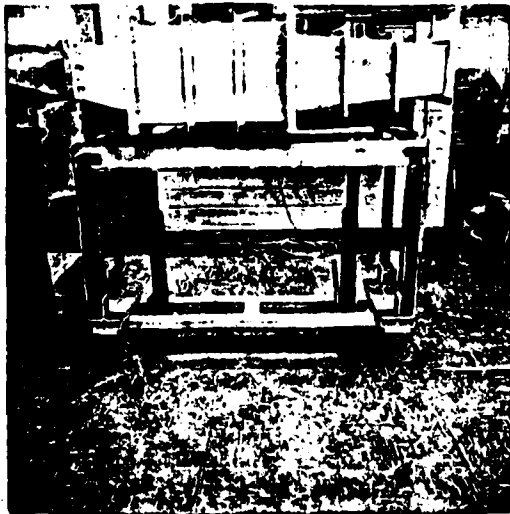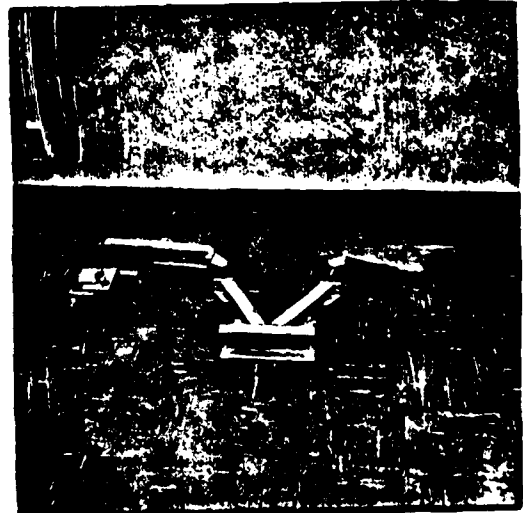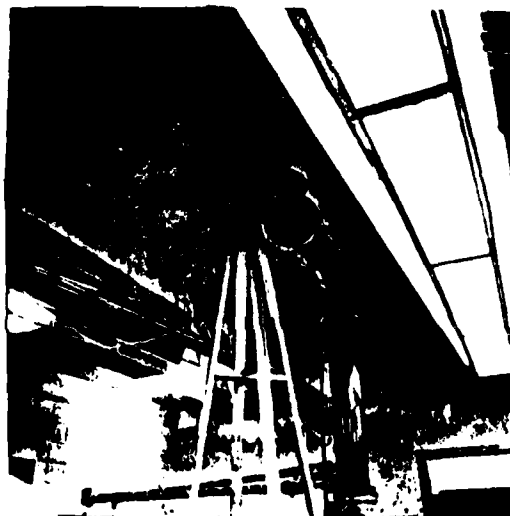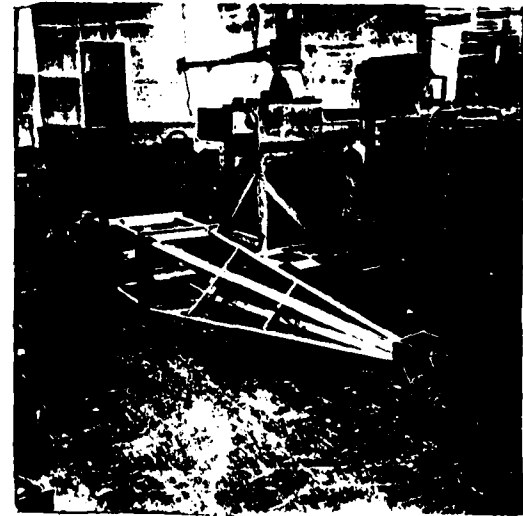
The circulator was disassembled after the trial test series, and the interior of all the components was cleaned by a professional purification firm.

Great care was exercised in reassembling the circulator following the component cleaning.

VI   Theoretical Consideration and Analysis

   A.   Preliminary Consideration of Relationships Among Fractional
         Fluctuations of Flow and Thermodynamic Properties for Laser
         Technology Applications

   Based on the equation of state for ideal gases,

$$\frac{P}{\rho T} = R \tag{A-1}$$

a differential equation of the thermodynamic properties may be derived,

$$\frac{d\rho}{\rho} + \frac{dT}{T} = \frac{dP}{P} \quad \text{or} \quad \frac{d\rho}{\rho} = \frac{dP}{P} - \frac{dT}{T} \tag{A-2}$$

where P denotes static pressure, T is gas temperature, ρ the gas density

and R is the gas constant.

When the thermodynamic process is assumed to be isobaric, dP = 0, thus,

$$\frac{d\rho}{\rho} = -\frac{dT}{T} .$$

If the process is assumed to be isentropic,

$$\frac{dP}{P} = \frac{k}{k-1}\frac{dT}{T} , \text{ where } k = \text{specific heat ratio.} \tag{A-3}$$

Combining Equations (A-2) and (A-3) yields

$$\frac{d\rho}{\rho} = \frac{1}{k-1}\frac{dT}{T} \tag{A-4}$$

and

$$\frac{d\rho}{\rho} = \frac{1}{k}\frac{dP}{P} \tag{A-5}$$

   The thermodynamic properties in fractional fluctuations may be re-
lated in accordance with Equations (A-4) and (A-5), and furthermore, if

$\Delta\rho$, ΔT and ΔP are very small, then it may be approximated to show that

128

$$\frac{\Delta \rho}{\rho} \approx \frac{1}{k-1} \frac{\Delta T}{T} \qquad (A-6)$$

and

$$\frac{\Delta \rho}{\rho} \approx \frac{1}{k} \frac{\Delta P}{P} \qquad (A-7)$$

where $k = \dfrac{C_P}{C_\sigma}$ denotes the specific heats ratio.

Since all the thermodynamic properties are functions of Eulerian space coordinates, X_i and time, t, i.e.

$$\rho = \rho (X_i, t)$$

$$P = P (X_i, t) \qquad (A-8)$$

$$T = T (X_i, t)$$

The exact differential of any of the above quantities should consist of two temporal and spatial components. For example,

$$d\rho = \frac{\partial \rho}{\partial t} dt + \frac{\partial \rho}{\partial X_i} dX_i \qquad (A-9)$$

and

$$d\rho = (d\rho)_t + (d\rho)_{X_i} \qquad (A-10)$$

where $\dfrac{\partial \rho}{\partial t} dt = (d\rho)_t$ denotes the temporal component, and

$\dfrac{\partial \rho}{\partial X_i} d_{X_i} = (d\rho)_{X_i}$, the spatial component.

Similarly, $dP = (dP)_t + (dP)_{X_i} \qquad (A-11)$

$$dT - (dT)_t + (dT)_{X_i} \qquad (A-12)$$

129

Combining Equations (A-4), (A-5), (A-10), (A-11), and (A-12)

results in

$$\frac{(d\rho)_t}{\rho} = \frac{1}{k-1} \frac{(dT)_t}{T} \tag{A-13}$$

and

$$\frac{(d\rho)_{X_i}}{\rho} = \frac{1}{k-1} \frac{(dT)_{X_i}}{T} \tag{A-14}$$

$$\frac{(d\rho)_t}{\rho} = \frac{1}{k} \frac{(dP)_t}{P} \tag{A-15}$$

$$\frac{(d\rho)_{X_i}}{\rho} = \frac{1}{k} \frac{(dP)_{X_i}}{P} \tag{A-16}$$

Equations (A-13) and (A-15) relate the fractional density fluctuations
to fractional temperature and pressure fluctuations on temporal or time
varying basis, meaning that these differential components are determined at
a fixed position point while time elapses. In other words, these time
varying differential components are measured by a stationary sensor or probe
such as hot-wire probe or pressure transducer, at a fixed position point.
On the other hand Equations (A-14) and (A-16) show the relationships among
the fluctuations on spatial or freezer-time basis. In our experimental
analysis, regardless of steady or unsteady state, the spatial differential
components can be obtained by a technique of instant measuring and record-
ing of the distribution of the properties, such as photographic technique
which is capable of freezing and picturing the gas property distributions
in a space.

130

So far, only the thermodynamic properties have been treated with
the fractional relationship. However, in the laser gas dynamic involving
time varying velocity vector and acceleration vector, the fractional
density fluctuations can be related to fractional velocity fluctuations.

The continuity equation for unsteady compressible fluid flows is
given by

$$- \frac{\partial \rho}{\partial t} = \frac{\partial(\rho V_i)}{\partial X_i} \tag{A-17}$$

or

$$- \frac{d\rho}{dt} = \rho \frac{\partial V_i}{\partial X_i} \tag{A-18}$$

and

$$- \frac{d\rho}{\rho} = \frac{\partial V_i}{\partial X_i} dt \tag{A-19}$$

For the sake of physical and mathematical simplicity supported by
experimental justifications, the flow is assembed to be one-dimensional,
unsteady, and compressible. Then Equation (A-19) may become

$$- \frac{d\rho}{\rho} = \frac{\partial V}{\partial X} dt \tag{A-20}$$

and the momentum equation is given as

$$\frac{\partial V}{\partial t} + V \frac{\partial V}{\partial X} = - \frac{1}{\rho} \frac{\partial P}{\partial X} \tag{A-21}$$

and $\left(\frac{\partial P}{\partial \rho}\right) = a^2$ where a denotes the sonic speed.

Combining Equations (I-20) and (I-21) yields

$$- \frac{1}{\rho V} \frac{\partial(\rho V)}{\partial t} dt = \frac{1}{\rho V} \frac{\partial(\rho V)}{\partial X} dX + \frac{1}{\rho M^2} \frac{\partial \rho}{\partial X} dX + \frac{\partial V}{\partial X} \frac{dX}{V} \tag{A-22}$$

where $M = \frac{V}{a}$ is the Mach number of the flow.

131

Since Equation (A-22) consists of two parts separated by variables of time and space, it may be implied respectively that

$$\frac{1}{\rho V} \frac{\partial(\rho V)}{\partial t} dt = 0 \qquad (A-23)$$

and

$$\frac{1}{\rho V} \frac{\partial(\rho V)}{\partial X} dX + \frac{1}{\rho M^2} \frac{\partial \rho}{\partial X} dX + \frac{\partial V}{\partial X} \frac{dX}{V} = 0 \qquad (A-24)$$

From Equation (I-23) it may be deduced that

$$\frac{(d\rho)_t}{\rho} = -\frac{(dV)_t}{V} \qquad (A-25)$$

for time varying component,

and from Equation (A-24), the spatial component gives

$$\frac{(d\rho)_x}{\rho} = -\left(\frac{\partial M^2}{M^2+1}\right) \frac{(dV)_x}{V} \qquad (A-26)$$

Assuming the flow steady, Equation (A-26) becomes the only component, thus

$$\frac{d\rho}{\rho} = -\left(\frac{\partial M^2}{M^2+1}\right) \frac{dV}{V} \qquad (A-27)$$

However, in general application for unsteady flow of compressible fluids

$$-\frac{d\rho}{\rho} = -\frac{(d\rho)_t + (d\rho)_x}{\rho} = \left[\frac{(dV)_t}{V} + \frac{2M^2}{(M^2+1)} \frac{(dV)_x}{V}\right] \qquad (A-28)$$

132

where $(dV)_t = \dfrac{\partial V}{\partial t} dt$ and $(dV)_x = \dfrac{\partial V}{\partial X} dX$

and $(\Delta V)_t = \dfrac{\partial V}{\partial t} \Delta t$, $(\Delta V)_X = \dfrac{\partial V}{\partial X} \Delta X$

also $\lim_{\Delta t \to 0} \Delta t = dt$ and $\lim_{\Delta X \to 0} \Delta X = dX$.

Examination of Equation (A-28) indicates that the fractional density fluctuation may be determined by measuring $(\Delta V)_t$ by a stationary velocity probe such as hot-wire or LDV (Laser Doppler Velocimeter) and finding $(\Delta V)_X$ by freezing the velocity field by some means of instant recording.

In view of the fact that the required $\Delta\rho/\rho$ for a particular laser may be around 1×10^{-6} the commonly accepted assumption of incompressibility for low Mach number flow may be shown to be inadequate for the laser flow in the cavity.

B. Heat Transfer Characteristics of Army Closed Cycle Circulator
    For High Energy Pulsed Lasers

Nomenclature

A flows cross-sectional area

C acoustic velocity

$C_h = (m\ C_p)_h$ hot laser gas flow capacity rate

$C_c = (m\ C_p)_c$ coolant flow capacity rate

C_p specific heat under constant pressure

C_o stagnation acoustic velocity

C_{pc} C_p of coolant

D duct diameter

F frictional resistance per unit mass

f frictional coefficient

H overall heat transfer coefficient

k specific heat ratio

L duct length

L_{max} maximum duct length for sonic chocking occurrence in the duct

M Mach number

M_2 Mach number at Section 2 for example

m mass flow rate

m_A mass flow rate in the main loop

m_B mass flow rate in the bypass loop

P static pressure

q thermal or mechanical energy efflux per unit mass

R engineering gas constant

134

S   tube surface area

T_c static temperature of coolant flow

T_{ci} coolant temperature at heat exchanger inlet

T_{co} coolant temperature at heat exchanger outlet

T_h static temperature of laser gas flow

T_{hi} laser gas temperature at heat exchanger inlet

T_{ho} laser gas temperature at heat exchanger outlet

T_o stagnation temperature

T_{o3} stagnation temperature at Section 2 for example

ΔT temperature difference between laser gas and coolant flows

      across the tube

ΔT_i temperature difference between the counter flows at heat

      exchanger inlet

ΔT_o temperature difference between the counter flows at heat

      exchanger outlet

ΔT_s initial temperature difference between the counter flows in

      the heat exchanger

t   time

V   flow velocity

V_c coolant flow velocity

V_h laser gas flow velocity

W   tube wetted perimeter

X   one-dimensional space coordinate

ρ fluid density

ρ_c coolant density

      time duration for transient process

135

*   fluid and thermal properties at the Mach number is unity

Circulator Systems Description and Specifications

The circulator system is shown schematically in Figure B-1 and consists

of the following major components: a 150 horse power motor driven compres-

sor; a diverter valve and 4 inch (0.102 m) by-pass to permit varying flow

rates; a compressor exit heat exchanger; a Daniel flow meter; a cavity

inlet heat exchanger; a laser cavity; acoustic attenuators upstream and

downstream of the cavity; a compressor inlet heat exchanger; a pulsed

electron beam gun and laser gas excitation power modulator producing 50 kV

peak voltage and 1000 ampere peak current at a pulse repetition frequency

up to 125 pulse per second; an instrumentation system including data

recording and reduction; a control system for starting and stopping the

circulator operation; interconnecting ducts.

The compressor exit heat exchanger (Young Radiator, Model HF-803-DR-1P)

is a shell and tube design having overall dimensions of 8.38 inches (0.213 m)

in diameter and 27 inches (0.686 m) in length. Water is used as the coolant,

and the laser gas is single-passed in the counter flow direction in the

heat exchanger. The flow rate water of 4 lb/sec (1.816 Kg/sec) is supplied

from a reservoir through a centrifugal pump with a temperature maintained at

about $540^{o}R$ $(300^{o}K)$.

The pre-cooled gas then goes through the laser cavity inlet heat

exchanger (Young Radiator, Model HF-804-DR-1P) which is also a shell and

tube design having overall dimensions of 8.38 inches (0.213 m) in diameter

and 36 inches (0.914 m) in length. As before, the single-pass counter flow

136
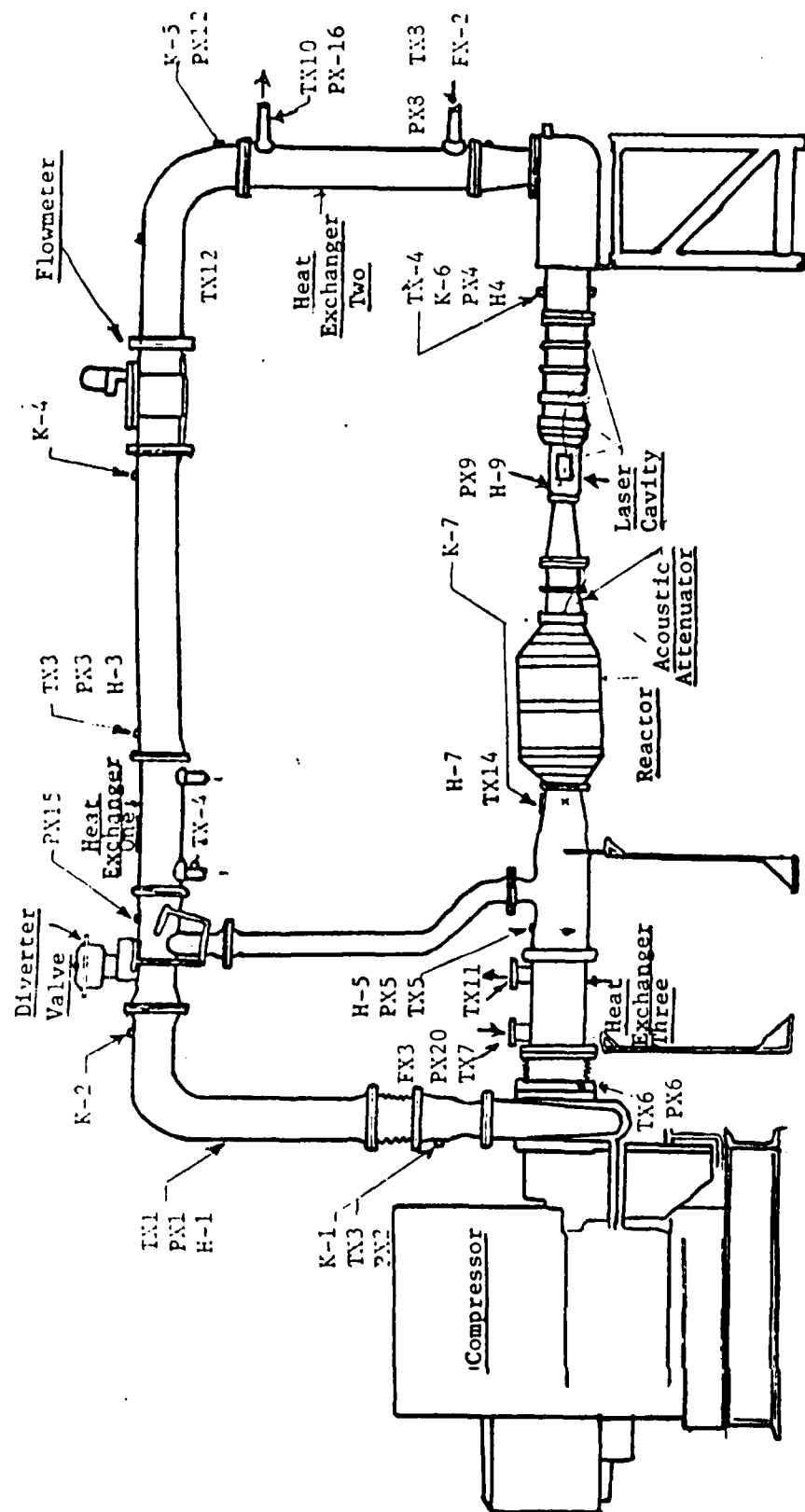
Figure B-1   Schematic of Closed Cycle Circulator

137

process is used. Freon TA is pumped as coolant at the rate
of 3.1 lb/sec (1.407 Kg/sec) to maintain the laser gas flow at the
temperature of about $360^{\circ}R$ ($200^{\circ}K$). The freon TA is returned to the
storage tank and cooled with a coiled flow of liquid nitrogen down to
approximately $296^{\circ}R$ ($164^{\circ}K$).

The compressor inlet heat exchanger (Young Radiator, Model F-1002-
DR-1P) is of the same design as the other two heat exchangers with over-
all dimensions of 10.75 inches (0.273 m) in diameter and 18 inches (0.457 m)
in length. The coolant or water is pumped at the rate of about 2 lbm/sec
(0.908 Kg/sec) into the exchanger at the maintained temperature of $540^{\circ}R$
($300^{\circ}K$). In all three heat exchangers tubing 3/8 inch (0.00953 m) OD brass
is employed to transport the laser gas.

The instrumentation system pertinent to this study consists of six
Kistler pressure transducers (Model 6602A) having a frequency response to
30 kH_z for the measurement of unsteady pressures around the circulator,
six hot-wire anemometers (TSI Model 1050) for the measurement of unsteady
velocities and temperatures with a frequency response to 15 kH_z, twelve
thermocouples (HY-CAL Model RIS-31-A-100-B-8-3-600) and nine pressure
transducers (Sanso-Matrix Model SP91A5.0) for measurements of steady flow
temperature and pressure in the circulator, respectively. The experimental
data collected are recorded in a multi-channel tape recorder (Bell & Howell
Model - VR3700 B) and then digitized for later reduction and analysis
through a computer (Model HP2100).

Specifications of the circulator system are presented in Table 1.

Table B-1. Closed-Cycle Circulator System Characteristics

Operating conditions

Gas composition (nominal 3:2:1 mix)	
Helium, mole percent	50.0
Nitrogen, mole percent	33.3
Carbon dioxide, mole percent	16.7
Mass flow rate, lb/sec	0.3 to 1.4
Pressure drop (maximum at 1.4 lb/sec) (psid)	
Total loop	(8.4)
Compressor exit heat exchanger	0.6
Flow meter	0.5
Cavity inlet heat exchanger	0.43
Cavity plus acoustic attenuators	6.0
Cavity exit heat exchanger	0.36
Compressor pressure ratio (maximum)	1.8
Compressor speed (rpm)	33,000
Laser cavity inlet temperature (^{o}K)	200 to 300
Laser cavity pressure (psia)	15
Running time (sec)	60

Static conditions

Pressure	
Maximum (psia)	30
Minimum (microns)	500

Coolant storage conditions

Water	
Capacity (gallons)	110
Pump outlet pressure (psia)	35.1
Freon TA	
Capacity (lb)	110
Pressure at $180^{o}K$ (psia)	100

Theoretical Analysis

Fluid and thermal characteristics of the recirculating laser gas flow may be analyzed by solving the following set of differential equations of mass, momentum, and energy conservation for unsteady one-dimensional flow:

Continuity equation;

$$\frac{\partial \rho}{\partial t} + \rho \frac{\partial V}{\partial \chi} + \frac{V \partial \rho}{\partial \chi} + \frac{\rho V}{A} \frac{dA}{d\chi} = 0 \qquad (B-1)$$

139

Momentum equation;

$$\frac{\partial V}{\partial t} + V \frac{\partial V}{\partial \chi} + \frac{1}{\rho} \frac{\partial P}{\partial \chi} + F = 0 \qquad (B-2)$$

Energy equation;

$$\frac{\partial P}{\partial t} - C^2 \frac{\partial \rho}{\partial t} + V \frac{\partial P}{\partial \chi} - C^2 \frac{\partial \rho}{\partial \chi} - (k-1) \rho (q + VF) = 0 \qquad (B-3)$$

where $F = \frac{4f}{D} \frac{V^2}{2}$ is the frictional resistance in force per unit mass.

The above equations account for the effects of friction and heat transfer into and out from the gas as it flows around the circulator system.

The analysis of the complete circulator loop was divided into two parts due to the nature of the problems to be solved.

A. Heat Exchangers

The heat exchanger counter flow process, shown in Figure B-2 is modeled by the following set of differential equations [2] for the assumption of zero tube wall heat resistance and zero time varying wall temperature gradient:

$$C_h \frac{\partial T_h}{\partial t} + C_h V_h \frac{\partial T_h}{\partial \chi} = \frac{dq}{dt} \qquad (B-4)$$

$$C_c \frac{\partial T_c}{\partial t} + C_c V_c \frac{\partial T_c}{\partial (L-\chi)} = \frac{dq}{dt} \qquad (B-5)$$

$$\frac{dq}{dt} = - HW (T_h - T_c) V_h \text{ or } c \qquad (B-6)$$

The steady state temperature of the gas and coolant can be found from the resulting closed form steady state solutions to Eqs. (B-4) - (B-6)

$$\frac{C_h}{C_c} = \frac{T_{co} - T_{ci}}{T_{hi} - T_{ho}} , \qquad (B-7)$$

140

and

$$\ln \frac{T_{ho} - T_{ci}}{T_{hi} - T_{co}} = \frac{T_{ho} - T_{ci} - T_{hi} + T_{co}}{C_h} \frac{HS}{(T_{ho} - T_{hi})} . \tag{B-8}$$

A simultaneous solution to Eqs. (B-4) - (B-6) that accounts for both steady and transient states in the heat exchanger is obtained for the following boundary conditions:

a) when $t = \tau$, $\dfrac{\Delta T - \Delta T_i}{\Delta T_S - \Delta T_i} = 0.01$ at $\chi = 0$

$$\frac{\Delta T - \Delta T_o}{\Delta T_S - \Delta T_o} = 0.01 \text{ at } \chi = L$$

b) when $t = 0$, $\Delta T - \Delta T_S$ at $0 \leq \chi \leq L$.

Thus, the solution in dimensionless form may be approximated,

$$\frac{\Delta T}{\Delta T_S} = e^{-4.6\frac{t}{\tau}} + \frac{\Delta T_i}{\Delta T_S} \left(\frac{\Delta T_o}{\Delta T_i}\right)^{\frac{\chi}{L}} \left[1 - e^{-4.6\frac{t}{\tau}}\right] \tag{B-9}$$

where $\tau = 4.6 \ \alpha$ \hfill (B-10)

$$\Delta T = \Delta T \ (\chi, t) = T_u - T_c \tag{B-11}$$

$$\alpha = \frac{C_{pc} \ \rho_c D}{4H} \tag{B-12}$$

$$\begin{aligned}
\Delta T_s &= (T_{hi} - T_{ci}) \\
\Delta T_i &= (T_{hi} - T_{co}) \quad \text{in steady state} \\
\Delta T_o &= (T_{ho} - T_{ci})
\end{aligned} \tag{B-13}$$

A simultaneous solution of Eqs. (B-7) and (B-8) will yield values of T_{ho} and T_{co} for given C_h, C_c, H, S, T_{hi}, and T_{ci} in steady state after $t = \tau$, process time constant for the transient state relaxation. The variation of ΔT on χ and T in the exchanger can be found from Eq. (B-9) for the Eq. (B-8) values of the steady state temperature distribution and respective value of α.

141

Figure B-2 Heat Exchanger Schematic and Temperature
Distribution

(Heat Exchanger)
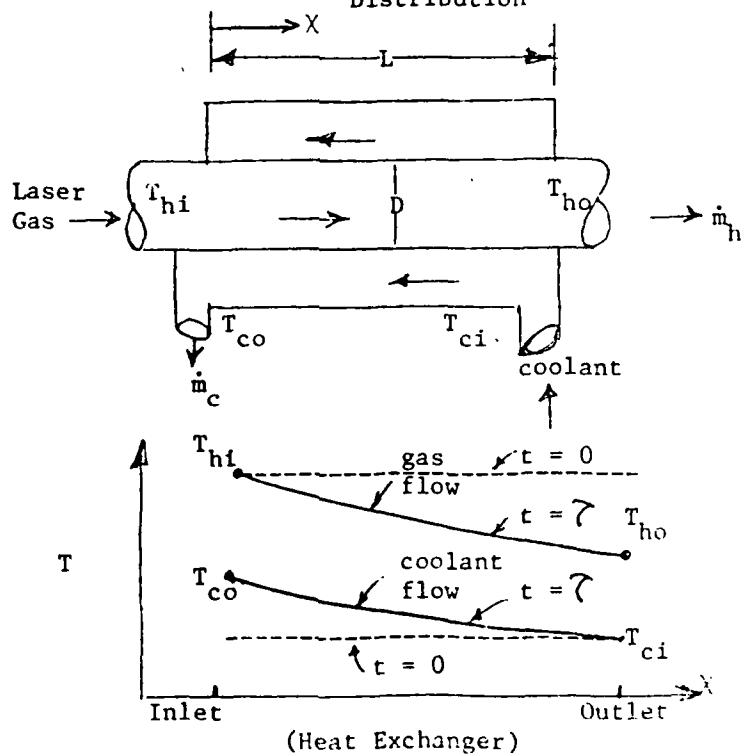
B. Flow Analysis

These equations for transient processes were used in a theoretical
evaluation of the recirculating gas transient fluid and thermal character-
istics of the other components to determine the dominant processes. This
evaluation showed the heat exchanger transient processes dominates those
transient processes occurring at other components of the circulator.
Therefore, by neglecting the transient processes at other components for
simplicity, the solutions to Eqs. (B-1) through (B-3) provide the required
steady state information between sections around the circulator loop.

142

The principal duct sections are shown in Figure B-3. Changes are made in the state variables of the gas as it flows through the components located at the duct sections junctions.

Figure B-3 Diagram of Circulator System Showing Duct
Sections, Principal Components and
Direction of Heat and Mass Flow

$$\dot{m} = \dot{m}_A + \dot{m}_B; \quad q_c + q_v = q_o = q_{ii} \pm q_{III}$$
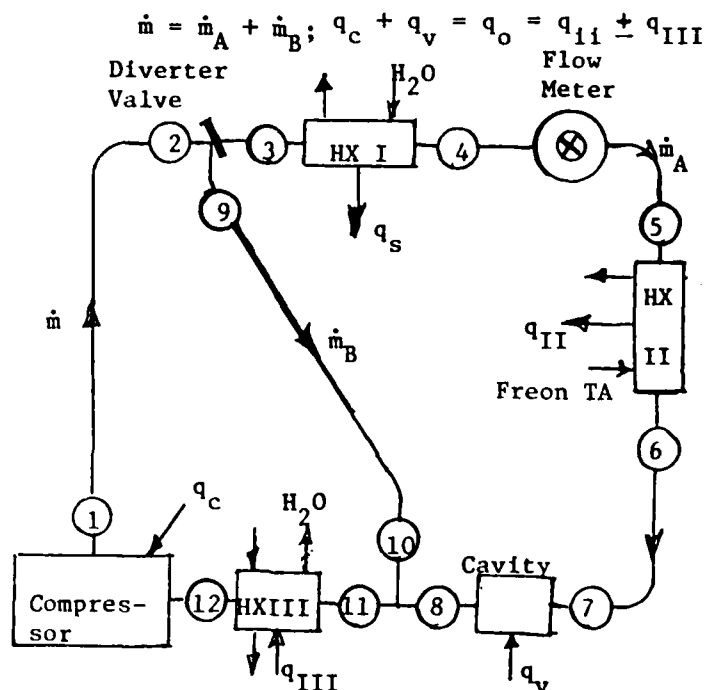
In practice, the heat losses in the by-pass, duct, and short interconnecting ducts was found to be relatively small, compared with the total energy level in the flow in the ducts. This justified the assumption of adiabatic process with friction for ducts between Sections 1 and 2, 4 and 5, 6 and 7, 8 and 11, and 9 and 10.

Equations to treat the flow in these sections are given below.

$$\rho_1 V_1 A_1 = \rho_2 V_2 A_2 \tag{B-14}$$

143

$$\frac{4\bar{f}L_{max}}{D} = \left(\frac{1 - M^2}{kM^2}\right) + \left(\frac{k+1}{2k}\right) \ln \frac{(k + 1) M^2}{2(1 + \frac{k-1}{2} M^2)} \qquad (B-15)$$

$$\bar{f} = \frac{1}{L_{max}} \int_0^{L_{max}} f \, d\chi \qquad (B-16)$$

$$4f\frac{L}{D} = \left(4\bar{f} \frac{L_{max}}{D}\right)_{M_1} - \left(4\bar{f} \frac{L_{max}}{D}\right)_{M_2} \qquad (B-17)$$

$$\frac{V_2}{V^*} = M_2 \sqrt{\frac{k + 1}{2(1+\frac{k-1}{2} M_2^2)}} = \frac{\rho^*}{\rho_2} \qquad (B-18)$$

$$\frac{P_2}{P^*} = \frac{1}{M_2}\sqrt{\frac{k + 1}{2(1+\frac{k-1}{2}M_2^2)}} \qquad (B-19)$$

$$\frac{T_2}{T^*} = \frac{k + 1}{2(1+\frac{k-1}{2}M_2^2)} \qquad (B-20)$$

$$V^* = \sqrt{kRT^*} = C_0\sqrt{\frac{2}{k+1}} \qquad (B-21)$$

$$C_0 = \sqrt{kRT_0}$$

With fluid and thermal characteristics at Section ①) given,
conditions at Sections ② can be obtained from the above equations.

Other duct Sections, for example Sections ④ to ⑤ , ⑥ to ⑦ .
etc. can be solved using the same procedures as those presented above
for Sections ① to ②.

The gas flow suffers a signifcant pressure loss as it flows through
the three heat exchangers. Here the effects of friction as well as

144

heat transfer must be considered in the flow analysis. Combining Eqs. (B-1), (B-2) and (B-3) results in the following relationship:

$$dM^2 = F_{T_o} \frac{dT_o}{T_o} + F_f \; 4f \; \frac{dX}{D} \qquad (B-22)$$

An approximate integration through trial iterations procedures using finite difference methods for the heat exchanger between Junctions ③ and ④, as an example, will yield the following equations:

$$M_4^2 - M_3^2 = \overline{F}_{T_o} \left(\frac{T_{04} - T_{03}}{\frac{T_{04} + T_{03}}{2}} \right) + F_{\overline{f}} \; 4\overline{f} \; \frac{L}{D} \qquad (B-23)$$

$$\text{where } \overline{F}_{T_o} = \overline{M} \; (1+k\overline{M}^2) \; (1 + \frac{k-1}{2} \; \overline{M}^2) \qquad (B-24)$$

$$\overline{F}_f = \frac{k\overline{M}^4(1 + \frac{k-1}{2} \; \overline{M}^2}{1 - \overline{M}^2} \;, \qquad (B-25)$$

$$\overline{M} = \frac{M_3 + M_4}{2} \;, \qquad (B-26)$$

$$\overline{f} = \frac{D}{2L} \; \ln \left(\frac{T_{03} - \overline{T}_c}{T_{04} - \overline{T}_c} \right), \qquad (B-27)$$

$$T_c = \frac{T_{ci} + T_{co}}{2} \;, \qquad (B-28)$$

$$T_{04} = T_4 + \frac{V_4^2}{2C_p} \;. \qquad (B-29)$$

Eq. (B-27) is derived based on the Reynolds analogy between the friction and heat transfer [3].

Other heat exchangers can be treated with similarity after first determining the inlet and outlet temperatures of laser gas flow at the heat exchangers using Eqs. (B-7) and (B-8).

145

The compressor and laser cavity components are also similarily analyzed except the change in the direction of the energy flux is made and its magnitude is given.

Experimental Thermal Performance Data and Discussion

A. Heat Exchangers

The closed cycle circulator was designed and fabricated by Rocketdyne Division of Rockwell International Corp. and delivered to Redstone Arsenal in accordance with the Army specifications. A series of acceptance tests were performed by Rocketdyne [4] to collect data collected for various flow conditions. Some of the data was analyzed by the above methods is presented in Table B-2 and is plotted in Figures B-4 and B-5. For the present analysis of the data, Eq. (B-8) was modified:

$$q = C_h \ (T_{ho} - T_{hi}) = \frac{\Delta T_i - \Delta T_o}{\ln \dfrac{\Delta T_i}{\Delta T_o}} \ HS \qquad (B-30)$$

Equation (B-30) was used for calculating the heat transfer performance of the heat exchanger for given end temperatures, and heat transfer co-efficient provided by the manufacturer and the specified tube surface area.

The analyzed data presented in Table B-2 shows that as the mass flow rate is increased, the heat flux is raised accordingly for compressor exit and cavity inlet heat exchangers. While the trend is reversed for the compressor inlet heat exchanger due to the effects from the diverter valve. As the diverter valve reduces the gas flow into the cavity, an increasing fraction of the high temperature gas flow is diverted through the 4-in by-pass pipe directly into the compressor inlet heat exchanger, causing the adverse effects.

146

Figure B-5 – Temperature Distributions Around the Circulator
for Various Flow Conditions

	ṁ at Cavity	Pentane HXII
Run A	1.634 lbm/sec	off
Run B	0.154 lbm/sec	off
Run C	0.213 lbm/sec	on
Run D	1.383 lbm/sec	on
Theoretical	1.4 lbm/sec	on

Compressor HXI   HXII   Cavity   HXIII   Compressor

Figure B-4 – Pressure Distributions Around the Circulator
for Various Flow Conditions

	ṁ at Cavity	Pentane HXII
Run A	1.634 lbm/sec	off
Run B	0.154 lbm/sec	off
Run C	0.213 lbm/sec	on
Run D	1.383 lbm/sec	on
Theoretical	1.4 lbm/sec	on

Compressor   HXI   HXII   Cavity   HXIII   Compressor

Evaluation of the analyzed data shows that only minor adjustments in the manufacturer's given heat transfer coefficients were required to verify the theoretical results from Eqs. (B-7) and (B-8). This evaluation verifies that these equations are a useful tool for first order trend predictions and early system design.

Figures B-4 and B-5 depict measured pressure and temperature distributions around the circulator. The distinctive effects of the cavity inlet heat exchanger operating with freon TA as the coolant is clearly noted. When the cavity inlet gas temperature must be maintained at approximately 360°R, the cavity inlet heat exchanger is required to extract nearly 100 BTU/sec of heat flux from the gas flow, while the compressor inlet heat exchanger (HXIII) is shown to add heat flux of more than 30 BTU/sec into the laser gas flow as listed in Table B-2.

When the diverter valve is shifting a major portion of gas flow into the bypass loop, supplying only about 10 percent of the flow into the cavity, HXIII carries a main load of heat extractions from the gas flow and HXI and HXII function only in a minor way in keeping the heat balance as shown by the heat flux, q, in Table B-2.

These steady state experimental data of temperature and pressure for four flow rates with and without HXII in operation with freon TA are compared with the results of theoretical models delineated in Eqs. (B-13) through (B-29), and are shown in Figures B-4 and B-5. Excellent agreement between the experiment and theory was noted after proper adjustments of friction and heat transfer coefficients were made in the theoretical model for $\dot{m} = 1.4$ lbm/ sec, therby verifying the theory and providing a tool for accurate predictions of fluid and thermal characteristics of the recirculating flow. This tool

148

Table B-2 Heat Exchanger Performance Data

Heat Exchanger	$\dot{m}_h$ (lbm/sec)	$\dot{m}_c$ (lbm/sec)	T_{hi} (°R)	T_{co} (°R)	T_{ho} (°R)	T_{ci} (°R)	q (BTU/sec)
Model HF-803-DR-1P	1.634**	4.0	707	567.8	592	530	61.62
(Young Radiator)	0.154**	4.0	709	530.7	536	531.1	8.74
8.38" x 27"	0.213*	4.0	631	527.5	531	527.8	6.98
Coolant – Water	1.383*	4.0	635	536.3	548	528.5	39.45
S = 50.6 ft²							
H = 0.01434 BTU/ft² °R sec							
Model HF-804-DR-1P	1.634**	3.1	592	524.9	580		6.43
(Young Radiator)	0.154*	3.1	536	521.7	538		0.105
8.38" x 27"	0.213*	3.1	531	321.9	327	306	14.25
Coolant – Pentane	1.383*	3.1	548	355.2	348	287	90.70
S = 67.1 ft²							
H = 0.0118 BTU/ft² °R sec							
Model F-1002-DR-18	1.634**	2.0	577	527.8	559	517.8	26.64
(Young Radiator)	0.154**	2.0	659	551.6	578	531.1	85.96
10.75" x 18"	0.213*	2.0			468.7	527.8	73.49
Coolant – Water	1.383*	2.0	416		468	528.5	-35.45
S = 52.0 ft²							
H = 0.01136 BTU/ft² °R sec							

Note: *   Pentane Heat Exchanger in operation
       **   Pentane Heat Exchanger not in operation

149

is then directly useful for developing scaling laws in the engineering design of larger circulator systems based on the principle of similitude treating the theoretical model through dimensionless parameters.

Experimental analysis of transient flows has been initiated and yet to be completed in the near future; therefore, comparison with and verification of the theoretical model are not presented in this paper.

Conclusions

Theoretical models depicting the steady and transient states of recirculating flows in the closed cycle air circulator are presented. Based on the limited experimental data collected to date, the steady state theoretical model was compared with experimental results and was satisfactorily verified. Since the models were developed in terms of dimensionless parameters, it has been shown that the scaling laws established through this study with the small scale CCC system is applicable for designing a larger scale CCC system.

References

[1] Cason, C., et al. "A Small Closed Cycle Circulator Experimental Plan for Repetively Pulsed 200°K High Pressure Electric Discharge Lasers" Tech Report RH-76-12, Aug. 1976, U. S. Army Missile Command, Redstone Arsenal, AL 35809.

[2] Kalinin, E. K. "Tubular Heat Exchangers with Bilateral Heat Transfer Augmentation and Calculation of a Heat Exchanger Under Unsteady Operating Conditions", Chapter 8, Heat Exchangers: Design & Theory Sourcebook by Afgan, N. & Schlunder, E. U., McGraw-Hill Book Co., 1974.

[3] Hicks, B. L., et al. "The One-Dimensional Theory of Steady Fluid Flow in Ducts with Friction and Heat Addition", NASA Tech. Note, No. 1336 (1947).

[4] Ferris, D. F., Final Report "Closed Cycle Gas Recirculator", Aug. 1977, DAAH01-76-C-0961, Rocketdyne Div. Rockwell International, Calif.

C. Results of Unsteady Flow Analysis in the Cavity Region
    by the Method of Characteristics

Since detailed descriptions of the computer code are based on
the method of characteristics which are capable of solving unsteady
gasdynamic problems of a one-dimensional nature in the cavity region
with a pulsed energy input have been presented in previous reports
in 1978 and 1979, only a typical set of results from the computer-
assisted calculations of the flow field is presented in this report
for the purpose of demonstrating the capability and limitations of
the computer code.

This set of results takes into account the present cavity
dimensions (5 cm x 5 cm x 25.9 cm) with a pulsed energy input of
16.5881 BTU per cubic ft.

Spatial distributions of velocity, pressure, density and tem-
perature for seven time frames from the instant of energy input are
plotted in Figures C-1 through C- 12. Temporal distributions of
velocity, pressure, density and temperature for five sections in the
cavity region are presented in Figures C-13 through C-22.

These Figures depict abrupt changes in flow and thermodynamic
properties along flow passages upstream and downstream of the cavity
for given time frames following the input of pulsed energy, as well
as time-dependent variations of these properties at given sections
along the cavity ducts.
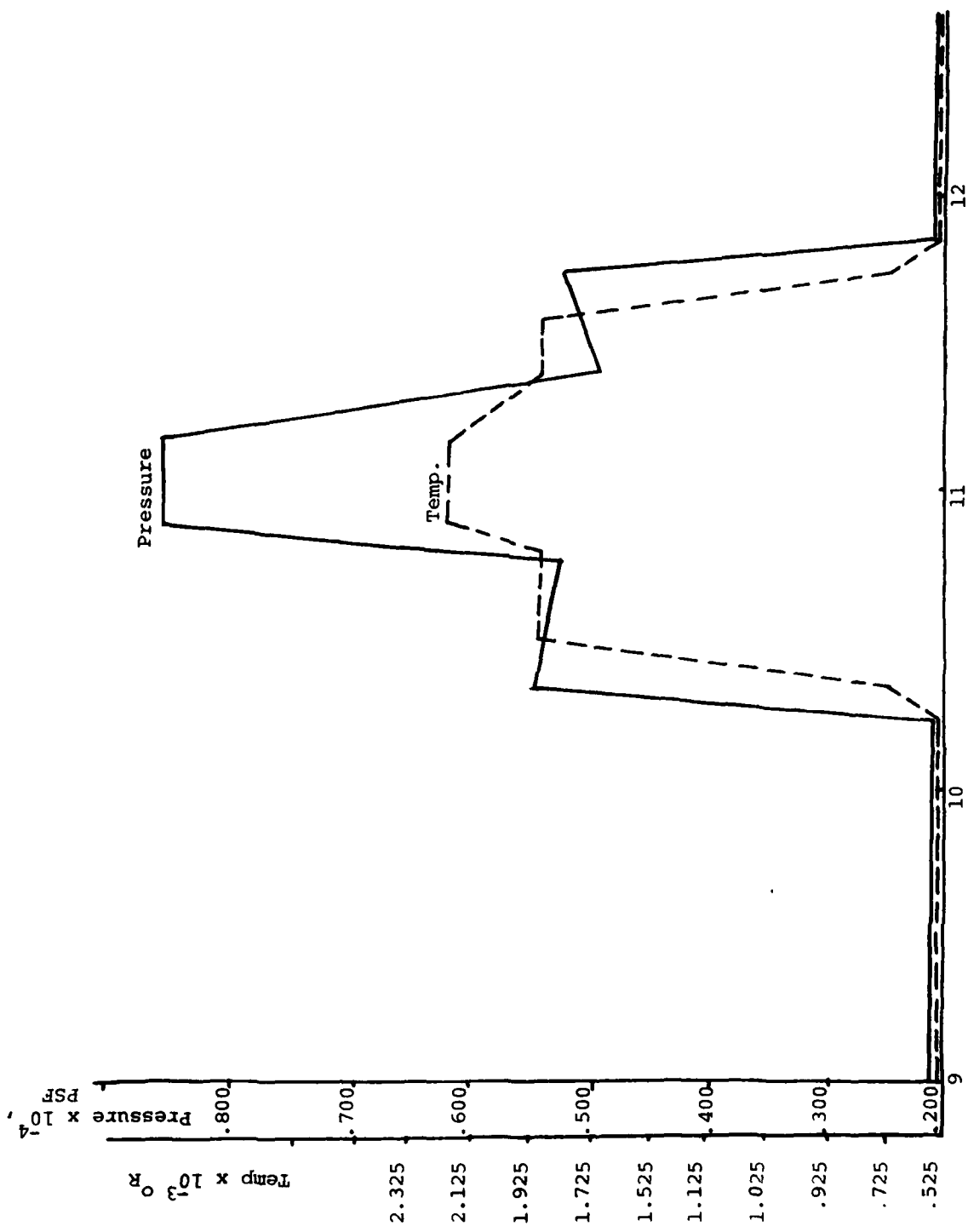
Figure C-1. Typical Distribution of Flow Conditions in Circulator for Time Frame .2

152
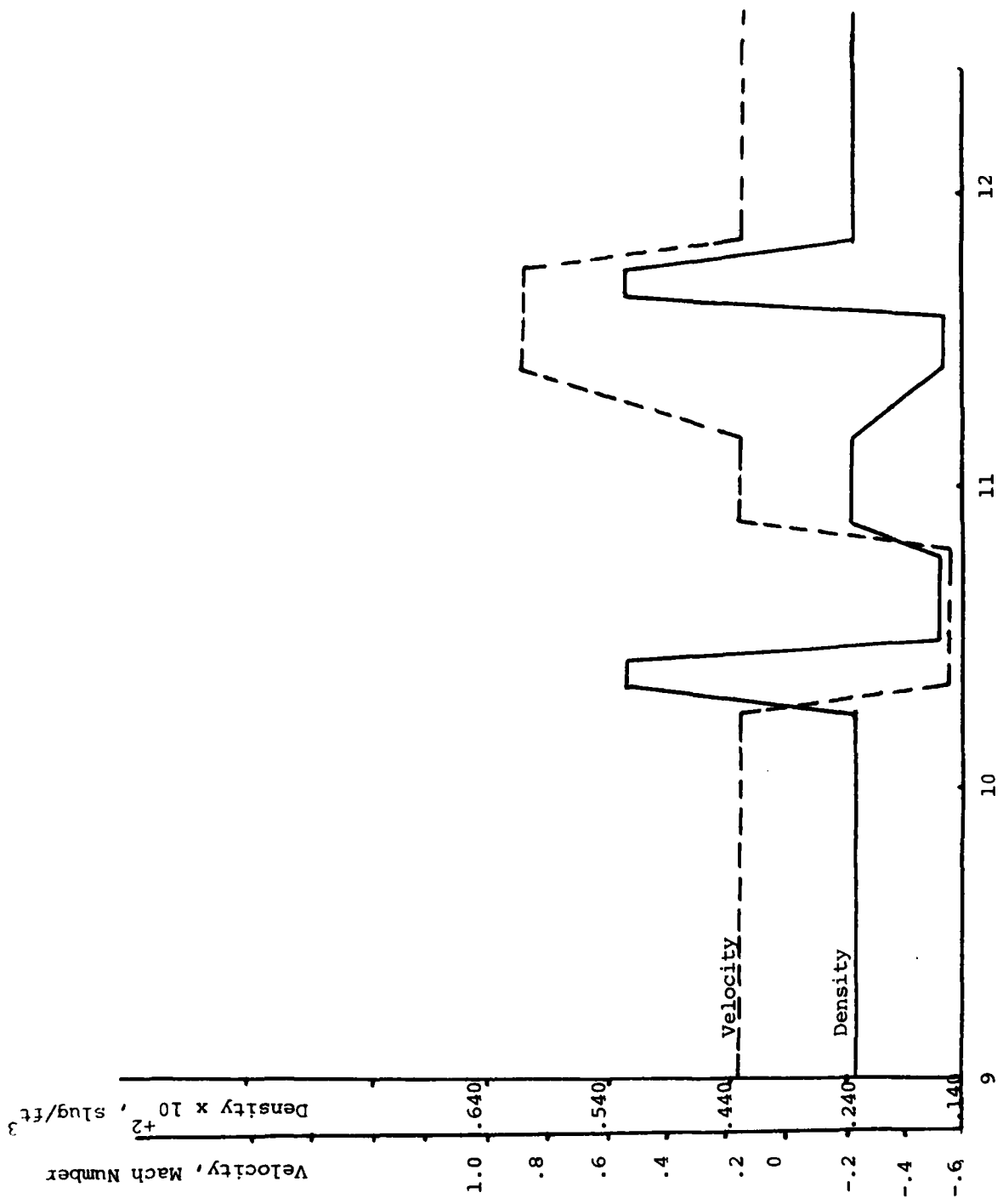
Figure C-2. Typical Distribution of Flow Conditions in Circulator for Time Frame .2
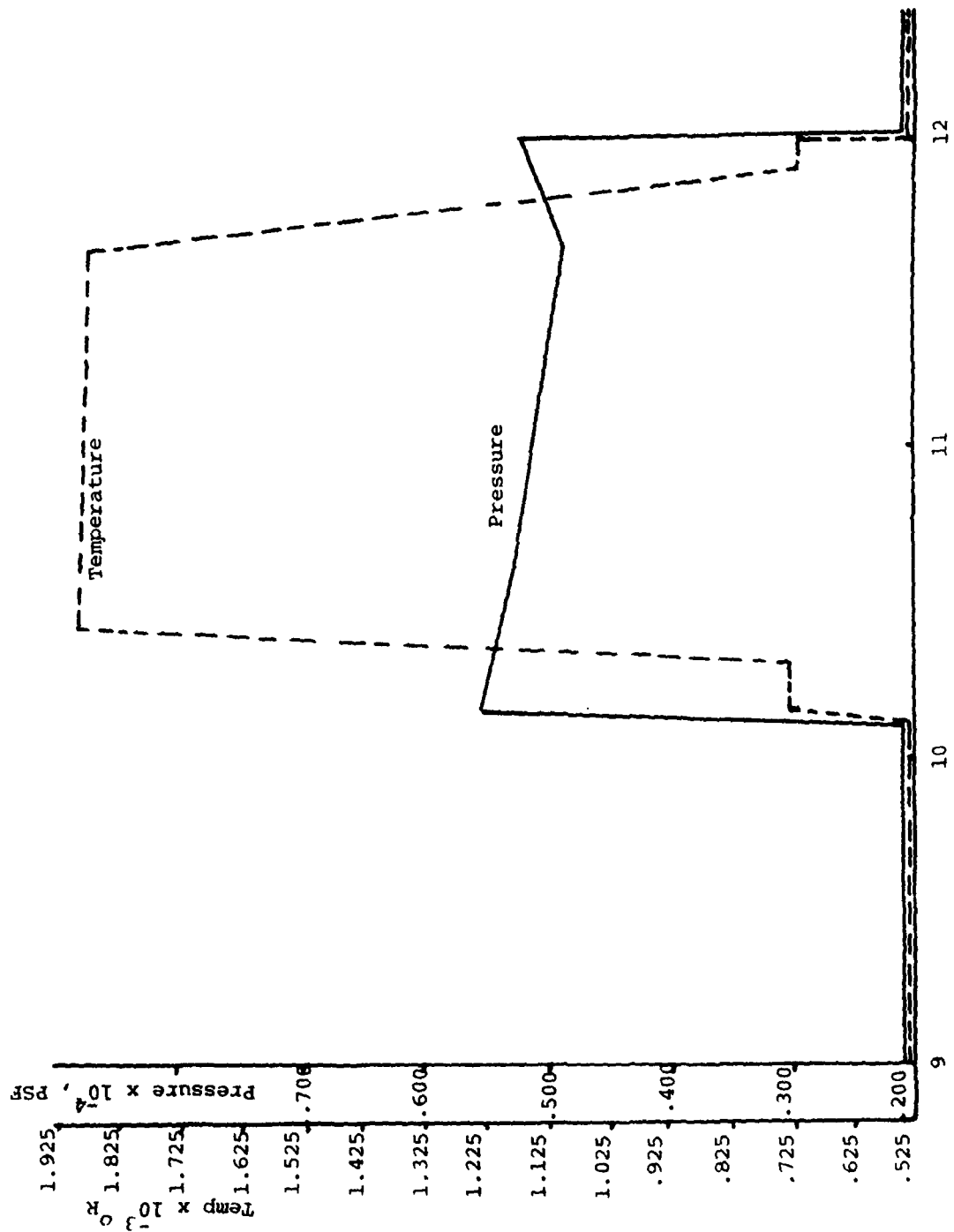
Figure C-3. Typical Distribution of Flow Conditions in Circulator for Time Frame .3

154
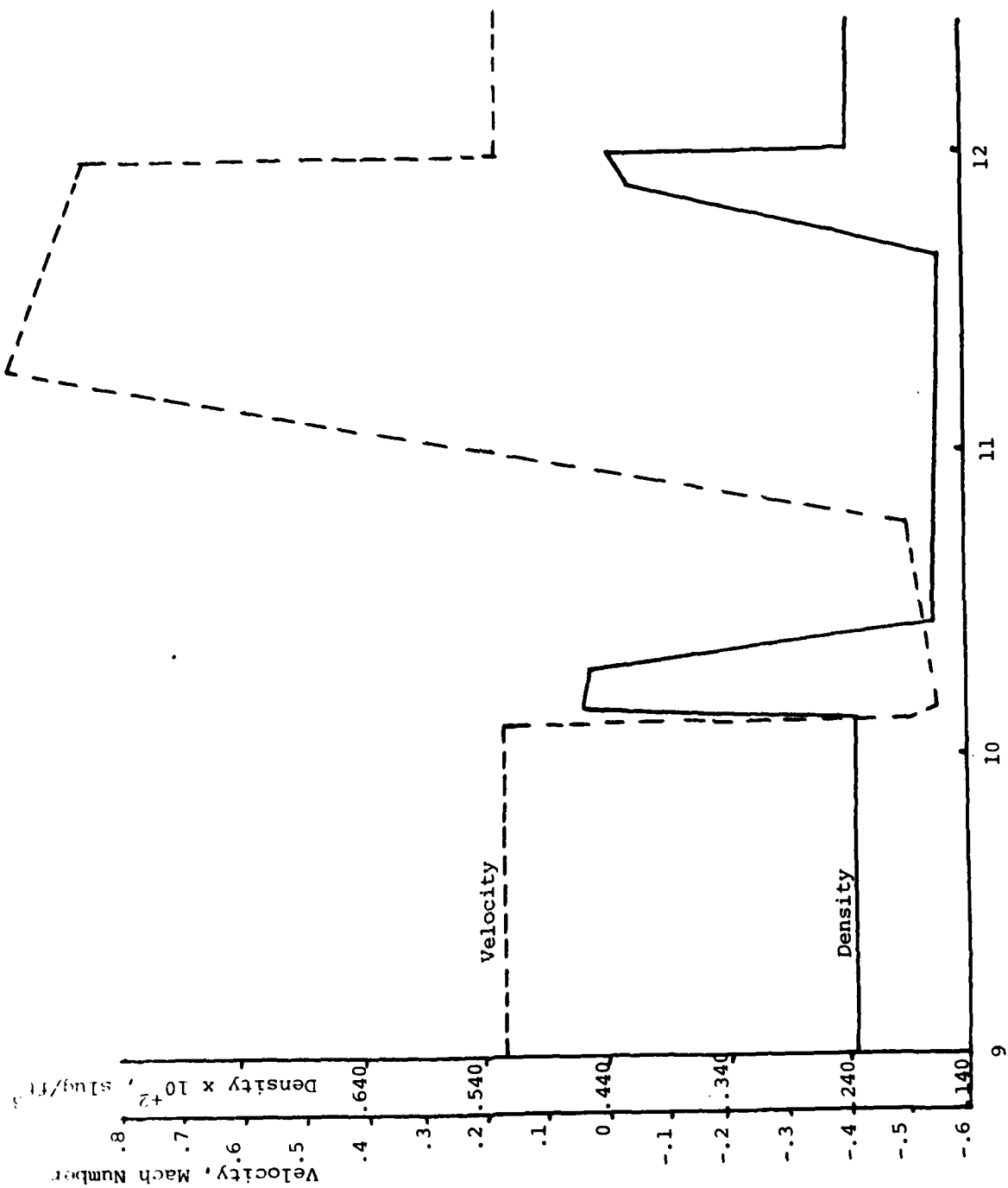
Figure C-4. Typical Distribution of Flow Conditions in Circulator for Time Frame .3
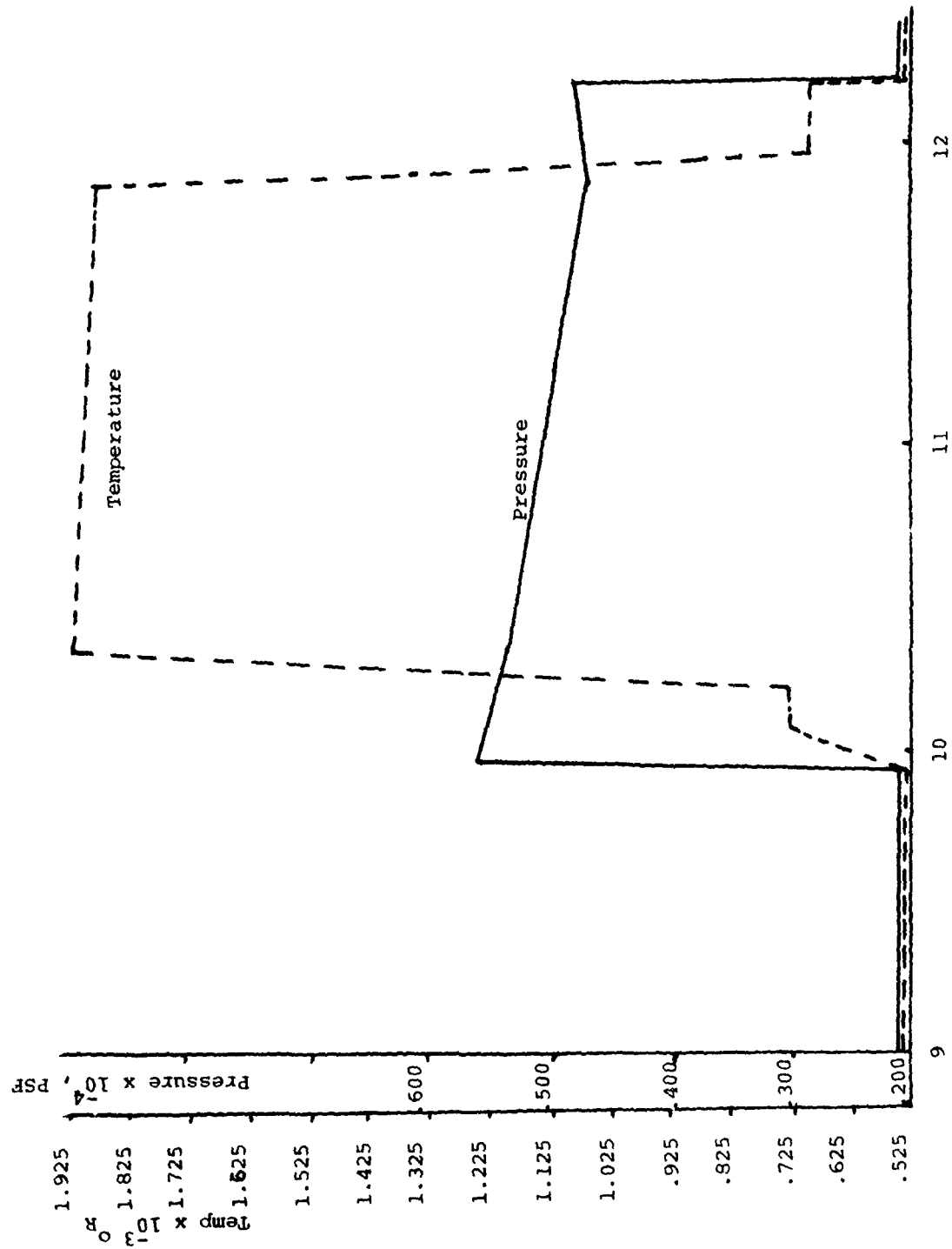
Figure C-5. Typical Distribution of Flow Conditions in Circulator for Time Frame .4
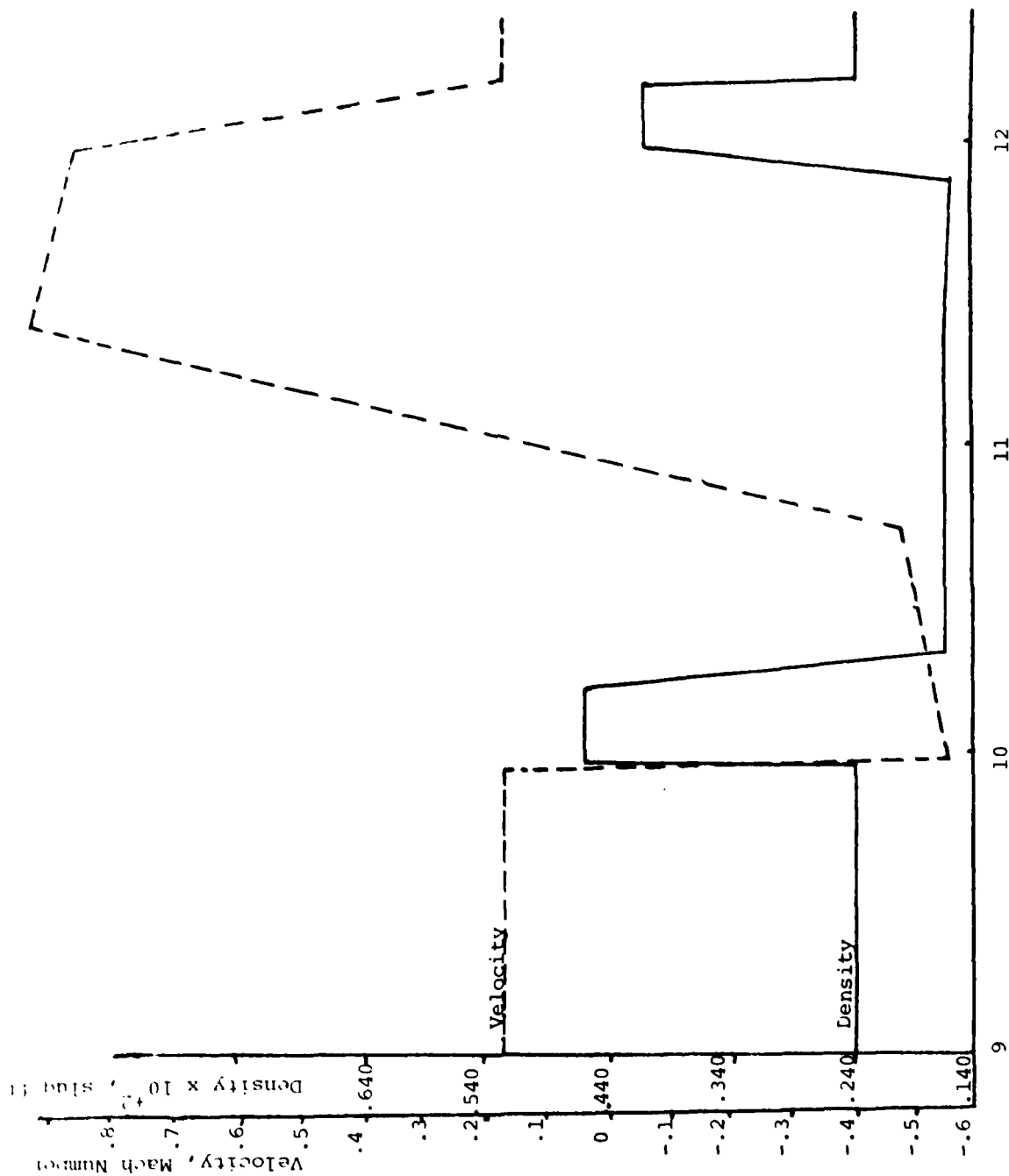
Figure C-6. Typical Distribution of Flow Conditions in Circulator for Time Frame .4
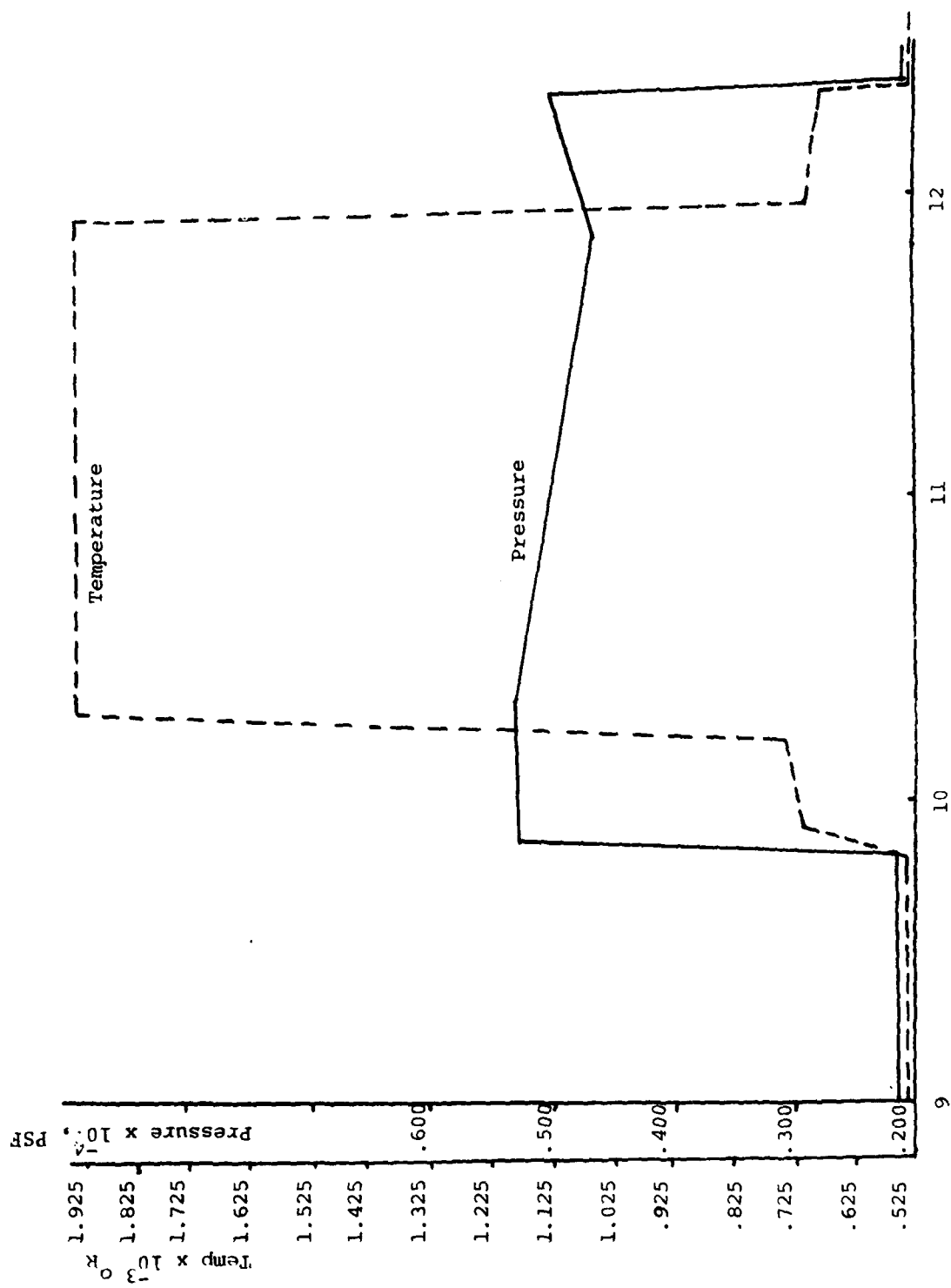
Figure C-7. Typical Distribution of Flow Conditions in Circulator for Time Frame .5

158
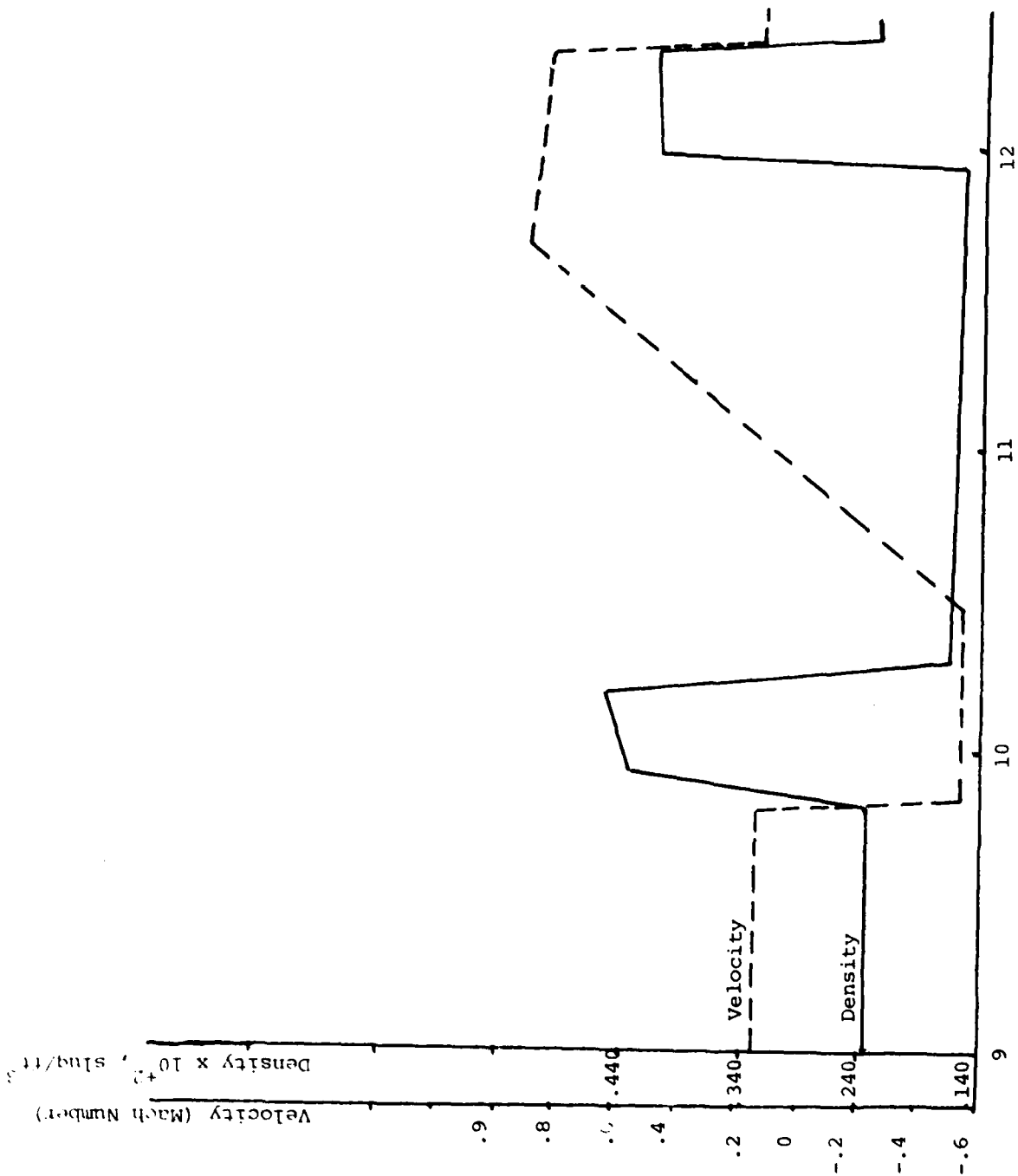
Figure C-8. Typical Distribution of Flow Conditions in Circulator for Time Frame .5
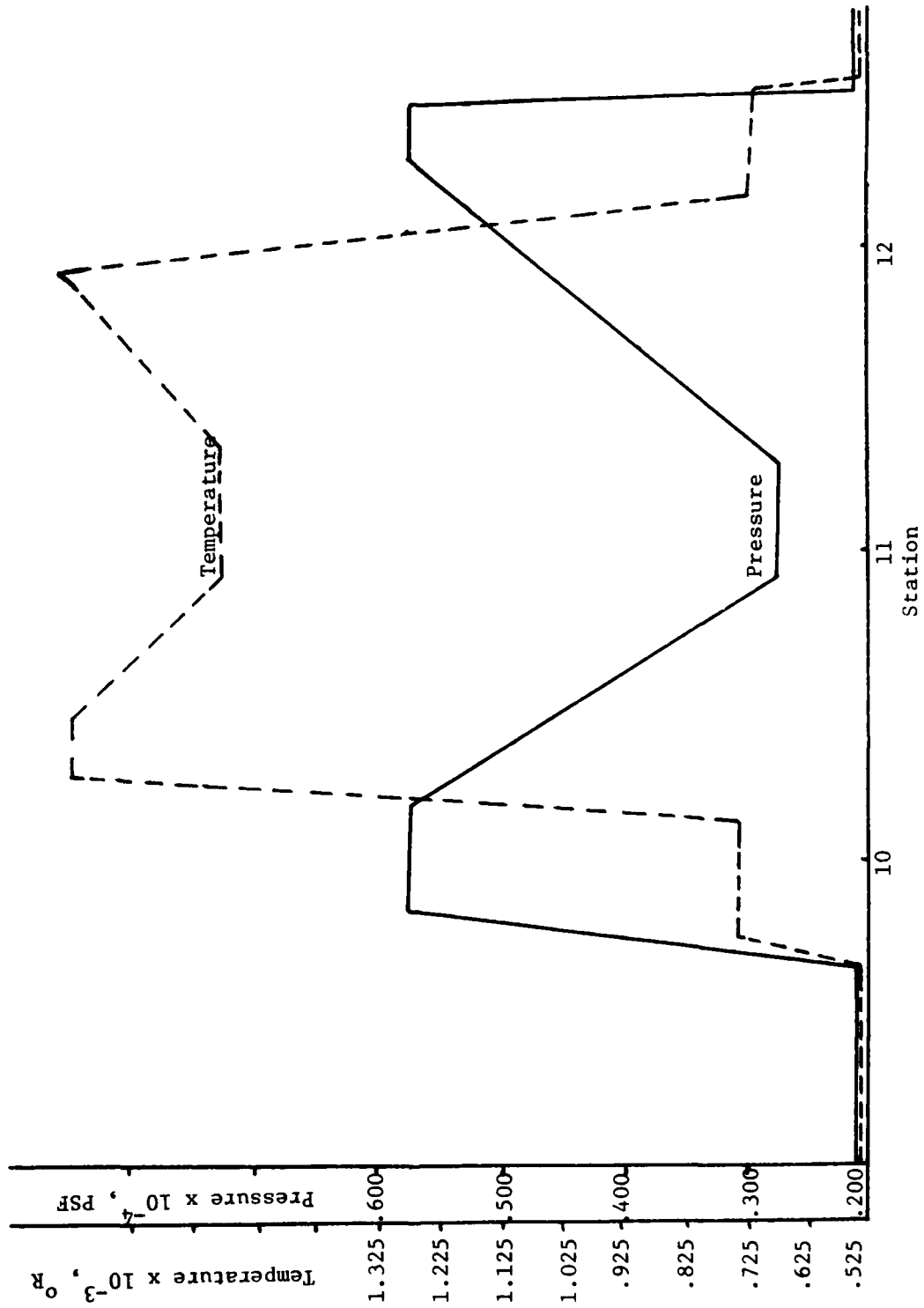
Figure C-9. Typical Distribution of Flow Conditions in Circulator for Time Frame .6

160
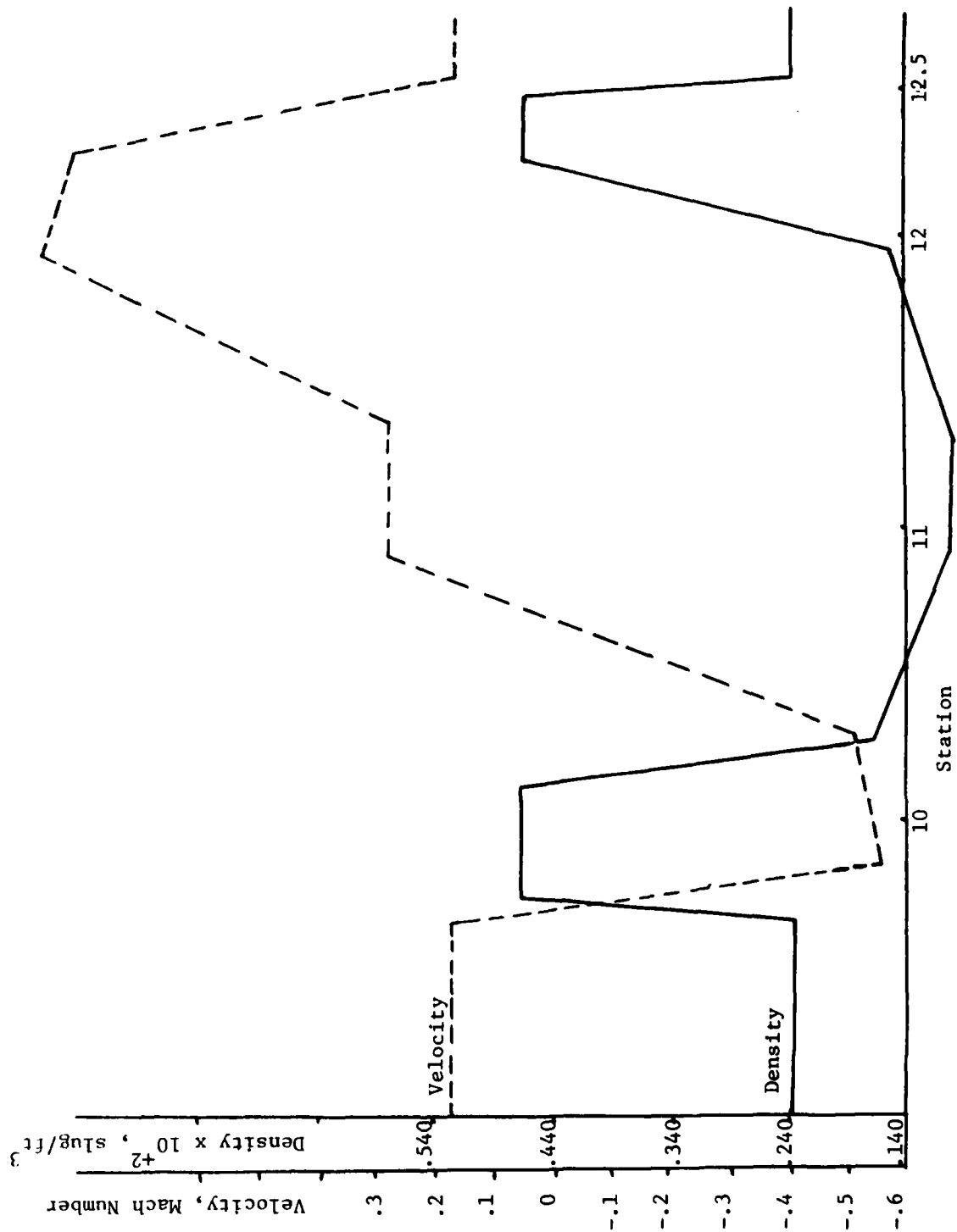
Figure C-10. Typical Distribution of Flow Conditions in Circulator for Time Frame .6

Pressure x 10^{-4}, PSF

Temp x 10^{-3} °R

Temperature

Pressure

9   10   11   12   12.8

.200 .300 .400 .500 .600

.525 .625 .725 .825 .925 1.025 1.125 1.225 1.325 1.425 1.525 1.625 1.725
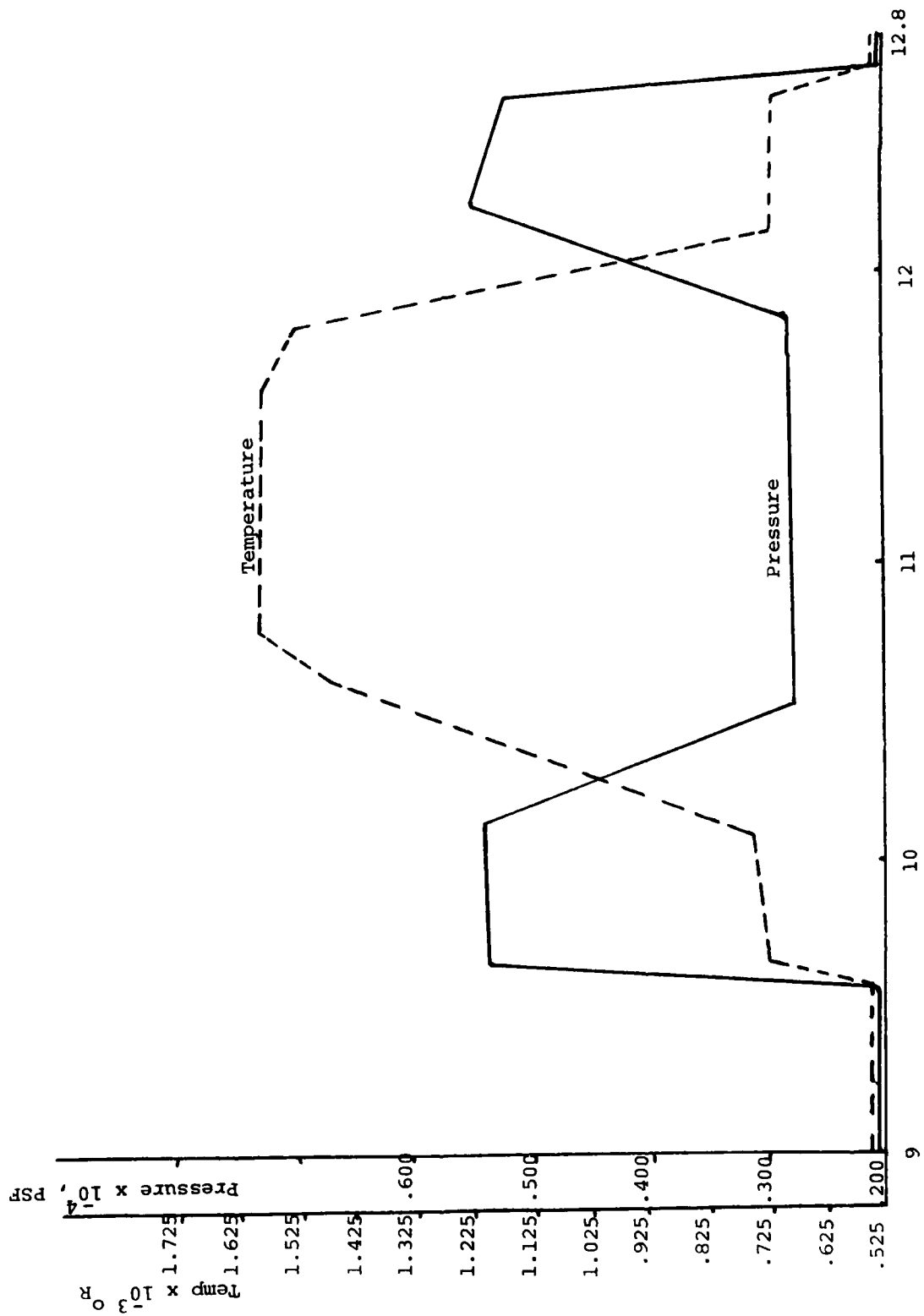
Figure C-11 Typical Distribution of Flow Conditions in Circulator for Time Frame .7

162
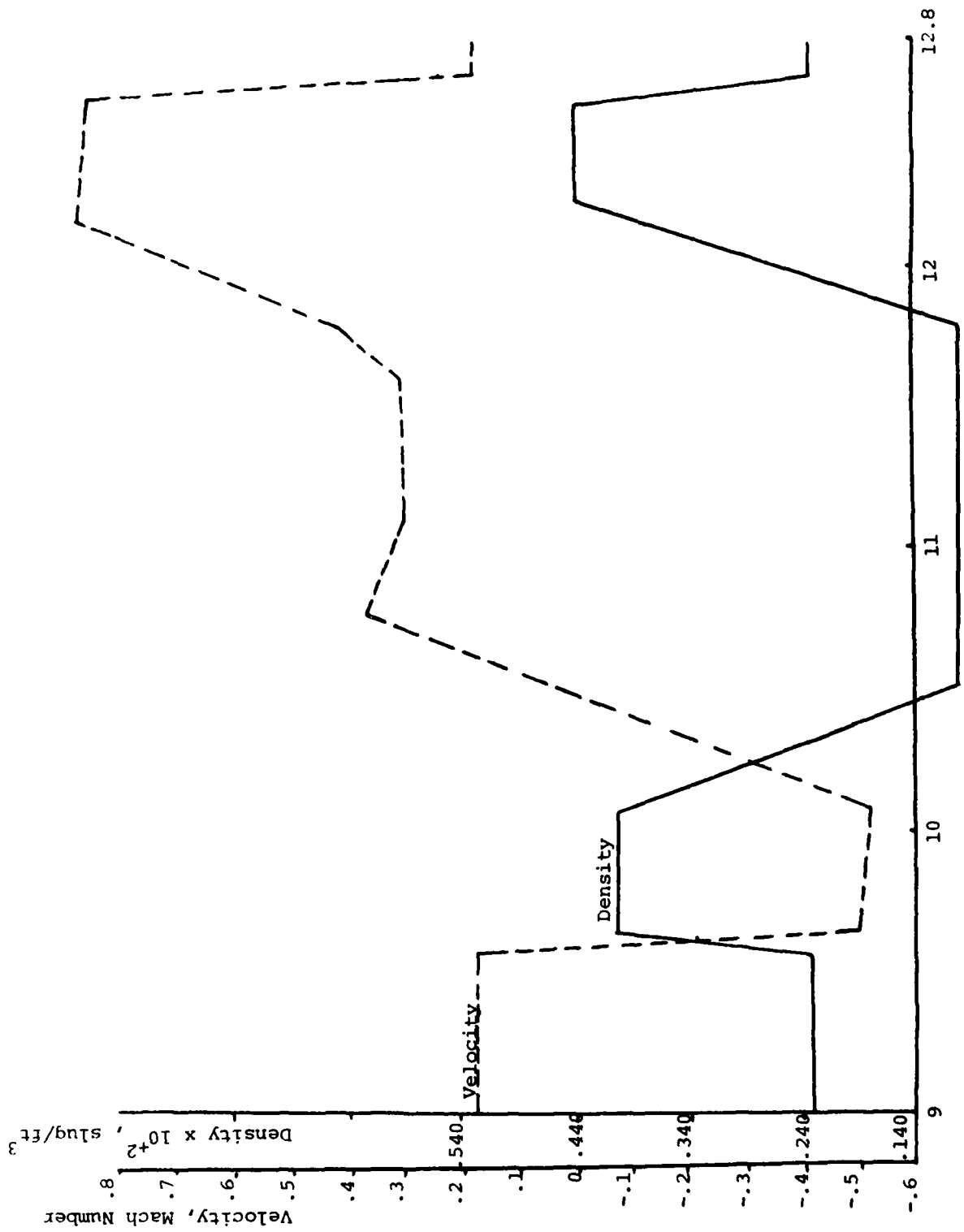
Figure C-12. Typical Distribution of Flow Conditions in Circulator for Time Frame .7
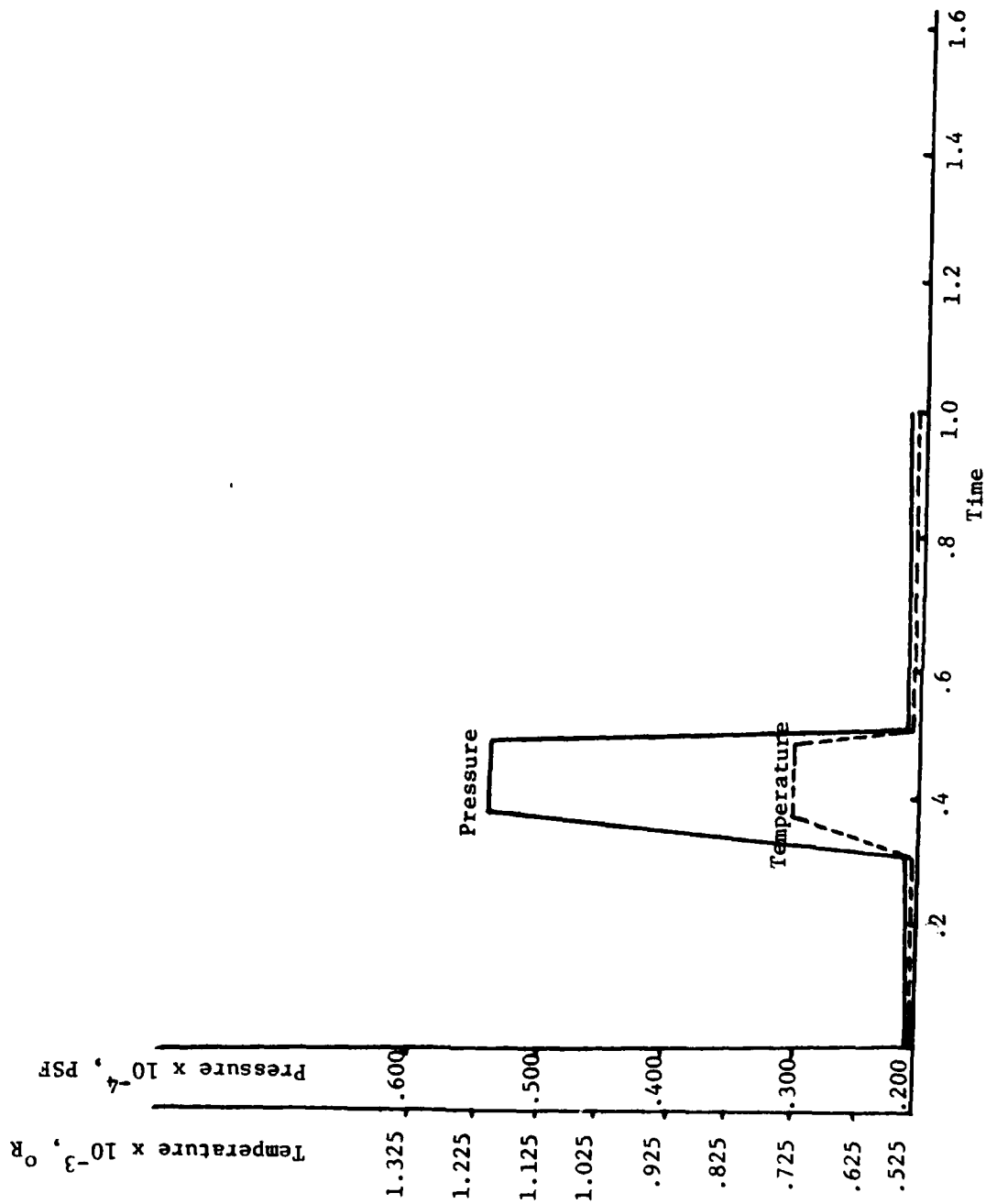
Figure C-13. Typical Distribution of Flow Conditions in Circulator for Station 10

164
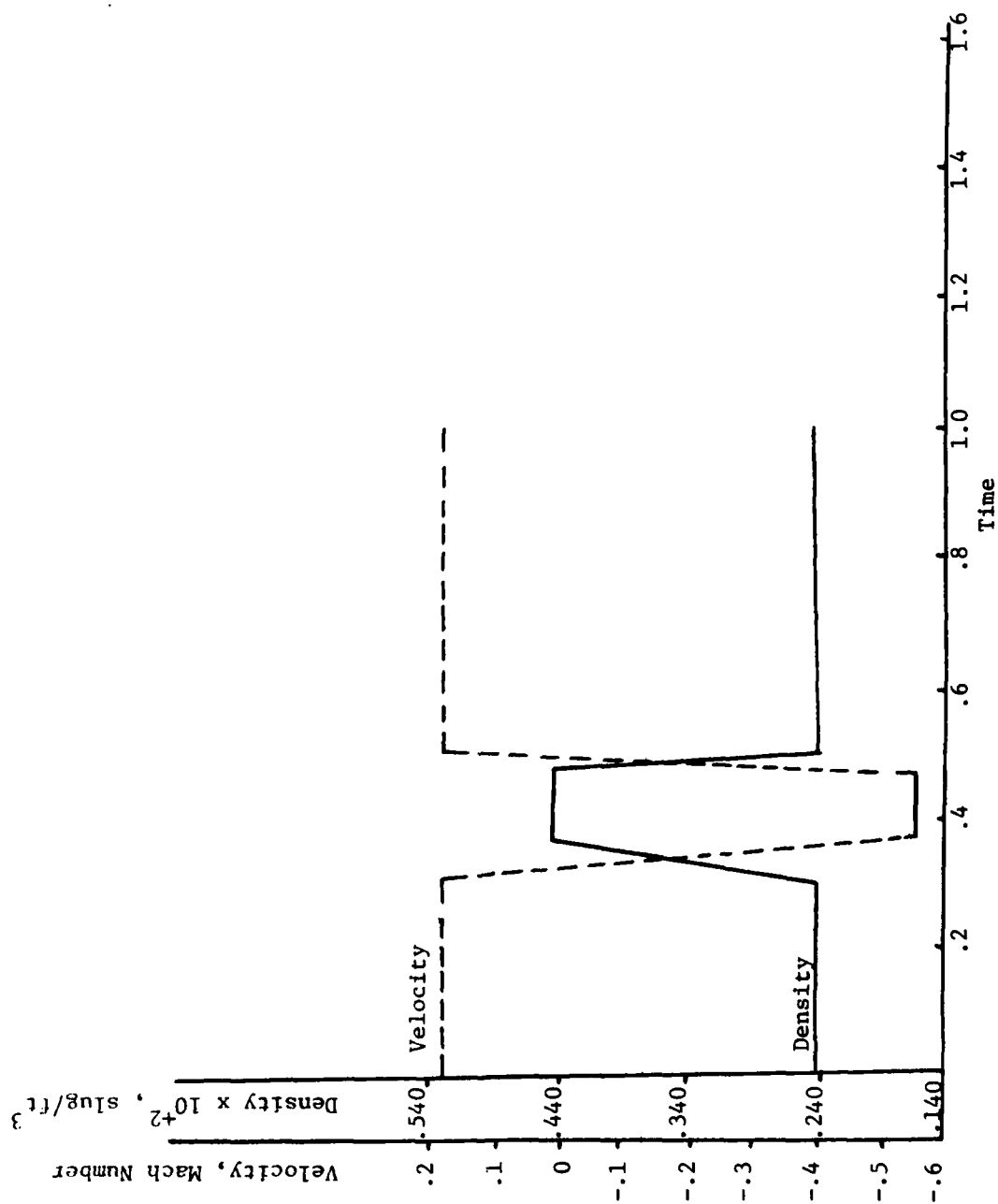
Figure C-14. Typical Distribution of Flow Conditions in Circulator for Station 10

165
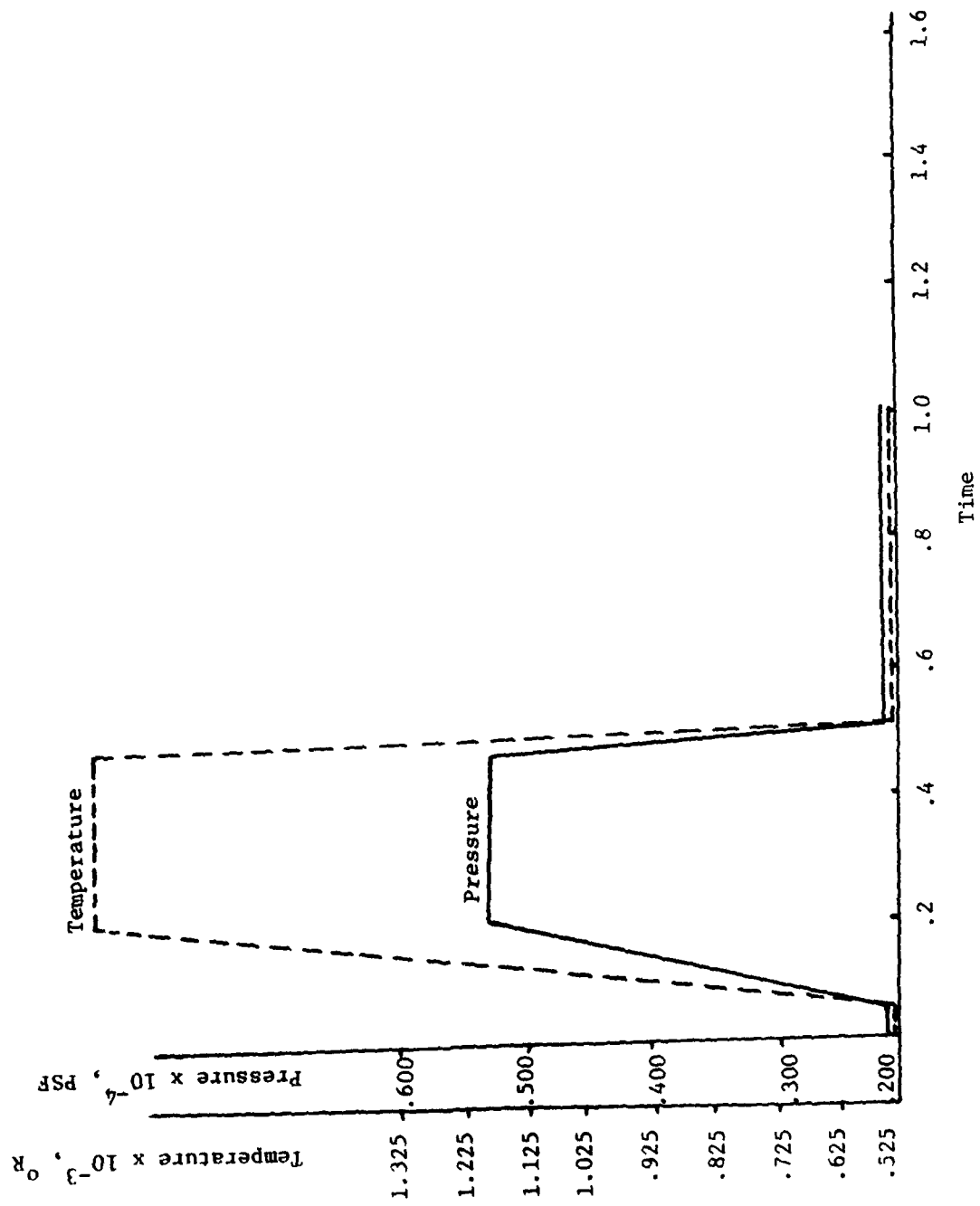
Figure C-15. Typical Distribution of Flow Conditions in Circulator for Station 10.5

166
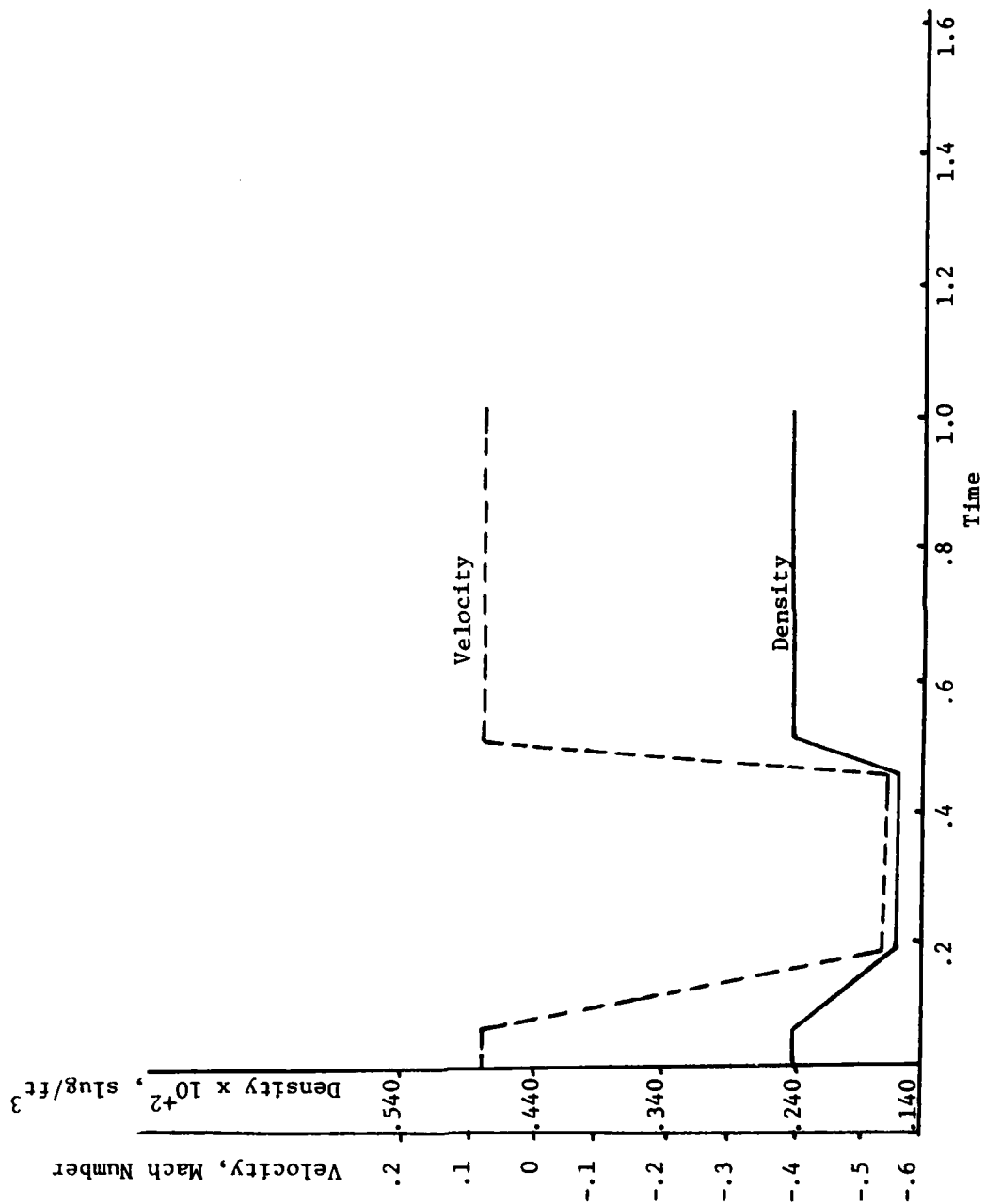
Figure C-16. Typical Distribution of Flow Conditions in Circulator for Station 10.5
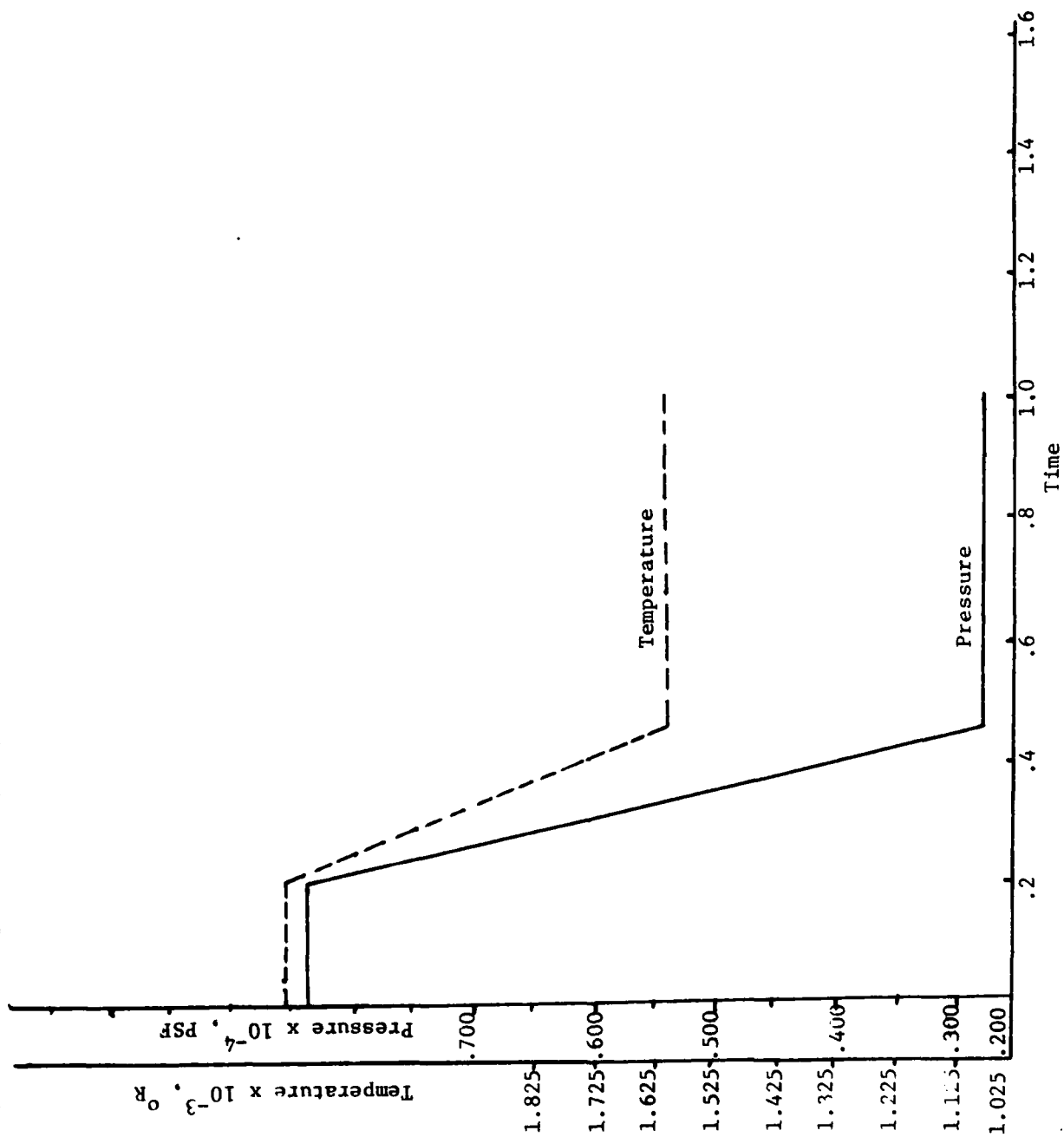
Figure C-17. Typical Distribution of Flow Conditions in Circulator for Station 11

168
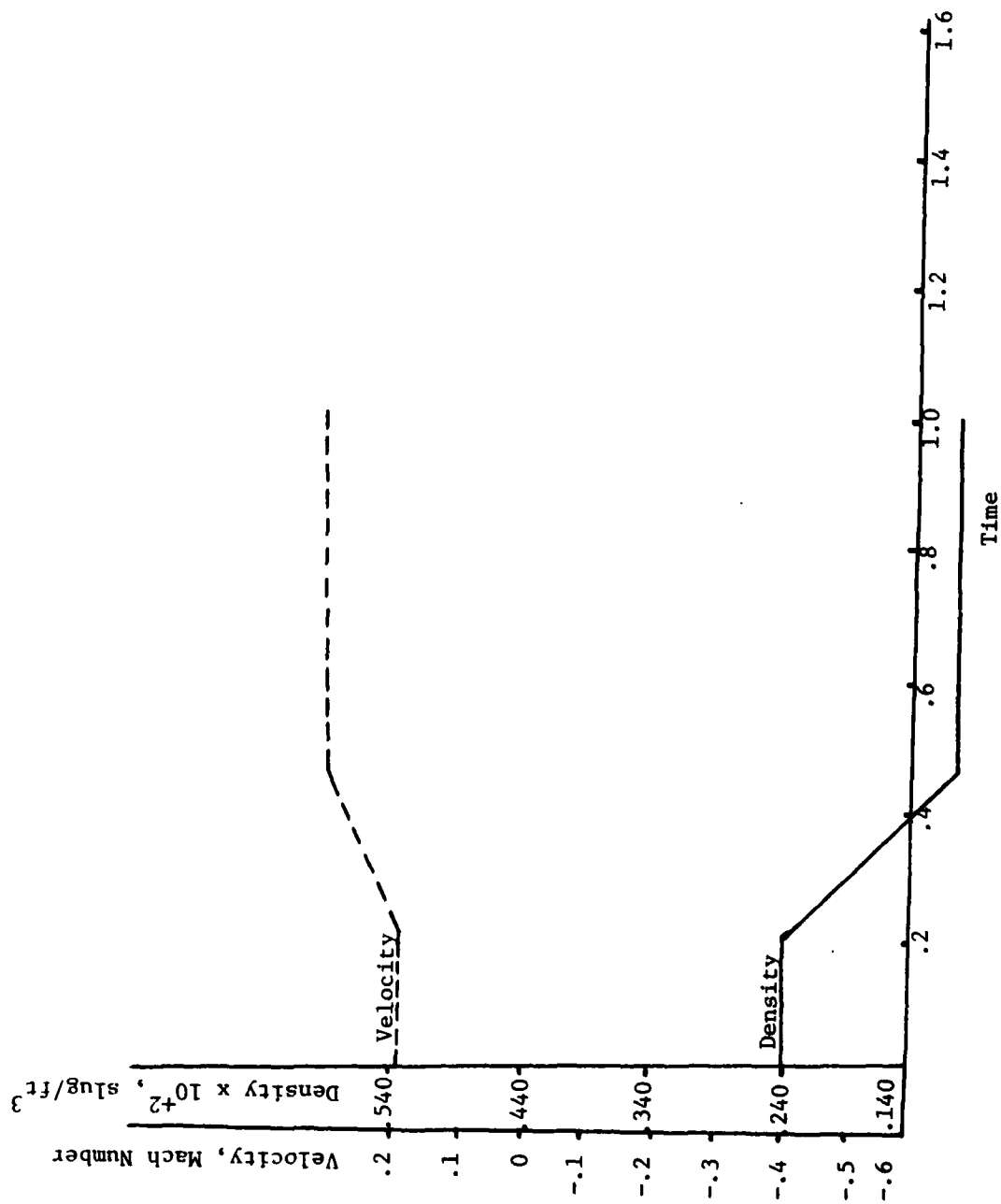
Figure C-18. Typical Distribution of Flow Conditions in Circulator for Station 11
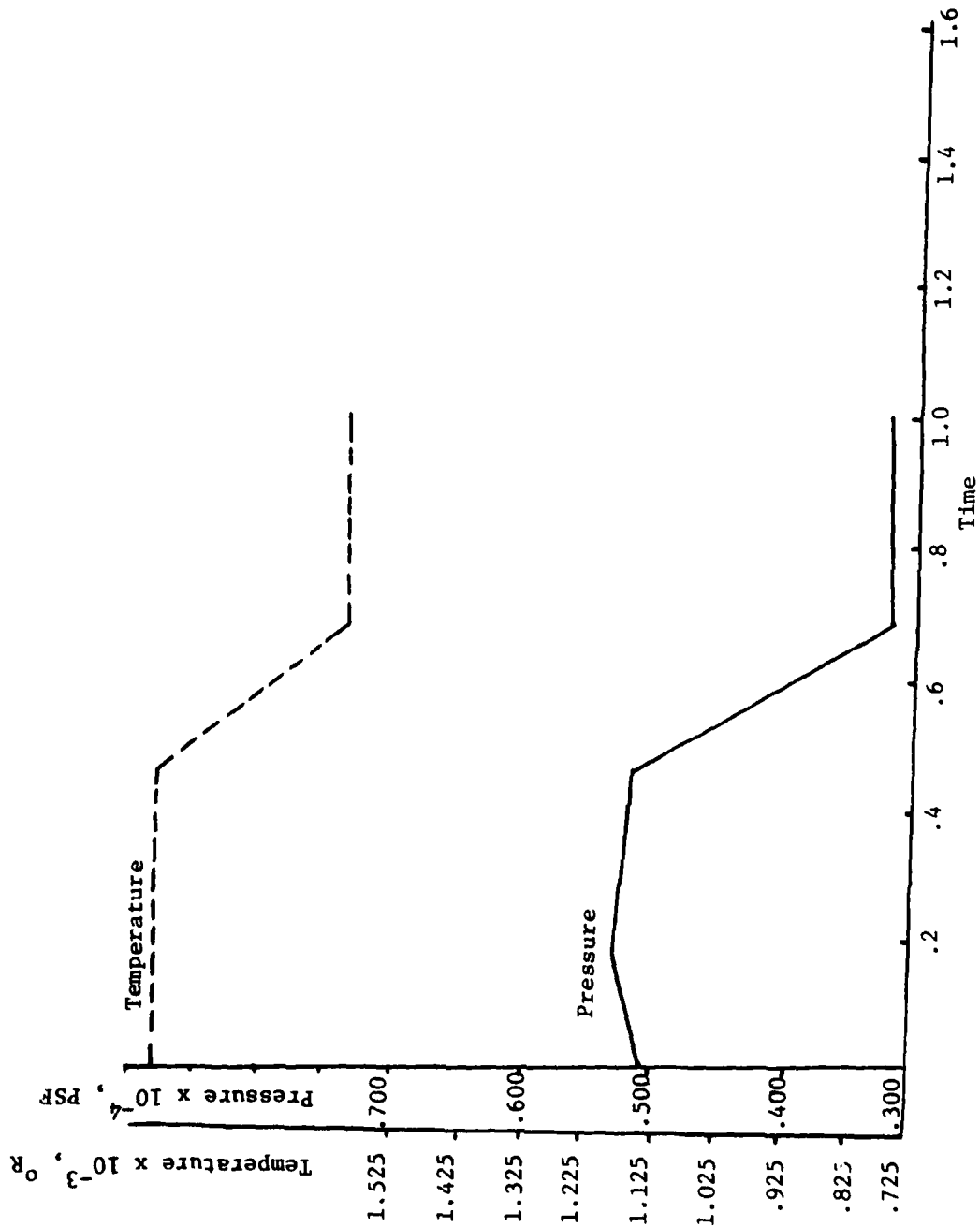
Figure C-19. Typical Distribution of Flow Conditions in Circulator for Station 11.5

170
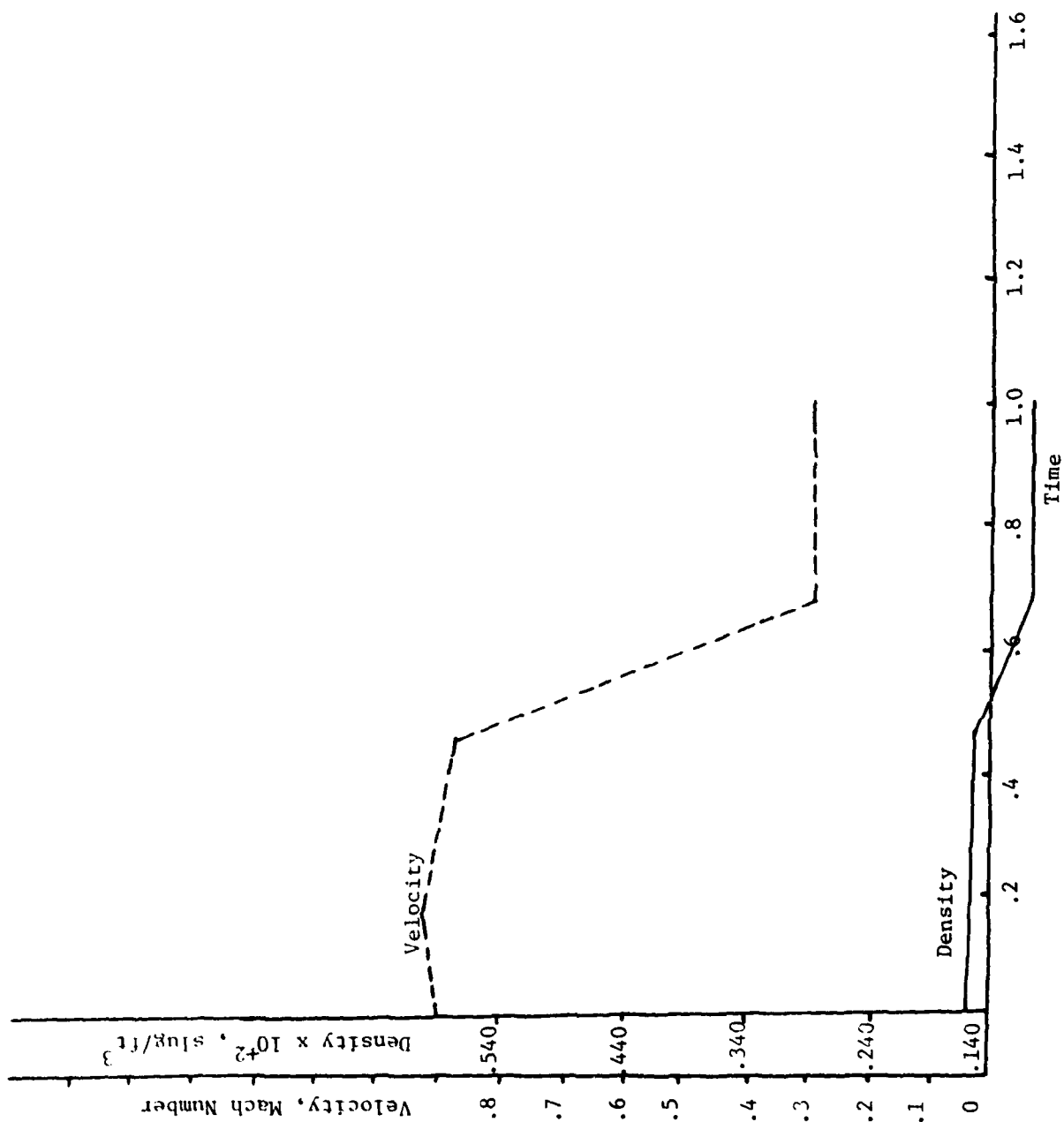
Figure C-20. Typical Distribution of Flow Conditions in Circulator for Station 11.5

171
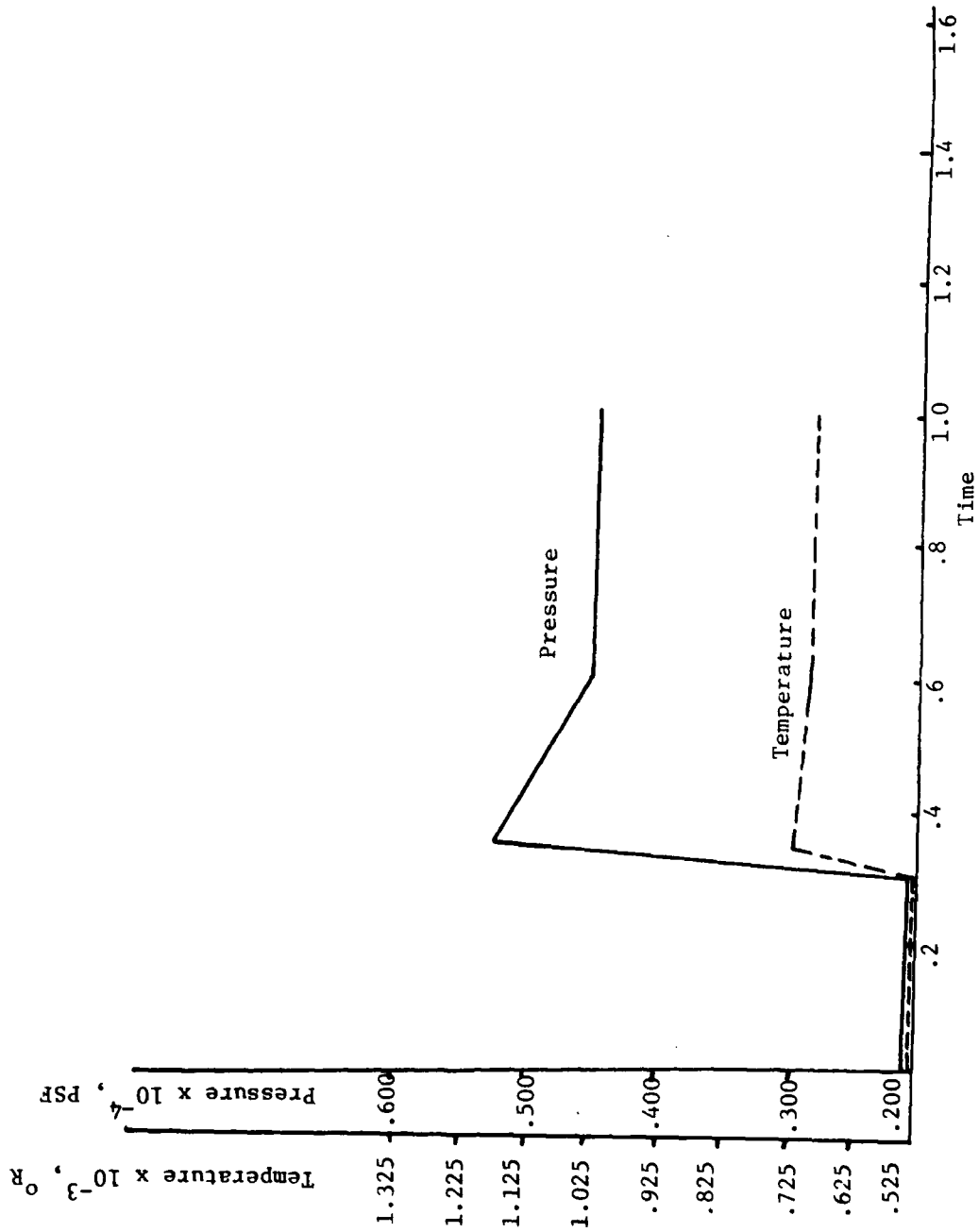
Figure C-21. Typical Distribution of Flow Conditions in Circulator for Station 12

172
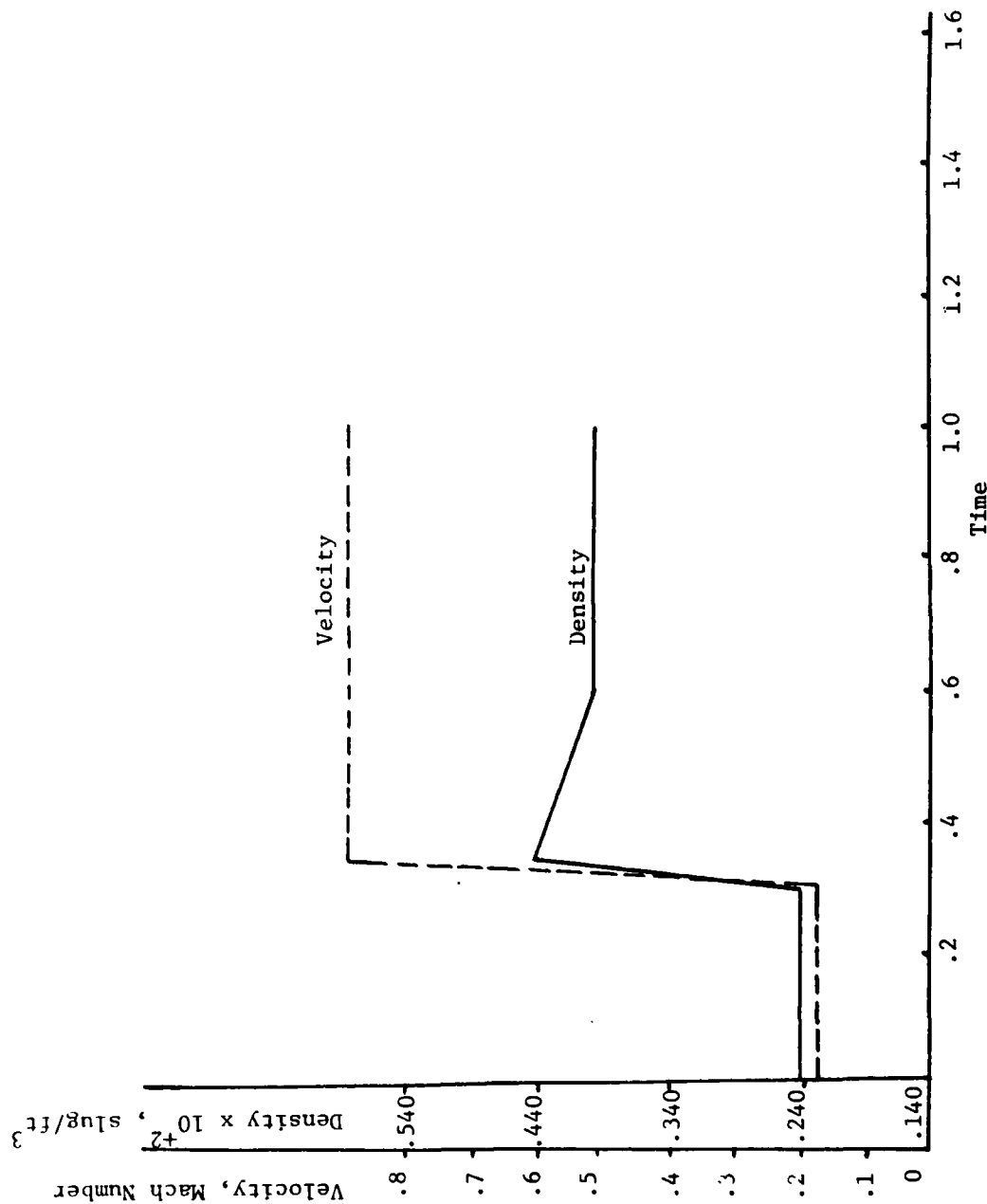
Figure C-22. Typical Distribution of Flow Conditions in Circulator for Station 12

173

D. Unsteady, One-Dimensional Flow Calculation

The equations of continuity, momentum, and energy for a compressible one-dimensional flow are

$$\frac{\partial \rho}{\partial t} + \rho \frac{\partial u}{\partial \chi} + u \frac{\partial \rho}{\partial \chi} + \rho \frac{u}{A} \frac{dA}{d\chi} = 0 \qquad (D-1)$$

$$\frac{\partial u}{\partial t} + u \frac{\partial u}{\partial \chi} + \frac{1}{\rho} \frac{\partial P}{\partial \chi} + \frac{4f}{D} \frac{u^2}{2} = 0 \qquad (D-2)$$

$$\frac{\partial P}{\partial t} - C^2 \frac{\partial \rho}{\partial t} + u \frac{\partial P}{\partial \chi} - C^2 \frac{\partial \rho}{\partial \chi} - (K-1) \; \rho \; (q + \frac{4f}{D} u^3) = 0 \qquad (D-3)$$

where the unknowns are the density (ρ), the velocity (u), and the pressure (P) which are functions of position (χ) and time (t). The flow is influenced by the friction coefficient for the flow (f), heat addition (q), the cross-section area (A), hydraulic diameter (D) and the physical properties of the gas represented by the speed of sound (C) and the ratio of specific heats (k).

To solve this set numerically, a finite difference method was chosen in which the spatial derivatives are replaced by centered difference formulas of the type

$$\left(\frac{\partial u}{\partial \chi} \right)_n = \frac{u_{n+1} - u_{n-1}}{\chi_{n+1} - \chi_{n-1}} \qquad (D-4)$$

where $(\partial u / \partial \chi)_n$ is approximation at point n to the derivative. The time derivative is taken to be a backward difference given by for example,

$$\left(\frac{\partial u}{\partial t} \right)_n = \frac{u_n(t) - u_n(t-\Delta t)}{\Delta t} \qquad (D-5)$$

The above methods were applied to the governing equations to produce

a set of 3n equations in 3n unknowns where n is the number of nodes in the system. The continuity, momentum, and energy equation at an arbitrary node is given by

$$R_1^n = \frac{1}{\Delta t}\,\rho_n(t) - \frac{1}{\Delta t}\,\rho_n(t-\Delta t) + u_n(t)\left[\frac{\rho_{n+1}(t) - \rho_{n-1}(t)}{\chi_{n+1} - \chi_{n-1}}\right]$$

$$+ \rho_n(t)\left[\frac{u_{n+1}(t) - u_{n-1}(t)}{\chi_{n+1} - \chi_{n-1}}\right] + \frac{\rho_n(t)\,u_n(t)}{A_n}\left[\frac{A_{n+1} - A_{n-1}}{\chi_{n+1} - \chi_{n-1}}\right] = 0$$

$$R_2^n = \frac{1}{\Delta t}\,u_n(t) - \frac{1}{\Delta t}\,u_n(t-\Delta t) + u_n(t)\left[\frac{u_{n+1}(t) - u_{n-1}(t)}{\chi_{n+1} - \chi_{n-1}}\right]$$

$$+ \frac{1}{\rho_n(t)}\left[\frac{P_{n+1}(t) - P_{n-1}(t)}{\chi_{n+1} - \chi_{n-1}}\right] + \frac{4f_n}{D_n}\,\frac{\left[u_n(t)\right]^2}{\left(\chi_{n+1} - \chi_{n-1}\right)} = 0 \qquad\text{(D-6)}$$

$$R_3^n = \frac{1}{\Delta t}\,P_n(t) - \frac{1}{\Delta t}\,P_n(t-\Delta t) + u_n(t)\left[\frac{P_{n+1}(t) - P_{n-1}(t)}{\chi_{n+1} - \chi_{n-1}}\right]$$

$$- \frac{C_n^2}{\Delta t}\left[\rho_n(t) - \rho_n(t-\Delta t)\right] - C_n^2\,u_n(t)\left[\frac{\rho_{n+1}(t) - \rho_{n-1}(t)}{\chi_{n+1} - \chi_{n-1}}\right]$$

$$-(k_n-1)\,\rho_n(t)\left\{q_n(t) + \frac{4f_n}{D_n}\,\frac{\left[u_n(t)\right]^3}{\left(\chi_{n+1} - \chi_{n-1}\right)}\right\} = 0 \qquad\text{(D-7)}$$

The equations are seen to be non-linear which requires that an iterative method be employed. A Newton Raphson method was selected in which each residual, R_i^n, is differentiated with respect to the 3n unknowns, giving the following set of equations, in general,

175

$$\frac{\partial R_i^n}{\partial \rho_1} \left(\delta\rho_1\right) + \frac{\partial R_i^n}{\partial u_1} \left(\delta u_1\right) + \frac{\partial R_i^n}{\partial P_1} \left(\delta P_1\right) + \cdots + \frac{\partial R_i^n}{\partial \rho_n}(\delta\rho_n)$$

$$+ \frac{\partial R_i^n}{\partial u_n} \left(\delta u_n\right) + \frac{\partial R_i^n}{\partial P_n} \left(\delta P_n\right) = - R_i^n \tag{D-8}$$

The values of the unknowns are corrected after each iteration by the solutions obtained for the above system of equations where

$$\rho_n^{(j)}(t) = \rho_n^{(j-1)}(t) + \left(\delta\rho_n\right)^{(j-1)} \tag{D-9}$$

$$u_n^{(j)}(t) = u_n^{(j-1)}(t) + \left(\delta u_n\right)^{(j-1)} \tag{D-10}$$

$$P_n^{(j)}(t) = P_n^{(j-1)}(t) + \left(\delta P_n\right)^{(j-1)} \tag{D-11}$$

where j represents the iteration cycle. The above method requires that the values of the unknowns be given for the previous time step at $t-\Delta t$.

To test the above numerical method, a 3 node circulator system was developed as shown in the Figure D-1. The areas were taken to be the same and no heat was introduced. An initial velocity of circulation of 1 m/sec was imposed. The solution, shown in Figure D-2, shows a decay of velocity as a function of time. All three nodes showed the same velocity history with no changes in density or pressure.

The numerical method described above appears to be stable and will be applied to more complex problems in the future.

176

$$\rho_1, u_1, P_1 \qquad \rho_2, u_2, P_2$$

$$A_1 = A_2 = A_3$$

$$g_1 = g_2 = g_3$$

$$\rho_3, u_3, P_3$$
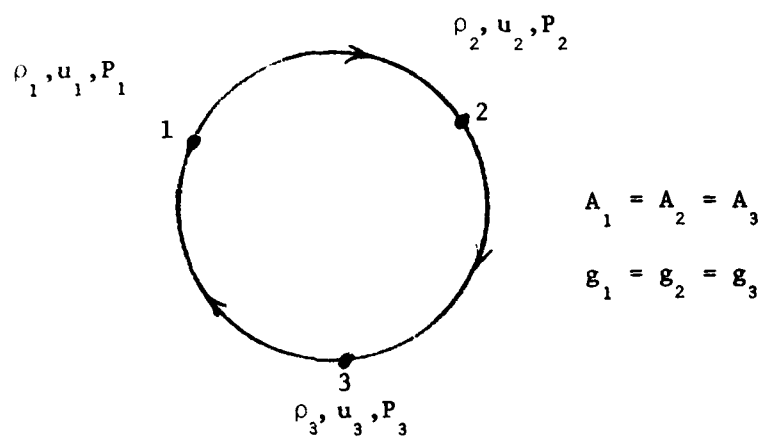
Figure D-1.   A THREE NODE CIRCULATION SYSTEM
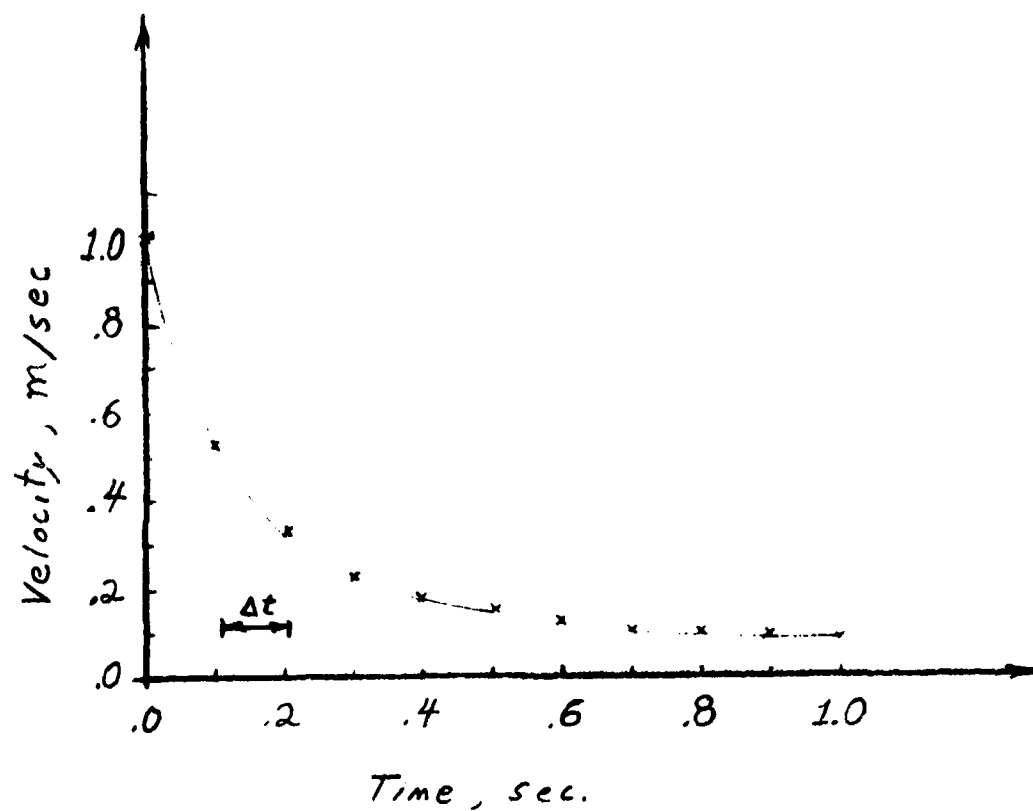
Figure D-2 VELOCITY HISTORY FOR SIMPLE CIRCULATOR HAVING INITIAL

VELOCITY, INSTANT FRICTION COEFFICIENT, CONSTANT AREAS

AND NO HEAT ADDITION

REFERENCES

1. Cason, C. et al., "A Small Scale Closed Cycle Circulator Experimental Plan for Repetitively Pulsed 200°K High Pressure Electric Discharge Lasers" Technical Report RH-76-12 US Army Missile Command, August 1976.

2. Rocketdyne Division of Rockwell International Corporation, "Operating Manual of Closed Cycle Gas Recirculator".

3. Merzkirch, Wolfgang, "Flow Visualization," Academic Press, New York, 1974.

4. Born and Wolf, "Principle of Optics," Pergamon Press, Oxford, 1970, p. 459-464.

5. Riley, George, F., "Analysis of Laser Wave-Front Deformation by Aerodynamic Window" Naval Plant Report Office, East Hartford, Connecticut, November, 1975.

6. Saunders, J.B., "A Simple Interferometric Method for Workshop Testing of Optics," Applied Optics 9, p 1623, 1970.

SECTION 2

SHORT WAVELENGTH RESONATOR ANALYSIS

VII. Iterative Ray-tracing Computer Code IRAYT

Introduction and Summary

A general discussion of the iterative ray-tracing code IRAYT, a presentation of some of the details of the approach, and results of numerical studies and corresponding closed-form analyses of certain aspects of unstable resonators as they apply to excimer lasers will be given in the following pages. A parallel, but briefer, presentation of this material is given in another section in the form of "telegraphic" summary statements.

The need for an iterative ray-tracing code, which grew out of the quite different range of values of Fresnel numbers of typical excimer lasers as compared to other gas lasers, is first given. A discussion is then given of the desired basic features of such a code, which guided the development of various portions of the computer program. A number of features are presumably unique, since previous ray-tracing programs have been non-iterative and concerned with imaging problems. In particular, suitable interpolation schemes and other details are necessary in order to carry out iterations, and techniques were required for evaluating the magnitude of various aberrations and other quantities for successive iterations. The latter evaluations permit one to compare numerical ray-tracing predictions of various properties, such as wave-front curvature, on successive round-trips through the resonator with results of closed-form analyses which are worked out herein for some cases.

In most of the discussions, it is tacitly assumed that we are concerned with positive-branch unstable resonators. Presumably the methodology and several of the closed-form analyses also apply to negative-branch resonators, however.

A moderately detailed presentation is given of the method which was adopted for tracing individual rays. This material is germane to material presented later regarding optical aberrations in excimer lasers and their connection with the conic parameter κ which appears in the surface function used in the ray-tracing scheme.

One of the features of the code is the possibility of starting a wave which is tilted with respect to the optic axis and can have wavefront curvature, then following the radiation through successive round-trips and obtaining successive numerical values (by least-squares-fitting) of the tilts and curvatures of the wave. The proper functioning of the computer program in such respects can be tested by comparison with predictions of closed-form analyses. A closed-form analysis is given of the effects of tilt of the resonator mirrors on the tilt of the wave after one or more round-trips, and it is noted that numerical tests with IRAYT were in good agreement with the analysis. By including an infinite number of round-trips in the closed-form analysis one can predict the effect of tilt of each of the mirrors on the tilt of the converged output of a resonator, that is to say on the resulting rotation of the optic axis. The equations so derived are found to agree with those predicted in a quite different manner by other workers.

In a somewhat similar vein, a closed-form analysis is given of the effect of perturbing the spacing of the mirrors from their confocal

position. With the assumption of a collimated starting beam, a first-order derivation is given of the effect of a small perturbation of the mirror spacing on the radius of curvature of the output beam after one or more round-trips. Calculations were made with IRAYT, with results which agree quite well with the closed-form predictions. If the analysis is extended to an infinite number of round-trips, one obtains an equation for the predicted radius of curvature of the converged output beam from the resonator. The equation agrees with that given earlier by Anan'ev.

A good deal of attention has been paid to the spherical aberration of the output wave which will result if spherical mirrors are used in configurations with beam apertures which are relatively large compared to mirror spacing, since such configurations may be desirable in excimer lasers. The spherical aberration associated with one mirror, for example the primary mirror of a resonator, is of course well-known, but is re-derived for completeness. It happens that the spherical aberration produced by the secondary mirror of a positive-branch confocal unstable resonator, as considered here, tends to partially cancel the aberration produced by the primary mirror. Equations are derived giving the magnitude of the net spherical aberration, for a single round-trip, as a function of the magnification and primary mirror curvature and, separately, as a function of the magnification and the mirror spacing. Several IRAYT calculations confirmed the analysis. By summing the effects of an infinite number of round-trips through the resonator, we obtain values of the multi-pass spherical aberration.

182

The simplest single measure of the deleterious effects of departure of the output wave of a resonator from the desired uniphase behavior is the root-mean-square value of the phase deviations over the output plane or, equivalently, the root-mean-square value of the optical path difference. The value of this parameter, the RMSOPD, resulting from spherical aberration is worked out, and comparisons are given of closed-form predictions and numerical results of IRAYT. The agreement is only fair for relatively small numbers of mesh points, but becomes satisfactory for larger numbers of mesh points.

The spherical aberration inherent in a confocal resonator with spherical mirrors can of course be removed by modifying the figuring of one of the mirrors. We have considered the case of adding a correction of fourth order, i.e., of the form $\alpha_2 (X^2 + Y^2)^2$ to the surface function of the secondary mirror. This is readily done in the IRAYT code by simply reading in a suitable value for the appropriate aspheric coefficient. A numerical case was worked out in closed form, and the same case was run with the IRAYT program, with results that agreed quite satisfactorily.

Elimination of spherical aberration can of course be accomplished by use of parabaloidal mirrors, though this may entail complexity of fabrication. We have considered the possibility of eliminating the fourth-order aberration by choosing suitable values of the conic coefficient κ of each of the mirrors. From the derivation it follows that it is only necessary to choose the conic coefficients of the two mirrors such that their ratio equals the magnification M. A pair of parabaloids ($\kappa = 0$ for each) is then one special case. There are also

183

special cases for which one of the mirrors is spherical, i.e., has a κ value of unity, while the value of κ for the other mirror is M or 1/M.

Having determined the above criterion for a combination of a spherical and an ellipsoidal mirror, one needs the relationship between the conic parameter κ and the ellipticity e. This is worked out and found to have a rather simple form.

Some numerical investigations of fourth-order aberrations are discussed. These included the case of a fully decentered alignment, for which the RMSOPD was much worse than for centered alignment, as expected.

Having determined that spherical aberration may be quite pronounced for certain designs utilizing spherical mirrors and that such aberrations can be eliminated by various non-spherical-mirror arrangements, we consider possible residual aberrations resulting from departure of the actual resonator from ideality. Such departures include increments in mirror spacing as compared to the idealized confocal value, as well as mirror tilts. A brief discussion of this problem of sensitivity to misadjustments is given, including numerical examples. The conclusion drawn here is that fairly extensive studies of misadjustment sensitivities should be made for major candidates for excimer resonators. The numerical calculations with IRAYT should be relatively straightforward.

184

Need for an Iterative Ray-Tracing Code

Since the advent of large-scale computers, it has been recognized that numerical ray-tracing is an efficient method for assessing optical quality of imaging optical systems. Large-scale computer codes have been prepared for this purpose. An example is the POLYPAGOS[1] code prepared at the Aerospace Corporation. So far as is known, all such codes have been of non-iterative (i.e., single-pass) type, since the properties of interest have all been those of conventional imaging optical systems, not those of optical resonators. The geometric-optics approximation which is necessarily involved in such codes is generally well satisfied for imaging systems, for which the Fresnel number is large.

Laser resonators are, in general, quite different from imaging systems. In particular: (1) by their very nature, resonators involve feedback of a part of the radiation and hence any numerical calculation must involve a criterion of self-consistency, usually achieved by iterative calculations, and (2) for most lasers which have existed until recently the combination of at least moderately small transverse dimensions and moderately long wavelength was such that Fresnel numbers were fairly small and hence wave-optics calculations were required. Consequently the computational modelling of transverse modes in laser resonators has until recently involved iterative calculations of wave-optics type, with iteration continued until a condition of self- consistency has been achieved to within a reasonable tolerance. The wave-optics calculations of propagation have been carried out by a variety of approaches, including in particular (1) direct numerical evaluation of Fresnel integrals which describe the propagation, (2) finite-

185

difference solutions of the reduced Maxwell's equations, and (3)
treatment of propagation by Fourier transforms, using the efficient
FFT computer algorithm. Regardless of the particular method used, all
such calculations necessarily involve use of a transverse grid with
spacing of mesh points small enough to represent reasonably well the
ripples in the transverse distribution of the optical amplitude and
phase. This requirement translates into a requirement that the number
of mesh points in each of the two transverse dimensions be at least
comparable in magnitude to a suitable Fresnel number of the system.
For a typical CO_2 resonator we might consider a beam half-width of
$a = 5$ cm. a mirror spacing of $L = 300$ cm, and a wavelength of about
10^{-3} cm, corresponding to a tube Fresnel number of 83.3. For a full
two-transverse-dimension calculation, this imposes fairly stringent
requirements, but they can be met moderately well using a 128 x 128
or 256 x 256 transverse grid. Of course, for a one-transverse-
dimension approximation, it is easy to use 512 or more mesh points,
and hence to very readily predict detailed diffractive structure of an
empty-cavity mode of such a resonator.

It appears that for the desired types of high-energy excimer lasers,
the resonator will have transverse dimensions which are fairly large,
having perhaps a full width of 50 cm, while of course the wavelength
is fairly short. We will consider the wavelength $\lambda = 0.351 \times 10^{-4}$ cm.
If we take $a = 25$ cm, $L = 300$ cm, we obtain a tube Fresnel number of
0.6×10^5 . It is clear that the optical behavior of such resonators
with Fresnel number of the order of 10^5 will be quite different from
that of resonators with Fresnel number of the order of 10^2. Clearly it
will be entirely impracticable to do wave-optics calculations with mesh

186

points numbering 10^5 in each transverse dimension, and hence some other approach is necessary. At the same time it appears that diffractive effects are likely to be much less important than for the former class of resonators, and hence a geometric-optics approximation is likely to be suitable. Of course, a geometric-optics treatment will be adequate for handling various perturbations of the wave front only if such perturbations have a spatial size such that the associated Fresnel number is greater than about unity; that seems likely to be the case for most perturbations.

We have just argued that for typical excimer resonators, wave-optics calculations are not necessary, but geometric-optics treatments may be quite adequate. But of course it is still necessary to satisfy the self-consistent requirement which is the essence of a resonator, and the obvious way to achieve this is by iterating the calculations. This line of reasoning shows the need for an iterative ray-tracing computer code, a need which we have attemped to meet with the IRAYT code to be described below.

Desired Basic Features of Iterative Ray-Tracing Code

The intended function of the computer code is, of course, to determine an optical field which is self-replicating to within a multiplicative constant on each round-trip through a resonator, much as for a wave-optics resonator code. Of primary interest are unstable resonators arranged to produce an essentially collimated output. The most common cases of interest are simple two-mirror standing-wave designs in a confocal arrangement, but it is desired that the code be sufficiently flexible to handle a variety of possible designs which could include, for example, ring resonators. The self-consistency (self-replicating) property is expected to be obtainable by starting through the system a wave which has, to a fair degree of approximation, the general features of the final self-consistent wave, then calculating its passage through the optical system, and iterating the calculation until self-consistency is achieved. It will be convenient to start the wave in the portion of the system where a quasi-collimated beam is expected, though this is not essential. It can be shown that if the starting wave has a small tilt relative to the optic axis, the tilt will be reduced with successive passes through the system. Similarly, if the launched wave has a curvature (whether zero or otherwise) that differs from that for a self-consistent solution, the curvature will be modified on successive passes so as to converge to the self-consistent value.

The present approach of course employs the geometric-optics approximation. It is assumed that a surface of constant optical phase is orthogonal to the set of rays, the behavior of which is calculated

188

from geometric optics. That is to say, the rays are assumed to propagate along straight paths in a vacuum and to obey simple rules of reflection at a mirror surface. Attention is here being limited to reflective elements only because of the intended applications. Extension of the code to include refractive elements would be quite straightforward.

The desired output of a resonator is, of course, a wave with simple properties such that it can be propagated over great distances and focused so that most of the energy falls onto an area whose minimum extent is determined by wave optics, i.e., the central bright zone of a Fraunhofer pattern. Deviations of the output wave from ideality of course reduce the amount of energy falling within the central far-field region. One convenient measure of the optical quality is the ratio I/I_0 of the actual intensity I in the center of the far field, with the results of deviations from ideality taken into account, to the central intensity I_0 which would be achievable with an ideal beam. An ideal output beam of course has uniform intensity over the unobscured output area, and has constant phase over a plane or a surface with slight curvature. In general, departures from uniform intensity are not as deleterious as departures from uniformity of phase, hence we will limit attention to the latter. For relatively small departure from the desired uniphase property, the reduction in central far-field brightness varies in a simple (namely exponential) manner with the root-mean-square (r.m.s.) departure of phase from ideality. We let $\Delta \phi_{rms}$ denote the root-mean-square value of the incremental phase, in radians, of the optical field. It can be shown that

$$\frac{I}{I_0} \simeq \exp (- \Delta \phi_{rms}^2) \simeq 1 - \Delta \phi_{rms}^2 .$$

In the present, geometric-optics, approach the incremental phase $\Delta \phi$

189

is simply calculated as a ratio of an incremental value ΔZ of the
total length of a ray and the optical wavelength, i.e.

$$\Delta \phi = 2 \pi \frac{\Delta Z}{\lambda} .$$

One of the principal results of the code is a table of the values of
the optical path differences (OPD's) ΔZ associated with the various rays
which are traced through the system. This table can be printed out
numerically, of course. A more convenient form of output of this array
consists of a simulated interferogram generated by printing alphabetic
characters or blanks. In addition, the root-mean-square value of ΔZ
over the entire array is calculated on each iteration and printed. Also,
the corresponding value of I/I_0 defined by the exponential equation above
is printed.

Other measures of output optical quality, in addition to the table
of values of ΔZ, etc. mentioned above, include the results of a least-
squares fit to the two-dimensional table of ΔZ by a set of functions
representing some of the primary aberrations, e.g., tilt along each of
two axes, sphere, cylinder. As an optional feature, it is possible to
evaluate the r.m.s. value of ΔZ after subtraction of the effects of a
specified number of the aberration functions from the least-squares fit.

In order to perform iterative calculations, it is necessary after
each round-trip through the system to interpolate along the transverse
coordinates x and y to find starting values for the next iteration of
several parameters associated with each starting ray. The parameters
include the direction cosines of the ray and the cumulative value of the
optical path difference. The interpolation is carried out by a third-
order Bessel interpolation scheme along each of the two transverse
coordinates.

Method for Tracing Individual Rays

At any given stage of a ray-tracing procedure one has available the position of the last point of intersection with a mirror surface and the direction cosines of the ray after that reflection. One then proceeds to find the point of intersection with the next optical surface and, following that, the direction cosines of the ray after reflection. In general, the equations and numerical procedures are considerably simplified (at least for reflecting surfaces which are surfaces of revolution) if the calculations can be performed in the natural coordinate system of the mirror considered, such that the z-axis is along the axis of symmetry of the mirror. But naturally the various mirrors may in general be oriented with respect to one another in various ways. It thus becomes necessary to perform coordinate transformations (translations and rotations) in proceeding from one mirror surface to the next. There is some latitude in the choice of a method of specifying the position and orientation of the various mirrors. We have elected to specify by input data the position and orientation of each mirror relative to a fixed, "absolute" (or laboratory) reference system. While this may seem an obvious choice, it is notable that the POLYPAGOS[1] code is based on specifying the position and orientation of each mirror relative to the coordinate system of the last previous mirror. The coordinate translations are, of course, trivial. The rotations are relatively straightforward but do require caution in reversing the order of rotation in performing an inverse rotation of angles. In preparing to calculate the point of intersection with a mirror, one first performs the "direct" transformation (subroutine TFDATR) which involves rotation first about the y-axis through an angle θ_y, then performs a rotation about

the new x-azis through an angle Θ_x. After finding the point of inter-section and direction cosines of reflected ray in the coordinate system of the mirror, an "inverse" transformation (subroutine TFIRTA) is per-formed which involves rotation first about the x-azis through an angle $(-\Theta_x)$. For many applications, of course, one or both of the rotation angles are zero; to save computer time, tests are made such that no rotational transformation is made at all when the corresponding rotation angle is zero.

Coordinates of the point of intersection of a ray with a mirror, and direction cosines of the reflected ray, are calculated in the natural coordinate system of the mirror, using a subroutine INTREF (mnemonic intended to represent "intersection and reflection"). The equations and methods are very similar to those proposed by Spencer and Murty.[2] For convenience we have used notation which is almost identical to theirs, although some of the variable names in the computer program correspond to other terminology. The surface of the mirror can be represented by

$$F(X,Y,Z) = Z - \frac{c\rho^2}{1 + (1 - \kappa c^2 \rho^2)^{\frac{1}{2}}} - \sum_{i=1}^{N} \alpha_i \rho^{2i} = 0. \quad \text{(VII-1)}$$

Here we have

$$\rho^2 = (X^2 + Y^2).$$

The coefficients α_i permit representation of surfaces more general than rotated conic sections. (In the code, they are named CASPH as a mnemonic for "aspheric coefficients"). In most of the discussion to follow it will be assumed, for simplicity of terminology, that the α_i are all zero. The equation then represents revolved conic sections. The vertex curvature is c, and the conic parameter κ determines the type of conic section, in accordance with the table below.

192

Types of Surfaces Associated with Various Values of κ

Range or value of κ	Type of Surface
κ < 0	Hyperboloid
κ = 0	Paraboloid
0 < κ < 1	Hemelipsoid of revolution about major axis
κ = 1	Hemisphere
κ > 1	Hemelipsoid of revolution about minor axis

The partial derivatives of the surface function are needed. They can be written as

$$F_x = \frac{\partial F}{\partial x} = - X E,$$

$$F_y = \frac{\partial F}{\partial y} = - Y E,$$

$$F_z = \frac{\partial F}{\partial z} = 1,$$

(VII-2)

where

$$E = \frac{c}{(1 - \kappa c^2 \rho^2)^{\frac{1}{2}}} + 2 \sum_{j=1}^{N} j \alpha_j \rho^2 {(j-1)}.$$

For cases where the coefficients α_i (representing departure from a conic surface of revolution) are all zero, we may use the simpler, but equivalent equation:

$$F(X,Y,Z) = Z - \tfrac{1}{2}c(\rho^2 + \kappa Z^2).$$

(VII-3)

We then have

$$F_x = - c X,$$

$$F_y = - c Y,$$

$$F_z = 1 - \kappa c Z.$$

(VII-4)

193

(It may be noted that in the computer program we have adopted the opposite convention of sign regarding vertex curvature; the above equations are deliberately kept in the same form as those of Spencer and Murty).

To determine the point of intersection of a ray with the given surface, we write the equation of the ray in parametric form:

$$X = X_0 + k\,s,$$
$$Y = Y_0 + l\,s, \qquad\qquad (VII\text{-}5)$$
$$Z = Z_0 + m\,s.$$

Here (k, 1, m) are the direction cosines of the ray (note that here k has an entirely different meaning than the κ in the equations above). (In the code AI, BI, and CI are used instead of k, 1, m, and TPAR as a mnemonic for "t-parameter" is used instead of s). Here X_0, Y_0, and Z_0 represent the coordinates of the last point of intersection. One method of approach would be to substitute the above parametric equations into the surface equation and attempt to solve directly for the parameter s. Instead we use the Newton-Raphson iterative technique. As the first approximation s_0 to the value of s, we calculate simply the distance to the plane Z = 0, which gives

$$s_0 = -\frac{Z_0}{m}. \qquad\qquad (VII\text{-}6)$$

For successive approximations we put

$$s_{j+1} = s_j - \frac{F(X_j, Y_j, Z_j)}{F'(X_j, Y_j, Z_j)}, \qquad\qquad (VII\text{-}7)$$

194

where

$$X_j = X_0 + k\, s_j,$$
$$Y_j = Y_0 + 1\, s_j$$
$$Z_j = Z_0 + m\, s_j.$$

The iterations are continued until the magnitude of the next increment
to the parameter s becomes less than a specified tolerance, i.e., until

$$|s_j - s_{j-1}| < \varepsilon.$$

In order to calculate the direction cosines k', 1', m' after
reflection, we first determine the cosine of the angle θ between the
incident ray and the surface normal:

$$\cos\theta = \frac{(k\, F_x + 1\, F_y + m\, F_z)}{F_T}, \tag{VII-8}$$

where

$$F_T = (F_x^2 + F_y^2 + F_z^2)^{\frac{1}{2}}.$$

Now the law of reflection can be expressed by saying that the unit
vector normal to the surface is geometrically midway between outward-
pointing unit vectors which are parallel and antiparallel to the in-
coming and reflected rays, respectively. That is to say

$$\tfrac{1}{2}\left[\bar{e}' - \bar{e}\right] = A\,\bar{n}, \tag{VII-9}$$

where $\bar{e}$ and $\bar{e}'$ are unit vectors along incident and reflected ray, $\bar{n}$ is the
unit vector normal to the surface, and A is a constant. Now the
magnitude of the component of $\bar{e}$ or $\bar{e}'$ along the surface normal is just $\cos\theta$,
and hence the value of A is just $(-\cos\theta)$. Thus we have that

$$\bar{e}' = \bar{e} - 2\,\bar{n}\cos\theta. \tag{VII-10}$$

The unit vector $\bar{n}$ can be expressed as

$$\bar{n} = \frac{1}{F_T} (F_x, F_y, F_z).$$ (VII-11)

We can then put

$$k' = k - 2 \cos \theta \frac{F_x}{F_T},$$ (VII-12)

$$l' = l - 2 \cos \theta \frac{F_y}{F_T},$$ (VII-13)

$$m' = m - 2 \cos \theta \frac{F_z}{F_T}.$$ (VII-14)

This formulation and its embodiment in the IRAYT code were checked in various ways, including comparison calculations with a desk calculator and comparison to results of a previously prepared computed code which treats the special case of spherical mirrors (at possibly large tilt angles) by a different scheme.

Effects of Mirror Tilts on Tilt of Output Beam

We consider first a tilt of a small amount θ_x (we arbitrarily choose θ_x rather than θ_y for the present discussion, but tests were run for both rotations) about the x-axis applied to the primary mirror. We assume a collimated beam incident on the secondary mirror. The output beam after a single round-trip will obviously be rotated by the angle $2\,\theta_x$. If instead we had rotated the secondary mirror through an angle θ_x, the output beam after a single round-trip would be rotated through the angle $\frac{2}{M}\,\theta_x$. An IRAYT run for M = 2.5 and a secondary mirror tilt angle of 10^{-5} predicted a single-pass output-beam tilt of 0.7978×10^{-5}, in satisfactory agreement with the expected value of

$$\frac{2}{M}\,\theta_x = 0.8 \times 10^{-5}. \qquad (VII-15)$$

After repeated round-trips through the resonator, the output resulting from a starting wave which is collimated and parallel to the (relative to untilted system) optic axis is multiplied by the sum of the appropriate number of terms of the series

$$1 + M^{-1} + M^{-2} + M^{-3} \ldots$$

For example, after two passes one would expect the output beam to be tilted by

$$\frac{2}{M}\,\theta_x\,(1 + M^{-1}) = 0.112 \times 10^{-4}. \qquad (VII-16)$$

The IRAYT code predicted a value of $0.112\,002 \times 10^{-4}$, which is in very good agreement with the above.

The tilt of the converged output beam of a resonator resulting from tilt of one of the mirrors can be obtained by multiplying the expected

single-pass tilt by the sum of the infinite series given above, i.e., by the factor

$$1 + M^{-1} + M^{-2} + M^{-3} + M^{-4} \ldots = \frac{1}{(1 - M^{-1})} = \frac{M}{(M - 1)} \quad \text{(VII-17)}$$

The predicted tilt ϕ_S of output beam due to tilt ϕ_x of secondary mirror is thus

$$\phi_S = 2 \theta_x \frac{1}{(M - 1)} . \quad \text{(VII-18)}$$

For $M = 2.5$ and $\theta_x = 10^{-5}$, this predicts ϕ_S of 0.13333×10^{-4}. To test IRAYT in this respect, a collimated beam was launched having this amount of tilt with respect to the optic axis (and with the secondary mirror tilted by 10^{-5} radians). The results were self-consistent, in agreement with the prediction.

One can similarly show that the tilt ϕ_P of output beam due to tilt θ_x of primary mirror is

$$\phi_P = 2 \theta_x \frac{M}{(M - 1)} . \quad \text{(VII-19)}$$

The above equations for ϕ_S and ϕ_P have been derived earlier in a different fashion by Krupke and Sooy[3].

Output Curvature of Initially Collimated Beam

After One or Many Round-Trips Through A Near-Confocal Unstable Resonator

Consider the case of collimated radiation incident on an unstable-resonator secondary (convex) mirror with radius of curvature R_S. The radius of curvature of the diverging beam reflected from the mirror is, of course, $\frac{1}{2} R_S$. We let the actual mirror separation be denoted by L', where we also write

$$L' = L + \Delta L. \tag{VII-20}$$

Here L denotes the confocal-resonator mirror separation given by

$$R_P - R_S = 2 L. \tag{VII-21}$$

The expanding beam, after travelling a distance L', just prior to striking the primary mirror, has a radius of curvature of

$$R_{exp} = \frac{1}{2} R_S + L'. \tag{VII-22}$$

By substitution from above, we readily have that

$$R_{exp} = \frac{1}{2} R_S + \frac{1}{2} R_P - \frac{1}{2} R_S + \Delta L = \frac{1}{2} R_P + \Delta L. \tag{VII-23}$$

By the lens law, the radius of curvature of the output beam R_{out}, i.e., the beam after reflection by the primary mirror, is given by

$$\frac{1}{R_{out}} = \frac{2}{R_P} - \frac{1}{R_{exp}}. \tag{VII-24}$$

By assuming that ΔL is small compared to R_P we can write

$$\frac{1}{R_{exp}} = \frac{1}{\frac{1}{2} R_P + \Delta L} = \frac{1}{\frac{1}{2} R_P} \left[\frac{1}{1 + 2 \frac{\Delta L}{R_P}} \right] \approx \frac{1 - 2 \Delta L/R_P}{(R_P/2)} \quad . \tag{VII-25}$$

This combines with the equation for R_{out} to give

$$\frac{1}{R_{out}} \approx \frac{+ 4 \Delta L}{R_P 2} \quad . \tag{VII-26}$$

We can re-express the above in terms of L rather than R_P by noting

that

$$R_P - R_S = 2 L, \tag{VII-27}$$

and

$$R_P/R_S = M. \tag{VII-28}$$

The above combine to give

$$R_P \left[1 - \frac{1}{M} \right] = 2 L, \tag{VII-29}$$

$$\frac{1}{R_P} = \frac{1}{2L} \left[1 - \frac{1}{M} \right] = \frac{1}{2L} \frac{(M - 1)}{M} \quad . \tag{VII-30}$$

We then obtain

$$\frac{1}{R_{out}^{SP}} = \frac{(M - 1)^2}{M^2} \frac{\Delta L}{L^2} \quad . \tag{VII-31}$$

This is for a single round-trip, starting with a collimated beam incident

on the secondary (convex) mirror of a near-confocal system.

As an example, we have used IRAYT to calculate a system with $M = 2$,

$L = 200$ cm, $\Delta L = \pm 1$ cm. The above equation predicts

$$\frac{1}{R_{out}^{SP}} = \pm 0.625 \times 10^{-5} \text{ cm}^{-1}. \tag{VII-32}$$

The output of the IRAYT code includes a least-squares fit to the coefficient

C_3 of the expansion term $(X^2 + Y^2)$, being half the value of the wave-front

curvature. For single-pass cases the numerical results were 0.3117×10^{-5} and 0.3132×10^{-5}, respectively, corresponding to curvatures of 0.6234×10^{-5} and 0.6264×10^{-5}. These are in quite satisfactory agreement with the 0.625×10^{-5} prediction for single-pass output curvature from the approximate closed-form analysis given above.

For multiple passes through the resonator, one expects the output curvature to be multiplied by a sum of as many terms of the series

$$1 + M^{-2} + M^{-4} + M^{-6} \ldots$$

as there are round-trip passes. For example, for $M = 2$ and two passes through the system, one expects the curvature to be increased by the factor

$$1 + 2^{-2} = 1.25 .$$

The numerical values of the IRAYT results for the curvature of the output wave for two and one round-trips, respectively were found to be in the ratio of 1.2545, which is in reasonably good agreement with the above prediction.

The above closed-form analysis can be extended to predict the focal distance of the converged output of a near-confocal resonator. One merely sums the above series to completion, thereby obtaining the factor

$$1 + M^{-2} + M^{-4} + M^{-6} \cdot \cdot \cdot = \frac{1}{(1 - M^{-2})} = \frac{M^2}{(M^2 - 1)} \qquad \text{(VII-33)}$$

$$= \frac{M^2}{(M + 1)(M - 1)} .$$

For the focal distance of the converged output of a resonator we have

$$R^\infty_{out} = R^{SP}_{out} \frac{(M + 1)(M - 1)}{M^2} = \frac{M^2}{(M - 1)^2} \frac{L^2}{\Delta L} \frac{(M + 1)(M - 1)}{M^2}$$

$$= \frac{(M + 1)}{(M - 1)} \frac{L^2}{\Delta L} . \qquad \text{(VII-34)}$$

The above expression was given earlier by Anan'ev.[4]

In order to test the code regarding the radius of curvature of output for a converged solution, one could of course have iterated for many round-trips. Instead we used the above equation to predict the expected results and launched a starting wave with that curvature. The fact that a single round-trip was then self-reproducing with respect to curvature confirmed proper behavior of the code in this respect.

First Order Prediction of Spherical Aberration in Confocal Unstable Resonator with Spherical Mirrors

An approximate prediction of the amount of spherical aberration can be made by considering the optical path difference between distances along a nominal ray path in a spherical mirror system and in a corresponding parabaloidal mirror system (i.e., one having the same values of vertex curvatures). For convenience we consider (1) the incremental path length associated with the primary mirror along the path ABC in Figure E-1 and (2) the incremental path length associated with the second mirror along the path CDE in the figure. The reference plane through points A, C, and E is normal to the optic axis of the system.

The equation for the spherical surface of the primary mirror can be written as

$$(Z - R)^2 + \rho^2 = R^2, \tag{VII-35}$$

where the Z axis is parallel to the optic axis, R is the radius of curvature of the mirror, and ρ is given by

$$\rho^2 = X^2 + Y^2. \tag{VII-36}$$

The origin of coordinates has been placed at the intersection of the optic axis with the mirror. The surface equation can be rewritten as

$$Z^2 - 2ZR + \rho^2 = 0. \tag{VII-37}$$

The desired solution (i.e., the one with proper choice of sign in front of the square root) for Z is given by

$$\frac{Z}{R} = 1 - \sqrt{1 - \left(\frac{\rho}{R}\right)^2}. \tag{VII-38}$$

Figure E-1

204
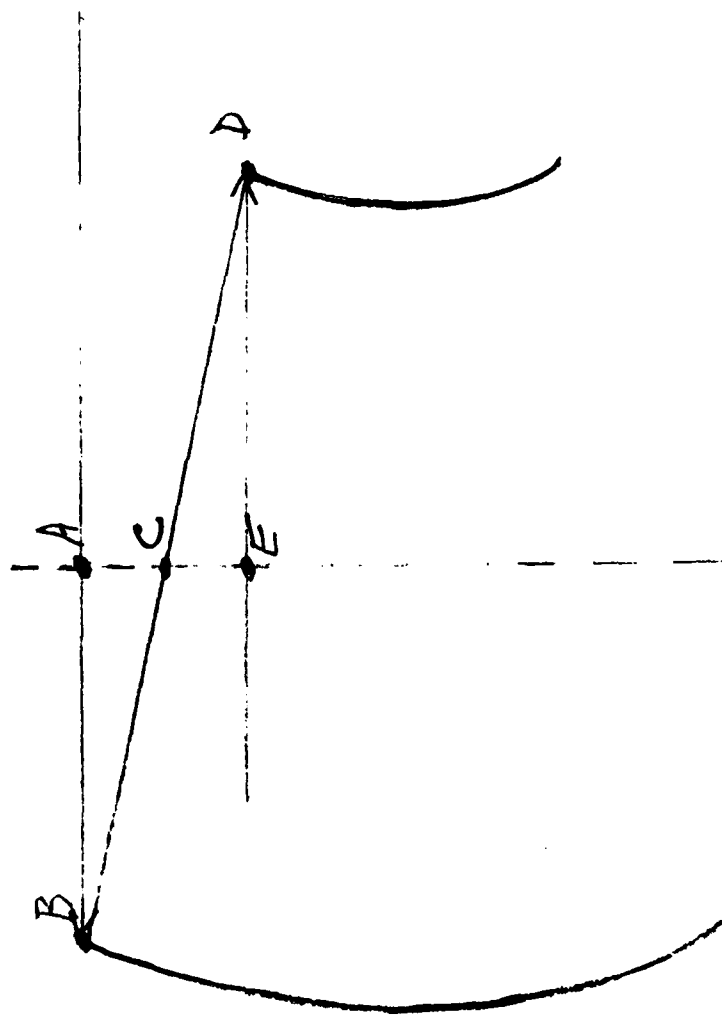
Now ρ/R is small compared to unity, and it is useful to write the first few terms of the series expansion of the radical. This gives

$$\frac{Z}{R} = 1 - \left[1 - \frac{1}{2} \left(\frac{\rho}{R} \right)^2 - \frac{1}{8} \left(\frac{\rho}{R} \right)^4 \cdots \right] \quad . \tag{VII-39}$$

The value associated with retaining only the first two terms of the series expansion is the value associated with a parabaloidal mirror. Thus the incremental value of $\frac{Z}{R}$ is approximated by the third term in the square brackets. The optical path difference is double this amount in magnitude, since the ray traverses both segment AB and segment BC. (We here ignore the fact that the segment BC is tilted relative to the optic axis). We can then write as the first-order approximation to the incremental OPD associated with the primary mirror

$$\Delta Z_P = \frac{1}{4} \frac{\rho_P^4}{R_P^3} \quad . \tag{VII-40}$$

The magnitude of the incremental OPD associated with the path CDE to and from the secondary mirror can of course be written in the same form as the above, except with subscripts indicating secondary rather than primary mirror. Thus we have that

$$\Delta Z_S = \frac{1}{4} \frac{\rho_S^4}{R_S^3} \quad . \tag{VII-41}$$

Because of the nature of a confocal resonator we have that the magnitude of the radius of curvature R_P of the primary mirror is M times as large as the radius of curvature R_S of the secondary mirror. Also, the value of

ρ_P associated with the intersection of the ray with the primary mirror will be M times as large as the value of ρ_S associated with the intersection of the ray with the secondary mirror. Thus we can rewrite the above as

$$\Delta Z_S = \frac{1}{4} \frac{\rho_P^4}{M^4} \frac{M^3}{R_P^3} = \frac{1}{M} \frac{1}{4} \frac{\rho_P^4}{R_P^3} . \qquad (VII-42)$$

The two OPD contributions tend to cancel, of course, since one mirror is concave while the other is convex. Thus the overall OPD, ΔZ, is (to first order) given by

$$\Delta Z = (1 - 1/M) \frac{1}{4} \frac{\rho_P^4}{R_P^3} . \qquad (VII-43)$$

All of this, of course, is for a single round-trip through the resonator. Some numerical examples have been worked out and are given in the table below:

$-R_S$ (cm)	R_P (cm)	L (cm)	M	$\left[\dfrac{\Delta Z \times 10^{10}}{\rho_P^4}\right]$
300	700	200	2.333	4.164
400	800	200	2.000	2.441
500	900	200	1.800	1.524
600	1000	200	1.667	1.000
800	1200	200	1.500	0.482
1000	1400	200	1.400	0.260

Numerical ray-tracing calculations have been performed for several values of ρ_P for each of the above cases and compared to the above predictions; the agreement was quite satisfactory.

In the equation given above, the specific dependence is on R_p, the radius of curvature of the primary mirror. We can recast this in terms of the mirror separation L as the independent variable. We have for a confocal resonator that

$$L = \frac{1}{2}\left[R_P - |R_S|\right] = \frac{1}{2} R_P (1 - 1/M).$$

(VII-44)

This immediately leads to

$$\frac{1}{R_P} = \frac{1}{2L} (1 - 1/M).$$

(VII-45)

We can rewrite the equation for the overall increment ΔZ of OPD as

$$\Delta Z = (1 - 1/M)^4 \frac{1}{32} \frac{\rho_P^4}{L^3}.$$

(VII-46)

From the above equation it is clear that, for a resonator design with L and the maximum value of ρ_P specified, the dependence on the choice of magnification, and hence of output coupling, is of the simple form $(1 - 1/M)^4$. Some numerical examples are listed in the table below:

M	Outcoupling = $1 - M^{-2}$	Factor $(1 - 1/M)^4$
2.5	0.84	0.1296
2.0	0.75	0.0625
1.5	0.556	0.0123
1.32	0.426	0.0034

It is clear from the above table that the magnitude of the one-pass spherical aberration depends rather strongly on the magnification M.

For the self-consistent multiple-pass resonator situation, the total incremental OPD due to spherical aberration is simply the sum of contributions for various values of ρ_P, where the first such value is ρ_{max}, the second is $\rho_{\frac{max}{M}}$, the N-th is $\rho_{\frac{max}{M^N}}$, etc. The total multi-pass OPD increment is thus

$$\Delta Z_{MP} = (1 - 1/M)\frac{1}{4} \; \frac{\rho_P^4}{R_P^3} \left[1 + (M^{-4}) + (M^{-4})^2 + (M^{-4})^3 \cdots \right. \qquad (VII-47)$$

The series can be readily summed, and gives

$$\Delta Z_{MP} = (1 - 1/M)\frac{1}{4} \; \frac{\rho_P^4}{R_P^3} \; \frac{1}{(1 - M^{-4})} \qquad . \qquad (VII-48)$$

When written in terms of L as the independent variable, this becomes

$$\Delta Z_{MP} = (1 - 1/M)^4 \; \frac{1}{32} \; \frac{\rho_P^4}{L^3} \; \frac{1}{(1 - M^{-4})} \; . \qquad (VII-49)$$

208

Root-Mean Square Optical Path Difference Resulting from Spherical Aberration

The equations derived earlier predict a contribution to optical path difference which can be written as

$$\Delta Z = C_5 \, (X^2 + Y^2)^2, \qquad\qquad (VII-50)$$

where the form of C_5 as a function of M and of L or R_p has been worked out for both single-pass and multi-pass cases. The use of notation C_5 to designate this expansion coefficient for the aberration contribution is merely for consistency with notation in the present version of the IRAYT computer program.

Our calculations and the IRAYT program itself are limited to rectangular apertures, though not limited to square apertures. For purposes of testing the code it was convenient to specialize some calculations to the square-aperture case. We will work out here the contribution to OPD resulting from spherical aberration. In general, the rms value of a function f (X,Y) is given by

$$f_{rms} = \sqrt{< f^2 > - < f >^2} \, . \qquad\qquad (VII-51)$$

With f (X,Y) having the form given above, we will have

$$<f^2> = \frac{I_2}{I_0} \, , \qquad\qquad (VII-52)$$

$$<f> = \frac{I_1}{I_0} \, , \qquad\qquad (VII-53)$$

where

$$I_0 = \int_0^a dX \int_0^a dY \, , \qquad\qquad (VII-54)$$

$$I_1 = \int_0^a dX \int_0^a dY \quad f(X,Y),$$ (VII-55)

$$I_2 = \int_0^a dX \int_0^a dY \quad f^2(X,Y).$$ (VII-56)

For simplicity we have considered the contribution from only one quadrant of the aperture; this will not effect the overall result, which is an average over the entire aperture. The half-width of the aperture is denoted by a. We immediately have that

$$I_0 = a^2.$$ (VII-57)

For I_1 we can write

$$I_1 = C_5 \int_0^a dX \int_0^a dY \quad (X^4 + 2\, X^2\, Y^2 + Y^4),$$ (VII-58)

$$I_1 = C_5 \int_0^a dX \quad (a\, X^4 + \frac{2}{3}\, a^3\, X^2 + \frac{1}{5}\, a^5),$$ (VII-59)

$$I_1 = C_5 a^6 \left[\frac{1}{5} + \frac{2}{9} + \frac{1}{5} \right] = \frac{28}{45}\, a^6 C_5.$$ (VII-60

This immediately gives

$$< f > = \frac{28}{45}\, a^4 C_5$$ (VII-61)

For I_2 we have

$$I_2 = C_5^2 \int_0^a dX \int_0^a dX \quad \left[X^8 + 4\, X^6\, Y^2 + 6\, X^4\, Y^4 + 4\, X^2\, Y^6 + Y^8 \right].$$ (VII-62)

After carrying out the integration over dY, we have that

$$I_2 = C_5^2 \int_0^a dX \quad \left[a\, X^8 + \frac{4}{3}\, a^3\, X^6 + \frac{6}{5}\, a^5\, X^4 + \frac{4}{7}\, a^7\, X^2 + \frac{1}{9}\, a^9 \right].$$ (VII-63)

$$I_2 = a^{10} \left[\frac{1}{9} + \frac{4}{21} + \frac{6}{25} + \frac{4}{21} + \frac{1}{9} \right] c_5^2 , \qquad \text{(VII-64)}$$

$$I_2 = \frac{1328}{1575} \ a^{10} \ c_5^2 . \qquad \text{(VII-65)}$$

We thus immediately have that

$$< f^2 > = \frac{1328}{1575} \ a^8 \ c_5^2 . \qquad \text{(VII-66)}$$

For the rms value of the spherical-aberration contribution to the OPD we have

$$\sqrt{< f^2 > - < f >^2} = \sqrt{a^8 \ c_5^2 \left[\frac{1328}{1575} - \frac{784}{2025} \right]} , \qquad \text{(VII-67)}$$

$$\text{RMSOPD} = 0.675288 \ a^4 \ c_5.$$

As a test of the IRAYT computer program, we have calculated the RMSOPD due to spherical-aberration for a case with mirror separation L of 200 cm, a magnification M of 2.0, and an aperture half-width of 50 cm. We first note that the closed-form equations given above would predict a C_5 value of

$$C_5 = (1 - 1/M)^4 \ \frac{1}{32L^3} = (1/2)^4 \ \frac{1}{32 \ (200)^3} , \qquad \text{(VII-68)}$$

$$C_5 = 0.2441 \times 10^{-9}.$$

By comparison, the results of an IRAYT calculation using a mesh of 11 X 11 gave a C_5 value of 0.2466×10^{-9}, which is in satisfactory agreement.

The directly-computed value of the RMSOPD is not as good. Using the 11 X 11 mesh, the IRAYT computer program calculated an RMSOPD of 0.1450 X 10^{-2} cm, whereas the above formula using the latter value of C_5 predicts an RMSOPD value of 0.1041 X 10^{-2} cm. The inaccuracy seems to stem largely from the finiteness of the number of mesh points, and is reduced considerably as a larger number of mesh points is used. A similar IRAYT calculation using a 41 X 41 mesh led to a directly-calculated value of the RMSOPD of 0.1140 X 10^{-2}, in reasonable agreement with the closed-form prediction of 0.1041 X 10^{-2} cm.

Other numerical tests of this same sort were carried out, and confirmed satisfactory operation of the IRAYT code in the present respect; for brevity these are not reported here in detail.

The above discussion relates to the amount of spherical-aberration resulting from a single round-trip of initially collimated radiation in a resonator in nominally confocal arrangement such that no output curvature is present. The net RMSOPD could, of course, be reduced somewhat by choosing a slightly off-confocal arrangement such that an appropriate amount of curvature is present to cancel part of the $(X^2 + Y^2)^2$ OPD contribution. The optimal value of output wave-front curvature is not so easy to calculate in the present square-aperture case as for a circular-aperture arrangement. For the latter arrangement, of course, it is well-known that the aberration can be expanded in Zernike polynomials, and the fourth-order Zernike polynomial includes some second order contribution, R^2, as well as spherical-aberration, R^4, contribution[5].

Choice of Asphericity Parameter of Convex Mirror to Eliminate Fourth-Order Aberrations Introduced by Spherical Primary Mirror

We have already shown that the single-pass fourth-order aberration resulting from sphericity of the mirrors will be of the form

$$\Delta Z = C_5 \rho^4 = C_5 \, (X^2 + Y^2)^2. \tag{VII-69}$$

The first-order closed-form prediction for C_5 is (in the present discussion we ignore signs of OPDs for simplicity):

$$C_5 = (1 - 1/M)^4 \, \frac{1}{32 \, L^3} \, . \tag{VII-70}$$

For a numerical example with $M = 2.5$, $L = 250$ cm, the above equation predicts a value of 0.2592×10^{-9} for C_5. A number of calculations were carried out for such a confocal resonator, with mirror vertex curvatures of 0.003 and 0.0012 cm^{-1}, respectively. For the unperturbed resonator with spherical mirrors, the least-squares value of C_5 came out as 0.25931×10^{-9}, in good agreement with the above prediction.

One expects to be able to cancel the fourth-order aberration by introducing a fourth-order aspheric correction onto the secondary mirror. The mirror surface correction only needs to be half as large as the total optical-path difference correction, since the mirror surface increment affects both the incident and reflected ray. Since the correction is of fourth-order in ρ, and the value of ρ at the secondary mirror is only $1/M$ times as large as at the primary mirror, the aspheric correction needs to be increased by a factor of M^4. The prediction then is that the fourth-order aberration will be essentially eliminated if the mirrors are basically spherical except that an aspheric term is added to the secondary mirror corresponding to

$$\alpha_2 = -\frac{M^4}{2} C_5 , \qquad\qquad (VII-71)$$

where the value of C_5 is as given above. Of course α_2 is the co-efficient of ρ^4 in the surface function of the mirror, as described earlier. For the same numerical example as considered above, the predicted required value of α_2 is

$$\alpha_2 = -\frac{(2.5)^4}{2} \ X \ 0.2592 \ X \ 10^{-9} = -0.50625 \ X \ 10^{-8}. \qquad (VII-72)$$

When this asphericity was introduced into the calculations, the overall value of the calculated root-mean-square optical path difference RMSOPD for a 20 cm X 20 cm output aperture, calculated with an 11 X 11 mesh was reduced from $0.244 \ X \ 10^{-5}$ cm to $0.194 \ X \ 10^{-8}$ cm, i.e., by about three orders of magnitude. This seems to confirm the first-order analysis and also proper functioning of that portion of the IRAYT code.

It is also possible to introduce the desired amount of fourth-order correction to a spherical surface by instead adopting an ellipsoidal surface with a suitable value of the conic parameter κ. The required value of vertex curvature is of course the same as for spherical or parabaloidal mirrors.

Choice Of Ratio Of Conic Parameters Of Ellipsoidal Mirrors So As To Eliminate Fourth-Order Spherical- Aberration

We consider the ellipse formed by slicing the ellipsoid of revolution through the z-y plane, and write its equation

$$z = a - a (1 - b^{-2} y^2)^{\frac{1}{2}} . \qquad \text{(VII-73)}$$

The first few terms in the expansion of z give

$$z = \frac{a}{2b^2} y^2 + \frac{a}{8b^4} y^4 \ldots \qquad \text{(VII-74)}$$

We note that

$$\frac{a}{b^2} = c, \qquad \text{(VII-75)}$$

where c is the vertex curvature. Also we have that

$$\frac{a}{b^4} = \frac{a^3}{b^6} \frac{b^2}{a^2} = c^3 \kappa , \qquad \text{(VII-76)}$$

where κ is the conic parameter. The above expansion can then be written as

$$z (y) = \frac{1}{2} c y^2 + \frac{1}{8} c^3 \kappa y^4 \ldots \qquad \text{(VII-77)}$$

We will use subscripts P and S to denote primary and secondary mirror, respectively, of a nominally confocal unstable resonator of magnification M. The mirror curvatures then are in the ratio

$$\frac{c_S}{c_P} = M. \qquad \text{(VII-78)}$$

If only the first term in the above expansion were non-vanishing (i.e., for parabaloidal mirrors), fourth-order (and indeed all higher-order) aberrations would vanish. We wish to choose values of the conic

parameters κ_S and κ_P such that the magnitudes of the fourth-order contributions from each of the mirrors are equal and hence cancel. We must, of course, compare the terms for values of y which are in the ratio of M. Thus we require that

$$\frac{1}{8} c_P^3 \kappa_P y^4 = \frac{1}{8} c_S^3 \kappa_S (y/M)^4 \qquad \text{(VII-79)}$$

This can be rewritten as

$$\frac{1}{8} c_P^3 \kappa_P y^4 = \frac{1}{8} M^3 c_P^3 \kappa_S \frac{y^4}{M^4} . \qquad \text{(VII-80)}$$

This immediately leads to the requirement that

$$\kappa_S = M \kappa_P . \qquad \text{(VII-81)}$$

When the ratio of values of the conic parameters is M as required by the above equation, the fourth-order aberration should vanish for an ideally-aligned system.

The above equation applies, of course, whenever both mirrors are ellipsoidal, and includes the special cases of spherical mirrors, parabaloids, and ellipsoids.   Certain special cases are of particular interest. First, parabaloidal mirrors obviously satisfy the above ratio requirement since both κ_S and κ_P are zero. Second, the primary mirror may be spherical, i.e., $\kappa_P = 1$. The secondary (i.e., feedback) mirror will need to be a surface of revolution about the minor axis, with $\kappa_S = M$. Third, the secondary mirror may be spherical, i.e., $\kappa_S = 1$. The primary mirror will then need to be a surface of revolution about the major axis, with $\kappa_P = \frac{1}{M}$.

216

The above prediction of cancellation of spherical aberration by using one spherical and one elliptical mirror was tested by IRAYT calculations for a resonator with M = 2.5, L = 250 cm, aperture size of 10 cm X 10 cm using an 11 x 11 transverse mesh. For both mirrors of spherical figure the single-round-trip IRAYT calculation gave $C_5 = 0.259 \times 10^{-9}$. When the primary mirror was replaced with an ellipsoidal mirror with $\kappa = 0.4$, the IRAYT calculation gave a value of C_5 about four orders of magnitude less.

Relationship Between the Conic Parameter κ For an Ellipsoid of Revolution and the Eccentricity e

For an ellipsoid of revolution about the z axis, with vertex at the origin, we have the equation

$$\frac{(z-a)^2}{a^2} + \frac{\rho^2}{b^2} = 1, \tag{VII-81}$$

where

$$\rho^2 = x^2 + y^2.$$

For simplicity of derivations we will simply consider the ellipse in the z-y plane, described by the equation

$$\frac{(z-a)^2}{a^2} + \frac{y^2}{b^2} = 1. \tag{VII-82}$$

To find the vertex curvature in terms of a and b, we can write

$$z = a - a \left[1 - \frac{1}{b^2} y^2 \right]^{\frac{1}{2}}, \tag{VII-83}$$

$$\frac{dz}{dy} = \frac{a}{b^2} y \left[1 - \frac{1}{b^2} y^2 \right]^{-\frac{1}{2}}, \tag{VII-84}$$

$$\frac{d^2z}{dy^2} = \frac{a}{b^2} \left[1 - \frac{1}{b^2} y^2 \right]^{\frac{1}{2}} + \frac{a}{b^4} y^2 \left[1 - \frac{1}{b^2} y^2 \right]^{-3/2}. \tag{VII-85}$$

The surface curvature at the vertex is just the above evaluated at $y = 0$, i.e.,

$$c = \left(\frac{d^2z}{dy^2} \right)_{y=0} = \frac{a}{b^2}. \tag{VII-86}$$

We next rewrite the equation of the ellipse as

$$z = a - (a^2 - \gamma y^2)^{\frac{1}{2}}, \tag{VII-87}$$

where

$$\gamma = \frac{a^2}{b^2} \quad .$$

We multiply the above equation for z by

$$\frac{a + (a^2 - \gamma y^2)^{\frac{1}{2}}}{a + (a^2 - \gamma y^2)^{\frac{1}{2}}} \quad . \tag{VII-88}$$

The numerator simplifies immediately, and we obtain

$$z = \frac{\gamma y^2}{a + (a^2 - \gamma y^2)^{\frac{1}{2}}} \quad . \tag{VII-89}$$

By substituting for γ we obtain

$$z = \frac{\frac{a}{b^2} y^2}{1 + (1 - b^{-2} y^2)^{\frac{1}{2}}} \quad . \tag{VII-90}$$

By substituting the expression for vertex curvature c, we can rewrite this as

$$z = \frac{c y^2}{1 + \left[1 - (b/a)^2 c^2 y^2 \right]^{\frac{1}{2}}} \quad . \tag{VII-91}$$

If we define κ by the equation

$$\kappa = \frac{b^2}{a^2} \quad , \tag{VII-92}$$

we immediately obtain the expression

$$z = \frac{c y^2}{1 + (1 - \kappa c^2 y^2)^{\frac{1}{2}}} \quad . \tag{VII-93}$$

This is just the form of the equation used in the ray-tracing except that ρ replaces y in the equation immediately above.

To obtain the relation between the conic parameter κ and the eccentricity e, we note that by definition the eccentricity of an ellipse with semi-major axis a and semi-minor axis b is given by

$$e = \frac{(a^2 - b^2)^{\frac{1}{2}}}{a} = \left[1 - (b/a)^2\right]^{\frac{1}{2}} . \qquad (VII-94)$$

This then leads to the simple relationship

$$e = \left[1 - \kappa\right]^{\frac{1}{2}} , \kappa \leq 1. \qquad (VII-95)$$

The above is applicable for cases where $\kappa \leq 1$. When $\kappa > 1$, the roles of a and b are reversed, i.e., a is the semi-minor axis, and b is the semi-major axis. The equation defining the eccentricity then interchanges a and b, and the resulting expression for the eccentricity e in terms of the conic parameter κ becomes

$$e = \left[1 - \frac{1}{\kappa}\right]^{\frac{1}{2}} , \kappa \geq 1. \qquad (VII-96)$$

If c and κ are given, one can of course solve for a and b. We repeat from above the equations

$$c = \frac{a}{b^2} , \qquad (VII-97)$$

$$\kappa = \frac{b^2}{a^2} . \qquad (VII-98)$$

Simple multiplication of the two expressions gives

$$a = \frac{1}{c\kappa} . \qquad (VII-99)$$

Multiplication of the equation for c by the square root of each side of the equation for κ gives

$$b = \frac{1}{c\kappa^{\frac{1}{2}}} . \qquad (VII-100)$$

220

Some Numerical Investigations of Fourth-Order Aberrations

Several numerical calculations of a single-round-trip of an initially collimated beam were made with IRAYT for the nominal case of $M = 2.5$, $L = 250$ cm, vertex curvatures of primary and secondary mirrors of $c_s = 0.003$ and $c_p = 0.0012$, mostly for an output aperture of 20 cm X 20 cm. For most cases a transverse mesh of 11 X 11 points was used.

The predicted value of spherical aberration for the nominal system with both mirrors being spherical was in good agreement with closed-form predictions, as mentioned earlier. In addition we tested combinations in which one or both mirrors were parabaloidal. For both mirrors of parabaloidal form, the IRAYT values of the coefficient C_5 of $(X^2 + Y^2)^2$ and of the overall RMSOPD were several (about four) orders of magnitude less than for the case with both mirrors spherical.

The earlier derivation regarding spherical aberration predicted an OPD increment, ΔZ, resulting from a spherical (as contrasted to parabaloidal) primary mirror which can be written as $\Delta Z_p = \frac{1}{4} c_p^3 \rho^4$, and hence predicted that the value of the least-squares-fit to coefficient of the ρ^4 term would be $C_5 = 0.25 \, c_p^3$. For the parameters described above this corresponds to a numerical value of C_5 of 0.432×10^{-6}. The numerical results of a single-round-trip IRAYT calculation included a least-squares-fit estimate for C_5 of 0.4319×10^{-6}, which is in quite satisfactory agreement.

The contribution from a spherical secondary mirror is predicted to be less than the above by the factor M^{-1}. Thus, the predicted value of C_5 for a resonator with parabaloidal primary but spherical secondary mirror is 0.1728×10^{-6}. An IRAYT calculation gave a numerical least-squares-fit value for C_5 of 0.17278×10^{-6}, which is also in good agreement with the predicted value.

If we combine (by subtraction) the closed-form predictions of C_5 for each of the mirrors as given above, we obtain a prediction of an overall C_5 of $(0.432 - 0.1728) \times 10^{-6} = 0.2592 \times 10^{-6}$. If instead we combine the two IRAYT values, we obtain a prediction of $(0.4319 - 0.17278) \times 10^{-6} = 0.25912 \times 10^{-6}$. An IRAYT calculation (20 cm X 20 cm aperture, 11 X 11 mesh) gave a least-squares-fit value for C_5 of 0.2593×10^{-6} for a single-round-trip in a resonator with both mirrors of spherical shape.

The IRAYT code includes the option of a decentered alignment. (Such an arrangement is known to have advantages in terms of fraction of the far field energy contained within the first lobe). For fully decentered systems with square output apertures, the maximum distance of a ray from the optic axis is of course just twice as much as for the centered-alignment case. Hence, any aberration of the simple form ρ^N would be expected to be increased by a factor of 2^N. In particular, the spherical aberration ($N = 4$) would be expected to be larger for the decentered case by a factor of 2^4. An IRAYT run was made for a fully decentered case with spherical mirrors. The value of C_5 from the least-squares fit came out to be 0.2598×10^{-6}, as compared to the value of 0.2593×10^{-6} for a centered system. The overall RMSOPD was only increased by about a factor of 13 instead of a factor of $2^4 = 16.0$. This discrepancy is presumably (in fact almost certainly) due merely to the rather small number of mesh points (11 X 11) used in the calculations.

Residual Fourth-Order Aberration Resulting from Perturbing Mirror Spacing from Confocal Arrangement

Even with a pair of parabaloidal mirrors, the laser output will be aberrated if the mirror spacing is perturbed from the confocal arrangement. The principal effect, of course, will be sphericity of output wave, i.e., a focusing or defocusing. Conceivably the sphericity could be removed by additional optics, or might even be desired for some applications. In addition, there will be higher-order aberrations, of which the most significant is a fourth-order contribution. To briefly investigate this, IRAYT runs were made for perturbed values of mirror spacing. Specifically runs were made with $L = 249$ and 251 cm, as compared to a confocal spacing of 250 cm, for a case with $M = 2.5$. After removal of the spherical component of the output wave (from a single-round-trip of a collimated input wave), the (least-squares-fit value of the) coefficient C_5 of the fourth-order term was found to be about 0.41×10^{-11} (as compared to 0.259×10^{-9} for a pair of spherical mirrors with confocal spacing). This residual fourth-order aberration is sufficient to be bothersome for a system with large aperture.

A closed-form estimate of the residual value of C_5 to be expected for a case such as above, with off-confocal spacing of parabaloidal mirrors, can be made as follows. We can take the point of view that the mirrors are perturbed spheres, and make use of the earlier analysis. For simplicity, we consider a ray going in the "reverse" direction through one-round-trip of the system. That is, we consider an incident ray parallel to the optic axis, which strikes the outer edge of the primary mirror. The reflected ray (to first order) travels in such a direction that it would (if not intercepted by secondary mirror) intersect

223

the optic axis at a distance $R_S/2$ behind the confocal position of the secondary mirror. But since we have perturbed the position of the secondary mirror by an amount ΔL, the intersection point will be at a distance

$$\frac{R_S}{2} + \Delta L \qquad\qquad\qquad (VII-101)$$

behind the secondary mirror. The ratio of the value ρ_S at which the ray strikes the secondary mirror to the value ρ_P at which the ray had reflected from the primary mirror will then be

$$\rho_S/\rho_P = \frac{\dfrac{R_S}{2} + \Delta L}{\dfrac{R_P}{2}} . \qquad\qquad (VII-102)$$

Since $R_P/R_S = M$, this can be written as

$$\frac{1 + \dfrac{2\Delta L}{R_S}}{M} .$$

From the present point of view, the mirrors have started as spherical and then had a fourth-order correction made to them. The above equation differs from our previous treatment of the fourth-order aberration of spherical-mirror resonators only by the fractional change of $2\Delta L/R_S$ for the fourth-order contribution from the secondary mirror. That contribution had been found to be

$$\Delta Z_S = \frac{1}{4} \frac{\rho_S^4}{R_S^3} . \qquad\qquad\qquad (VII-103)$$

If we keep only the first two terms in the expansion of the fourth power of the above ratio ρ_S/ρ_P, we can put

$$\rho_S \approx \rho_P \frac{1}{M^4} \left[1 + \frac{8\Delta L}{R_S} \right].\qquad\text{(VII-104)}$$

We then can obtain, in place of the former expression, that

$$\Delta Z_S = \frac{1}{4} \frac{\rho_P^4}{M^4} \left[1 + \frac{8\Delta L}{R_S} \right] \frac{M^3}{R_P^3} .\qquad\text{(VII-105)}$$

The residual term involving ΔL will not be corrected by the use of parabaloidal mirrors. Hence the first-order prediction of the residual contribution to C_5 (the coefficient of the fourth-order term in ρ) is

$$\frac{2\Delta L}{MR_S} \frac{1}{R_P^3} = \frac{2\Delta L}{R_P^4} .\qquad\text{(VII-106)}$$

For the above numerical example, we have $R_P = 833.33$ cm, $\Delta L = 1$ cm. The above equation predicts an incremental C_5 of 0.415×10^{-11}, which is in quite satisfactory agreement with the numerical results from the IRAYT calculations as mentioned above.

The present calculations of the results of perturbing the mirror spacing are, of course, quite preliminary. It is felt that a detailed computational study should be made of the effects of various perturbations for resonator design candidates. In addition to mirror spacing, one would, of course, want to include the effects of perturbation of mirror orientations. A very brief test was made of the latter by merely tilting the primary mirror by small amounts. For a tilt angle of 100 microradians, it appears that a sufficient amount of aberration will be introduced to be significant for large aperture systems.

225

REFERENCES

1. S. Brewer, <u>POLYPAGOS</u>: <u>Polychromic Program for the Analysis of General Optical Systems</u>, Air Force Report No. SAMSO-TR-70-411, Aerospace Report No. TR-0059 (6311)-1, 1 September 1970.

2. G. H. Spencer and M. V. R. K. Murty, J. Opt. Soc. Am. <u>52</u>, 672 (1962).

3. W. F. Krupke and W. R. Sooy, JQE<u>5</u>, 575 (1969).

4. Y. A. Anan'ev, Sov. J. Quant. Electron., <u>1</u>, 565 (1972).

5. M. Born and E. Wolf, <u>Principles of Optics</u> (Pergamon, New York, 1964), 2nd ed.

```
      PARAMETER NNX=65, NNY=5', NMX=45, NMY=45
      DOUBLE PRECISION XA,YA, A,AA,BA,CA,XI,YI,ZI,AI,BI,CI
      DOUBLE PRECISION XR,YR,TP,AR,BR,CR,SCRV,AKAPA
      DOUBLE PRECISION XCRD,YCRD,ZCRD,THETX,THETY
      DOUBLE PRECISION ZERO,ONE,TPAR,        TWO   ,DELLL
      DOUBLE PRECISION YMAGX,YMAGY
      DOUBLE PRECISION FIX,FIY,FNX,FNY,XFRAC,YFRAC,XFMAX,YFMAX
      DOUBLE PRECISION XF,YF,XO,YO
      DOUBLE PRECISION CASPH
      DOUBLE PRECISION CDIST
      DOUBLE PRECISION EPSXD, PSYD
      DOUBLE PRECISION CXTLT,CYTLT,CSPHR
      DIMENSION JDIST(10)
      DIMENSION XA(10),YA(10),ZA(10),AA(10),BA(10),CA(10)
      DIMENSION XI(10),YI(10),ZI(10),AI(10),BI(10),CI(10)
      DIMENSION XR(10),YR(10),ZR(10),AR(10),BR(10),CR(10)
      DIMENSION SCRV(10),AKAPA(10)
      DIMENSION XCRD(10),YCRD(10),ZCRD(10),THETX(10),THETY(10)
      DIMENSION XFF(NNX),   YFF(NNY),   DELZS(NNX,NNY)
      DIMENSION XOUT(NMX,NMY),  YOUT(NMX,NMY),AOUT(NMX,NMY),BOUT(NMX,NMY)
      DIMENSION DELZST(NMX,NMY), AOUTT(NMX,NMY),  BOUTT(NMX,NMY)
      DIMENSION NNASP(10)
      DIMENSION CASPH(10,7)
      COMMON XA,YA,ZA,AA,BA,CA,XR,YR,ZR,AR,BR,CR,XI,YI,ZI,AI,BI,CI,
     1XCRD,YCRD,ZCRD,THETX,THETY,SCRV,AKAPA,CASPH
  70 FORMAT(1H0)
  77 FORMAT(1H1)
  70 FORMAT(1X,3F20.12)
  81 FORMAT(1X,7F10.5)
  84 FORMAT(8E10.5)

  89 FORMAT(1X,FF10.5,F10.4, 10.5,I1)
  99 FORMAT(1X,9E13.5)
     ZERO=0.0
     ONE=1.
     TWO=2.0
     DATA FI/3.1415926536/
   1 READ (5,81,END=9990)XNMI ,PRALL,PRDUS,CPLT,XPLTR,FITLS,FPNTP
     WRITE(6,77)
     WRITE(6,81)            XNMI ,PRALL,PRDUS,CPLT,XPLTR,FITLS,PPNTP
     INMAX=XNMI+2.0
     DO 10 I=1,INMAX
     READ (5,89)XCRD(I),YCRD(I),ZCRD(I),THETX(I),THETY(I),SCRV(I),
    1AKAPA(I),NNASP(I)
     WRITE(6,89)XCRD(I),YCRD(I),ZCRD(I),THETX(I),THETY(I),SCRV(I),
    1AKAPA(I),NNASP(I)
     NASPH=NNASP(I)
     IF(NASPH)7,7,6
   6 READ (5,84)(CASPH(I,J),J=1,NASPH)
     WRITE(6,84)(CASPH(I,J),J=1,NASPH)
   7 IF(DABS(SCRV(I)).GT.1.0D0)  SCRV(I)=1.0D0/SCRV(I)
  10 CONTINUE
```

227

```
      READ (5,78)CXTLT,CYTLT,ISPHR
      WRITE(6,78)CXTLT,CYTLT,ISPHR
      XMONC=0.0
      IF (((CXTLT .NE. 0.0) .OR. (CYTLT .NE. 0.0)  .OR.
     1 (ISPHR .NE. 0.0))    XMONC =1.0
C********INPUT VALUES OF XLAM.(FOR INTERFEROMETRIC PLOT)
C********(FOR FAR-FIELD CALCULATIONS AND BEAM-QUALITY
C********MICRONS, BUT ARE CONVERTED INTERNALLY TO CM.
C********EACH IS THAT OF HE-NE.
      READ (5,81            )FNX,FNY,XFMAX,YFMAX,XLAMI,XMAG1,XMITR
      IF(XNITR .EQ. 0.0) XNITR=1.0
      WRITE(6,81            )FNX,FNY,XFMAX,YFMAX,XLAMI,XMAG1,XNITR
      READ (5,81)CFFLD,SATUR,PLMIN,WRFFI,XNDFA,SYMBL,XLAM
      WRITE(6,81)CFFLD,SATUR,PLMIN,WRFFI,XNDFA,SYMBL,XLAM
      IF(XNDFA .EQ. 0.0)XNDFA=5.0
      READ (5,81)XNFFX,XNFFY,A10A2X,A10A2Y
      WRITE(6,81)XNFFX,XNFFY,A10A2X,A10A2Y
      EPSXS=EPSXD
      EPSYS=EPSYD
      NX=FNX
      NY=FNY
      IF(( NX .GT. MNX) .OR. (NY .GT. MNY))  GO TO
      IF ((XNITR .GT. 1.0) .AND. (( NX .GT. MVX)  .OR.  (NY .GT. MNY))
     160 TO 370


      IF(XLAM .EQ. 0.0) XLAM=0.6328
      IF(XLAMI .EQ. 0.0) XLAMI=0.6328
      XLAM=XLAM*1.0E-4
      XLAMI=XLAMI*1.0E-4
      WRITE(6,76)
      XMAGX=SCRV(2)/SCRV(3)
      IF(XMAG1 .NE. 0.0) XMAGX=1.0D0
      XMAGY=XMAGX
      IF(A10A2X .EQ. 0.0)A10A2X=1.0/XMAGX
      IF(A10A2Y .EQ. 0.0)A10A2Y=1.0/XMAGY
      DO 4 IMIR=2,IMMAX
      CDIST(IMIR) = DSQRT( (  XCRD(IMIR) - XCRD(I-1))**2 +
     1 (YCRD(IMIR) - YCRD(IMI-1))**2 +
     2 (ZCRD(IMIR) - ZCRD(IMI-1))**2 )
      WRITE(6, 99) IMIR,CDIST IMIR)
    4 CONTINUE
   99 FORMAT('   CDIST(',I2,') =   ',E20.12)
      DO 5 I=1,NX
      DO 5 J=1,NY
    5 DELZS(I,J) = 0.0
      XMITR=1.0
   11 WRITE(6,94)XMITR
   94 FORMAT(1H1,'   ITERATION   ',F4.0)
      IF(XMITR-1.0)13,15,12
   12 DO 13 I=1,NX
      DO 13 J=1,NY
      DELZST(I,J) =   DELZS(I,J)
```

```
      AOUTT(I,J) = AOUT(I,J)
      BOUTT(I,J) =  BOUT(I,J)
   13 CONTINUE
   15 WRITE(5,70)
      IF(PRFLL)9,9,9
    9 WRITE(5,93)
   93 FORMAT(1X,'        XF            YF            OPD            X
     1    Y            Z            A            B            C  ')
      WRITE(5,70)
    9 DO 200 IXX=1,NX
      FIX=IXX
      XFRAC=2.0*(FIX-1.0)/(FNX-1.0)
      XF=(-XFMAX+XFRAC*XFMAX)        + EPSXD*XFMAX
      XFF(IXX)=XF
      XO=XF/XMAGX
      DO 200 IYY=1,NY
      FIY=IYY
      YFRAC=2.0*(FIY-1.0)/(FNY-1.0)
      YF=(-YFMAX+YFRAC*YFMAX)        + EPSYD*YFMAX
      YFF(IYY)=YF
      YO=YF/XMAGY
      XIN=XO
      YIN=YO
      XA(1)=XO
      YA(1)=YO
      ZA(1) = ZCRD(1)
      OPDIN=0.0
      IF (XNONC  .NE.  0.0)   PDIN = CXTLT*XO + CYTLT*YO + CSPHR/TWO*
     1(XO**2 + YO**2)
      IF(XMITR-1.0)20,20,22




   20 AA(1)=0.0
      BA(1)=0.0
      CA(1)=1.0
      IF (XNONC .EG. 0.0)  GO TO 25
      AA(1) = CXTLT + CSPHR*X
      BA(1) = CYTLT + CSPHR*YO
      CA(1) = DSQRT(1.0D0 - AA(1)**2 - BA(1)**2)
      GO TO 25
   22 CALL        INTRP(XIN,YIN,XOUT,YOUT,    3.0,DELZST,OPDIN,NMX,NMY)
      CALL        INTRP(XIN,YIN,XOUT,YOUT,    3.0,AOUTT,AIN ,NMX,NMY)
      CALL        INTRP(XIN,YI ,XOUT,YOUT,    3.0,BOUTT,BIN ,NMX,NMY)
      AA(1) = AIN
      BA(1) = BIN
      CA(1) = DSQRT(1.0D0 - A (1)**2 - BA(1)**2)
   25 CONTINUE
      DELLZ = ZERO
      IF(PRNTP)27,27,26
   26 WRITE(6,95)XA(1),YA(1),OPDIN
```

```
   95 FORMAT(' XA(1)=',E13.6,'   YA(1)=',E13.6,'   OPDIN=',E17.6)
      WRITE(6,95)AA(1),BA(1),CA(1)
   96 FORMAT(' AA(1)=',E13.6,'   BA(1)=',E13.6,'   CA(1)=',E20.12)
   27 DO 140 IMIR=2,INMAX
      CALL TFDATR(IMIR-1,IMIR)
      IF(PRDGS)112,112,110
  110 WRITE(6,1001)IMIR,XI(IMIR),YI(IMIR),ZI(IMIR)
 1001 FORMAT(1X,14HTFDATR,  IIR=,I2,6H   XI=,E20.12,6H   YI=,E20.12,
     16H   ZI=,E20.12)
      WRITE(6,1002)IMIR,AI(IMIR),BI(IMIR),CI(IMIR)
 1002 FORMAT(1X,14HTFDATR,  IIR=,I2,6H   AI=,E20.12,6H   BI=,E20.12,
     16H   CI=,E20.12)
  112 INEF1=0
      IF(IMIR .EQ.INMAX) INEF1=1
      NASPH=NNASP(IMIR)
      CALL      INTREF(IMIR,INEF1,NASPH,TPAR)
      DELLZ = DELLZ + TPAR - ODIST(IMIR)
      IF(PRDGS)120,120,114
  114 WRITE(6,1003)IMIR,XR(IMIR),YR(IMIR),ZR(IMIR),TPAR
 1003 FORMAT(1X,14HINTREF,  IIR=,I2,6H   XR=,E20.12,6H   YR=,E20.12,
     16H   ZR=,E20.12,7H   TPA=,E20.12)
      WRITE(6,1004)IMIR,AR(IMIR),BR(IMIR),CR(IMIR)
 1004 FORMAT(1X,14HINTREF,  IIR=,I2,6H   AR=,E20.12,6H   BR=,E20.12,
     16H   CR=,E20.12)
  120 CALL TFIRTA(IMIR,IMIR)
      IF(PRDGS)124,124,122
  122 WRITE(6,1005)IMIR,XA(IMIR),YA(IMIR),ZA(IMIR)
 1005 FORMAT(1X,14HTFIRTA,  IIR=,I2,6H   XA=,E20.12,6H   YA=,E20.12,
     16H   ZA=,E20.12)
      WRITE(6,1006)IMIR,AA(IMIR),BA(IMIR),CA(IMIR)
 1006 FORMAT(1X,14HTFIRTA,  IIR=,I2,6H   AA=,E20.12,6H   BA=,E20.12,
     16H   CA=,E20.12)
  124 CONTINUE
  140 CONTINUE
      IF(PRDGS .GT. 0.0)WRITE(6,1008)DELLZ
 1008 FORMAT('                    DELLZ=',E15.8)
      OPDSM=OPDIN + DELLZ
      DELZS(IXX,IYY) = OPDSM
      IF(XNITR-1.0) 127,127,126
```



```
  126 XOUT(IXX,IYY) = XA(INMAX)
      YOUT(IXX,IYY) = YA(INMAX)
      AOUT(IXX,IYY) = AA(INMAX)
      BOUT(IXX,IYY) = BA(INMAX)
  127 IF(PRALL)200,200,199
  199 WRITE(6,92)XF,YF,OPDSM,XA(INMAX),YA(INMAX),ZA(INMAX),AA(INMAX),
     1BA(INMAX),CA(INMAX)
```

```
200 CONTINUE
    SOPD=0.0
    SOPDS=0.0
    DO 230 I=1,NX
    DO 230 J=1,NY
    SOPD = SOPD + DELZS(I,J)
230 SOPDS = SOPDS + DELZS(I,J)**2
    SOPD = SOPD/FNX/FNY
    SSOPD =  SOPD**2
    SOPDS = SOPDS/FNX/FNY
    RMSOP = SQRT(SOPDS - SSOPD)
    WRITE(6,75)
    WRITE(6,95)RMSOP
 95 FORMAT('   RMSOP= ',E14.8)
    DLPHI= RMSOP/XLAM*2.0*PI
    RLINT = EXP(-DLPHI**2)
    WRITE(6,91)XLAM,RLINT
 91 FORMAT(1H0,'  FOR XLAM =',E14.6,',NOMINAL RELATIVE CENTRAL INTEN
   1TY =',E14.6)
    IF(FITLS .GT. 0.0)CALL FITLSQ(DELZS,NX,NY,XFF,YFF,NA,NNX,NNY,0.0
    IF(CPLT .LT. 1.0) GO TO 150
    WRITE(6,94)XMITR
                         CALL CONTR (DELZS,NX,NY,XLAMI,XPLTR,NNX,NNY)
150 XMITR=XMITR+1.0
    IF(XMITR-XNITR)11,11,160
160 IF(FITLS .LT. 2.0) GO TO 170
    WRITE(6,77)
                         CALL FITLSQ(DELZS,NX,NY,XFF,YFF,NB,NNX,NNY,1.0
170 IF(CFFLD .GT. 0.0)CALL FRPROP(FNX,FNY,XFMAX,YFMAX,XLAM ,A10A2X,
   1A10A2Y,XNFFX,XNFFY,EPSXS,EPSYS,SATUR,PLMIN,0.01,XNDFA,WRFFI,DELZ
   2SYMBL)
    GO TO 1
200 WRITE(6,97)
 97 FORMAT('      DIMENSION TROUBLE RE NX, NY, ETC.')
999 STOP
    END
```

231

```
      SUBROUTINE INTREF(I,INE 1,NASPH,TPAR)
      DOUBLE PRECISION XA,YA, A,AA,BA,CA,XI,YI,ZI,AI, 1,C
      DOUBLE PRECISION XR,YR,ZR,AR,BR,CR,SCRV,AKAPA
      DOUBLE PRECISION XCRD,YCRD,ZCRD,THETX,THETY
      DOUBLE PRECISION TEST,F,FP,DELT,TPAR,ONE,TWC
      DOUBLE PRECISION CASPH, HOSQ,RADC,E,XJJ,FX,FY,FZ,FT,COSTH
      DIMENSION XA(10),YA(10),ZA(10),AA(10),BA(10),CA(10)
      DIMENSION AI(10),YI(10),ZI(10),AI(10),BI(10),CI(10)
      DIMENSION XP(10),YR(10),ZR(10),AR(10),BR(10),CR(10)
      DIMENSION SCRV(10),AKAP (10)
      DIMENSION XCRD(10),YCRD(10),ZCRD(10),THETX(10),THETY(10)
      DIMENSION CASPH(10,7)




      COMMON XA,YA,ZA,AA,BA,C ,XR,YP,ZR,AP,BR,CR,XI,YI,ZI,AI,EI,CI,
     1XCRD,YCRD,ZCRD,THETX,TH TY,SCRV,AKAPA,CASPH
      ONE=1.0
      TWC=2.0
      TEST=0.000000001
      IITER=0
      TPAR=-ZI(I)/CI(I)
100   XR(I)=XI(I) + AI(I) * T AR
      YR(I)=YI(I) + BI(I) * TPAR
      ZR(I)=ZI(I) + CI(I) * T AR
      IF(NASPH)110,110,120
110   F      =ZR(I)+SCRV(I)/TW *(XR(I)**2+YR(I)**2+AKAPA(I)*ZR(I)**2)
      FX=SCRV(I)*XR(I)
      FY=SCRV(I)*YR(I)
      FZ=ONE+AKAPA(I)*SCRV(I)*ZP(I)
      GO TO 142
120   RHOSQ=XR(I)**2 + YR(I)**2
      IF(RHOSQ .EG. 0.0) RHOSQ=1.0D-50
      RADC=DSQRT(ONE - AKAPA( )*SCRV(I)**2*RHOSQ)
      F = ZR(I) + SCRV(I)*RHO Q/(ONE + RADC)
      DO 130 II=1,NASPH
      F = F - CASPH(I,II) * RHOSQ ** II
130   CONTINUE
      E = -SCRV(I)/RADC
      DO 140 JJ=1,NASPH
      XJJ=JJ
      E = E + TWO * XJJ * CASPH(I,JJ) * RHOSQ **(JJ-1)
140   CONTINUE
      FX=-E*XR(I)
      FY=-E*YR(I)
      FZ=ONE
142   FP = AI(I)*FX + BI(I)*FY + CI(I)*FZ
      DELT=-F/FP
      TPAR=TPAR+DELT
      IF(DABS(DELT)-TEST)  5,150,150
```

232

```
150 IITER=IITER+1
    IF(IITER-10)100,100,999
999 WRITE(6,998)
998 FORMAT(1X,16H IITER IN INTREF)
  5 IF(INEF1)20,20,10
 10 AR(I)=AI(I)
    BR(I)=BI(I)
    CR(I)=CI(I)
    GO TO 300
 20 FT=DSQRT(FX**2+FY**2+FZ**2)
    COSTH=(AI(I)*FX+BI(I)*FY+CI(I)*FZ)/FT
    AR(I)=AI(I) - TWO * COSTH * FX/FT
    BR(I)=BI(I) - TWO * COSTH * FY/FT
    CR(I)=CI(I) - TWO * COSTH * FZ/FT
300 RETURN
    END
```

SUBROUTINE TFDATR (I,J)

DOUBLE PRECISION XA,YA,ZA,AA,BA,CA,XI,YI,ZI,AI,BI,CI

```
      DOUBLE PRECISION XR,YR,ZR,AR,BR,CR,SCRV,AKAPA
      DOUBLE PRECISION XCRD,YCRD,ZCRD,THETX,THETY
      DOUBLE PRECISION XINT1,YINT1,ZINT1,AINT1,BINT1,CINT1
      DOUBLE PRECISION XINT2,YINT2,ZINT2,AINT2,BINT2,CINT2
      DOUBLE PRECISION XINT3,YINT3,ZINT3,AINT3,BINT3,CINT3
      DIMENSION XA(10),YA(10),ZA(10),AA(10),BA(10),CA(10)
      DIMENSION XI(10),YI(10),ZI(10),AI(10),BI(10),CI(10)
      DIMENSION XR(10),YR(10),ZR(10),AR(10),BR(10),CR(10)
      DIMENSION SCRV(10),AKAPA(10)
      DIMENSION XCRD(10),YCRD(10),ZCRD(10),THETX(10),THETY(10)
      COMMON XA,YA,ZA,AA,BA,CA,XR,YR,ZR,AR,BR,CR,XI,YI,ZI,AI,BI,CI,
     1XCRD,YCRD,ZCRD,THETX,THETY,SCRV,AKAPA
      XINT1=XA(I) - XCRD(J)
      YINT1=YA(I) - YCRD(J)
      ZINT1=ZA(I) - ZCRD(J)
      AINT1=AA(I)
      BINT1=BA(I)
      CINT1=CA(I)
      YINT2=YINT1
      BINT2=BINT1
      IF(THETY(J))100,200,100
  100 ZINT2=ZINT1*DCOS( THETY(J)) - XINT1*DSIN( THETY(J))
      CINT2=CINT1*DCOS( THETY(J)) - AINT1*DSIN( THETY(J))
      XINT2=ZINT1*DSIN( THETY(J)) + XINT1*DCOS( THETY(J))
      AINT2=CINT1*DSIN( THETY(J)) + AINT1*DCOS( THETY(J))
      GO TO 300
  200 ZINT2=ZINT1
      CINT2=CINT1
      XINT2=XINT1
      AINT2=AINT1
  300 XINT3=XINT2
      AINT3=AINT2
      IF(THETX(J))400,500,400
  400 YINT3=YINT2*DCOS( THETX(J)) - ZINT2*DSIN( THETX(J))
      BINT3=BINT2*DCOS( THETX(J)) - CINT2*DSIN( THETX(J))
      ZINT3=YINT2*DSIN( THETX(J)) + ZINT2*DCOS( THETX(J))
      CINT3=BINT2*DSIN( THETX(J)) + CINT2*DCOS( THETX(J))
      GO TO 600
  500 YINT3=YINT2
      BINT3=BINT2
      ZINT3=ZINT2
      CINT3=CINT2
```

234

```
   600 CONTINUE
       XI(J)=XINT3
       YI(J)=YINT3
       ZI(J)= ZINT3
       AI(J)=AINT3
       BI(J)=BINT3
       CI(J)=CINT3
       RETURN
       END
```

```
       SUBROUTINE TFIRTA (I,J)


       DOUBLE PRECISION XA,YA,ZA,AA,BA,CA,XI,YI,ZI,AI,BI,CI




       DOUBLE PRECISION XR,YR,ZR,AR,BR,CR,SCRV,AKAPA
       DOUBLE PRECISION XCRD,YCRD,ZCRD,THETX,THETY
       DOUBLE PRECISION XINT1,YINT1,ZINT1,AINT1,BINT1,CINT1
       DOUBLE PRECISION XINT2,YINT2,ZINT2,AINT2,BINT2,CINT2
       DOUBLE PRECISION XINT3,YINT3,ZINT3,AINT3,BINT3,CINT3
       DIMENSION XA(10),YA(10),ZA(10),AA(10),BA(10),CA(10)
       DIMENSION XI(10),YI(10),ZI(10),AI(10),BI(10),CI(10)
       DIMENSION XR(10),YR(10),ZR(10),AR(10),BR(10),CR(10)
       DIMENSION SCRV(10),AKAPA(10)
       DIMENSION XCRD(10),YCRD(10),ZCRD(10),THETX(10),THETY(10)
       COMMON XA,YA,ZA,AA,BA,CA,XR,YR,ZR,AR,BR,CR,XI,YI,ZI,AI,BI,CI,
      1XCRD,YCRD,ZCRD,THETX,THETY,SCRV,AKAPA
       XINT1=XR(I)
       YINT1=YR(I)
       ZINT1=ZR(I)
       AINT1=AR(I)
       BINT1=BR(I)
       CINT1=CR(I)
       XINT2=XINT1
       AINT2=AINT1
       IF(THETX(I))100,200,100
   100 YINT2=YINT1*DCOS(-THETX(I)) - ZINT1*DSIN(-THETX(I))
       BINT2=BINT1*DCOS(-THETX(I)) - CINT1*DSIN(-THETX(I))
       ZINT2=YINT1*DSIN(-THETX(I)) + ZINT1*DCOS(-THETX(I))
       CINT2=BINT1*DSIN(-THETX(I)) + CINT1*DCOS(-THETX(I))
       GO TO 300
   200 YINT2=YINT1
       BINT2=BINT1
       ZINT2=ZINT1
       CINT2=CINT1
   300 YINT3=YINT2
       BINT3=BINT2
       IF(THETY(I))400,500,400
```

235

```
  400 ZINT3=ZINT2*DCOS(-THETY(I)) - XINT2*DSIN(-THETY(I))
      CINT3=CINT2*DCOS(-THETY(I)) - AINT2*DSIN(-THETY(I))
      XINT3=ZINT2*DSIN(-THETY(I)) + XINT2*DCOS(-THETY(I))
      AINT3=CINT2*DSIN(-THETY(I)) + AINT2*DCOS(-THETY(I))
      GO TO 600
  500 ZINT3=ZINT2
      CINT3=CINT2
      XINT3=XINT2
      AINT3=AINT2
  600 CONTINUE
      XA(J)=XINT3 + XCRD(I)
      YA(J)=YINT3 + YCRD(I)
      ZA(J)=ZINT3 + ZCRD(I)
      AA(J)=AINT3
      BA(J)=BINT3
      CA(J)=CINT3
      RETURN
      END




      SUBROUTINE CONTR(PLOT,NX,NY,XLAM,XPLTR,NNX,NNY)
      DIMENSION PLOT(NNX,NNY)
      DIMENSION GRAPH(131),SYBOL(50)
      DATA (SYMBOL(I),I= 1,10)/1H ,1HY,1H ,1HX,1H ,1HW,1H ,1HV,1H ,1HU/
      DATA (SYMBOL(I),I=11,20)/1H ,1HT,1H ,1HS,1H ,1HR,1H ,1HQ,1H ,1HP/




      DATA (SYMBOL(I),I=21,30)/1H ,1HO,1H ,1HN,1H ,1HM,1H ,1HL,1H ,1HK/
      DATA (SYMBOL(I),I=31,40)/1H ,1HJ,1H ,1HI,1H ,1HH,1H ,1HG,1H ,1HF/
      DATA (SYMBOL(I),I=41,50)/1H ,1HE,1H ,1HD,1H ,1HC,1H ,1HB,1H ,1HA/
      WRITE(6,1001)
 1001 FORMAT(1H0,'      CONTOU  PLOT OF OPTICAL PATH DIFFERENCE')
      WRITE(6,76)
      DO 120 K=1,131
  120 GRAPH(K)=SYMBOL(1)
      IF(XPLTR)115,115,105
  105 XLL=PLOT(1,1)
      XUL=PLOT(1,1)
      DO 110 I=1,NX
      DO 110 J=1,NY
      IF(PLOT(I,J).LT.XLL) XLL=PLOT(I,J)
  110 IF(PLOT(I,J).GT.XUL) XUL=PLOT(I,J)
      XRNG=XUL - XLL
      WRITE(6,112)XLL,XUL
  112 FORMAT(1X,'Z=  ',E10.4,'   A=  ',E10.4)
      GO TO 114
  115 WRITE(6,113)XLAM
  113 FORMAT(1X,' XLAM=  ',E10.4)
  114 WRITE(6,76)
```

236

```
   76 FORMAT(1H0)
      DO 140 J=1,NY
      DO 135 I=1,NX
      IF(XPLTR)130,130,132
  130 K=PLOT(I,J)/XLAM*2.0+24.5
      GO TO 135
  132 K = (PLOT(I,J) - XLL)/XRNG*50.0+1.0
  133 IF(K.GT.50) K=50
      IF(K.LT.1)K=1
  135 GRAPH(I)=SYMBOL(K)
      WRITE(6,136)GRAPH
  136 FORMAT(1X,131A1)
  140 CONTINUE
      WRITE(6,76)
      WRITE(6,75)
      RETURN
      END



      SUBROUTINE FITLSQ(FCN      ,NX,NY,XFF,YFF,NA,NNX,NNY,XNDD)
      DIMENSION XFF(NNX),YFF(NNY),FCN(NNX,NNY)
      DIMENSION G(10,11),COF(10)
      GNX=NX
      GNY=NY
      NAP1=NA+1
      DO 10 I=1,NA
      DO 10 J=1,NAP1
   10 G(I,J)=0.0
      DO 40 I=1,NX
      XG=XFF(I)
      DO 40 J=1,NY
      YG=YFF(J)
      DO 35 K=1,NA
      G(K,NA+1)=G(K,NA+1) - FCN(I,J)*FFIT(K,XG,YG)
      DO 30 L=1,NA
      G(K,L) =  G(K,L) + FFIT(K,XG,YG) * FFIT(L,XG,YG)




   30 CONTINUE
   35 CONTINUE
   40 CONTINUE
  200 CONTINUE
      LIMK = NA - 1
      IF(LIMK) 43,43,44
   43 COF(1)=-G(1,2)/G(1,1)
      GO TO 62
   44 DO 50 K=1,LIMK
      IC=K+1
      DO 50 I=IC,NA
      FACT=-G(I,K)/G(K,K)
```

237

```fortran
      LIMJ=NA+2
      DO 50 J=K,LIMJ
50    G(I,J) = FACT * G(K,J) + G(I,J)
      COF(NA) = -G(NA,NA+1)/G(NA,NA)
      LIMI=NA-1
      DO 70 IA=1,LIMI
      I=NA-IA
      XB = G(I,NA+1)
      IP=I+1
      DO 60 J=IP,NA
60    XB = XB + G(I,J)*COF(J)
      COF(I) = -XB/G(I,I)
70    CONTINUE
62    CONTINUE
      DO 80 I=1,NA
80    WRITE(6,84)I,COF(I)
84    FORMAT(1X,'COF(',I2,')=',6E15.8)
      SOPD =0.0
      SOPDS =0.0
      DO 100 I=1,NX
      XG=XFF(I)
      DO 100 J=1,NY
      YG=YFF(J)
      FCNN=FCN(I,J)
      DO 90 K=1,NA
      FCNN = FCNN - COF(K) * FFIT(K,XG,YG)
90    CONTINUE
      IF (XMOD .NE. 0.0)    FC (I,J) = FCNN
      SOPD = SOPD + FCNN
      SOPDS = SOPDS + FCNN**2
100   CONTINUE
      SOPD = SOPD/GNX/GNY
      SSOPD = SOPD**2
      SOPDS = SOPDS/GNX/GNY
      RMSOP = SQRT(SOPDS - SSOPD)
      WRITE(6,98)NA,RMSOP
98    FORMAT(1H0,'   REDUCED RMSOP, BASED ON FIRST ',I3,' FUNCTIONS, IS
     1,E16.8)
      IF(XMOD .NE. 0.0)WRITE(:,97)
97    FORMAT(1H0,'ARRAY OF OPDS HAS BEEN MODIFIED BY SUBROUTINE FITLSG')
      RETURN
      END
```

```
      FUNCTION FFIT(K,XG,YG)
      GO TO (10,20,30,40,50,60,70),K




   10 FFIT=XG
      GO TO 1000
   20 FFIT=YG
      GO TO 1000
   30 FFIT=(XG**2+YG**2)
      GO TO 1000
   40 FFIT=XG**2
      GO TO 1000
   50 FFIT= (XG**2+YG**2)**2
      GO TO 1000
   60 FFIT = YG**3
      GO TO 1000
   70 FFIT = XG**2 * YG
      GO TO 1000
 1000 RETURN
      END
```

239

```
      DIMENSION U(4),VALL(4)
      DIMENSION XT(NMX,NMY), YT(NMX,NMY), FT(NMX,NMY)
      XNCR = XT(2,1) - XT(1,1)
      YNCR = YT(1,2) - YT(1,1)
      IXARG = (X        - XT(1,1))/XNCR +1.0
      IF(IXARG .LT. 2) IXARG=2
      JYARG = (Y        - YT(1,1))/YNCR +1.0
      IF(JYARG .LT. 2) JYARG=2
      DO  20 IXRUN=1,4
      IXRUM=IXRUN-2
      DO  10 JYRUN=1,4
      JYRUM=JYRUN-2
      U(JYRUN) = FT(IXARG + IXRUM,JYARG + JYRUM)
 10   CONTINUE
      FRACT=(Y - YT(IXARG,JYARG))/(YT(IXARG,JYARG+1) - YT(IXARG,JYARG))
      VFRAC = FRACT - 0.5
      VAL             = (U(3) +  (2))/2.0 + VFRAC*(U(3) - U(2))
      IF(XNTOR - 2.0) 139,138,137
137   VAL=VAL + VFRAC*(VFRAC**2-0.25) * (U(4) - 3.0*U(3) + 3.0*U(2)
     1- U(1))/6.0
138   VAL=VAL + (VFRAC**2-0.25) * (U(4) - U(3) - U(2) + U(1))/4.0
139   VALL(IXRUN) = VAL
 20   CONTINUE
      DO  30 IXRUN=1,4
      U(IXRUN) = VALL(IXRUN)
 30   CONTINUE
      FRACT=(X - XT(IXARG,JYARG))/(XT(IXARG+1,JYARG) - XT(IXARG,JYARG))
      VFRAC = FRACT - 0.5
      VAL             = (U(3) + U(2))/2.0 + VFRAC*(U(3) - U(2))
      IF(XNTOR - 2.0) 239,238,237
237   VAL=VAL + VFRAC*(VFRAC**2-0.25) * (U(4) - 3.0*U(3) + 3.0*U(2)
     1- U(1))/6.0
238   VAL=VAL + (VFRAC**2-0.25) * (U(4) - U(3) - U(2) + U(1))/4.0
239   F       =        VAL
      RETURN


      END
```

240

```fortran
      SUBROUTINE  FRPROP(FNX,FNY,XFMAY,YFMAY,XLAM,A1OA2X,A1OA2Y,
     1XNFFX,XNFFY,EPSX,EPSY,SATUR,PLMIN,FNOA,XNDFA,WRFFI,DELZS,SYMBL)

      PARAMETER NNX=85, NNY=51
      DIMENSION FFI(101)
      DIMENSION FCTX(101),FCTY(101)
      DIMENSION GRAPH(131),SYMBOL(50),DELZS(NNX,NNY)
      DIMENSION SYMBOM(50)
      COMPLEX UNFLD(NNX,NNY), FFFCX, FFFCY,CPHSE
      COMPLEX AY(101), BY(101), FAY(101), FBY(101)
      COMPLEX FFAMP
      DOUBLE PRECISION FNX,FNY,XFMAY,YFMAY
70    FORMAT(1H0)
77    FORMAT(1H1)
83    FORMAT(1X,10E12.6)
86    FORMAT(' ARRAY SIZE EXCEDED DIMENSION')
87    FORMAT(' COLLIMATED-BEAM FRESNEL NUMBER ALONG X IS FNOX= ',F10.5)
88    FORMAT(' COLLIMATED-BEAM FRESNEL NUMBER ALONG Y IS FNOY= ',F10.5)
89    FORMAT(1X,' INCREMENTAL FAR-FIELD ARGUMENTS ARE  ',2E16.8)
      DATA PI/3.1415926536/
      DATA (SYMBOL(I),I= 1,10)/1H ,1HY,1H ,1HX,1H ,1HW,1H ,1HV,1H ,1HU/
      DATA (SYMBOL(I),I=11,20)/1H ,1HT,1H ,1HS,1H ,1HR,1H ,1HQ,1H ,1HP/
      DATA (SYMBOL(I),I=21,30)/1H ,1HO,1H ,1HN,1H ,1HM,1H ,1HL,1H ,1HK/
      DATA (SYMBOL(I),I=31,40)/1H ,1HJ,1H ,1HI,1H ,1HH,1H ,1HG,1H ,1HF/
      DATA (SYMBOL(I),I=41,50)/1H ,1HE,1H ,1HD,1H ,1HC,1H ,1HB,1H ,1HA/
      DATA (SYMBOM(I),I= 1,10)/1HY,1HX,1HW,1HV,1HU,1HT,1HS,1HR,1HQ,1HP/
      DATA (SYMBOM(I),I=11,20)/1HO,1HN,1HM,1HL,1HK,1HJ,1HI,1HH,1HG,1HF/
      DATA (SYMBOM(I),I=21,30)/1HE,1HD,1HC,1HB,1HA,1HY,1HX,1HW,1HV,1HU/
      DATA (SYMBOM(I),I=31,40)/1HT,1HS,1HR,1HQ,1HP,1HO,1HN,1HM,1HL,1HK/
      DATA (SYMBOM(I),I=41,50)/1HJ,1HI,1HH,1HG,1HF,1HE,1HD,1HC,1HB,1HA/
      GNX=FNX
      GNY=FNY
      XFMAX=XFMAY
      YFMAX=YFMAY
      XMAG2X =1.0
      XMAG2Y =1.0
```

```fortran
      NFFLX=XNFFX
      NFFLY=XNFFY
      NCNTX=(NFFLX+1)/2
      NCNTY=(NFFLY+1)/2
      IF(XNFFX .GT. 101.0)WRITE(6,86)
      IF(XNFFY .GT. 101.0)WRITE(6,86)
      IF(SATUR .EQ. 0.0) SATUR =1.0
      IF(PLMIN .NE. 0.0) CPLTT=50.0/ALOG(PLMIN)
      NX=GNX
      NY=GNY
      WNFLX=2.0*XFMAX*(GNX+1. )/GNX
      WNFLY=2.0*YFMAX*(GNY+1.0)/GNY
```

```fortran
      DXTLA = (XFMAX * (GNX+1.0)/GNX) **2 /FNOA
      DYTLA = (YFMAX * (GNY+1.0)/GNY) **2 /FNOA
      WFFLX = XNDFA*    DXTLA/WNFLX
      WFFLY = XNDFA*    DYTLA/WNFLY
      FNOA=(WNFLX/2.0)**2/DXTLA
      FNOY=(WNFLY/2.0)**2/DYTLA
      WRITE(6,77)
      WRITE(6,87)FNOX
      WRITE(6,88)FNOY
      XINCF=WFFLX/XNFFX
      YINCF=WFFLY/XNFFY
      XINCN=WNFLX/GNX
      YINCN=WNFLY/GNY
      XMIDFX=(XNFFX+1.0)/2.0
      XMIDFY=(XNFFY+1.0)/2.0
      FFARX = XINCF/DXTLA*WNFLX
      FFARY = YINCF/DYTLA*WNFLY
      WRITE(6,89)FFARX,FFARY
      WRITE(6,76)
      WRITE(6,75)
   75 FORMAT(' FAR-FIELD INTENSITY')
      WRITE(6,76)
      AVINT=1.0
      AVAMP=SQRT(AVINT)
      DO 108 I=1,NX
      DO 108 J=1,NY
      PHSE = DELZS(I,J) / XLAM * 2.0 * PI
      CPHSE = CMPLX(0.0,PHSE)
      UNFLD(I,J) = AVAMP * CEXP(CPHSE)
  108 CONTINUE

      FACTX=XMAG2X/A10A2X
      OFFSX=EPSX*GNX   /2.0*(FACTX-1.0)/FACTX
      XMID=(GNX   +1.0)/2.0
      X2=XMID-OFFSX-GNX   /2.0/FACTX
      X3=XMID-OFFSX+GNX   /2.0/FACTX
      DO 350 J=1,NX
      XJ=J

      XJ=XJ-0.5
      FCTR=0.0
      IF(XJ-X2+1.0)320,320,310
  310 IF(XJ-X2)311,311,312
  311 FCTR=XJ+1.0-X2
      GO TO 320
  312 IF(XJ-X3+1.0)313,314,314
  313 FCTR=1.0
      GO TO 318
  314 IF(XJ-X3)315,320,320
  315 FCTR=X3-XJ
      GO TO 318
```

```fortran
  309 IF(XJ-X3+1.0)318,318,31
  317 FCTR=X3-X2
  319 CONTINUE
  320 FCTX(J) =        FCTR
  350 CONTINUE
      FACTY=XMAG2Y/A1GA2Y
      OFFSY=EPSY*GNY   /2.0*(FACTY-1.0)/FACTY
      YMID=(GNY   +1.0)/2.0
      X2=YMID-OFFSY-GNY   /2.0/FACTY
      X3=YMID-OFFSY+GNY   /2.0/FACTY
      DO 370 J=1,NY
      XJ=J
      XJ=XJ-0.5
      FCTR=0.0
      IF(XJ-X2+1.0)330,330,32
  326 IF(XJ-X2)321,321,322
  321 FCTR=XJ+1.0-X2
      GO TO 319
  322 IF(XJ-X3+1.0)323,324,324
  323 FCTR=1.0
      GO TO 328
  324 IF(XJ-X3)325,330,330
  325 FCTR=X3-XJ
      GO TO 328
  319 IF(XJ-X3+1.0)328,328,327
  327 FCTR=X3-X2
  328 CONTINUE
  330 FCTY(J) =        FCTR
  370 CONTINUE
      XINTS = 0.0
      DO 380 JNX=1,NX
      DO 380 JNY=1,NY
      XINTS=XINTS+(1.0 - FCTX(JNX)*FCTY(JNY))*UNFLD(JNX,JNY)*
     1CONJG(UNFLD(JNX,JNY))
  380 CONTINUE
C********NOTE THAT DEN WILL ALSO BE USED LATER FOR NORMALIZATION.
      DEN =   GNX*GNY * (1.0 - 1.0/FACTX/FACTY)
      XINTS = XINTS/DEN

      WRITE(6,76)
      WRITE(6,76)
      WRITE(6,76)
      XMXI=0.0
      DO 400 IFY=1,NFFLY
      YIF = IFY
      YFAR = (YIF - XMIDFY)*YINCF
      DO 336 JNX=1,NX
      AY(JNX) = CMPLX(0.0,0.0)
      BY(JNX) = CMPLX(0.0,0.0)
      DO 335 JNY=1,NY
      YJ=JNY
      YNEAR=(YJ-YMID )*YINCN
      ARGY =(YNEAR**2 - 2.0 * YNEAR * YFAR)/DYTLA*PI
      ARGSY=SIN(ARGY)
      ARGCY=COS(ARGY)
      FFFCY=CMPLX(ARGCY,ARGSY)
      AY(JNX) = AY(JNX) + UNFLD(JNX,JNY) * FFFCY
      BY(JNX) = BY(JNX) + UNFLD(JNX,JNY) * FFFCY * FCTY(JNY)
  335 CONTINUE
  336 CONTINUE
      DO 390 IFX=1,NFFLX
```

```fortran
      XIF = IFX
      XFAR = (XIF - XMIDFX)*XINCF
      FAY(IFX) = CMPLX(0.0,0.0)
      FBY(IFX) = CMPLX(0.0,0.0)
      DO 345 JNX=1,NX
      XJ=JNX
      XNEAR=(XJ-XMID )*XINCN
      ARGX =(XNEAR**2 - 2.0 * XNEAR * XFAR)/DXTLA*PI
      ARGSX=SIN(ARGX)
      ARGCX=COS(ARGX)
      FFFCX=CMPLX(ARGCX,ARGSX)
      FAY(IFX) = FAY(IFX) + AY(JNX) * FFFCX
      FBY(IFX) = FBY(IFX) + BY(JNX) * FFFCX * FCTX(JNX)
  345 CONTINUE
      FFAMP = FAY(IFX) - FBY(IFX)
      FFI(IFX) =   FFAMP * CONJG(FFAMP)

      FFI(IFX) = FFI(IFX)/XINTS
      IF( (IFY .EQ. NCNTY) .AND. (IFX .EQ. NCNTX) ) CNTI=FFI(IFX)
      IF( FFI(IFX) .GT. XMXI) XMXI= FFI(IFX)
  390 CONTINUE
      IF(WRFFI .GT. 0.0)WRITE(6,83)YFAR
      IF(WRFFI .GT. 0.0)WRITE(6,83)(FFI(I),I=1,NFFLX)

      DO 120 K=1,131
  120 GRAPH(K)=SYMBOL(1)
      DO 135 I=1,NFFLX
      XK= FFI(I)/        SATUR
```

```fortran
      IF(PLMIN)131,131,130
  130  ARG=PLMIN/XK
      K =CPLTT*ALOG(ARG)
      GO TO 132
  131 K = XK*50.0+1.0
  132 IF(K.GT.50) K=50
      IF(K.LT.1)K=1
      IF(SYMBL)111,111,110
  110 GRAPH(I)=SYMBOM(K)
      GO TO 135
  111 GRAPH(I)=SYMBOL(K)
  135 CONTINUE
      WRITE(6,136)GRAPH
  136 FORMAT(1X,131A1)
  140 CONTINUE
C*********COMPLETE LOOP ON IFY
  400 CONTINUE
      WRITE(6,76)
      WRITE(6,76)
      WRITE(6,76)
      WRITE(6,78)CNTI
   78 FORMAT('     CENTRAL I/I  =   ',E13.6)
      WRITE(6,79)XMXI
   79 FORMAT('     MAXIMUM I/I  =   ',E13.6)
      RETURN
      END
```

```
2.00000      .00000        .00000       1.00000      1.00000       2.00000       .00000
 .00000      .00000        .00000       1.00000      1.00000       .00000        .00000
 .00000      .00000      250.00000       .00000      1.00000      -.00030       1.00000
 .00000      .00000        .00000        .00000      1.00000      -.00012       1.00000
 .00000      .00000        .00000       7.00000      1.00000       .00000        .00000
 .00000000000000     .000000000000000   2.000000000000000
      .00000000000000
11.00000     11.00000     10.00000      .00000       .00000       .00000        3.00000
 1.00000      1.00000       .00100     10.00000     10.00000       .00000       1.00000
33.00000     33.00000       .00000       .00000      5.00000       1.00000       .35100

CDIST( 2)=     .25000000000000+003
CDIST( 3)=     .25000000000000+003
CDIST( 4)=     .00000000000000
```

245

ITERATION   1.

RMSOP=   .24462200-005

FOR XLAM =   .351000-004,NOMINAL RELATIVE CENTRAL INTENSITY =   .525513+000

COF(1)= -.43922962-013
COF(2)= .10646844-013
COF(3)= .61451631-011
COF(4)= -.11984083-013
COF(5)= -.25930658-009
COF(6)= -.68787865-016
COF(7)= -.26484270-015

REDUCED RMSOP, BASED ON FIRST 7 FUNCTIONS, IS .51483278-010

246

ITERATION   1.

CONTOUR PLOT OF OPTICAL PATH DIFFERENCE

Z=   -.1037-004   A=   .0000

```
    I G I
  KG      GK
  GD      DG
I   AAA   I
    AAAAA
G  AAAAA  G
    AAAAA
I   AAA   I
  GD      DG
  KG      GK
    I G I
```

247

ITERATION   2.

RMSOP=   .25042938-005

FOR XLAM =   .351000-004,NOMINAL RELATIVE CENTRAL INTENSITY =   .817286+000

COF(1)= -.12641865-012
COF(2)= .10911575-012
COF(3)= .76120929-010
COF(4)= -.11891371-013
COF(5)= -.26630676-009
COF(6)= -.11846397-014
COF(7)= -.27450955-014

REDUCED RMSOP, BASED ON FIRST   7 FUNCTIONS, IS   .14194124-008

248

ITERATION   2.

    CONTOUR PLOT OF OPTICAL PATH DIFFERENCE

Z=   -.1064-004   A=   .0000

```
      I G I
   KG      GK
   GD      DG
 I   AAA    I
     AAAAA
 G   AAAAA  G
     AAAAA
 I   AAA    I
    G       G
   KG      GK
      I G I
```

ITERATION   3.

RMSOP=   .25106596-005

FOR XLAM =   .351000-004,NOMINAL RELATIVE CENTRAL INTENSITY =   .817106+000

COF(1)= -.10591979-012
COF(2)= .93867381-013
COF(3)= .14246547-039
COF(4)= -.98016436-014
COF(5)= -.26676265-009
COF(6)= -.97208547-015
COF(7)= -.23322061-014

REDUCED RMSOP, BASED ON FIRST   7 FUNCTIONS, IS   .21974580-008

ITERATION   3.

CONTOUR PLOT OF OPTICAL PATH DIFFERENCE

Z=   -.1064-004   A=   .0000

```
    I G I
 KG      GK
 GD      DG
I    AAA    I
    AAAAA
G   AAAAA   G
    AAAAA
I    AAA    I
 GD      DG
 KG      GK
    I G I
```

COF(1)= -.5919233c-013
COF(2)= -.62198930-013

REDUCED RMSOP, BASED ON FIRST   2 FUNCTIONS, IS   .25106590-00?

ARRAY OF OPDS HAS BEEN MODIFIED BY SUBROUTINE FITLSQ

251

COLLIMATED-BEAM FRESNEL NUMBER ALONG X IS FNOX=   .01000
COLLIMATED-BEAM FRESNEL NUMBER ALONG Y IS FNOY=   .01000
 INCREMENTAL FAR-FIELD ARGUMENTS ARE   .90909089-001   .15151515+000

    FAR-FIELD INTENSITY

```
XXXYYYYYYYVSRQPPQQQPOLJHFEDCCCDEFHJLOPQQGPPQRSVYYYYYYYXXX
YXXYYYYYYYWUSRRRSTUTRPMJHGFEEEFGHJMPRTUTSRRRSUWYYYYYYYXXY
YYYYYYYYYYYYYXXYYYYYYUQNLJIHHHIJLNQUYYYYYXXYYYYYYYYYYYYYY
YYYYYYYYYYYYYYYYYYYXTQNLJIHGGGHIJLNQTXYYYYYYYYYYYYYYYYYYY
YYYYYYYYYYYYYYWUTROMJHFECBAAAAABCEFHJMORTUWYYYYYYYYYYYYYY
WWXYYYYYYYVSPNMLKJHFECAXWVUUUUUVWXACEFHJKLMNPSVYYYYYYYXWW
SSTWYYYYYUPMJIGFFEDCAYWVTSSRRRSSTVWYACDEFFGIJMPLYYYYWTSS
JGRUYYYYRMIGEDCCBBAYXVUTSRRRRRSTUVXYABBCCDEGIMRYYYYURQG
PPRUYYYVOKHEDBBAAAAYXWVUUTSSSTUUVWXYAAAABBDEHKOVYYYURPP
QQSWYYYSMIFDCPAAABBCCCBAYYXXXYYABCCCJBAAAECDFIMSYYYWSJJ
QRUYYYYVOKGECBAABCDFIKMLJHFEEEFHJLMKIFDCBAABCEGKOVYYYURG
OPSXYYXQKGDBAYYABDFNVWNGCAXWVWXACGNWVNHDBAYYABDGKGXYXSPO
KLORTQLHDAYWWWYBFLUPGAVSQONNNOQSVAGPULFBYWWWYADHLQTROLK
HIJMNMIEAXVUUVWAELMEWSOMKJIIIJKMOSWEMLEAWVUUVXAEIMNMJIH
EFGIKJFBXVTSSTUXDHFXSOKIGFFEFFGIKOSXFHDXUTSSTVXBFJKIGFE
CDEHIHEAWUSRRSTWBFCUPLIGEDDCDDEGILPUCFBWTSRRSUWAEHIHEDC
CCEGIHEAWTSRRRTWBEBUPLIFEDCCCDEFILPUBEBWTRRRSTWAEHIGECC
CDEHIHEAWUSRRSTWBFCUPLIGEDDCDDEGILPUCFBWTSRRSUWAEHIHEDC
EFGIKJFBXVTSSTUXDHFXSOKIGFFEFFGIKOSXFHDXUTSSTVXBFJKIGFE
HIJMNMIEAXVUUVWAELMEWSOMKJIIIJKMOSWEMLEAWVUUVXAEIMNMJIH
KLORTQLHDAYWWWYBFLUPGAVSQONNNOQSVAGPULFBYWWWYADHLGTROLK
OPSXYYXQKGDBAYYABDHNVWNGCAXWVWXACGNWVNHDBAYYABDGKQXYXSPO
QRUYYYYVOKGECBAABCDFIKMLJHFEEEFHJLMKIFDCBAABCEGKOVYYYURQ
QQSWYYYSMIFDCBAAABBCCCBAYYXXXYYABCCCBBAAABCDFIMSYYYWSGQ
PPRUYYYVOKHEDBBAAAAYXWVUUTSSSTUUVWXYAAAABBDEHKOVYYYURPP
QQRUYYYYRMIGEDCCBBAYXVUTSRRRRRSTUVXYABBCCDEGIMRYYYYURQG
SSTWYYYYUPMJIGFFEDCAYWVTSSRRRSSTVWYACDEFFGIJMPUYYYYWTSS
WWXYYYYYYYVSPNMLKJHFECAXWVUUUUUVWXACEFHJKLMNPSVYYYYYYYXWW
YYYYYYYYYYYYYYWUTROMJHFECBAAAAABCEFHJMORTUWYYYYYYYYYYYYYY
YYYYYYYYYYYYYYYYYYYXTQNLJIHGGGHIJLNQTXYYYYYYYYYYYYYYYYYYY
YYYYYYYYYYYYYXXYYYYYYUQNLJIHHHIJLNQUYYYYYXXYYYYYYYYYYYYYY
YXXYYYYYYYWUSRRRSTUTRPMJHGFEFEFGHJMPRTUTSRRRSUWYYYYYYYXXY
XXXYYYYYYYVSRQPPQQQPOLJHFEDCCCDEFHJLOPQQQPPQRSVYYYYYYYXXX
```

    CENTRAL I/IO =   .829989+000
    MAXIMUM I/IO =   .829989+000

VIII.   MODE FORMATION AND COMPARISONS TO DENTAL CODE

          Computer modelling of transverse-mode-formative properties are

related to certain concepts as outlined below. These notions were

introduced by, or grew out of the papers of, the Russian group; for

brevity we will simply refer to Ananev. The initializing radiation is

conceived of as spontaneous-emission radiation which is randomized in

direction. The portion of it which remains within the resonator after

the first trip down the resonator is essentially just the fraction of

the full 4π sterradian solid angle which is subtended by a mirror,

i.e., a geometric angle. In geometric optics a wave with a given

(fairly small) inclination relative to the optic axis has its inclina-

tion reduced by a factor of $1/M$ (where M is the magnification of a

confocal unstable resonator) by a round-trip through the resonator.

After a number of round-trips the inclination will be reduced to a

value equal to the diffraction angle of the output aperture. These

concepts lead to a prediction (which we refer to as given by the Ananev

formula) that the number of round-trips required to form the mode is

proportional to the ratio of the natural logarithms of a Fresnel

number and the resonator magnification. These notions seem quite

plausible, but of course physical plausibility arguments should not be

considered fully convincing in themselves. It does not seem clear to us

whether the Russian group experimentally observed blurring of the far

field distribution or other indication of an incompletely formed mode,

though they may have. They do clearly indicate that they observed a

well-formed mode, i.e., a suitably concentrated far-field pattern, in

cases where the resonator magnification was deliberately made quite

large such that the Ananev formula predicted that mode formation should be complete.

Computer modelling of mode-formation properties, both in the present work and in calculations elsewhere with the DENTAL code, are based to a considerable extent on a physical conceptualization similar to that given above. Of course the wave-optics calculations are presumably a fuller test of the effects of successive round-trips through the resonator than are the geometric-optics arguments given above. The modelling is necessarily incompletely realistic, however, in that each round-trip must be considered as a sort of indivisible entity. In actuality, of course, the physical problem is considerably more complicated in that (even in a semi-classical approximation) the radiation must be considered to be distributed continuously over all space variables and time. It would require an extremely large effort to attempt a full calculation for such a problem, and it appears that very little work along this line has ever been done. Because of possible inadequacies of the overall conceptualization associated with the Ananev approach and the wave-optics modelling, it will be particularly important to have available the results of the experimental investigation of mode-formation properties which is being carried out at MIRADCOM. It should be emphasized that the wave-optics modelling of this problem is meaningful only insofar as the above-outlined physical conceptualization of the problem is meaningful and valid.

Two alternative modelling approaches were available for modelling of mode buildup. In one of them certain suitably independent and suitably defined transverse modes would be obtained and their appropriate properties

254

introduced into a differential equation for buildup with time of the
radiation intensity within each of the modes. In the other approach,
which is thought to be the better of the two and is the one which has
been pursued, the time dependence is simply treated by calculating the
effects of successive round-trip passages of the radiation through the
resonator. This automatically encompasses the effects of simultaneous
presence of radiation in various transverse modes. This approach also
permits ready determination of the effect of "the simultaneous presence
of radiation in several transverse modes" on the far-field pattern at
various points in time. The effects of gain with varying degrees of
saturation could be readily modelled with the present code. In fact,
use of that option does not seem appropriate because the radiation
intensity is far below saturation during the "mode-buildup time" of
current interest. Use of the empty-cavity program option is equivalent
to gain-filled calculations with uniformly distributed unsaturated gain,
and the results are readily applicable to any desired time dependence
of the small-signal gain.

In accordance with the above discussions, wave-optics modelling of
transverse-mode formation properties has been performed by carrying out
calculations for various combinations of Fresnel number and magnification
of a positive-branch confocal unstable resonator with uniformly distributed
small-signal gain. In these calculations the far-field distribution (in
the one-transverse-dimension approximation inherent in the present code)
was calculated after each round-trip. The near-field distribution was in
some cases also plotted after each round-trip in the present calculations,
but is considered to be of only secondary interest,

255

As a preliminary stage, the option was employed of introducing a tilted initializing wave. After successive round-trips the tilt angle was found to be systematically reduced, and the magnitude of the reduction agreed with the geometric-optics prediction of a factor of 1/M.

The major mode-formation-modelling calculations started the calculations with a wave which had no systematic tilt, but which had a phase distribution obtained from a random-number sequence, with the phase being distributed uniformly over the entire 2π. This is intended to simulate an isotropic angular distribution of the sponteneous emission radiation which initiates the radiation buildup.

The results of the mode-formation modelling caclulations can be best examined by thumbing through the computer-generated graphs of far-field intensity after successive passes through the resonator. Each of these graphs occupies two pages of computer paper, however, and reproduction of these plotter-type prints would be excessively voluminous for inclusion in this report. To condense the computer output to more manageable proportions we have summarized the results of each run on one graph in which is plotted two numerical results associated with the far-field plot obtained after each round-trip. These results are (1) the value of the ratio of peak far-field intensity I_p to the nominal intensity I_o which would result from a uniphase output wave, and (2) the angular position, relative to the straight-ahead direction, of the peak, expressed as the ratio of the angular deviation θ, to the "diffraction angle" λ/D, where λ is the wavelength and D is the full width of the output aperture. For comparison purposes, each plot includes an indication of the value of

$$N_{MF} = (\ln F_2 / \ln M),$$ (VIII-1)

where N_{MF} denotes the estimate of the number of round-trips required for mode formation. Here F_2 is the Fresnel number associated with the primary mirror,

$$F_2 = \frac{a_2^2}{\lambda L},$$ (VIII-2)

and M is the magnification of the positive-branch confocal unstable resonator being considered. Note that for the case of fully-decentered-alignment resonators, i.e., cases with $\varepsilon = 1.0$, there would be considerable plausibility in using a somewhat larger value of N_{MF} based on the larger value of F_2 associated with choosing the distance from the optic axis to the mirror edge, which in this case is $2 a_2$ rather than merely a_2, as the parameter for use in evaluation of F_2, i.e., in basing N_{MF} on four times as large a value of F_2 as for the centered-alignment cases ($\varepsilon = 0$).

Several of the cases treated used an equivalent Fresnel number F_{eq} of 9.6 and a magnification of M = 2.0. This corresponds to $F_2 = 76.8$, and $N_{MF} = 6.26$. Figs. F-1 and F-2 are results obtained for conventional centered-alignment, i.e., $\varepsilon = 0.0$, for the stated values of resonator parameters but with two independent sets of random numbers used to start the iterations in a manner simulating buildup from randomized spontaneous emission. It is readily apparent from comparison of the two plots that there is substantial variation from case-to-case in the details of the mode-buildup behavior. In each of these two cases there is an initial

257

"oscillation" of the peak-intensity far-field direction, followed by a monotonic approach to the central direction. Also, there is not a monotonic increase of I_p/I_o in either of these cases. The indicated value of N_{MF} seems a reasonable estimate of the approximate time for the mode to be fully formed with respect to angular divergence, although it appears that from one to four additional round-trips are required for the intensity to approach its final value. It would seem desirable to have several (more than two) statistically independent calculations for each set of resonator parameters, in order to obtain suitable estimates of both the average number of round-trips required to satisfy some suitable mode-formation criterion (say 90% of fully-converged I_p/I_o or an angular deviation of less than half a diffraction angle, or some similar thing) and the variability from case to case.

Fig. F-3 is for a fully-decentered-alignment case ($\varepsilon = 1.0$) with the same Fresnel number, i.e., $F_{eq} = 9.6$, $M = 2.0$. The mode formation seems to be reasonably complete in a number of round-trips given by the nominal formula, i.e., in $N_{MF} = 6.26$. If one instead uses four times as large a value of F_2, as mentioned above, the estimated number of round-trips would be 8.26. From this case alone, it seems difficult to choose whether the best estimate of the required number of round-trips to achieve reasonably good mode formation is six or eight. Certainly eight seems a large enough value.

Fig. F-4. presents results for a case with smaller Fresnel number, namely $F_2 = 12.8$, but the same magnification, $M = 2$. The predicted number of round-trips for mode formation is $N_{MF} = 3.7$. From the plot it is clear that the angular position of the far-field maximum is rather well centered after four round-trips, but the peak intensity is still increasing

for several more round-trips.

Fig. F-5 returns to the original Fresnel number, $F_2 = 76.8$, but uses an increased magnification, $M = 4$. As a result, the predicted number of round-trips for mode formation is only half that of the cases in Figs. F-1 and F-2, namely $N_{MF} = 3.1$. It appears that the far-field peak is well oriented in direction after four passes, while the peak intensity requires about five round-trips to settle down.

One computer run was made in a rather naive fashion using input data describing a very large Fresnel number, such as seems likely to be typical of excimer lasers. The number of mesh points allotted to the near-field complex optical amplitude distribution was only moderate, namely a total of 512 mesh points, of which 256 were on the aperture and the other 256 were allotted as a "guard band" such as is necessary in FFT calculations. Results were not at all typical of what one would expect for an actual physical situation with very large Fresnel number. This is readily understandable, of course. To model in any reasonably reliable way the diffraction behavior one must assign a number of mesh points several times as large as the equivalent Fresnel number. It is essentially impossible to employ a number of mesh points of the order of 10^4 or greater, or in any event it would be quite expensive. Hence it appears that modelling of mode buildup in resonators with the very large Fresnel numbers associated with excimer lasers will be expensive, if not impracticable. One can instead hope to investigate trends for more moderate values of Fresnel number and for various values of magnification.

259

Calculations were also made for a resonator with rather small magnification which is being employed in experimental studies. The parameters are $F_2 = 81.37$, $M = 1.32$. The sensitivity of the predicted number of round-trips to magnification is clearly evidenced here, for we have $N_{MF} = 15.8$, which is considerably larger than for the previously-discussed cases. Results are presented in Fig. F-6. Unfortunately the maximum number of iterations which were calculated was not enough to fully test the Ananev prediction, since the mode was not well formed at the end of twenty iterations. In any event, these results seem to indicate that, for this particular combination of F_2 and M at any rate, the Ananev prediction of a strong dependence of N_{MF} on M is confirmed. This point seemed, in fact, to be the one which was most stressed by the Russian investigators, who pointed out that a very large magnification could be used to avoid possible problems associated with mode formation times.

From inspection of these results one can attempt to discern trends and to come to some tentative conclusions. Because of the apparantly pronounced statistical variability between physically identical cases, it would appear that a considerably larger number of calculations similar to those discussed above would be necessary to characterize the problem area. The tentative conclusions are:

(1) The behavior of both the near-field and far-field distributions after successive round-trips is significantly different for calculations made with different sets of random numbers used to determine the phase distribution of the initializing wave. This seems to imply that the physical behavior of a resonator in this respect varies

substantially from pulse to pulse and hence that any statements made about mode-buildup time should be interpreted only in a statistical sense as representative of an ensemble of cases. In this respect, of course, the present tentative findings differ from the Ananev formulation. It would be interesting if shot-to-shot differences in mode-buildup properties could be experimentally observed.

(2) The far-field distributions at early stages were not as randomized as had been expected. After only a few round-trips the far-field distribution has usually taken on a rather regular shape similar qualitatively to final shape. The pattern is of course different in specific respects from the final pattern, and in particular is in general not symmetric about the optic axis.

(3) It seems somewhat meaningful to make the subjective statement that the eventual settling down of the far-field pattern to its final form, as far as angular deviation is concerned, seems to be largely a monotonic decrease in its angle of tilt with respect to optic axis.

(4) The decrease in tilt angle can in at least some cases be readily discerned after it is reduced below one diffraction angle. Thus, there is some arbitrariness in definition of the time at which mode formation is complete. It seems reasonable to adopt the definition that mode formation is complete when the center of the far-field distribution becomes and remains displaced by less than one diffraction angle.

261

(5)   The results of calculations for various combinations of
Fresnel number, magnification, and random-number sequence are
in reasonable qualitative agreement with the Ananev formula for
mode-formation time. The statistical variability seems to pre-
clude anything but a very tentative conclusion in this respect
without performance of a number of statistically-independent
calculations for each combination of magnification and Fresnel
number.

(6)   For very large Fresnel numbers the geometric angle within
which the spontaneous emission is retained on the first resonator
pass becomes relatively large, and the number of mesh points re-
quired to represent such large tilt angles becomes quite large.
For this reason one could not expect to be able to reliably model
systems with Fresnel numbers as large (perhaps 10^4) as those
associated with typical excimer laser designs, unless one used an
enormously large number of transverse mesh points with a
correspondingly large computer time. This limitation on wave-
optics modelling capability was observed in one computer run.

It seems clear that it is entirely impractical to expect to perform
wave-optics calculations at Fresnel numbers as large as those typical
of excimer lasers, hence this avenue is closed as a method of investigation
of mode-formation dynamics for such lasers. The following recommendation
is made as an alternative: Perform a number of statistically-independent
wave-optics mode-formation-dynamics-modelling calculations for each of a
substantial number of combinations of magnification and Fresnel number,

and use these to investigate trends of average value and statistical spread of number of round-trip times for mode-formation as a function of M and F_2. The best estimate of the mode-formation properties for excimer-range values of F_2 would then be based on the trends determined for moderate values of F_2. One should note that statistical fluctuations in number of round-trips for mode-formation imply statistical fluctuations of energy on target for pulsed-mode high-energy laser operation in regimes where mode-formation is incomplete within a pulse, since laser pointing systems obviously cannot respond sufficiently rapidly to compensate for variations in effective pointing angle over a few round-trip transit times.

MODE FORMATION
DEPENDENT FAR FIELD EFFECTS

Figure F-1

264
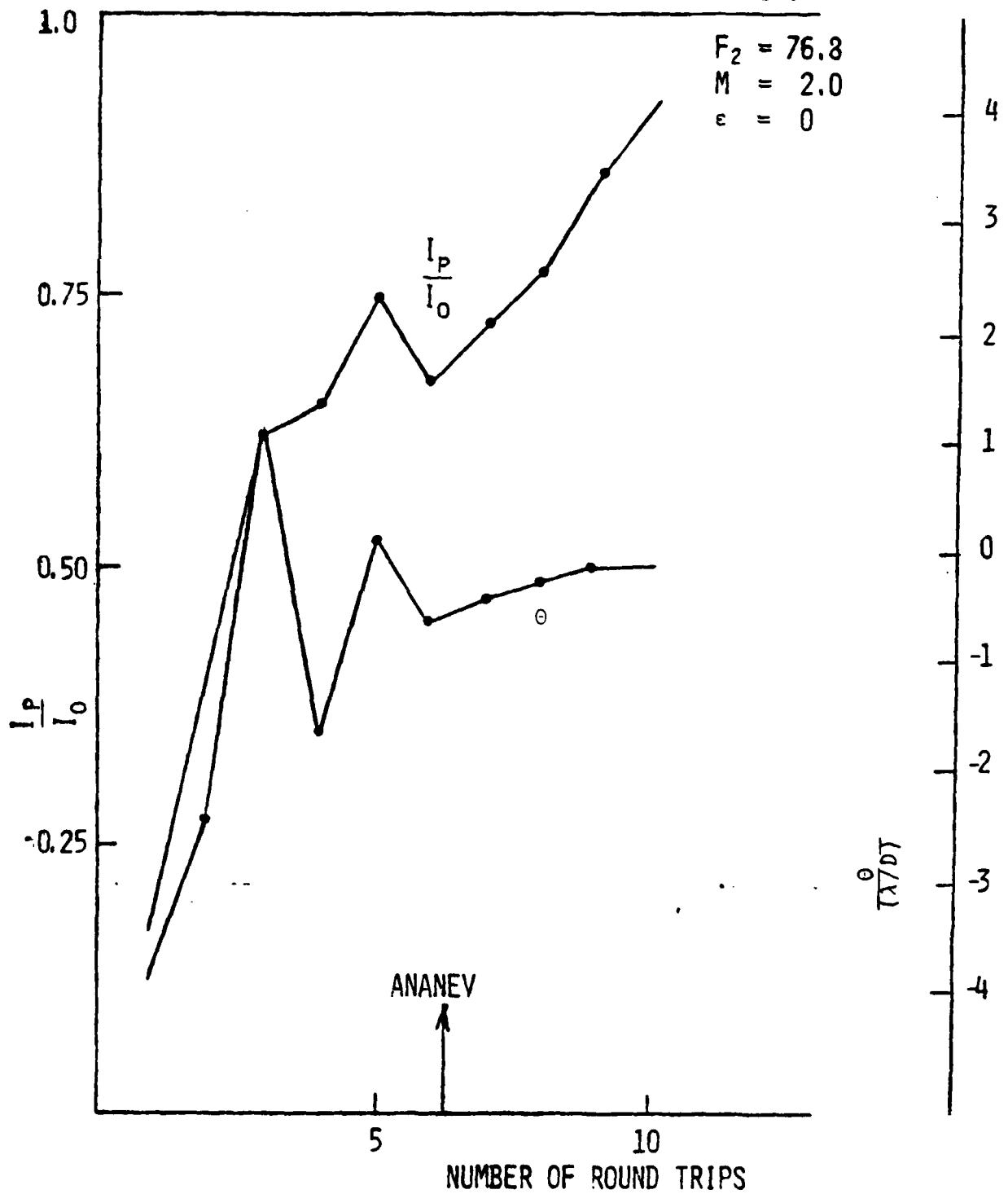
MODE FORMATION
DEPENDENT FAR FIELD EFFECTS
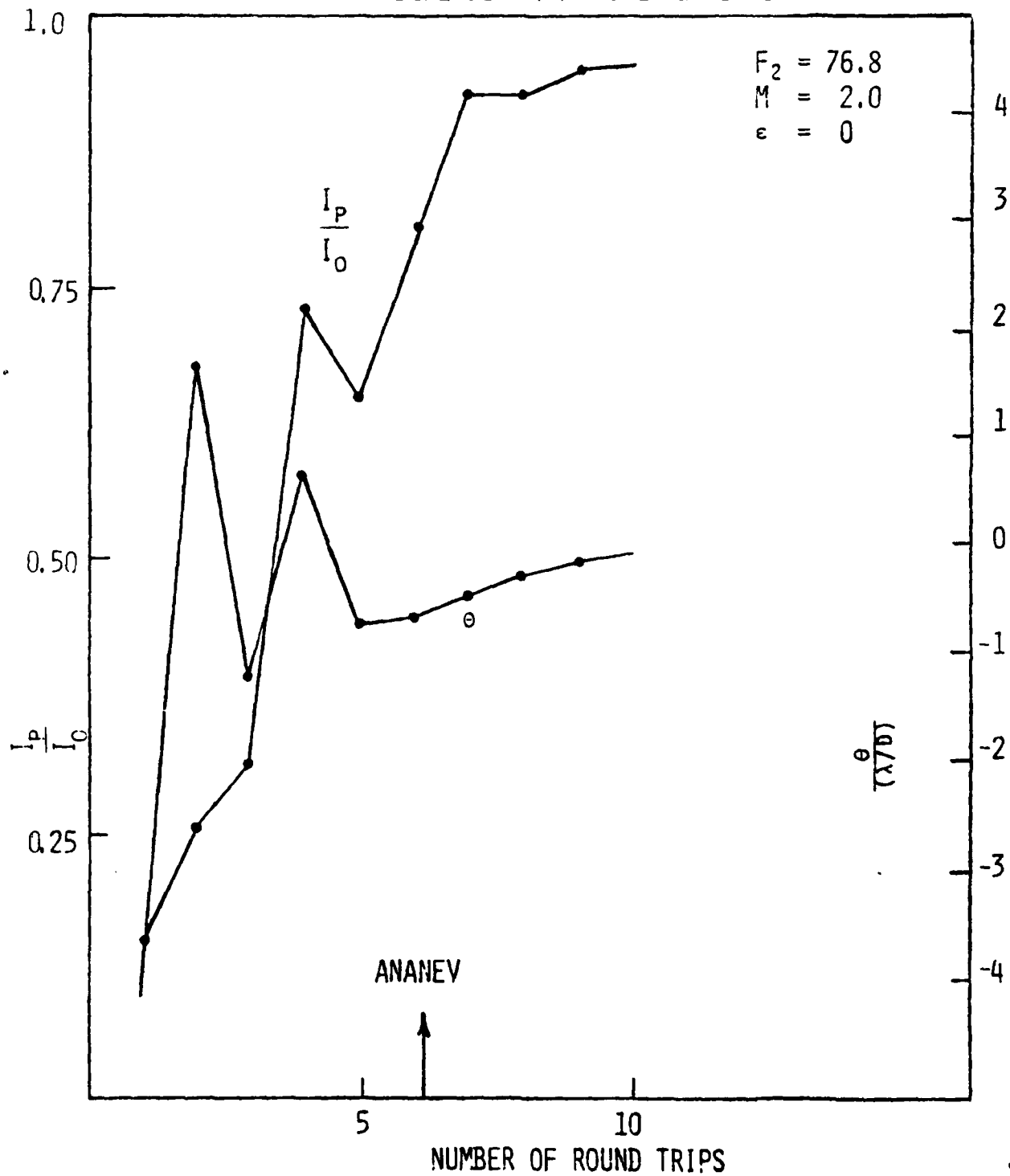
Figure F-2
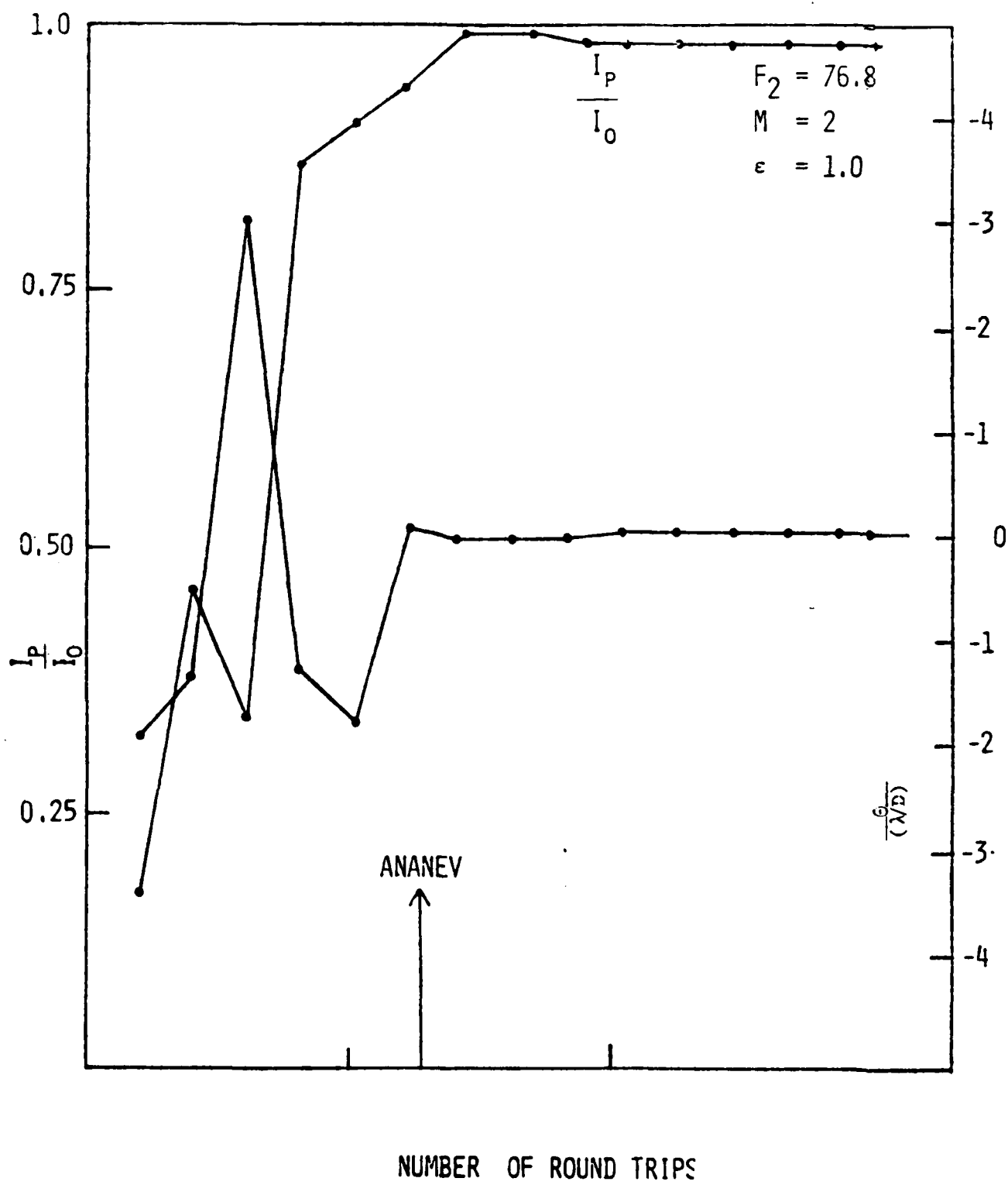
MODE FORMATION DEPENDENT FAR FIELD EFFECTS

Figure B-3

266

Figure F-4

267
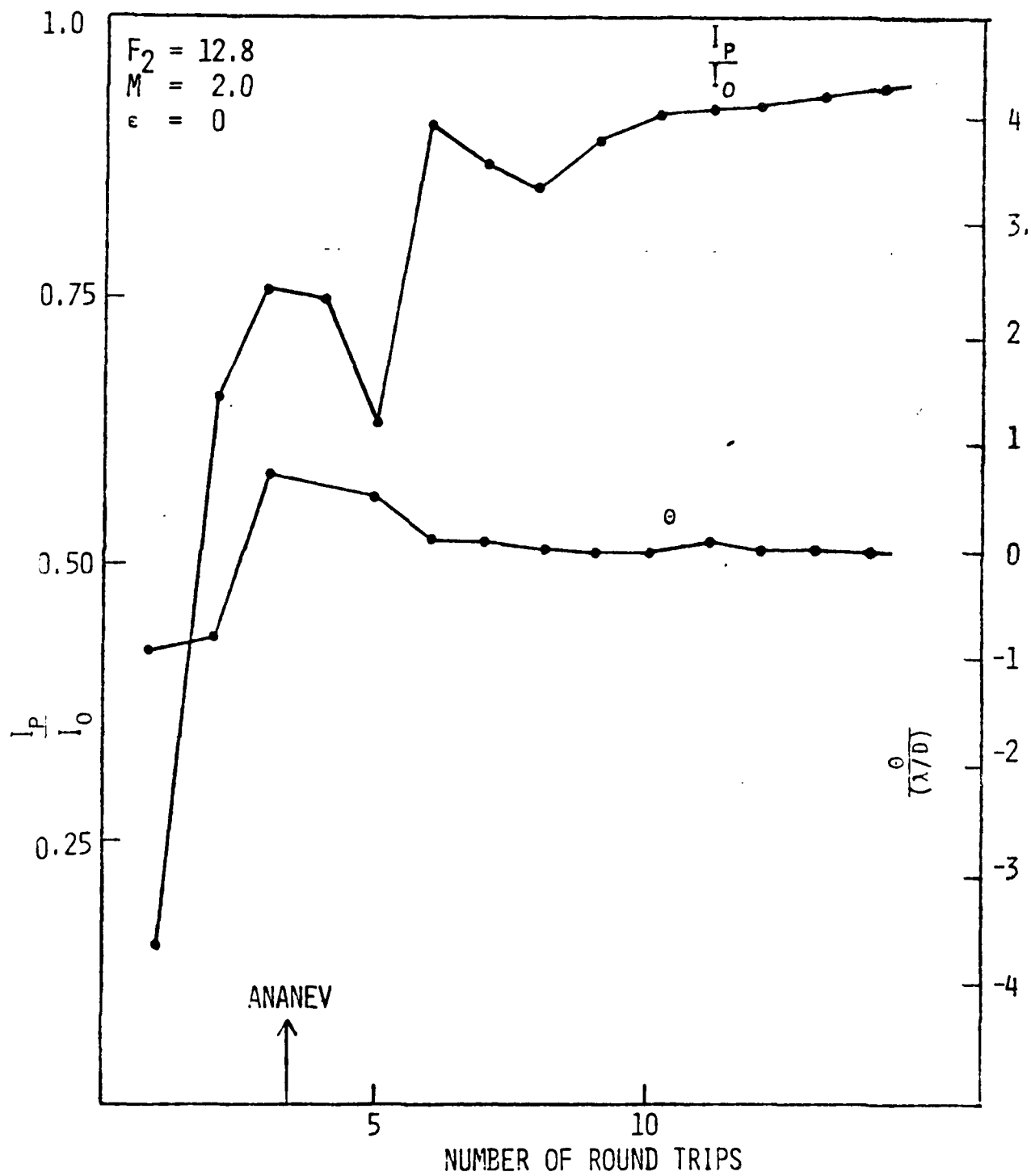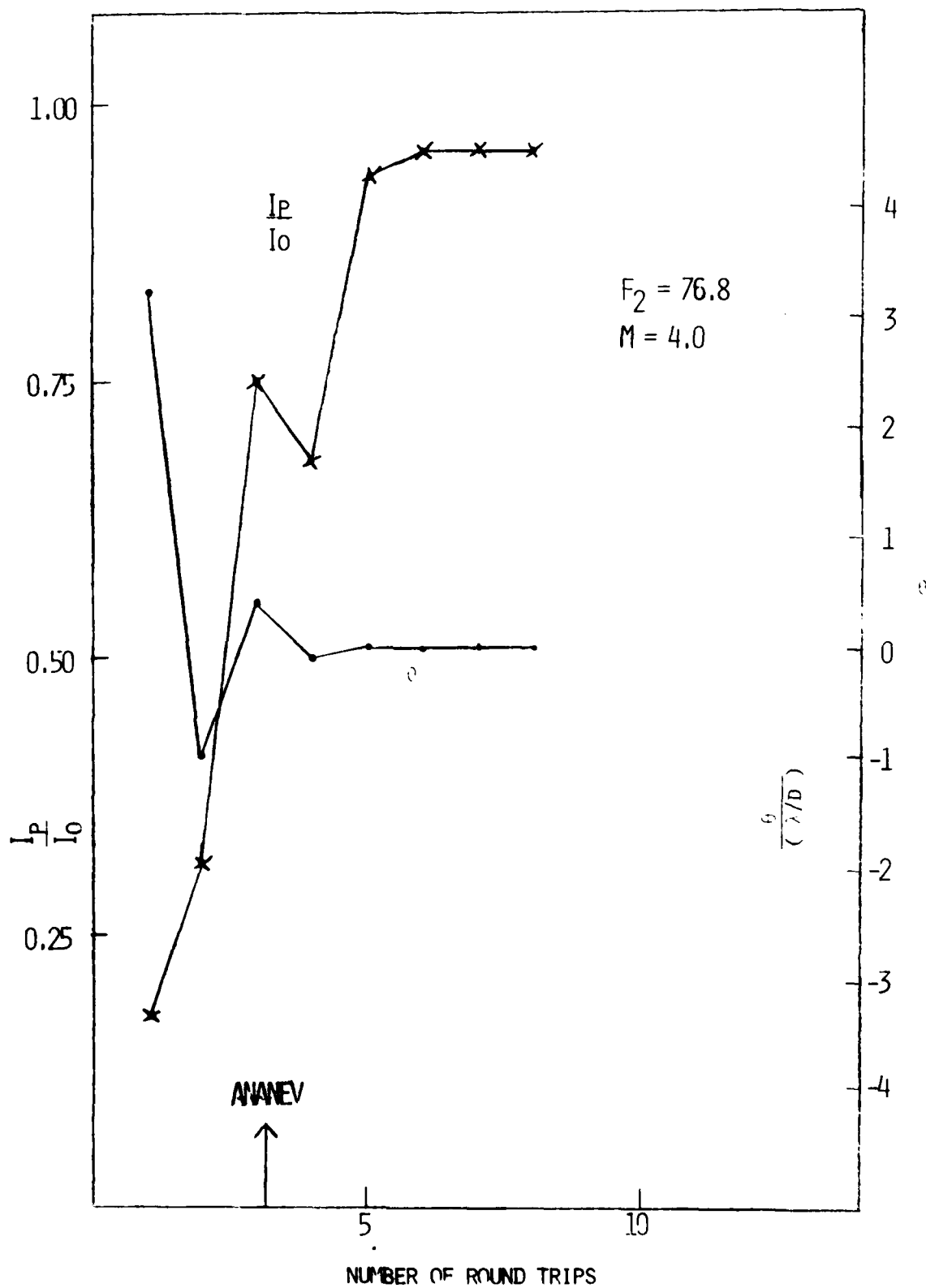
Figure F-5

Figure F-6

269
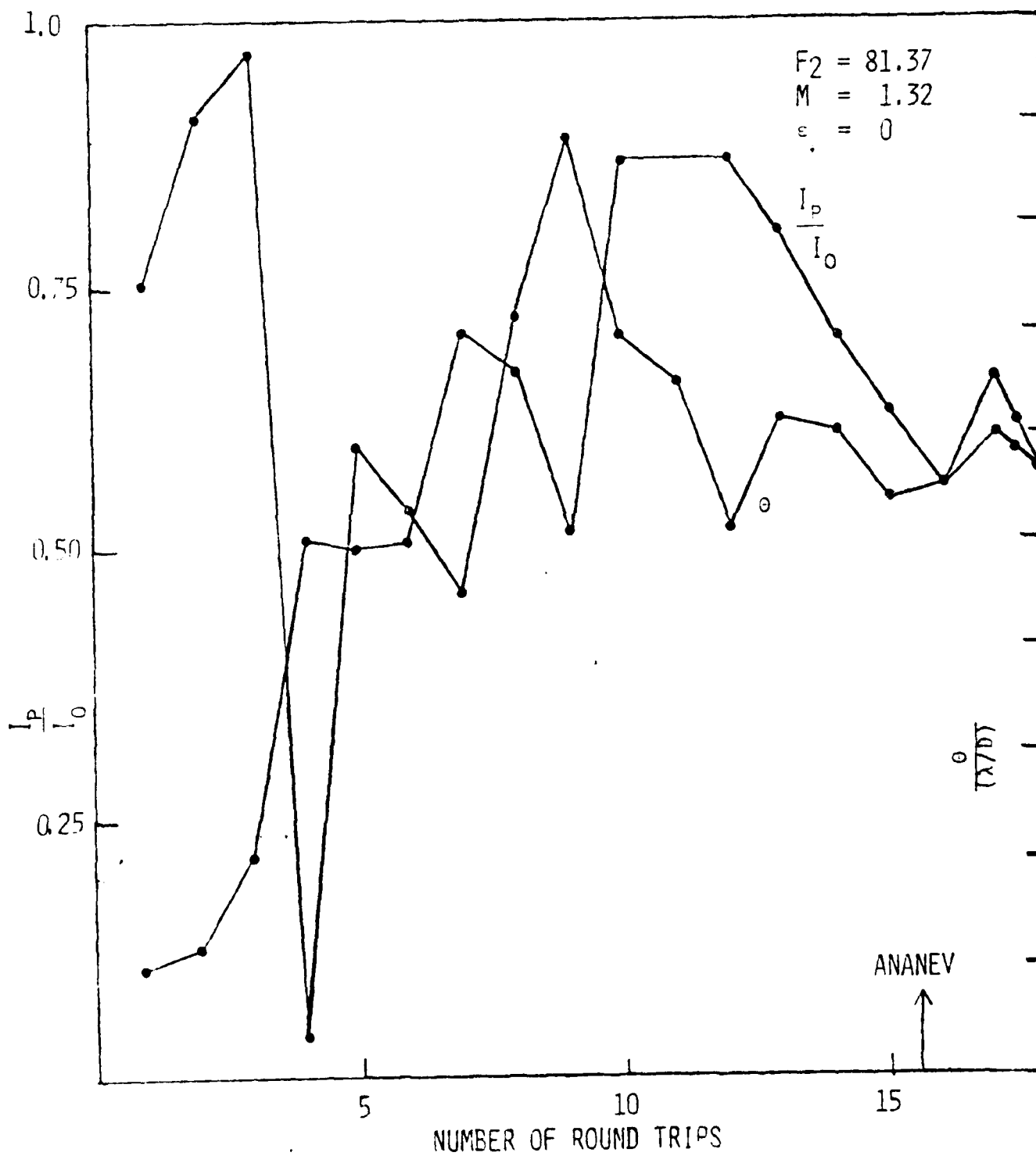
IX.   _Sensitivity of Spherical-Aberration-Induced_

   Degradation in Beam Quality to Output Coupling

   We have separately derived equations for the root-mean-square

optical path difference RMSOPD over a square aperture in terms of the

coefficient here designated C_5, of the expansion term $C_5 r^4 = C_5 (x^2 + y^2)^2$

for the OPD and of the halfwidth, a, of the output beam. The derivation

assumes a confocal positive branch resonator with each mirror having a

spherical figure. The result is

$$RMSOPD = 0.675288 \ a^4 \ C_5. \hspace{3cm} (IX-1)$$

The rms variation of phase over the output beam, $\Delta\phi_{rms}$, is then

$$\Delta\phi_{rms} = \frac{2\pi}{\lambda} \ RMSOPD. \hspace{3cm} (IX-2)$$

   For relatively small variations of phase over the output beam, the

Strehl ratio, I/I_0, giving the ratio of central far-field intensity (for

an unobscured aperture) to the intensity of a uniphase beam with the same

intensity is given approximately by

$$\frac{I}{I_0} \approx \exp (-\Delta\phi_{rms}^2). \hspace{3cm} (IX-3)$$

   From equations which we have derived earlier, it follows that the

coefficient C_5 can be expressed in terms of the magnification M and the

mirror spacing L of a confocal resonator as follows:

$$C_5 = (1 - 1/M)^4 \ \frac{1}{32} \frac{1}{L^3} \frac{1}{(1 - M^{-4})} \hspace{3cm} (IX-4)$$

The above equations in combination give the Strehl intensity ratio

as a function of L, M, λ, and a. In order to explore the sensitivity of

270

spherical-aberration-induced degradation in beam quality we have cal-culated and plotted the Strehl ratio (defined as if the output were unobscured) for a fixed value of $L = 400$ cm, a wavelength λ of 0.3514 X 10^{-4} cm, and various combinations of M and a. We have plotted the Strehl ratio as a function of the full width, 2a, of the output beam. The curves have somewhat arbitrarily been labeled with the geometric output coupling as an alternative to the magnification. M, the value of geometric output coupling being simply $(1 - M^{-2})$.

There is a weakness, at least in principle, of the above approach in that it calculates the effect of phase aberrations on the central far-field intensity as if the output were not obscured by the feedback mirror. We have also made numerical calculations which account for the output obscuration, and find the results are very little different from those obtained with the above equations. We have chosen to present the un-obscured-aperture equations and associated plot since the equations are simpler and thereby permit a more convenient interpretation.

It is immediately evident from the plot that spherical-mirror resonators become entirely unacceptable for beam widths as large as 30 to 60 cm, depending on the acceptable level of beam quality degradation. (Note that the negative exponential dependence of Strehl ratio is not fully valid for ratios as low as the minimum value shown on the plot).

It is also clear from the plot that resonators with large output couplings produce more degradation than those with smaller outcouplings. To compare resonators with different outcouplings one could of course compare values of Strehl ratios of the two resonators at fixed beam size.

As an alternative, and perhaps more useful for comparison, one can compare values of beam width at which each of the two resonators produce the same amount of beam-quality degradation as measured by the Strehl ratio. Although it may not be immediately obvious, it appears that from the plots this ratio is approximately independent of the value of Strehl ratio chosen for the comparison. That approximate independence is understandable from consideration of the equations given above. The dependence of the RMSOPD on M is contained in two factors. Of the two, the factor

$$\frac{1}{(1 - M^{-4})}$$ represents the ratio of the overall effect with repeated re-

flections in the resonator to the effect of spherical aberration for a single-pass situation such as might be inspected interferometrically. This factor does not vary greatly with outcoupling, ranging from about 0.98 to about 0.88 for the range of outcoupling shown in the plot. The other factor involving M is of the form $(1 - 1/M)^4$, which can be written as $\left(\frac{M - 1}{M}\right)^4$.

But of course the dependence of RMSOPD on the halfwidth a is of the form a^4. It follows that, to a reasonable degree of approximation, the value of a (and hence of the full width 2a) at which a given RMSOPD occurs is proportional to the one-fourth power of the reciprocal of the factor given above involving M. That is to say, one expects the value of beam width at which a given level of beam-quality degradation occurs will be approximately proportional to the quantity

$$\frac{M}{(M - 1)}.$$

The above simple prediction seems in agreement with the plots.
For instance, the predicted ratio for 65% outcoupling as compared to
85% outcoupling is 1.5.

SENSITIVITY OF SPHERICAL
ABERRATION INDUCED DEGRADATION
IN BEAM QUALITY FOR SQUARE
APERTURES ON GEOMETRIC
OUTCOUPLING

BEAM WIDTH 2A (CM)

Figure IX-1

274
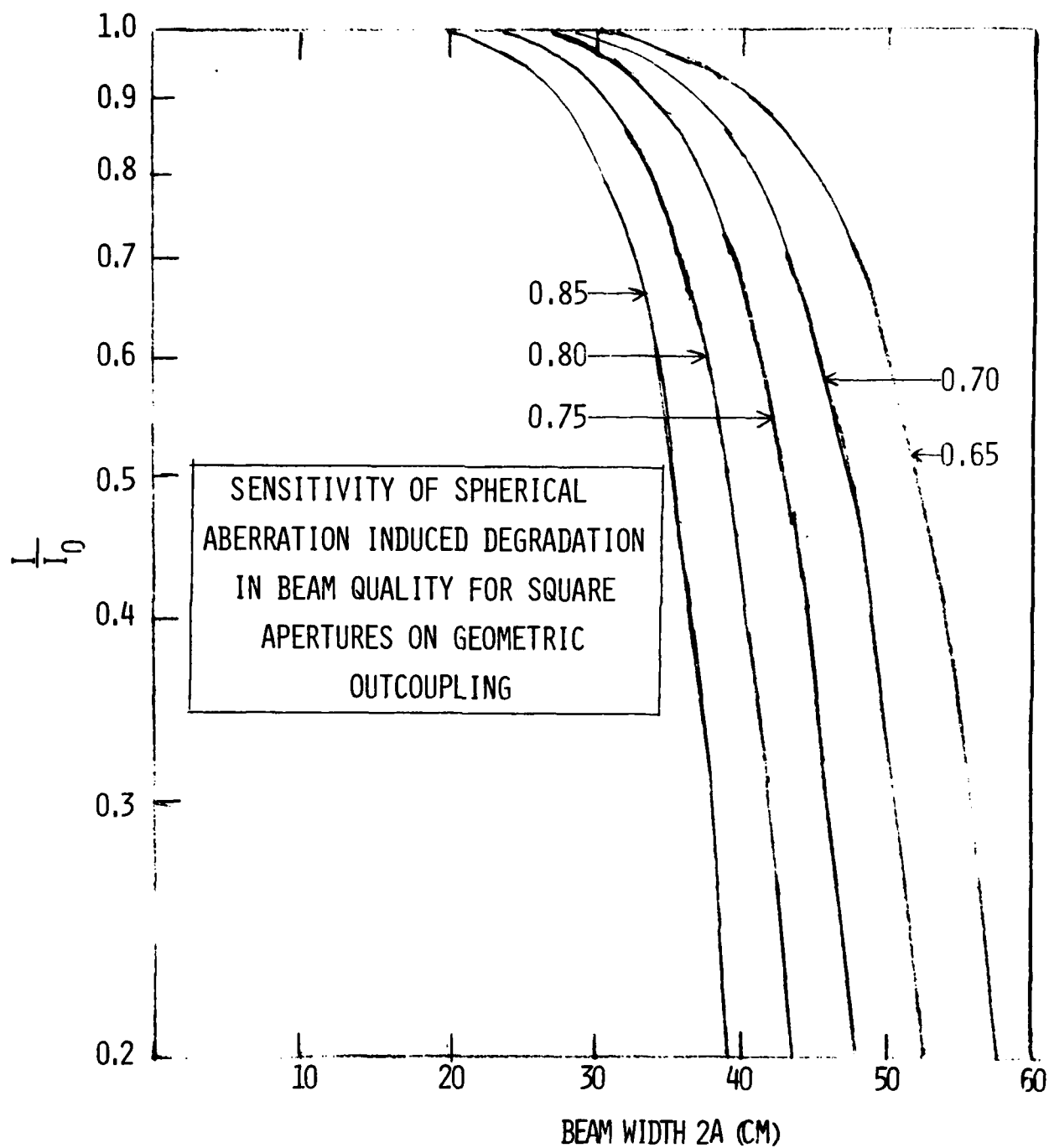
APPENDIX A

Test	DVP	IVP	OVP	PVP	Test Date	Time	
0-1					May 31, 1979	1:32 PM	before flow
0-2					May 31, 1979	1:34 PM	
0-3					May 31, 1979	1:40 PM	after flow
1-1					June 1, 1979	10:05 AM	before flow
1-2	16.25	15.75	0	15.5	June 1, 1979	10:13 AM	
1-3	13.5	15.75	0	15.5	June 1, 1979	10:18 AM	
1-4	10.25	15.75	0	15.5	June 1, 1979	10:20 AM	
1-5	7.5	15.75	0	15.5	June 1, 1979	10:23 AM	
1-6					June 1, 1979	10:31 AM	after flow
2-1	16.5	16	0	15.5	June 1, 1979	11:02 AM	before flow
2-2	16.5	16	0	15.5	June 1, 1979	30 sec.	
2-3	12.75	16	0	15.5	June 1, 1979	2 min. 30 sec.	
2-4	9.75	16	0	15.5	June 1, 1979	3 min. 57 sec.	
2-5	8	16	0	15.5	June 1, 1979	6 min. 10 sec. after flow	

DVP: Diverter Valve Position   OVP: Outlet Hx (water) Valve Position
IVP: Inlet Hx (water) Valve Position   PVP: Pentane Hx Valve Position

276

Test	DVP	IVP	OVP	PVP	Test Date	Time	
3-0	14.5	16.25	0	15.5		2:06 PM	before flow
3-1	16.25	16.25	0	15.5		23 sec.	
3-2	16.25	16.25	0	15.5		3 min. 30 sec.	
3-3	16.25	16.25	0	15.5		6 min. 30 sec.	
3-4	11.4	16.25	0	15.5		7 min. 30 sec.	
3-5	9.25	16.25	0	15.5		9 min. 25 sec.	after flow
4-0	16.5	16.0	0	15.25			before flow
4-1	16.5	16	0	15.5		30 sec.	
4-2	13	16	0	15.5		1 min. 50 sec.	
4-3	11.8	16	0	15.5		3 min. 33 sec.	
4-4	10	16	0	15.25		4 min. 20 sec.	
4-5	9.5	16.0	0	15.25		10 min. 39 sec.	
4-6	10	16	0	15.25		10 min. 47 sec.	after flow

DVP: Diverter Valve Position   OVP: Outlet Hx (water) Valve Position

IVP: Inlet Hx (water) Valve Position   PVP: Pentane Hx Valve Position

Test	DVP	IVP	OVP	PVP	Test Date	Time
5-1					June 12, 1979	Pre Test
5-2	19.5				June 12, 1979	50 sec.
5-3	12-1/2				June 12, 1979	3 min. 29 sec.
5-4	10				June 12, 1979	5 min.
5-5	12				June 12, 1979	5 min. 48 sec.
6-1	18				June 12, 1979	30 sec.
6-2	15.5				June 12, 1979	2 min. 0 sec.
6-3	13.5				June 12, 1979	3 min. 30 sec.
6-4	12.5				June 12, 1979	5 min. 50 sec.
7-1					June 15, 1979	Pre Test
7-2	18				June 15, 1979	1 min. 15 sec.
7-3	15-1/2				June 15, 1979	2 min. 26 sec.
7-4	12.6				June 15, 1979	3 min. 30 sec.
7-5	11				June 15, 1979	4 min. 20 sec.
7-6	13				June 15, 1979	5 min. 40 sec.

DVP: Diverter Valve Position   OVP: Outlet Hx (water) Valve Position

IVP: Inlet Hx (water) Valve Position   PVP: Pentane Hx Valve Position

278

Test	DVP	IVP	OVP	PVP	Test Date	Time
8-1					June 15, 1979	Pre Test
8-2	18-1/2				June 15, 1979	45 sec.
8-3	13-1/2				June 15, 1979	2 min. 15 sec.
8-4	9.8				June 15, 1979	5 min. 3 sec.
8-5	10.2				June 15, 1979	6 min. 40 sec.
8-6	10.7				June 15, 1979	10 min. 18 sec.
8-7	10.6				June 15, 1979	11 min. 43 sec.
8-8	10.9				June 15, 1979	14 min. 3 sec.
9-1					June 19, 1979	Pre Test
9-2	16				June 19, 1979	23 sec.
9-3	15				June 19, 1979	1 min. 37 sec.
9-4	14.5				June 19, 1979	3 min. 37 sec.
9-5	11				June 19, 1979	4 min. 45 sec.
9-6	9				June 19, 1979	5 min. 30 sec.
9-7					June 19, 1979	12 min. 23 sec. after flow

DVP: Diverter Valve Position   OVP: Outlet Hx (water) Valve Position

IVP: Inlet Hx (water) Valve Position   PVP: Pentane Hx Valve Position.

279

Test	DVP	IVP	OVP	PVP	Test Date	Time
10-1					June 20, 1979	Pre Test
10-2	10				June 20, 1979	45 sec.
10-3	10				June 20, 1979	2 min. 52 sec.
10-4	10				June 20, 1979	2+ min. 45 sec.
10-5	10				June 20, 1979	6 min. 45 sec.
10-6	10				June 20, 1979	8 min. 45 sec.
10-7	10				June 20, 1979	10 min. 45 sec.
10-8	10				June 20, 1979	13 min. 2 sec.
11-1	16				June 21, 1979	Pre Test
11-2	10.3				June 21, 1979	2 min.
11-3	10.3				June 21, 1979	4 min.
11-4	10.3				June 21, 1979	6 min.
11-5	10.3				June 21, 1979	8 min.
11-6	8.6				June 21, 1979	10 min.
11-7	8.6				June 21, 1979	12 min.
11-8	8.6				June 21, 1979	14 min.
11-9	8.6				June 21, 1979	16 min.

DVP: Diverter Valve Position   OVP: Outlet Hx (water) Valve Position
IVP: Inlet Hx (water) Valve Position   PVP: Pentane Hx Valve Position

Test	DVP	IVP	OVP	PVP	Test Date	Time
12-1	10.4				June 21, 1979	20 sec.
12-2	10.4				June 21, 1979	40 sec.
12-3	10.4				June 21, 1979	60 sec.
12-4	10.4				June 21, 1979	1 min. 30 sec.
12-5	10.4				June 21, 1979	2 min.
13-0					June 25, 1979	Pre Test
13-1					June 25, 1979	Pre Test
13-2	11.1				June 25, 1979	2 min.
13-3	8.3				June 25, 1979	4 min.
13-4	10.3				June 25, 1979	6 min.
13-5	12				June 25, 1979	8 min.
13-6	14.5				June 25, 1979	10 min.
13-7	9.1				June 25, 1979	12 min.
13-8	11.6				June 25, 1979	14 min.

DVP: Diverter Valve Position   OVP: Outlet Hx (water) Valve Position

IVP: Inlet Hx (water) Valve Position   PVP: Pentane Hz Valve Position

281

Test	DVP	IVP	OVP	PVP	Test Date	Time
14-1	11.5				June 25, 1979	2 min.
14-2	9				June 25, 1979	4 min.
14-3	9.9				June 25, 1979	6 min.
14-4	11.6				June 25, 1979	8 min.
14-5	10.5				June 25, 1979	10 min.
14-6	11.4				June 25, 1979	12 min.
14-7	13.9				June 25, 1979	14 min.
14-8	14.5				June 25, 1979	16 min. after flow
15-1	12				June 25, 1979	4 min. 32 sec.
15-2	11				June 25, 1979	6 min. 5 sec.
15-3	11				June 25, 1979	8 min. 45 sec.
15-4	10.8				June 25, 1979	10 min. 25 sec.
15-5	9.9				June 25, 1979	11 min. 40 sec.
15-6	9.4				June 25, 1979	14 min. 30 sec.
15-7	9.7				June 25, 1979	16 min. 40 sec.

DVP: Diverter Valve Position   OVP: Outlet Hx (water) Valve Position

IVP: Inlet Hx (water) Valve Position   PVP: Pentane Hx Valve Position

Test	DVP	IVP	OVP	PVP	Test Date	Time
16-1					June 28, 1979	Pre Test
16-2	9.8				June 28, 1979	3 min. 35 sec.
16-3	10.8				June 28, 1979	5 min. 25 sec.
16-4	11.6				June 28, 1979	7 min. 56 sec.
16-5	12.2				June 28, 1979	9 min. 22 sec.
16-6	12.8				June 28, 1979	11 min. 20 sec.
16-7	13.1				June 28, 1979	12 min. 26 sec.
16-8	13.3				June 28, 1979	13 min. 49 sec.
17-1					June 28, 1979	Pre Test
17-2	10				June 28, 1979	2 min.
18-1	10.3				June 28, 1979	2 min.
18-2	10				June 28, 1979	4 min.
18-3	9.9				June 28, 1979	6 min.
18-4	9.8				June 28, 1979	8 min.
18-5	9.7				June 28, 1979	10 min.
18-6	9.7				June 28, 1979	12 min.

DVP: Diverter Valve Position   OVP: Outlet Hx (water) Valve Position

IVP: Inlet Hx (water) Valve Position   PVP: Pentane Hx Valve Position

283

Test	DVP	IVP	OVP	PVP	Test Date	Time
19-1					June 29, 1979	Pre Test
19-2	10				June 29, 1979	2 min.
19-3	9.6				June 29, 1979	4 min.
20-1					June 29, 1979	Pre Test
20-2	10.4				June 29, 1979	2 min.
20-3	10.4				June 29, 1979	4 min.
20-4	10.5				June 29, 1979	6 min.
20-5	10.5				June 29, 1979	8 min.
20-6	10.5				June 29, 1979	10 min.
21-1					June 29, 1979	Pre Test
21-2	9.8				June 29, 1979	2 min.
21-3	9.8				June 29, 1979	4 min.
21-4	9.8				June 29, 1979	6 min.
21-5	9.8				June 29, 1979	8 min.

DVP: Diverter Valve Position   OVP: Outlet Hx (water) Valve Position
IVP: Inlet Hx (water) Valve Position   PVP: Pentane Hx Valve Position

Test	DVP	IVP	OVP	PVP	Test Date	Time
22-1					June 29, 1979	Pre Test
22-2	9.7				June 29, 1979	2 min. 50 sec.
22-3	9.4				June 29, 1979	4 min. 50 sec.
22-4	9.3				June 29, 1979	6 min. 50 sec.
22-5	9.2				June 29, 1979	8 min. 50 sec.
22-6	9.0				June 29, 1979	10 min. 50 sec.
23-1	11				June 29, 1979	2 min.
23-2	11				June 29, 1979	4 min.
23-3	11				June 29, 1979	6 min.
23-4	11				June 29, 1979	8 min.
24-1					July 5, 1979	Pre Test
24-2	10.3				July 5, 1979	1 min.
24-3	10.3				July 5, 1979	2 min.
24-4	10.3				July 5, 1979	3 min.
24-5	10.3				July 5, 1979	4 min.
24-6	10.3				July 5, 1979	5 min.
24-7	10.3				July 5, 1979	7 min. after flow

DVP; Diverter Valve Position OVP: Outlet Hx (water) Valve Position
IVP: Inlet Hx (water) Valve Position PVP: Pentane Hx Valve Position

285

Test	DVP	IVP	OVP	PVP	Test Date	Time
25-1					July 9, 1979	Pre Test
25-2					July 9, 1979	After Vacuum
25-3	10.4				July 9, 1979	1 min.
25-4	10.3				July 9, 1979	2 min.
25-5	10.3				July 9, 1979	4 min.
25-6	10.3				July 9, 1979	6 min.
25-7	10.3				July 9, 1979	8 min.
25-8	10.2				July 9, 1979	10 min.
25-9	10.2				July 9, 1979	12 min. 30 sec. after flow
26-1					July 10, 1979	Pre Test
26-2	11.8				July 10, 1979	1 min.
26-3	11.8				July 10, 1979	2 min.
26-4	11.8				July 10, 1979	4 min.
26-5	11.8				July 10, 1979	6 min.

DVP: Diverter Valve Position OVP: Outlet Hx (water) Valve Position
IVP: Inlet Hx (water) Valve Position PVP: Pentane Hx Valve Position

Test	DVP	IVP	OVP	PVP	Test Date	Time
27-1					July 11, 1979	Pre Test
27-2	11.3				July 11, 1979	1 min.
27-3	11.3				July 11, 1979	2 min.
27-4	11.3				July 11, 1979	4 min.
27-5	11.2				July 11, 1979	6 min.
27-6	11.2				July 11, 1979	8 min.
27-7					July 11, 1979	Immediately after turn off
28-1					July 18, 1979	Pre Test
28-2					July 18, 1979	
28-3					July 18, 1979	
29-1					July 19, 1979	Pre Test
29-2	10				July 19, 1979	
29-3	10				July 19, 1979	

DVP: Diverter Valve Position   OVP: Outlet Hx (water) Valve Position
IVP: Inlet Hx (water) Valve Position   PVP: Pentane Hx Valve Position

Test	DVP	IVP	OVP	PVP	Test Date	Time
30-1					July 23, 1979	Pre Test
30-2	14.5				July 23, 1979	35 sec.
30-3	12.2				July 23, 1979	2 min. 10 sec.
30-4	9.9				July 23, 1979	5 min. 10 sec.
30-5	10.9				July 23, 1979	7 min. 10 sec.
30-6	11.5				July 23, 1979	10 min. 20 sec.
30-7					July 23, 1979	15 min. 10 sec. after flow
31-1					July 23, 1979	Pre Test
31-2	9.6				July 23, 1979	1 min. 20 sec.
31-3	11				July 23, 1979	3 min. 50 sec.
31-4	10.8				July 23, 1979	6 min. 10 sec.
31-5	11.6				July 23, 1979	7 min. 30 sec.

DVP: Diverter Valve Position   OVP: Outlet Hx (water) Valve Position

IVP: Inlet Hx (water) Valve Position   PVP: Pentane Hx Valve Position

288

Test	Px_1	Px_2	Px_3	Px_4	Px_5	Px_6	Px_7	Px_8	Px_9	Tx_1	Tx_2
0-1	772	1007	760		730	720	38	758	769	13.5	22.7
0-2	1290	1236	775		738	690	38	758	780	13.5	23.1
0-3	760	1179	750		713	704	38	758	757	13.5	24.7
1-1	763	768	762		761	760		763	762	25.3	24.3
1-2	1270	1206	778		767	728		764	776	112.8	24.5
1-3	1347	1289	729		711	681		764	724	141.8	25.0
1-4	1156	1110	774		657	627		764	723	141.8	25.8
1-5	1007	1032	851		638	610		764	754	141.2	26.8
1-6	735	1103	739		715	719		765	733	109.7	29.8
2-1	754	1146	758		745	739		766	753	64.5	32.3
2-2	1295	1228	785		763	718		768	778	98.2	
2-3	1447	1375	753		728	690		766	745	128.6	32.0
2-4	1217	1152	815		687	647		766	757	133.2	31.9
2-5	762	1078	765		749	744		766	760	100.6	32.4

Px Unit: Torr
Tx Unit: $^\circ$c

Test	Tx_3	Tx_4	Tx_5	Tx_6	Tx_7	Tx_8	Tx_9	Tx_{10}	Tx_{11}	F-1
0-1	22.2	21.6	21.9	23.9	23.0	19.8	23.2	22.6	23.3	
0-2	22.5	22.3	22.2	38.5	23.9	19.9	24.2	22.7	28.7	
0-3	22.5	21.9	22.6	30.9	28.1	20.0	33.2	22.8	37.2	
1-1		21.8	22.4	26.4	23.3	20.4	24.9	22.7	25.1	
1-2		22.7	84.6	48.9	25.1	20.8	26.3	22.7	34.6	
1-3		24.6	110.5	60.6	32.2	21.0	33.8	22.8	43.9	
1-4		35.9	62.4	55.1	37.5	21.1	43.3	22.9	43.3	
1-5		51.0	84.2	45.3	42.4	20.8	50.1	23.0	46.7	
1-6		31.1	54.7	44.4	46.4	20.8	42.7	23.9	36.5	
2-1		28.4	34.9	35.6	19.4	20.9	19.6	28.4	19.8	
2-2		34.3	65.2	41.0	19	20.8		28.6	25.6	
2-3		39.5	90.8	48.0	21.6	20.8	22.5	28.2	29.4	
2-4		40.1	69.0	64.7	24.8	20.9	30.2	29.2	30.5	
2-5		37.2	56.0	42.1	27.8	20.9	29.2	29.3	29.6	

Test	Px$_1$	Px$_2$	Px$_3$	Px$_4$	Px$_5$	Px$_6$	Px$_7$	Px$_8$	Px$_9$	Tx$_1$	Tx$_2$
3-0	753	806	766		745	738		777	753	33.6	30.3
3-1	1288	1289	788		758	708		777	771	68.0	30.4
3-2	1306	1304	755		723	680		777	740	129.3	30.4
3-3	1373	2002	779		740	701		777	759	142.3	31.2
3-4	1411	2014	786		724	692		777	759	139.6	31.4
3-5	1100	1295	846		661	627		777	759	132.9	31.9
4-0	752	756	765		745	734		775	751	55.2	33.7
4-1	1231	2125	774		749	699		774	760	98.4	32.8
4-2	1409	2196	769		744	700		774	755	124.2	32.8
4-3	1425	2203	775		735	696		774	756	130.3	32.8
4-4	1165	2199	829		687	644		774	· 759	126.7	32.8
4-5	1133	2197	827		669	630		774	752	134.0	34.3
4-6	1113	2195	799		650	611		774	728	133.9	34.0

Px Unit: Torr
Tx Unit: $^\circ$c

Test	Tx$_3$	Tx$_4$	Tx$_5$	Tx$_6$	Tx$_7$	Tx$_8$	Tx$_9$	Tx 10	Tx$_{11}$	F-1
3-0		27.8	26.4	31.2	20.6	26.5	20.5	33.2	20.3	
3-1		29.6	44.6	33.0	19.3	26.6	19.7	33.1	22.6	
3-2		31.7	97.1	50.2	21.7	26.7	22.4	33.0	30.8	
3-3		31.3	113.7	56.1	24.3	26.8	25.3	33.0	34.8	
3-4		32.6	86.6	53.1	24.7	26.8	28.1	33.0	33.3	
3-5		38.2	86.6	36.5	25.8	26.9	33.2	33.2	30.7	
4-0		28.8	33.3	36.0	19.4	25.6	19.6	33.0	19.7	
4-1		31.0	64.8	39.0	19.6	25.2	20.1	33.0	25.2	
4-2		32.3	90.6	46.7	21.2	25.2	22.0	33.0	29.2	
4-3		33.5	86.0	48.7	22.9	25.2	24.9	33.0	30.8	
4-4		35.0	63.1	41.5	23.6	25.2	29.6	33.1	28.4	
4-5		42.4	73.0	42.6	26.2	25.0	33.2		31.4	
4-6		41.0	69.2	43.7	26.0	25.2	32.5		31.1	

Test	Px_1	Px_2	Px_3	Px_4	Px_5	Px_6	Px_7	Px_8	Px_9	Tx_1	Tx_2
5-1	766	2307	766		764	763		763	765	24.1	23.4
5-2	1256	2226	772		761	719		764	768	94.7	23.5
5-3	1453	2091	767		752	720		764	763	124.9	23.8
5-4	1227	2287	821		704	670		764	767	122.3	23.9
5-5	1392	2296	786		730	700		764	764	128.4	24.3
6-1	1258	2246	775		752	717		765	769	111.9	27.5
6-2	1298	2242	767		741	707		765	760	129.6	27.8
6-3	1343	2281	746		722	692		765	741	138.1	28.2
6-4	1401	2287	752		720	694		765	743	142.8	28.9
7-1	761	2272	765		765	768		763	761	25.1	23.5
7-2	1242	2481	774		764	728		763	767	104.1	23.6
7-3	1246	2483	768		757	723		763	762	117.3	23.6
7-4	1375	2484	731		715	689		764	724	125.9	23.8
7-5	1299	2485	747		689	664		764	722	125.6	24.0
7-6	1335	2485	721		705	681		764	716	133.1	24.3

Px Unit: Torr

Tx Unit: $^\circ C$

293

Test	Tx$_3$	Tx$_4$	Tx$_5$	Tx$_6$	Tx$_7$	Tx$_8$	Tx$_9$	Tx$_{10}$	Tx$_{11}$	F-1
5-1		23.3	22.7	22.0	20.7	21.4	20.9	23.1	21.1	
5-2		22.0	61.0	36.6	20.8	21.3	21.4	23.1	26.0	
5-3		22.8	91.5	48.1	23.2	21.3	24.3	23.2	31.2	
5-4		28.1	53.6	41.2	24.2	21.4	30.1	23.2	28.7	
5-5		30.8	68.9	41.9	24.0	21.2	28.3	23.2	30.7	
6-1		26.7	79.1	43.4	20.9	20.9	21.8	23.4	28.2	
6-2		28.2	98.8	50.7	22.6	20.8	23.7	23.4	31.7	
6-3		28.2	109.3	53.9	23.8	21.0	25.0	23.5	33.7	
6-4		28.8	110.1	55.2	25.5	21.1	26.3	23.5	34.7	
7-1		22.6	21.6	22.6	21.0	20.3	21.3	24.6	21.4	
7-2		22.9	69.8	40.9	21.9	20.5	22.7	24.7	28.1	
7-3		23.4	85.2	46.6	23.2	20.5	24.0	24-7	30.8	
7-4		23.8	91.8	48.5	24.1	20.4	25.2	24.7	31.8	
7-5		25.9	70.1	47.2	24.6	20.3	28.5	24.7	30.8	
7-6		26.5	100.3	51.8	25.3	20.3	26.4	24.7	33.7	

Test	Px_1	Px_2	Px_3	Px_4	Px_5	Px_6	Px_7	Px_8	Px_9	Tx_1	Tx_2
8-1	760	849	764		751	759		764	758	75.5	28.6
8-2	1248	2241	776		756	723		764	767	110.4	28.9
8-3	1395	2353	772		752	724		764	765	130.8	29.1
8-4	1158	2351	826		683	657		765	759	129.1	29.6
8-5	1220	2355	824		701	675		765	767	132.3	30.2
8-6	1205	2351	763		661	638		765	719	138.0	31.4
8-7	1268	2359	814		705	681		765	765	138.4	32.0
8-8	1315	2362	803		710	690		765	764	141.1	32.9
9-1	758	2542	773		755	753		769	757	32.1	27.3
9-2	1189	2540	783		755	720		770	764	34.6	27.7
9-3	1268	2608	776		748	711		770	758	113.7	27.4
9-4	1300	2606	758		731	696		77C	741	128.8	27.6
9-5	1292	2603	745		679	653		770	713	132.1	27.9
9-6	1088	2599	838		667	636		770	752	128.1	28.1
9-7	754	854	768		739	743		770	751	94.5	30.0

Px Unit: Torr
Tx Unit: °C

295

Test	Tx$_3$	Tx$_4$	Tx$_5$	Tx$_6$	Tx$_7$	Tx$_8$	Tx$_9$	Tx$_{10}$	Tx$_{11}$	F-1
8-1		23.2	59.6	32.0	21.3	20.5	21.5	25.0	21.7	
8-2		25.0	77.4	43.3	21.6	20.4	22.3	25.0	28.6	
8-3		26.3	99.8	51.2	23.6	20.8	24.5	25.1	32.7	
8-4		36.1	64.3	41.7	26.0	20.4	32.9	25.2	30.6	
8-5		38.5	60.2	46.9	26.9	20.6	33.5	25.2	32.1	
8-6		39.7	66.1	51.3	27.6	20.6	33.4	25.4	33.5	
8-7		40.8	64.4	51.8	27.8	20.8	34.2	25.5	34.0	
8-8		41.5	73.7	54.1	28.1	20.8	33.8	25.7	35.1	
9-1	34.2	25.6	25.4	27.7	45.3	22.7	36.8	30.9	25.5	
9-2	32.1	25.3	26.8	27.1	22.5	22.6	22.8	30.9	23.1	
9-3	28.1	26.9	81.9	45.9	24.5	22.7	25.2	31.0	31.4	
9-4	30.4	28.1	98.7	52.1	27.0	22.8	27.8	31.0	35.2	
9-5	34.1	29.0	90.0	52.1	28.2	22.8	31.0	31.0	35.2	
9-6	45.7	34.6	72.8	40.5	29.2	22.8	35.9	31.0	33.4	
9-7	36.2	27.8	50.5	34.1	27.8	22.8	28.2	31.1	28.4	

296

Test	Px_1	Px_2	Px_3	Px_4	Px_5	Px_6	Px_7	Px_8	Px_9	Tx_1	Tx_2
10-1	764	2521	765		760	764		759	763	27.3	26.0
10-2	1308	2560	798		713	684		760	756	90.3	26.5
10-3	1169	2621	827		694	664		762	763	111.9	26.2
10-4	1142	2622	814		681	652		762	752	119.6	26.5
10-5	1117	2622	798		665	637		762	737	125.5	27.0
10-6	1096	2621	783		649	622		762	722	129.4	27.7
10-7	1074	2616	769		634	608		763	709	132.3	28.5
10-8	1135	2593	815		675	649		763	751	135.1	29.5
11-1	767	1402	762		767	770		759	767	23.5	23.3
11-2	1228	2642	818		718	680		760	770	107.7	23.7
11-3	1202	2617	805		698	667		761	758	118.7	23.9
11-4	1175	2598	790		681	651		761	742	125.3	24.5
11-5	1148	2592	773		663	634		761	726	129.7	25.2
11-6	1027	2589	819		642	614		761	740	129.8	26.0
11-7	1007	2588	808		628	600		761	728	131.3	26.8
11-8	990	2587	796		614	588		761	716	132.6	27.7
11-9	984	2585	762		643	615		768	664	133.4	28.6

Px Unit: Torr   Tx Unit: $^{\circ}C$

297

Test	Tx_3	Tx_4	Tx_5	Tx_6	Tx_7	Tx_8	Tx_9	Tx_{10}	Tx_{11}	F-1
10-1	28.1	23.7	24.0	26.3	24.9	20.4	29.6	26.8	24.5	
10-2	26.7	24.4	52.9	36.0	22.9	21.2	24.3	86.9	26.8	
10-3	40.2	35.3	53.8	37.0	26.0	21.2	31.3	26.9	29.2	
10-4	43.3	38.8	59.3	40.0	27.9	21.2	33.7	26.9	31.6	
10-5	45.9	41.6	63.8	42.7	29.7	21.3	35.8	26.9	33.7	
10-6	47.5	43.7	67.0	44.5	31.0	21.3	37.2	26.9	35.0	
10-7	48.7	45.4	69.2	46.0	32.0	21.2	38.3	27.0	36.3	
10-8	50.5	47.6	71.8	47.8	32.9	21.3	39.6	27.1	37.5	
11-1	23.8	22.2	23.1	25.2	23.5	19.5	23.7	24.6	23.8	
11-2	37.2	30.9	44.8	37.7	24.6	19.7	29.8	24.6	27.8	
11-3	41.2	35.7	52.8	41.7	26.5	19.6	31.9	24.8	30.4	
11-4	43.5	38.7	56.8	44.3	27.9	19.5	33.7	24.6	32.1	
11-5	45.1	40.9	60.0	46.2	28.9	19.5	34.9	24.6	33.5	
11-6	50.8	45.2	96.1	34.5	29.7	19.5	37.4	24.7	33.4	
11-7	51.0	47.1	99.0	35.3	30.3	19.5	38.0	24.8	34.0	
11-8	51.4	48.3	100.7	35.9	30.6	19.4	38.3	25.0	34.4	
11-9	53.0	50.0	82.2	40.0	30.9	19.4	39.1	25.2	34.3	

Test	Px_1	Px_2	Px_3	Px_4	Px_5	Px_6	Px_7	Px_8	Px_9	Tx_1	Tx_2
12-1	1317	2627	826		757	719		766	766	106.4	27.2
12-2	1319	2628	824		757	718		765	765	110.7	27.2
12-3	1320	2626	823		756	718		765	764	113.1	27.2
12-4	1320	2627	818		753	715		766	762	117.1	27.3
12-5	1321	2626	813		750	712		766	759	120.4	27.3
13-0	41	764	-7	40	4	-11	21	765	41	19.6	20.2
13-1	765	780	771	768	769	765	70	765	766	20.4	20.8
13-2	1398	2398	762	744	733	699	70	766	738	107.1	21.4
13-3	1098	1040	867	770	747	709	70	766	750	110.6	21.6
13-4	1215	1152	786	741	724	688	70	766	729	119.1	22.2
13-5	1308	1241	709	708	693	664	70	766	702	130.5	22.9
13-6	1208	1147	708	710	694	662	70	766	709	135.7	23.7
13-7	1043	989	769	702	671	639	70	766	689	130.0	24.5
13-8	1223	1159	667	668	642	618	70	767	660	138.4	25.7

Px Unit: Torr

Tx Unit: $^{\circ}C$

Test	Tx$_3$	Tx$_4$	Tx$_5$	Tx$_6$	Tx$_7$	Tx$_8$	Tx$_9$	Tx$_{10}$	Tx$_{11}$	F-1
12-1	35.5	31.2	44.8	37.8	23.2	20.3	27.9	31.5	26.5	
12-2	37.3	32.7	46.6	39.3	23.8	20.3	28.7	31.5	27.3	
12-3	38.2	33.6	47.6	40.4	24.2	20.3	29.3	31.5	27.9	
12-4	35.4	35.0	50.3	42.1	24.8	20.3	30.1	31.5	28.9	
12-5	40.4	36.1	52.4	43.8	25.5	20.3	30.9	31.5	29.8	
13-0	19.5	19.5	19.9	19.5	18.0	17.8	19.3	21.7	19.4	
13-1	19.9	19.8	20.1	19.1	20.7	18.4	20.0	19.4	18.6	
13-2	29.2	23.6	57.2	37.1	23.4	18.2	25.2	19.4	25.7	
13-3	42.6	35.9	63.3	28.1	25.1	18.2	31.4	19.4	25.0	
13-4	40.3	37.8	54.9	39.7	26.4	18.0	31.0	19.4	28.8	
13-5	33.2	35.0	91.6	47.2	26.6	18.1	27.5	19.4	31.5	
13-6	31.3	32.8	106.6	51.2	27.0	18.2	27.2	19.4	33.8	
13-7	45.4	37.8	78.2	38.0	27.7	18.3	34.2	19.6	28.7	
13-8	35.5	38.7	96.0	50.2	27.8	18.2	29.5	19.6	33.0	

Test	Px_1	Px_2	Px_3	Px_4	Px_5	Px_6	Px_7	Px_8	Px_9	Tx_1	Tx_2
14-1	1372	2350	774	767	738	718	70	767	758	141.2	28.3
14-2	1140	2350	857	781	742	714	70	767	761	132.7	29.3
14-3	1180	2343	800	753	715	689	70	767	737	134.0	30.8
14-4	1280	2342	723	720	684	664	71	767	710	139.0	30.9
14-5	1275	2348	806	774	737	713	70	767	759	136.7	31.6
14-6	1370	2351	780	774	738	718	70	767	762	141.9	32.3
14-7	1320	2348	762	768	736	713	70	768	759	145.5	33.0
14-8	769	2343	763	771	741	750	71	768	762	113.4	33.6
15-1	1419	2418	770	776	748	712	70	781	756	124.6	27.9
15-2	1375	2421	796	786	752	717	70	780	764	128.2	28.2
15-3	1360	2423	791	781	744	711	70	781	758	133.1	29.1
15-4	1337	2424	803	786	747	713	70	781	762	134.9	29.8
15-5	1238	2426	842	797	754	718	70	781	769	133.2	30.3
15-6	1185	2428	858	795	747	712	70	781	764	133.3	31.7
15-7	1219	2429	835	792	742	709	70	781	763	134.8	32.7

Px Unit: Torr
Tx Unit: °C

301

Test	Tx_3	Tx_4	Tx_5	Tx_6	Tx_7	Tx_8	Tx_9	Tx_{10}	Tx_{11}	F-1
14-1	38.2	37.9	91.4	52.6	28.7	18.3	31.4	19.9	34.6	
14-2	49.3	45.6	82.8	39.6	29.1	18.2	36.9	20.2	30.6	
14-3	46.7	45.4	71.1	45.8	29.5	18.3	35.8	20.4	32.1	
14-4	98.8	43.4	85.9	51.2	29.2	18.2	32.1	20.5	34.1	
14-5	44.8	44.6	67.6	49.8	29.3	18.3	34.7	20.8	33.1	
14-6	38.8	42.8	92.5	53.3	29.0	18.3	32.2	21.0	35.1	
14-7	35.2	41.0	117.4	56.7	29.0	18.2	29.3	21.3	36.8	
14-8	33.8	38.4	95.8	43.6	26.9	18.3	26.6	21.6	25.7	
15-1	30.9	29.1	84.8	45.5	25.5	24.3	26.2	27.1	30.2	
15-2	35.9	31.2	74.1	46.7	26.6	24.3	29.8	27.1	30.7	
15-3	39.8	37.8	75.0	49.1	28.4	24.4	32.0	27.1	32.8	
15-4	41.8	39.0	73.0	49.4	29.1	24.5	33.5	27.1	33.1	
15-5	46.6	41.8	63.4	47.1	29.7	24.5	36.0	27.1	32.2	
15-6	49.6	46.7	74.8	44.5	30.5	24.5	37.6	27.1	32.4	
15-7	48.8	47.9	72.3	46.5	30.8	24.6	37.4	27.2	33.3	

Test	Px_1	Px_2	Px_3	Px_4	Px_5	Px_6	Px_7	Px_8	Px_9	Tx_1	Tx_2
16-1	768	780	766	770	767	765	70	774	769	23.2	23.8
16-2	1202	2488	824	771	750	713	70	776	758	30.1	25.5
16-3	1307	2495	782	762	743	710	70	777	754	32.6	25.9
16-4	1364	2498	765	761	740	714	70	777	755	34.7	26.7
16-5	1377	2499	752	757	738	712	70	777	752	34.4	27.2
16-6	1369	2502	753	762	742	715	70	777	758	37.6	28.1
16-7	1350	2505	749	759	737	711	70	777	754	37.9	28.6
16-8	1348	2506	748	759	734	710	70	777	759	38.7	29.2
17-1	761	784	751	767	751	745	70	777	760	31.6	31.3
17-2	1256	2424	819	774	746	704	70	777	758	33.0	31.4
18-1	1247	2165	815	780	746	703	70	778	761	36.4	35.6
18-2	1231	2168	813	777	742	700	70	778	758	38.0	35.8
18-3	1228	2169	812	776	740	699	70	778	758	39.3	36.1
18-4	1214	2169	810	774	736	696	70	778	755	42.0	36.6
18-5	1217	2169	815	779	740	700	70	778	760	42.4	37.0
18-6	1205	2170	810	774	733	694	70	778	755	43.4	37.6

Px Unit: Torr   Tx Unit: $^{\circ}c$

303

Test	Tx_3	Tx_4	Tx_5	Tx_6	Tx_7	Tx_8	Tx_9	Tx_{10}	Tx_{11}	F-1
16-1	22.8	22.8	22.3	20.4	22.0	22.5	21.3	21.5	20.0	
16-2	26.2	35.3	26.3	36.2	26.1	22.4	31.0	22.0	26.9	
16-3	26.5	36.7	27.3	43.8	27.9	22.4	31.6	22.0	30.8	
16-4	26.7	37.4	29.3	48.2	29.3	22.4	31.8	22.0	33.7	
16-5	26.9	36.7	31.2	50.8	29.5	22.4	30.7	22.1	34.9	
16-6	27.5	35.7	38.8	53.8	30.1	22.4	30.7	22.1	36.8	
16-7	27.6	35.3	34.4	54.9	30.3	22.4	30.7	22.1	37.3	
16-8	28.0	35.0	35.9	55.9	30.6	22.4	31.0	22.1	38.8	
17-1	26.9	28.3	29.2	32.4	22.1	23.6	21.4	28.2	20.1	
17-2	27.3	38.0	34.3	40.0	25.7	23.6	30.5	28.3	27.2	
18-1	28.2	40.8	38.0	48.8	25.8	23.9	31.0	32.1	27.8	
18-2	28.8	44.0	40.5	45.2	28.7	23.8	34.4	32.3	30.9	
18-3	29.3	46.4	42.5	47.5	30.7	24.0	36.7	32.5	33.1	
18-4	29.9	48.7	44.5	49.2	32.5	24.1	38.5	32.7	34.8	
18-5	30.3	50.1	46.0	50.3	33.4	23.7	39.7	32.8	35.8	
18-6	30.7	51.6	47.4	51.2	34.3	23.7	40.7	33.0	36.7	

Test	Px_1	Px_2	Px_3	Px_4	Px_5	Px_6	Px_7	Px_8	Px_9	Tx_1	Tx_2
19-1	760	2403	757	764	757	757	70	771	761	24.2	25.3
19-2	1266	2092	868	803	783	746	70	772	788	26.8	25.2
19-3	1249	2091	869	799	777	741	70	771	784	31.9	25.4
20-1	760	2452	751	764	746	746	70	772	759	33.9	32.8
20-2	1228	2326	768	739	708	675	70	772	727	35.1	32.8
20-3	1207	2326	755	729	698	663	70	772	717	37.9	33.1
20-4	1188	2326	742	718	685	652	69	772	706	38.8	33.5
20-5	1169	2326	728	706	672	639	70	772	694	40.7	34.0
20-6	1150	2326	715	695	658	626	70	772	683	41.0	34.5
21-1	748	783	739	754	738	731	70	773	748	34.2	34.1
21-2	1247	2361	814	779	746	704	70	773	758	33.3	33.5
21-3	1246	2366	817	776	747	705	70	773	760	36.1	33.6
21-4	1239	2365	812	773	743	703	70	773	757	37.6	34.0
21-5	1239	2367	813	774	742	703	70	773	758	39.4	34.5

Px Unit: Torr
Tx Unit: $^{\circ}c$

Test	Tx$_3$	Tx$_4$	Tx$_5$	Tx$_6$	Tx$_7$	Tx$_8$	Tx$_9$	Tx$_{10}$	Tx$_{11}$	F-1
19-1	23.6	24.1	23.5	21.8	21.9	23.6	21.2	22.8	19.9	
19-2	23.6	33.4	29.8	34.3	24.8	23.3	29.6	22.8	25.2	
19-3	24.1	39.5	34.8	37.9	28.4	23.1	34.0	22.8	28.9	
20-1	25.1	32.4	34.9	33.7	22.4	23.2	21.7	25.8	20.4	
20-2	25.2	39.6	36.7	43.5	26.8	22.9	31.4	26.5	29.0	
20-3	25.5	41.9	38.6	46.2	28.4	22.7	33.2	26.8	31.0	
20-4	25.9	43.6	40.0	48.0	29.7	22.7	34.7	27.0	32.4	
20-5	26.3	44.8	41.1	49.0	30.4	22.6	35.3	27.3	33.3	
20-6	26.5	45.7	42.0	49.9	31.0	22.4	36.0	27.5	33.9	
21-1	26.5	32.2	33.0	37.7	22.2	23.1	21.5	30.2	20.2	
21-2	25.9	38.0	35.2	40.2	25.3	23.2	30.2	31.5	27.0	
21-3	26.2	41.6	38.3	43.9	27.6	23.1	33.1	31.6	29.7	
21-4	26.7	44.4	40.5	46.4	29.4	23.2	35.1	31.7	31.7	
21-5	27.1	46.8	42.4	48.1	30.5	23.1	36.5	31.8	33.1	

Test	Px_1	Px_2	Px_3	Px_4	Px_5	Px_6	Px_7	Px_8	Px_9	Tx_1	Tx_2
22-1	755	2451	748	768	750	746	70	773	756	27.1	29.1
22-2	1230	2230	821	774	747	707	70	773	757	31.2	29.1
22-3	1195	2232	835	777	747	708	70	773	758	33.9	29.5
22-4	1167	2232	838	775	743	704	70	773	755	35.8	30.1
22-5	1157	2239	842	776	742	704	70	773	756	38.1	30.8
22-6	1140	2234	842	779	737	700	70	773	753	40.3	31.5
23-1	1331	2373	775	765	731	700	70	773	752	39.7	34.0
23-2	1332	2377	780	769	735	704	70	773	756	41.2	34.6
23-3	1318	2378	772	764	727	697	70	773	750	42.4	35.0
23-4	1320	2381	775	767	729	700	70	773	753	43.3	35.6
24-1	758	2470	752	762	750	743	70	771	759	25.9	25.4
24-2	1268	2418	797	764	740	700	69	772	753	31.4	26.0
24-3	1254	2416	790	758	732	693	69	772	747	33.0	26.3
24-4	1245	2413	784	753	726	687	69	772	740	34.1	26.5
24-5	1233	2410	776	746	718	680	70	772	735	35.2	26.9
24-6	1222	2406	769	740	711	673	69	772	729	36.3	27.2
24-7	758	2399	748	760	740	736	70	772	758	38.5	28.0

Px Unit: Torr   Tx Unit: $°C$

Test	Tx$_3$	Tx$_4$	Tx$_5$	Tx$_6$	Tx$_7$	Tx$_8$	Tx$_9$	Tx$_{10}$	Tx$_{11}$	F-1
22-1	25.3	27.1	26.7	30.5	22.4	22.8	21.7	32.3	20.4	
22-2	25.6	37.5	33.6	38.4	25.9	22.9	30.9	32.2	27.1	
22-3	26.2	42.3	37.8	39.0	28.0	22.9	34.1	32.2	29.0	
22-4	26.4	45.5	40.8	39.4	29.4	22.8	36.1	32.2	30.3	
22-5	26.9	48.1	43.9	39.6	30.5	22.8	37.6	32.2	31.4	
22-6	27.3	50.0	45.5	39.7	31.2	22.9	38.5	32.2	32.2	
23-1	27.3	42.2	40.1	47.8	27.4	23.3	31.4	32.1	31.3	
23-2	27.6	43.5	40.9	50.6	29.7	23.1	34.0	32.2	33.9	
23-3	28.1	45.0	41.9	52.7	31.4	23.2	35.8	32.2	35.7	
23-4	28.3	46.1	42.8	54.0	32.4	23.3	36.9	32.3	36.7	
24-1	26.4	24.5	24.3	22.2	22.3	22.5	21.5	24.6	20.2	
24-2	27.3	37.2	33.1	41.8	27.4	22.7	31.9	24.6	29.4	
24-3	27.4	38.7	34.5	43.4	28.3	22.9	32.9	24.6	30.5	
24-4	27.7	39.8	35.4	44.2	28.7	23.0	33.6	24.6	31.0	
24-5	27.9	40.8	36.3	45.2	29.3	23.1	34.2	24.7	31.7	
24-6	28.0	41.6	37.2	45.9	29.7	23.1	34.7	24.7	32.2	
24-7	28.5	36.7	34.6	33.1	27.5	23.3	27.1	24.7	26.0	

308

Test	Px_1	Px_2	Px_3	Px_4	Px_5	Px_6	Px_7	Px_8	Px_9	Tx_1	Tx_2
25-1	760	780	757	758	756	752	20	767	760	21.3	21.8
25-2	766	2490	767	766	768	764	20	769	767	21.8	22.2
25-3	1256	2248	793	751	741	705	69	769	745	23.9	22.3
25-4	1248	2248	792	750	740	703	69	769	744	25.0	22.5
25-5	1227	2249	784	742	730	695	69	769	736	27.6	22.9
25-6	1206	2251	774	733	718	684	69	769	726	31.8	23.5
25-7	1186	2252	762	722	706	672	69	769	715	33.7	24.3
25-8	1165	2253	749	711	692	659	70	769	704	35.2	25.2
25-9	746	1986	741	744	735	736	70	769	744	36.9	26.3
26-1	761	2429	762	763	763	765	70	768	761	23.4	24.0
26-2	1338	2514	727	724	712	686	70	769	720	42.5	24.8
26-3	1329	2514	719	718	709	679	70	769	713	47.0	25.1
26-4	1297	2513	705	705	687	665	69	769	700	54.6	25.8
26-5	1270	2513	688	692	671	698	70	769	687	61.0	26.6

Px Unit: Torr
Tx Unit: $^\circ$C

Test	Tx_3	Tx_4	Tx_5	Tx_6	Tx_7	Tx_8	Tx_9	Tx_{10}	Tx_{11}	F-1
25-1	20.7	21.5	21.3	20.1	20.6	20.4	21.7	20.6	20.6	
25-2	21.3	22.6	22.8	20.8	20.4	20.5	21.7	20.5	20.5	
25-3	21.6	29.0	26.2	35.8	25.0	20.9	28.4	20.5	25.9	
25-4	21.8	32.0	28.1	37.8	26.1	20.9	29.8	20.5	27.2	
25-5	22.3	35.8	31.3	41.2	27.8	21.1	32.2	20.5	29.5	
25-6	22.7	38.5	33.7	43.5	29.2	21.2	33.9	20.5	31.1	
25-7	23.1	40.5	35.6	45.0	30.1	21.2	34.9	20.6	32.3	
25-8	23.4	42.0	37.8	46.2	30.7	21.2	35.7	20.7	32.9	
25-9	23.4	34.6	33.8	32.0	27.7	21.3	27.2	20.7	26.0	
26-1	23.1	22.3	22.0	21.0	23.5	21.4	22.7	21.5	21.4	
26-2	29.0	31.1	49.4	46.9	28.3	22.5	29.6	21.6	32.4	
26-3	25.4	31.6	51.4	48.4	29.0	22.6	30.3	21.6	33.4	
26-4	26.0	32.7	54.5	50.7	30.3	22.6	31.6	21.7	35.0	
26-5	26.7	33.8	57.2	52.4	31.0	22.7	32.5	21.7	36.1	

Test	Px_1	Px_2	Px_3	Px_4	Px_5	Px_6	Px_7	Px_8	Px_9	Tx_1	Tx_2
27-1	760	2503	762	761	763	763	70	769	761	22.5	24.0
27-2	1362	2369	767	751	737	712	69	769	747	54.7	25.4
27-3	1346	2369	757	743	728	703	69	769	738	57.8	25.8
27-4	1315	2369	739	727	708	685	69	769	722	64.1	26.6
27-5	1285	2368	721	711	690	668	70	769	707	68.2	27.4
27-6	1258	2368	705	696	673	651	69	769	692	72.2	28.4
27-7	749	2366	729	733	717	724	70	769	731	74.8	29.3
28-1	758	2548	743	764	749	752	70	777	755	28.8	28.9
28-2	1263	2267	778	757	731	699	70	777	742	30.7	28.9
28-3	1225	2341	758	742	703	675	70	778	724	60.0	33.7
29-1	760	2421	758	763	754	759	70		759	43.2	27.8
29-2	1249	2121	789	752	732	702	69	774	741	106.7	27.9
29-3	1130	2118	706	684	648	625	69	775	673	137.4	32.9

Px Unit: Torr
Tx Unit: $^{\circ}$c

311

Test	Tx_3	Tx_4	Tx_5	Tx_6	Tx_7	Tx_8	Tx_9	Tx_{10}	Tx_{11}	F-1
27-1	21.7	22.8	22.7	22.0	22.7	21.7	22.0	20.8	20.7	
27-2	23.3	34.8	35.0	49.2	28.8	21.0	31.8	20.9	33.9	
27-3	23.5	35.6	36.1	49.9	29.2	21.0	32.2	20.9	33.8	
27-4	23.8	36.9	37.5	51.0	29.9	20.8	32.8	20.9	34.5	
27-5	24.1	37.8	39.4	51.9	30.3	20.8	33.2	21.0	35.0	
27-6	24.4	38.5	40.1	52.4	30.4	20.7	33.3	21.0	35.2	
27-7	24.7	38.4	40.8	44.9	30.4	20.7	30.7	21.1	31.3	
28-1	33.8	27.6	27.2	24.0	23.7	24.6	23.0	30.0	21.7	
28-2	33.4	32.8	30.6	35.3	25.2	24.6	28.2	30.0	26.0	
28-3	35.1	41.1	37.4	45.5	29.6	26.0	33.9	30.4	31.7	
29-1	27.6	25.8	26.3	26.1	23.6		23.0	26.0	21.7	
29-2	27.8	32.8	30.2	37.2	25.4	24.2	28.9	26.1	26.5	
29-3	31.4	46.4	42.5	50.8	32.4	23.9	37.3	26.6	35.3	

Test	Px_1	Px_2	Px_3	Px_4	Px_5	Px_6	Px_7	Px_8	Px_9	Tx_1	Tx_2
30-1	770	2365	777	766	778	782	70	762	768	22.5	23.5
30-2	1228	2211	779	767	775	741	70	762	769	94.7	23.5
30-3	1378	2213	746	734	738	713	69	762	736	115.9	23.6
30-4	1247	2214	777	732	728	700	68	763	728	125.4	24.3
30-5	1273	2215	747	718	712	688	69	763	716	131.3	24.9
30-6	1264	2215	710	695	685	665	69	763	694	138.1	26.2
30-7	767	936	766	761	758	768	70	764	762	110.8	28.5
31-1	760	780	761	758	757	757	70	766	757	60.2	32.2
31-2	1228	2401	816	759	747	711	69	766	749	116.8	32.2
31-3	1266	2400	780	743	730	697	69	766	735	128.7	32.3
31-4	1306	2400	737	721	707	679	69	766	717	136.8	32.6
31-5	1312	2400	714	710	696	669	88	766	707	141.1	32.9

Px Unit: Torr
Tx Unit: °c

Test	Tx_3	Tx_4	Tx_5	Tx_6	Tx_7	Tx_8	Tx_9	Tx_{10}	Tx_{11}	F-1
30-1	22.7	22.6	22.4	22.9		22.0	22.6	22.0	21.4	
30-2	22.8	23.1	48.8	38.2	23.9	22.0	23.6	22.0	26.5	
30-3	23.0	25.8	51.2	44.8	25.7	22.1	26.2	22.0	29.5	
30-4	23.9	35.8	31.9	46.6	28.8	22.1	33.2	22.0	31.3	
30-5	24.2	38.1	34.0	50.5	30.0	22.1	33.5	22.0	33.7	
30-6	24.8	38.0	45.8	53.7	30.8	22.2	33.4	22.1	35.4	
30-7	25.7	30.7	39-6	38.3	27.2	22.3	26.8	22.2	25.8	
31-1	25.2	27.1	32.5	38.7	26.3	22.5	25.0	24.3	24.3	
31-2	25.9	36.0	33.2	41.9	26.7	22.7	31.3	24.7	27.8	
31-3	26.5	39.6	36.0	48.4	28.9	22.7	33.4	24.9	31.6	
31-4	27.3	39.4	39.4	53.3	30.1	22.9	33.1	25.0	34.4	
31-5	27.8	39.2	58.9	55.5	30.5	23.0	32.2	25.1	35.8	

314

APPENDIX B

advanced dynamic instrumentation **KISTLER**

PIEZOTRON® MINIATURE

Pressure Sensors

...WITH INTEGRAL ADAPTORS

Features

- LOW IMPEDANCE OUTPUT
- ACCELERATION COMPENSATED
- HIGH RESOLUTION 10,000 : 1 RANGE

- HIGH RESONANT FREQUENCY
- STABLE QUARTZ SENSORS
- KISTLER QUALITY
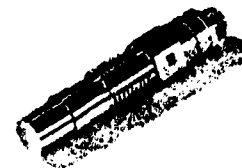
The new 201 Series Miniature Pressure Transducers with integral connector/adaptors are the latest development in this field. The 201 design is based on the highly successful 601 type quartz sensor produced for many years. However, the addition of Piezotron low impedance electronics adds important capabilities to this mini-gage. The 201 with its internal impedance converter gives a direct, high level, voltage signal with less than 100 ohms output impedance. Long, moving cables present no problem and special cables are not required. Also, a charge amplifier is no longer necessary. A less expensive coupler may be used, instead. All 201

Mini-Gages are interchangeable with 601 or 603 transducers for present or new uses.

The unit construction of the transducer and adaptor eliminates sealing problems and saves installation time.
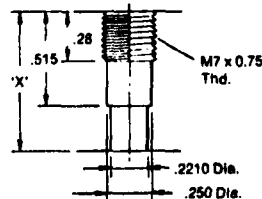
Four models of the 201 Sensor are offered with full scale ranges from 0 to 100 psi in Model 201B5 and 0 to 5,000 psi in Model 201B1.

The 201 is not limited by shock or vibration except in the most extreme environments, and is enclosed in a rugged, sealed, stainless steel case.

Dimensions — 201 Series

Coax. Conn. 1C-32 Thd.

.28 Dia.

9/32 Hex.

M7 x 0.75 Thd

.20

.32

.80

.235

1.4

.248 Dia.

.218 Dia.

Cavity Dimensions

.28

.515

'X'

M7 x 0.75 Thd.

.2210 Dia.

.250 Dia.
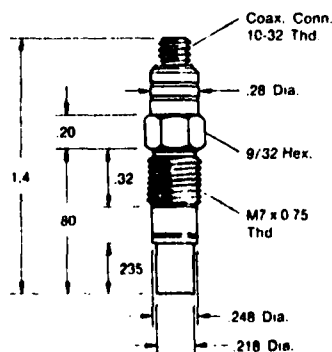
Dim. 'X'	.70 for Flush
	.74 Recessed

Flush mounting exposes the sensor to the pressure source for maximum fidelity. Recessed mounting affords a measure of protection for the sensor diaphragm, and permits use of ablative coating for maximum protection.

Recessed Mounting
**(where installation area is restricted)**
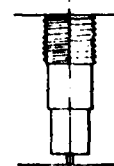
The cavity for the mounting must be carefully machined to match dimensions of individual transducer and seal. The optimum space between diaphragm and bottom of cavity is .002 in. High frequency response is somewhat impaired by this method of installation.

201 SERIES MINI-GAGE

Typical PIEZOTRON® Pressure Sensing System

COUPLER

128M (x) CABLE

201 TRANSDUCER

READOUT
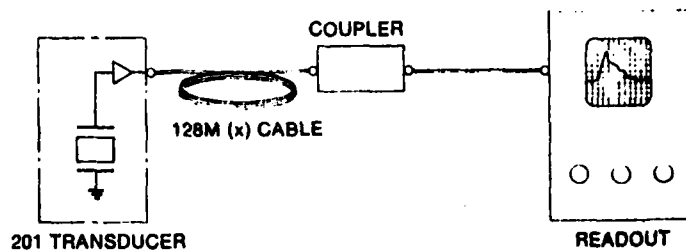
Couplers

To complete the system a wide choice of couplers is offered in the 548 and 549 series. Optional filters and several types of power inputs are available. Model 587D Coupler provides increased capability. Please refer to our Coupler Data Sheet for details.

In addition Models 583, 503D and 504D Laboratory Amplifiers are offered with extensive versatility and many options for more complete pressure studies.

Specifications

	UNITS	201B1	201B2	201B4	201B5
PERFORMANCE					
Pressure Range, 5V out	psi	5,000	500	200	100
Overrange	psi	7,500	750	300	150
Resolution (noise)	psi rms	0.05	0.005	0.002	0.001
Maximum Pressure	psi	15,000	5,000	2,000	1,000
Sensitivity	mV/psi	1	10	25	50
Linearity, B.F.S.L.	%	1	1	1	1
Resonant Frequency, nom.	kHz	500	500	500	250
Rise Time, 10-90%	μ sec	1	1	1	2
Time Constant, R.T.	sec	1,500	400	200	100
Low Frequency Response, −5%	Hz	0.0003	0.001	0.0025	0.005
High Frequency Response, +5%	Hz	200,000	200,000	200,000	100,000
ENVIRONMENTAL				Common Specs	
Vibration Sensitivity, max.	psi/g	0.002	0.002	0.002	0.002
Shock, 1 ms	g	5,000	5,000	5,000	5,000
Vibration Limit	g	500	500	500	500
Temperature Range	°F	−65 to 280	−65 to 280	−65 to 280	−65 to 280
Temperature Sensitivity Shift	/°F	0.03%	0.03%	0.03%	
ELECTRICAL					
Output Current, min.	mA	2	2	2	2
Polarity, pressure increase		Negative	Negative	Negative	Negative
Bias Voltage	V	11 ±2	11 ±2	11 ±2	11 ±2
Circuit Return		Case	Case	Case	Case
Output Impedance, max.	ohms	100	100	100	100
MECHANICAL					
Weight	gms	< 10	< 10	< 10	< 10
Case and Diaphragm Material		Stainless St.	Stainless St.	Stainless St.	Stainless St.
Mounting Torque	in-lb	24	24	24	24
Sealing		All Welded	All Welded	All Welded	All Welded
POWER SUPPLY					
Constant Current Source	mA	4 ±1	4 ±1	4 ±1	4 ±1
Supply Ripple, max.	mV rms	25	25	25	25
Supply Voltage, no load	VDC	20-30	20-30	20-30	20-30
Source Impedance, nom.	ohms	250 k	250 k	250 k	250 k

To order, Specify:

☐ Model 201B1, 201B2, 201B4, 201B5 (includes one each Model 600A3, Stainless Steel Sleeve .248 long, 600A6, Brass Seal, .060 long, and 600A11, Teflon Seal .060 long).

☐ Tap, Model 600A13 (M7 x 0.75) if required to thread mounting cavity.

☐ Model 128M (x) Cable, length (x) .... ft. Standard length, 10 ft.

☐ Extension Cables, see Data Sheet

☐ Model 623B Ruggedized Adaptor, 3/8-24 thd., 7/16" hex.

Choose:

☐ 548 Series Coupler

☐ 549 Series Coupler

☐ 587D Coupler

☐ 503D Dual-Mode Amplifier

☐ 504D Dual-Mode Amplifier

See data sheets on above electronics for choice of models & filters.

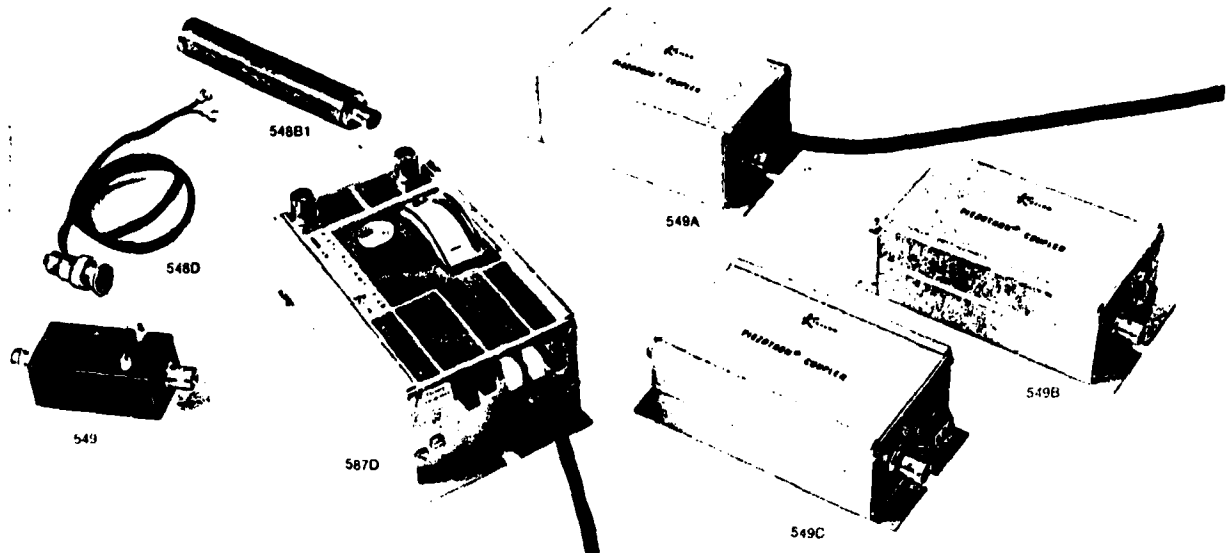## Kistler Instrument Company

division of Sundstrand Data Control, Inc

OVERLAKE INDUSTRIAL PARK, REDMOND, WASHINGTON 98052
PHONE 206/885-3737 · TWX 910/449-2860 · TELEX 3-2313

PRINTED IN USA

242-7/72

PIEZOTRON® Couplers

Kistler Instruments was recently awarded U.S. Patent No. 3,569,747 for its invention of Piezotron low impedance transducers. A miniature electronic circuit is built into the transducer housing which converts the high impedance generated charge to a high level voltage signal with a low impedance output below 100 ohms. The power to the transducer from a remote coupler and the signal from the transducer to the readout equipment are transmitted over a single inexpensive cable. This eliminates all of the inherent piezoelectric high impedance problems of electrical leakage, cable noise and signal attenuation and allows the transducers to be used in contaminated environments and with long and moving cables. Special low noise cables are not required and the use of charge amplifiers is eliminated. A wide selection of these transducers are now available for pressure, vibration, shock and impact measurements.

A series of external impedance converters is offered for use with existing high impedance transducers and is described in a separate brochure. In addition to the above application, converters extend the useage to load and force measurements.

To complete the low impedance system, a choice of couplers as described herein are offered. The coupler is a common interconnection device through which power is supplied to the Piezotron transducer (or converter) and the useful signal is extracted (de-coupled) and transmitted to the readout equipment.

Kistler's wide selection of couplers offers a choice of power requirements, and signal conditioning options tailored to the needs of industrial, laboratory and field use.

## PIEZOTRON SYSTEM DIAGRAM
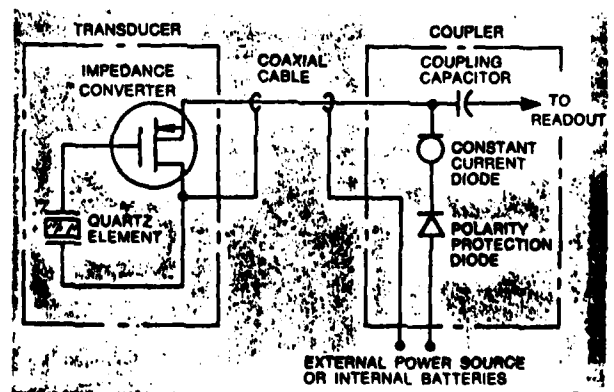
BASIC COUPLERS

548D is the simplest in the line. It is DC coupled and requires a 24V DC external power source. It should be remembered when using this coupler that an 11 volt bias results in the output with the useful signal impressed over it.
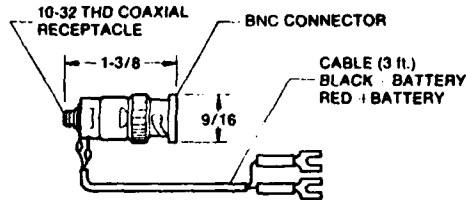
549 is AC coupled and eliminates the bias voltage, giving only the useful dynamic response of the transducer. It requires a 24V DC external power source.
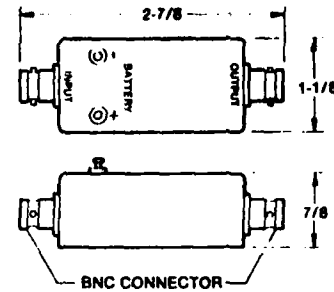
548B1 is AC coupled. It is self-contained and has an internal battery, so that no external power is required.
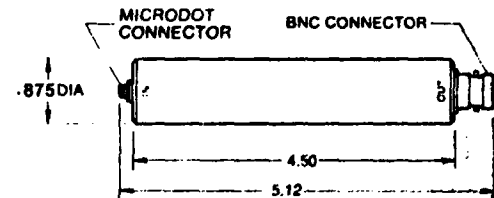
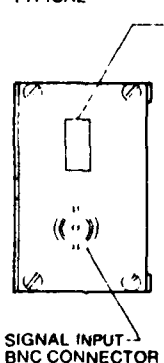| 548B1	548D	549	Specifications	Units
			Piezotron Input	
1 ± 0.1	3.9 ± 0.5	3.9 ± 0.5	Current (Note 1)	mA
5	10	10	Full Scale	Vpp
NA	NA	NA	Noise	µVpp
µDOT 10-32	µDOT 10-32	BNC jack	Connector	
			Impedance	k Ohm
			Transfer Characteristics	
1	1	1	Gain	
			Frequency Response w/1 meg load ± 5% 10 Vpp output	
NA	DC to Note 1	NA	DC mode	Hz
.03 to Note 1	NA	0.07 to Note 1	AC mode	Hz
NA	NA	NA	Filter Supplied, unless otherwise spec.*	
			Output	
<100 in series with 15µF	<100	<100 in series with 47µF	Impedance	Ohm
0	11 nominal	0	Bias	Volts
			Full Scale Signal	
5	10	10	Voltage	Vpp
			Current (± 20%)	mApp
BNC jack	BNC jack	BNC jack	Connector	
			Power	
Built-in Battery	+ 28 ± 4	+ 28 ± 4	Input	Volts
1 ± 0.1	3.9 ± 0.5	3.9 ± 0.5	Current	mA
None	Leads	Solderlugs	Connector	

The 549 A, B, & C Couplers incorporate plug-in filters to minimize extraneous signals. They are all AC coupled and offer 3 choices of power inputs.

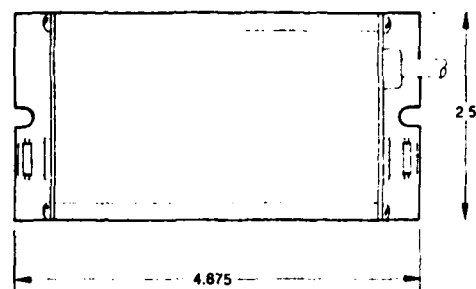549A is line powered. It includes a 3-wire cord for 115 Volt AC input.

549C is designed mainly for field or vehicle use and is powered by an external 12V DC power source. A DC to DC converter is incorporated for increasing the voltage to a level required for Piezotron applications.

549B has the added feature of being completely self-contained with internal batteries for which an 'ON-OFF' switch is provided. Three 9 volt, 500 mAh mercury batteries are included with the original unit, which will give about 125 hours operation. However, most types of 9 volt batteries may be used as replacements.
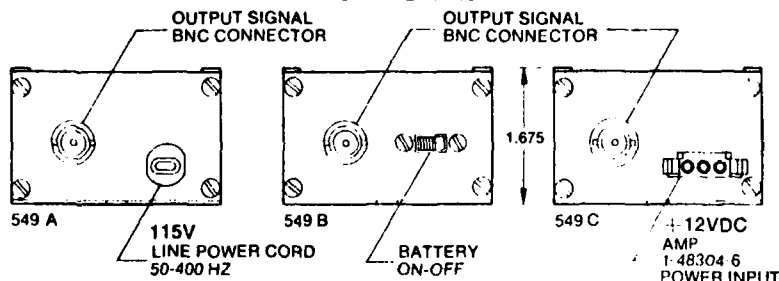

LEFT END VIEW – TYPICAL
FILTER NO. WINDOW
SIGNAL INPUT – BNC CONNECTOR
2.5
4.875

RIGHT END VIEWS
OUTPUT SIGNAL BNC CONNECTOR
OUTPUT SIGNAL BNC CONNECTOR
1.675
549 A — 115V LINE POWER CORD 50-400 HZ
549 B — BATTERY ON-OFF
549 C — +12VDC AMP 1-48304 6 POWER INPUT

COUPLERS WITH FILTERS

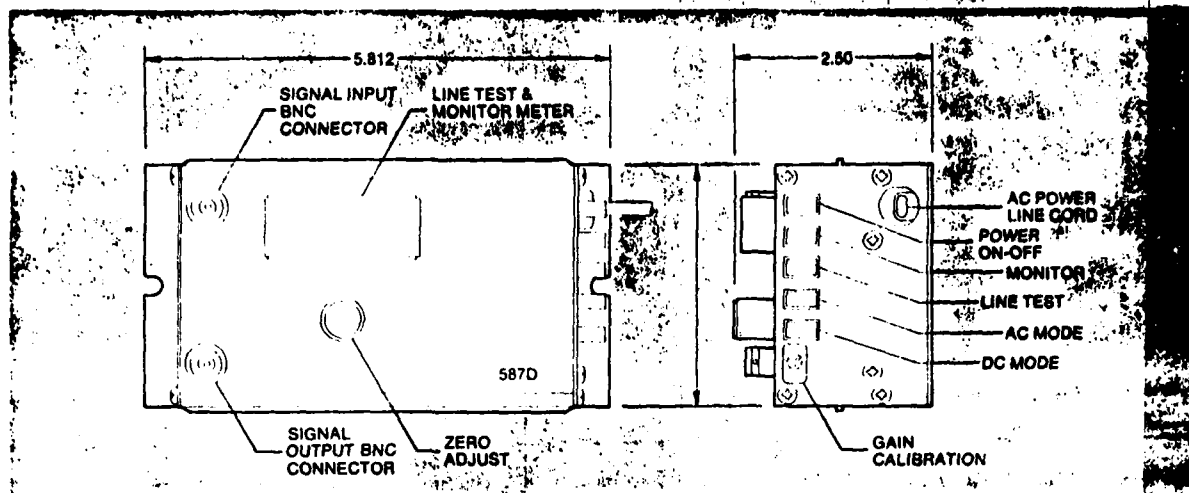| 549A	549B	549C	587D
.9 ± 0.5	2 ± 0.2	3.9 ± 0.5	3.9 ± 0.5
10	10	10	10
160	20	300	250
BNC jack	BNC jack	BNC jack	BNC jack
>200	~350	>200	20
	1	1	0.5 to 2
NA	NA	NA	0 to 70k †
0.07 to 300k	0.07 to 300k	0.07 to 300k	0.5 to 70k
545B14	545B14	545B14	545B13
<15 in series with 47µF	<15 in series with 47µF	<15 in series with 47µF	20
0	0	0	± 2.5 Adjustable
90	10	10	10
10	4	8	20
BNC jack	BNC jack	BNC jack	BNC jack
115 ± 10 80-400 Hz	3 Built-in Batteries	12 ± 2DC	115 ± 10 rms 80-400 Hz
10 rms	4 DC	160DC	10 rms
3-wire cord	None	AMP 1-48304-6	3-wire cord

† 150 kHz with 545B14 Filter

Note 1: A Piezotron current of less than 3.9mA will not effect the performance of the Piezotron Transducer. However, it limits the useable cable length. The maximum undistorted frequency at a given signal amplitude with a resistive load greater than 10k Ω is determined by the following relation:

$$f\,max\,[kHz] = \frac{.32 \times (\text{Piez. input current [mA]} - 1\,[mA])}{(\text{cable capacitance } [\mu F] \times (\text{Signal amplitude [Vpp]})}$$

*Optional: Bandwidth Limiting Filters (lowpass, 12 db/Octave roll-off)

Model 545B11	3 db down at 10kHz
Model 545B13	3 db down at 100kHz
Model 545B14	extends response capability beyond 100kHz
Model 545B16	3 db down at 1kHz
Model 545B17	3 db down at 5kHz
Model 545B18	3 db down at 60kHz

Diagram labels: 5.812, 2.50, SIGNAL INPUT BNC CONNECTOR, LINE TEST & MONITOR METER, AC POWER LINE CORD, POWER ON-OFF, MONITOR, LINE TEST, AC MODE, DC MODE, SIGNAL OUTPUT BNC CONNECTOR, ZERO ADJUST, 587D, GAIN CALIBRATION

587D Coupler, Line Powered

IN THE LABORATORY, where versatility and calibration techniques, are necessary and 115V AC power is accessible, we suggest the 587D Coupler.

It provides a complete and inexpensive system capability for low impedance transducers used in pressure, shock, vibration and force measurement. The coupler's frequency range of 0.1 to 100kHz makes it ideal for pressure measurement.

The 587D Coupler incorporates both AC and DC modes. The AC mode of operation is used for short term events, as in dynamic pressure and vibration, and where variable temperature conditions exist. The DC mode permits static calibration of pressure transducers and measurement of long term events up to the capability of the transducer.

This compact, sturdy, aluminum cased coupler has momentary-type push buttons for Line Test and Monitor. The Line Test Button gives an input integrity check, while the Monitor Button, when in DC mode, gives a direct systems readout or zero check. These indications are read on the integral meter. A choice of filters is provided to tailor response and adjustment. A Zeroing Knob is provided for ease of adjustment. In addition, there is an external screwdriver Calibration Adjustment with a range of 0.5 to 2X. When not matched to a system the coupler is set for unity gain. A viewing window is provided for determining the model number of the filter installed.

LAB AMPLIFIERS

For even greater versatility, please refer to our Piezotron and Dual Mode Amplifier data sheets, i.e. 583, 584, 503D and 504D. With these, an additional wide variety of features and options are offered including range control, time constant selection, calibration facility, automatic zeroing, a variety of output signals for various readout instruments and many others. 19" rack mounted, multi-channel couplers are available.

Ordering Information, Specify:

Model 548B1 Piezotron Coupler w/138M3 Cable (length 3 ft.)

Model 548D Piezotron Coupler

Model 549 Piezotron Coupler w/138M3 Cable (length 3 ft.)

Model 549A Piezotron Coupler w/138M3 Cable (length 3 ft.)

Model 549B Piezotron Coupler w/138M3 Cable (length 3 ft.) and 3 NEDA 1604M Batteries

Model 549C Piezotron Coupler w/138M3 Cable (length 3 ft.) and mating power connector KP 42

Model 587D Piezotron Coupler w/138M3 Cable (length 3 ft.)

Set of 3 Replacement Batteries, NEDA 1604M Type (for 549B Coupler)

1 Replacement Battery, Mallory No. 303932 or Equal (for 548B1 Coupler)

See Kistler's Transducer Cables & Cable Adaptors Data Sheet.